Imperial College London

Optical Spectroscopic Studies of Charge Carrier Dynamics in Lead Halide Perovskite Solar Cells

Weidong Xu

Submitted to the Imperial College London for the degree of Doctor of Philosophy
Centre of Processable Electronics and Department of Chemistry
October 2022

Declaration

Statement of Originality

I hereby declare that the contents of this thesis are a summary of my own work, except where specific reference is made to the contribution of others. This thesis has not been submitted in whole or in part for consideration for any other degree or qualification at this or any other university.

Copyright Declaration

Weidong Xu

London, October 2022

Abstract

This thesis focuses on using various optical spectroscopic methodologies to study the impact of different materials and device processing on charge carrier dynamics that correlate to device performance in perovskite solar cells (PSCs). The underlying dynamics, including recombination, transport and transfer, are mainly investigated by voltage-dependent photoluminescence (PL), electroluminescence (EL), time-resolved photoluminescence (TRPL) and transient absorption (TA) spectroscopy. Different-processed perovskite layers with controlled morphology and defect densities, and their contacted charge transport layers (CTLs) with varied energetics and mobilities are studied.

At open circuit (OC), for high-quality perovskites with lower defect densities, as fewer charges recombined non-radiatively, the PSC is expected to show larger PL emission. Likewise, perovskite films with interlayers or their complete cells with suppressed surface/interface recombination are also supposed to show high PL at OC. When a PSC is switched to short circuit (SC), most of the charges should be extracted to the external circuit, such that the device PL is expected to be significantly reduced. Thus, this thesis introduces a figure of merit, named device OC to SC PL quenching efficiency (PLQ_{OC-SC}), for estimating the charge extraction efficiency in different-processed PSCs. The results show that efficient PSCs have high values of (PLQ_{OC-SC}), while low values are observed in the cells with either severe non-radiative recombination or impeded charge extraction.

In addition to the device OC to SC PL measurement, a more quantitative analysis based on operando PL measurements, which converts the absolute PL emission into quasi-fermi-level-splitting ($QFLS$), is implemented on PSCs with varied energetic alignment at the perovskite/electron transport layer (ETL) interface. This measurement system allows a real-time PL spectrum acquisition while doing a J-V scan. The results show that a mismatch of the interface energetic alignment will reduce device performance either by accumulating charges in bulk or by introducing surface recombination. More importantly, high $QFLS$ values indicative of substantial charge accumulation are observed in all devices, even at SC. This phenomenon can be attributed to the screening of the internal electric field by ion migration, which is evidenced by drift-diffusion-based simulation results.

In the final chapter, a simple TRPL method is demonstrated to characterise the kinetics of charge transport across the bulk perovskite and charge transfer from the perovskite layer to the CTLs. This work elucidates the dependence of these dynamics on film thickness, grain boundaries (GBs), and CTLs. Using asymmetric laser excitation, charge transport and transfer can be selectively probed by generating charges close to and far from the heterojunction interface. These results are further correlated with device performance. The finding suggests that both film thickness and GBs affect the asymmetry between electron and hole charge transport across the bulk perovskite and charge transfer from the bulk perovskite to the respective CTLs.

Acknowledgements

It is a wonderful research journey that I have enjoyed most. In addition, it is the people who helped me make this more fantastic.

- I want to acknowledge my supervisor Prof James Durrant significantly, for giving me unceasing encouragement and support. I appreciate his patience in guiding me into the spectroscopic field and teaching me how to think like a physicist. Thank you for imparting valuable knowledge to me. I would also like to thank my co-supervisor, Prof Martyn McLachlan, for his consistent support and help.
- My sincere thanks to China Scholarship Council and Imperial College London for funding me to be able to complete this PhD study.
- I want to thank my collaborators, Dr Tian Du, Dr Thomas Macdonald, Dr Chieh-Ting Lin, Dr Yong Li, Dr Xufeng Ling, Xueping Liu and Ganghong Min, for giving me continuous perovskite materials and devices support, Dr Michael Sachs and Lucy Hart for their numerical simulation help. Without you, I couldn't have done this thesis.
- I would like to thank Dr Benjamin Moss for his help in building the operando PL system, and for teaching me many new skills in LabVIEW, MATLAB, electrochemical spectroscopy, and, most importantly, climbing.
- Special thanks to Dr Jinhyun Kim (JK) for teaching me all his excellent lab skills, especially in PL and TA spectroscopy measurements, at the beginning of my study.
- Huge thanks to Dr Xiaoe Li for your always kindness and consistent support in both lab and life, and also to Dr Pabitra Shakya Tuladhar for your unceasing technical support and mental care.
- Many thanks to the other Durrant group members, Richard, Hyojung, Seb, Yifan, Camilo, Tack-ho, Jiaying, Anna, Helen, Reshma, Shababa, Sacha, Carlota, Ludmilla, Yu-Han, Ernest, Madeleine, Laia, Jinho, Ching-Hong, Wenxing, Yiwen, Tianhao, Lei, Caiwu, Deping, Teng, Sora, Sam, Aniket, Lousie, for your continuous support on both science and more importantly many other wonderful things we've been doing together. Thank you for all the parties we've danced to, all beers we've cheered, and all the BANDGAPs we've celebrated.

- Thanks to the Centre for Plastic Electronics for the support and friendships—from the wonderful Cohort 9 and various close friends I have made along the way.
- To Muzi, thank you for your company at my most difficult time, for celebrating the great times, and for understanding me.
- Most importantly, enormous thanks for my family's steadfast love and support, mother, father, sister and brother-in-law.

Dedication

To my parents and sister

‘So the problem is not so much to see what nobody has yet seen, as to think what nobody has yet thought concerning that which everybody sees’

Erwin Schrodinger

‘Don’t bother just to be better than your contemporaries or predecessors
Try to be better than yourself’

William Faulkner

List of Publications

1. ***W Xu*** et al., Impact of interface energetic alignment and mobile ions on charge carrier accumulation and extraction in methylammonium-free p-i-n perovskite solar cells. *Ready to submit*.

2. ***W Xu***, TJ Macdonald et al., Mitigating ion migration for improving charge extraction and light stability in methylammonium lead triiodide perovskite solar cells by partial cation substitution with guanidinium. *Under preparation*.

3. ***W Xu*** et al., Asymmetric charge carrier transfer and transport in planar lead halide perovskite solar cells. *Cell Reports Physical Science*, **2022**, 3, 100890.

4. TH Lee, Y Dong, RA Pacalaj, SY Park, ***W Xu*** et al., Organic planar heterojunction solar cells and photodetectors tailored to the exciton diffusion length scale of non-fullerene acceptor. Just accepted, *Advanced Functional Materials*, **2022**.

5. J Kosco, Sl Gonzalez-Carrero, C Howells, T Fei, Y Dong, R Sougrat, G Harrison, Y Firdaus, R Sheelamanthula, B Purushothaman, F Moruzzi, ***W Xu*** et al., Generation of long-lived charges in organic semiconductor heterojunction nanoparticles for efficient photocatalytic hydrogen evolution. *Nature Energy*, **2022**, 7, 340-351.

6. T Du, TJ Macdonald, RX Yang, M Li, Z Jiang, L Mohan, ***W Xu*** et al., Additive-Free, Low-Temperature Crystallization of Stable α-FAPbI$_3$ Perovskite. *Advanced Materials*, **2022**, 34, 2107850.

7. T Du, F Richheimer, K Frohna, N Gasparini, L Mohan, G Min, ***W Xu*** et al., Overcoming Nanoscale Inhomogeneities in Thin-Film Perovskites via Exceptional Post-annealing Grain Growth for Enhanced Photodetection. Nano letters, **2022**, 22, 979-988.

8. J Wu, H Cha, T Du, Y Dong, ***W Xu*** et al., A comparison of charge carrier dynamics in organic and perovskite solar cells. *Advanced Materials*, **2022**, 34, 2101833.

9. Y Li#, ***W Xu***# (# equal contribution) et al., Homologous Bromides Treatment for Improving the Open-Circuit Voltage of Perovskite Solar Cells. *Advanced Materials*, **2021**, 34, 2106280.

10. X Ling#, H Zhu#, ***W Xu***# (# equal contribution) et al., Combined Precursor Engineering

and Grain Anchoring Leading to MA-Free, Phase-Pure, and Stable α-Formamidinium Lead Iodide Perovskites for Efficient Solar Cells. *Angewandte. Chemie*, **2021**, 60, 27299–27306.

11. T Macdonald, A Clancy, ***W Xu*** et al., Phosphorene Nanoribbon-Augmented Optoelectronics for Enhanced Hole Extraction. *Journal of the American Chemical Society*, **2021**, 143, 21549–21559.

12. X Zheng, T Hopper, A Gorodetsky, M Maimaris, ***W Xu*** et al., Multipulse terahertz spectroscopy unveils hot polaron photoconductivity dynamics in metal-halide perovskites. *The Journal of Physical Chemistry Letters*, **2021**, 12, 8732-8739.

13. C Lin, ***W Xu*** et al., Correlating the Active Layer Structure and Composition with the Device Performance and Lifetime of Amino-Acid-Modified Perovskite Solar Cells. *ACS Applied Materials & Interfaces*, **2021**, 13, 43505-43515.

14. T Du, S Ratnasingham, F Kosasih, T Macdonald, L, A, H Ahli, C Lin, S Xu, ***W Xu*** et al., Aerosol Assisted Solvent Treatment: A Universal Method for Performance and Stability Enhancements in Perovskite Solar Cells. *Advanced Energy Materials*, **2021**, 11, 2101420.

15. R Westbrook, T Macdonald, ***W Xu*** et al., Lewis Base Passivation Mediates Charge Transfer at Perovskite Heterojunctions. *Journal of the American Chemical Society*, **2021**, 143, 12230-12243.

16. R Westbrook, ***W Xu*** et al., 2D Phase purity determines charge-transfer yield at 3d/2d lead halide perovskite heterojunctions. *Journal of Physical Chemistry Letters*, **2021**, 12, 3312–3320.

17. XJ She, C Chen, G Divitini, B Zhao, Y Li, J Wang, JF Orri, L Cui, ***W Xu*** et al., A solvent-based surface cleaning and passivation technique for suppressing ionic defects in high-mobility perovskite field-effect transistors. *Nature Electronics*. **2020**, 3, 2520-1131.

18. T Du, ***W Xu*** et al., Light-intensity and thickness dependent efficiency of planar perovskite solar cells: Charge recombination versus extraction. *Journal of Materials Chemistry C*, **2020**, 8, 2050-7526.

19. C Lin, J Lee, J Kim, T Macdonald, J Ngiam, B Xu, M Daboczi, ***W Xu*** et al., Origin of Open-Circuit Voltage Enhancements in Planar Perovskite Solar Cells Induced by Addition of Bulky Organic Cations. Advanced Functional Materials, **2020**, 30, 1906763.

20. F Ambroz, ***W Xu*** et al., Room temperature synthesis of phosphine-capped lead bromide perovskite nanocrystals without coordinating solvents.
Particle & Particle Systems Characterization, **2019**, 37, 0934-0866.

21. T Du$^{\#}$, ***W Xu***$^{\#}$ (# equal contribution) et al., p-Doping of organic hole transport layers in p–i–n perovskite solar cells: correlating open-circuit voltage and photoluminescence quenching.
Journal of Materials Chemistry A, **2019**, 7, 18971-18979.

Abbreviation

Abbreviation	Description
AA	Amino acid
AAS	Aerosol-assisted solvent vapour annealing
AM 0	Air mass 0
AM 1.5	Air mass 1.5
AVA	Aminovaleric acid
BCP	Bathocuproine
CB	Conduction band
CTL	Charge transport layer
DMF	N,N-Dimethylmethanamide
DMSO	Dimethyl sulfoxide
DSSC	Dye-sensitized solar cell
$\Delta QFLS_{OC-SC}$	Reduction of quasi-Fermi level splitting from open circuit to short circuit
E_F	Fermi-level
E_g	Band gap
EL	Electroluminescence
EQE	External quantum efficiency
EQE_{EL}	Electroluminescence quantum yield
ETL	Electron transport layer
FA	Formamidinium
FF	Fill factor
FTO	Fluorine doped tin oxide
FWHM	Fullwidth half-maximum
GB	Grain boundary
HOMO	Highest occupied molecular orbital
HTL	Hole transport layer
ICBA	Indene-C60 bisadduct
IPH	Indene-C60-propionic acid hexyl ester

Abbreviation	**Description**
ITO	Indium-doped tin oxide
J_{SC}	Short circuit current density
J-V	Current density-voltage
LUMO	Lowest unoccupied molecular orbital
MA	Methylammonium
MAI	Methylammonium iodide
MAPbI_3	Methylammonium lead tri-iodide
MPP	Maximum power point
MWC	Microwave photoconductivity
OC	Open circuit
OPV	Organic solar cell
P3HT	Poly(3-hexylthiophene-2,5-diyl)
PCBM	Phenyl-C61-butyricacid methylester
PCE	Power conversion efficiency
PEDOT:PSS	Poly(3,4ethylenedioxythiophene)-Poly(styrene sulfonate)
PEIE	Polyethylenimine ethoxylated
PFN	Poly [(9,9-bis(3'-(N,N-dimethylamino)propyl)-2,7-fluorene)-alt- -2,7-(9,9-dioctylfluorene)]
PL	Photoluminescence
PL_{OC}	Open circuit PL emission intensity
PLQ	Photoluminescence quenching
PLQ_{film}	Photoluminescence quenching of films
PLQ_{OC-SC}	Open circuit to short circuit PL quenching efficiency
PLQY	Photoluminescence quantum yield
PL_{SC}	Short circuit PL emission intensity
PL-V	Photoluminescence-voltage
PNR	Phosphorene nanoribbon
PSC	Perovskite solar cell
PTAA	Poly[bis(4-phenyl)(2,4,6-trimethylphenyl)amine]
PTPD	Poly[N,N'-bis(4-butylphenyl)-N,N'-bis(phenyl)benzidine]

Abbreviation	**Description**
PV	Photovoltaic
$QFLS_{OC}$	Open circuit quasi-Fermi level splitting
$QFLS_{SC}$	Short circuit quasi-Fermi level splitting
$QFLS$	Quasi-Fermi-level-splitting
SC	Short circuit
SCLC	Space charge-limited current
SEM	Scanning electron microscopy
Spiro-OMeTAD	2,20,7,70-tetrakis[N,N-di(4-methoxyphenyl)amino]- -9,90-spirobiuorene
SRH	Shockley-Read-Hall
TA	Transient absorption
TCO	Transparent conductive oxide
TFT	Thin film transistor
TRPL	Time-resolved PL
UV-Vis	Ultraviolet-visible
VB	Valence band
V_{OC}	Open circuit voltage
XRD	X-ray diffraction

Contents

List of Tables

List of Figures

Chapter 1

Introduction

1.1 Motivation

Demand for clean and renewable energy is growing exponentially. Renewable energy made up 3 % and 8 % in 2020 and 2021 respectively,[1]; constituting more than half of the increase in global electricity supply in 2021 (see Figure 1.1). It can therefore be expected that renewable energy will soon dominate the energy market. The dramatic rise in demand for renewable energy can be traced back to two main factors: global growth and development as well as efforts to address climate change.

Access to energy in the form of electricity is a key marker of development and material prosperity. Electricity is needed for communication, supports trading, and stimulates enterprise. Energy access can also benefit health by purifying and pumping water, providing heat for cooking, and keeping vaccines and medicines in fridges.[2] Education is improved by access to electricity as it allows for study in the evenings. Unfortunately, such benefits are still inaccessible for many rural families in the developing world, as 11 % of people in the world lack access to electricity [3] and 8.4 % lack access to low-cost energy,[4] such that traps the world's poorest in a cycle of poverty. Further, the development of new sectors of growth in the global economy requires increasing energy consumption. Renewable energy also increases financial security on a national scale. Traditional fossil fuels, such as oil, are not distributed equally between

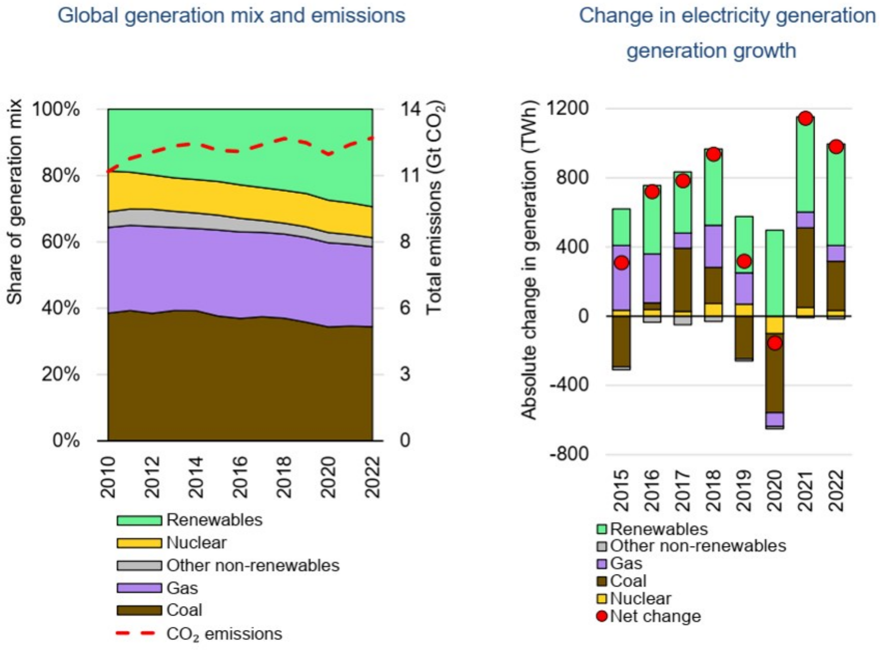

Figure 1.1: Global changes in electricity generation, 2010-2022. Copyright permission from Electricity Market Report 2021.

countries.[5] As such, prices can be easily influenced by policies and natural disasters leading to price fluctuations which drive economic crises.[6] Renewable energy, however, is more equitably distributed and therefore provides a long-term solution for achieving energy independence.[7]

An additional crucial factor driving renewable energy demand is climate change. Accelerating global average temperatures are caused by vast emissions of greenhouse gas, i.e., carbon dioxide, into the atmosphere.[8] These emissions arise from fossil fuels burned to produce low-cost energy. Using fossil fuels has caused a sharp and growing disjuncture between the transforming climate and everyday priorities, especially concerning energy. Bridging this conflict is the foremost priority in the upcoming decades. This task will require a complete transformation in the energy infrastructure, replacing traditional energy sources with clean, green, and sustainable energy.[9]

While the advantages and necessity of renewable energy are apparent, renewable energy sources are still not the predominant energy resource in the energy sector.[1, 10] This can be attributed to many limitations in using renewable energy compared with traditional fossil energy resources, including a lack of capacity to produce electricity, low energy efficiency, high cost of electricity production, etc.[10] Developing new technologies to low costs and improve energy conversion

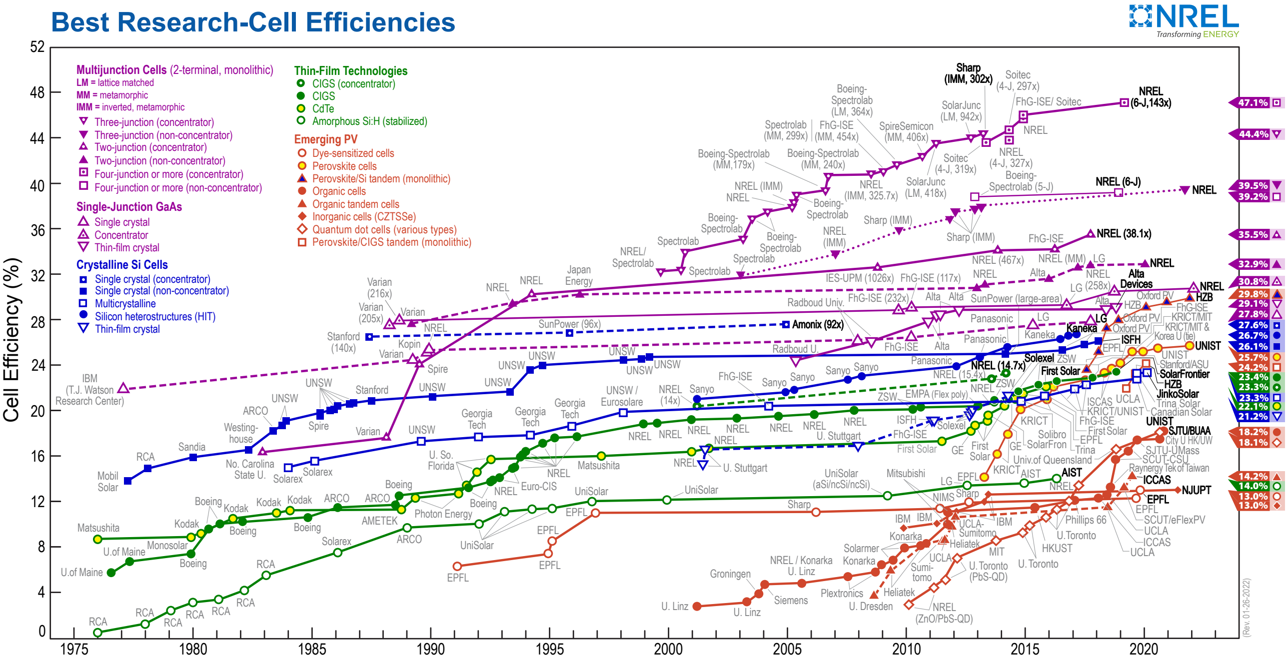

Figure 1.2: Best research solar cell efficiencies. Copyright permission from https://www. nrel.gov/pv/cell-efficiency.html

efficiency is an urgent technological requirement.

Sunlight is the most abundant and accessible sustainable resource and, consequently, the resource most suited to driving equitable global development and combating climate change. One of the most efficient ways to harvest sunlight is to convert it directly into electricity. Edmund Becquerel was the first to convert sunlight into electricity in 1839. However, it was not until 100 years later that photovoltaic (PV), or solar cells, were developed in Bell labs using crystalline silicon. These devices achieved a power conversion efficiency (PCE) of 4.5%.[11] Over the past few decades, the silicon solar cell has been further developed extensively, with their $PCEs$ reaching 26.1% for single crystal, 23.3% for multi-crystalline Si, and 26.7% for silicon heterostructures, as shown in Figure 1.2. Moreover, the substantial reduction in manufacturing costs have made these cells supply some of the cheapest electricity in history, with 0.06-0.08 USD/kWh in recent years.[12, 13] This leads to the current PV market being dominated by silicon solar cells.[14] As in the field of microelectronics, silicon has a combination of strengths that has made it difficult to displace as the favoured PV material. However, opportunities still exist for technologies that promise either significantly higher $PCEs$ or significantly lower processing costs. Tandem solar cells, which are designed to have much higher efficiency, could be a promising way to be alternative to single-junction silicon solar cells.[15, 16] In addition, the silicon solar cell modules are rather heavy and rigid,[17] limiting their applications in many special fields, such as PV-powered electric vehicles,[18] wearable and portable electronics,[19] and space applications.[20] Therefore, new technologies for producing lightweight solar cells are also desired.[17]

1.2 Working principle of a solar cell

1.2.1 Solar irradiance

The sun emits light with a range of wavelengths from ultraviolet to the infrared region of the electromagnetic spectrum. It gives out a power density of 0.62 MW cm^{-2} at its surface.[21] Due to the distance when the sunlight reaches just outside the earth's atmosphere, the power density is reduced to 135 mW cm^{-2}.[21] This spectrum outside the atmosphere, referred to as Air Mass 0 (AM 0), meaning zero atmospheres are present (see the black curve in Figure 1.3). Solar cells used for space power applications, like communications satellites, are generally characterised by using AM 0.

The sunlight is further absorbed and scattered by the atmosphere before reaching the earth's surface so that the spectrum is both attenuated and changed in shape. Although the sunlight varies in distribution and intensity depending on the altitude, location and time on the earth, for convenience, the solar industry uses a standard terrestrial solar spectrum defined as Air Mass 1.5 (AM 1.5), also shown in Figure 1.3, with integrated irradiance of 100 mW cm^{-2} for all standardized testing or rating terrestrial solar cells.[21] Here, the AM 1.5 corresponds to the sun being at an angle of 41.8° in elevation to represent the overall yearly average for mid-latitudes.[22]

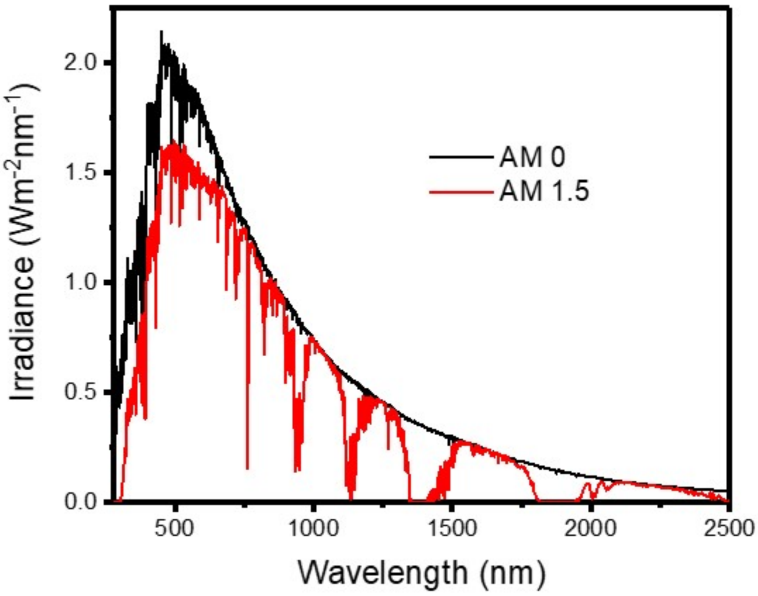

Figure 1.3: Extra-terrestrial solar spectrum of Air Mass 0 compared with terrestrial solar spectrum Air Mass 1.5. Reference data from NREL https://www.nrel.gov/grid/solar-resource/spectra-am1.5.html

1.2.2 Theory and design of a solar cell

A solar cell is a device that converts light into electricity. The operation of a solar cell requires three basic attributes: the absorption of light-generating electron-hole pairs; the separation of charge carriers of opposite types; the extraction of those charge carriers to an external circuit. More specifically, these processes can be described as: after the light is absorbed by its active layer (light absorbing layer) in a solar cell, electrons are excited to higher energy states forming excitons (bound electron-hole pairs) or free charge carriers (unbound electron-hole pairs), which are finally pulled out to an external circuit by some built-in asymmetry, usually different types of junctions.[21] The extra energy of the excited electrons generates a potential difference or electromotive force at two terminals of a cell. This force drives electrons to flow in the external circuit. These behaviours are then named the PV effect, whereby solar cell has another name for PV. Detailed illustrations of a few of these fundamentals are expanded further below.

Quasi Fermi-level

For a semiconductor in thermal equilibrium, the distribution of the electrons is described by a Fermi-Dirac distribution function:

$$f(E, E_F, T) = \frac{1}{e^{\frac{E-E_F}{k_B T}} + 1} \tag{1.1}$$

where $f(E, E_F, T)$ gives the average probability that an electron state at energy E will be occupied at temperature T. The Fermi-level (E_F) is defined as the energy level E when f=0.5.

A quasi Fermi-level is a term used for the Fermi-level when a semiconductor is under external disturbance. It describes the population of electrons separately in the conduction band (CB) and valence band (VB) of a semiconductor, when their populations are displaced from thermal equilibrium. This displacement could be caused by applying the semiconductor to a bias or exposure to light. The difference between the two separated quasi Fermi-levels is then named the quasi Fermi-level splitting ($QFLS$).

Photogeneration

After a photon is absorbed by a semiconductor, its energy is given to an electron in the crystal lattice by exciting the electron from the VB into the CB, leaving a hole behind. Thus, it can be said that photons absorbed in the semiconductor create electron-hole pairs, namely, photogeneration of charge carriers. However, not all photons from sunlight can be absorbed, but only those with energy greater than the band gap (E_g) of the semiconductor. Fortunately, the majority of the solar radiation, as shown in Figure 1.3, is composed of photons with energies greater than the band gap of commonly used solar cell absorbers, such as silicon (1.1 eV).

p-n junction

The most commonly known silicon solar cell is configured as a p-n junction. For simplification, this p-n junction can be imagined as attaching a layer of n-type silicon (which contains an

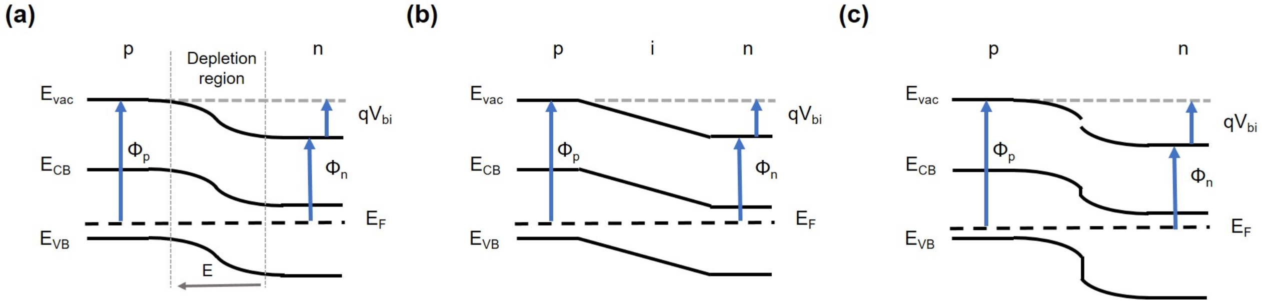

Figure 1.4: Semiconductor junctions of (a) p-n junction, (b) p-i-n junction and (c) heterojunction.

excess of electrons and is achieved by boron doping) to a layer of p-type silicon (which contains an excess of holes and is achieved by phosphorus doping). Since the work function (minimum energy required for removing an electron from a solid to the vacuum; the energy difference between Fermi energy and vacuum level) of the p-type silicon is larger than the n-type, the electrostatic potential on the n layer must be smaller than the p layer. Such that once the two layers are contacted, an electric field is established at the junction (interface) (see Figure 1.4a), and this potential difference is called built-in potential V_{bi}. The junction region is depleted of both electrons and holes, namely the depletion region, and is also known as the space charge region.

In the depletion region, the current is generated by separating the photogenerated electron-hole pairs due to the strong electric field. The electron is pushed by this field toward the n side, and the hole drifts toward the p side. In the space out of the depletion region, where the electric field is smaller, diffusion dominates the moving of the charge carrier, but the junction still plays a role by sweeping any electrons that reach it from the p side to the n side and by sweeping any holes that reach it from the n side to the p side, thereby creating a concentration gradient outside the depletion region.

This design thus allows electrical current to pass through the junction only in one direction and also drives photogenerated electrons and holes towards the n and p layers, respectively.

p-i-n junction

A p-i-n junction can be seen as a variation of a p-n junction. It is structured by a wide, undoped intrinsic semiconductor region in between a p-type semiconductor and an n-type semiconductor region. The same built-in potential V_{bi} is achieved as with the p-n junction with the same Fermi-levels of the doped regions. As there are no charges in the i-layer, the electric field extends over a wider region, and the potential variation is just linear, as shown in Figure 1.4b. In a solar cell using p-i-n junction, the wide depletion layer in the active layer results in the drift (motion of carriers driven by the electric field) of the photogenerated charge carriers rather than diffusion (motion of carriers from higher carrier concentration zones to lower carrier concentration zones) towards the contact layers, as illustrated in detail below. These charge carriers in the i-layer survive for a longer distance than in a doped layer. This design is preferred in PV materials where the diffusion lengths of their charge carriers are short, or photogenerated charge carriers in p or n layers are unlikely to contribute to the current.[21]

Typically, amorphous silicon thin-film cells use the p-i-n structure,[23] and CdTe cells use an n-i-p structure, which is an inversion of the p-i-n configuration as the sunlight is incident on the n-doped layer.[24]

Heterojunction

A heterojunction is an interface (junction) formed by attaching two different semiconductors of different band gaps, as opposed to a homojunction. This junction is designed for improving carrier collection or necessity because of the difficulty in achieving doping of available materials.[21] A discontinuity at the edges of the CB and VB is commonly formed at the junction due to the change of the band gap, see Figure 1.4c.

In the family of silicon solar cells, the heterojunction structure is also adopted to develop the Heterojunction with Intrinsic Thin-Layer (HIT) solar cell structure. The HIT solar cell is achieved by composing an intrinsic crystalline silicon wafer between two ultra-thin amorphous silicon layers.[25] HIT solar cells now hold the record for the most efficient single-junction silicon solar cell, with a conversion efficiency of 26.7%.[26] The heterojunctions are also widely used in other solar cells, such as organic PVs (OPVs) and the new emerging perovskite solar cells (PSCs).

1.2.3 Efficiency determination

To evaluate how well a solar cell performs, a current-voltage (J-V) scan is generally carried out under AM 1.5 illumination. Figure 1.5 shows an example of the J-V characteristics of a solar cell within its operation regime: 0 to V_{OC} (open circuit voltage). Here the V_{OC} corresponds to the operating voltage where the output current of the cell is zero. A short circuit current density (J_{SC}) can also be acquired from the J-V curve when the applied voltage equals zero. From the J-V data, the power density P can also be calculated by $P = J \times V$, which is demonstrated in red in Figure 1.5. When P reaches a maximum, the operating point is named of maximum power point (MPP) with a corresponding voltage of V_m and current density of J_m. The fill factor (FF) thus can be calculated by

$$FF = \frac{J_m V_m}{J_{SC} V_{OC}} \tag{1.2}$$

and the PCE can be calculated by

$$PCE = J_{SC} \times V_{OC} \times FF \tag{1.3}$$

These four parameters: V_{OC}, J_{SC}, FF and PCE are the key performance characteristics of a solar cell.

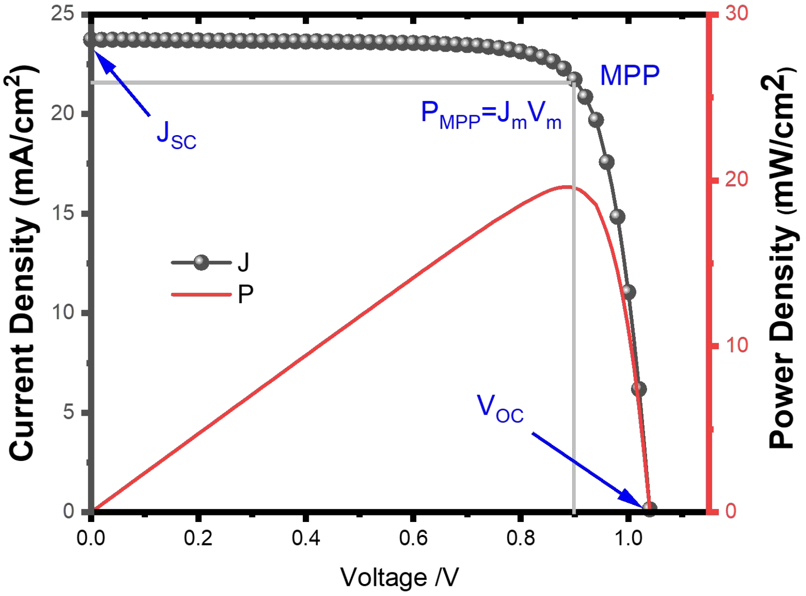

Figure 1.5: The J-V characteristics of a solar cell.

1.3 Perovskite solar cells

1.3.1 The development of perovskite solar cells

The term perovskite in this thesis specifically refers to a type of material that fits the chemical formula of ABX_3, where A is usually Cs or an organic cation, e.g., methylamonium (MA), formamidinium (FA), B is Pb or Sn, X is a halide anion, e.g., Cl, Br and I, as illustrated in the following section for further details. Recently, organic-inorganic metal hybrid halide PSCs have become one of the most attractive candidates for harnessing solar energy. This can be mainly attributed to their simple, low-cost fabrication processes coupled with high efficiency.[27, 28] A wide range of both wet-chemistry and vapour-based simple, low-cost techniques have been demonstrated to process PSCs. These techniques include inject printing,[29, 30] doctor-blade coating,[31, 32] slot die coating,[33] vacuum evaporation [34], and chemical vapour deposition,[35] etc., which have the potential to allow fast and easily scaled-up manufacture of solar cell panels. Additionally, since the first application of perovskite in PV in 2009, the performance of PSCs has developed enormously, with the highest PCEs reaching over 25% now, enabling the PSCs to challenge silicon PVs in terms of efficiency, see Figure

1.2.[36, 37]

Despite significant developments in the PCE of PSCs, scaling from laboratory techniques to high throughput industrial scale processes is crucial for commercialisation. Key challenges remain in producing large-area PSCs cells with high performance due to difficulties in forming large-area and high-quality perovskite films which are uniform, homogeneous and smooth.[38, 39] Over the past few years, many efforts have been paid to the development of perovskite solar modules. In addition to the development of a range of scaled-up perovskite deposition methodologies, many other strategies for improving perovskite compositions, interface contacts and module-fabrication processes have also been investigated.[28, 40] Among those reports, sheet-to-sheet blade-coating has demonstrated PCEs of 19-20% PCEs on cell level and 15.3% and 14.6% for modules with aperture areas of 33.0 and 57.2 cm^2, respectively;[41, 42] large-area PV modules of 144 cm^2 has also been demonstrated to have a PCE of 14.5%.[43] To date, however, breakthrough efficiencies (>20%) have only been reported in PSCs with active areas less than 1 cm^2. On an intermediate scale, Microquanta has demonstrated the highest certified minimodule PCE of 21.4% on an area of 19.3 cm^2.[44] Another important concern for PSC commercialization is their operating lifespans. At the earlier stage of the development of PSCs, their extremely short lifetime compared with silicon solar cells was the primary issue preventing them from commercialization.[45] Generally, stability issues occur in the perovskite material itself, with a number of factors that could deteriorate the perovskite layer, including light, moisture, and heat.[46, 47, 48, 49] This issue has been successfully mitigated using a number of strategies, such as insertion of contact layers, perovskite modification, and device encapsulation,[48, 40] to produce efficient cells with long working lifetimes of thousands of hours or even over one year.[50, 51, 52] Another significant concern is lead toxicity. The potential for lead leakage could be perceived as an environmental and public health risk when using perovskite solar cells in building-integrated PVs, as lead from the majority of halide perovskite can easily dissolve in water. Current regulations would suggest that the lead content in perovskite solar cells is low enough to be safe.[53, 54] However, studies have shown that perovskite leaking can result in lead entering into the food cycle, which is associated with far higher risks than other common contaminants.[53, 55] Therefore, developing lead-free perovskites or highly reliable new technologies to prevent lead leaking may be necessary. So far, lead-free, such as Sn-based, perovskites show relatively limited device performance($<15\%$) and stability.[56, 57] Thus, lead-based PSCs are still the dominant interest for commercialization. To lower the risk of lead leaking, some researchers have suggested approaches to develop lead-absorbing encapsulation technologies,[58, 59] while others have proposed an effective strategy could be to recycle the perovskites at the end of their lifetime.[60] Despite these concerns, the PSC has become one of the most promising PV candidates for the efficient generation low-cost green energy.

1.3.2 Chemical and crystal structures of perovskites

Perovskite materials adopt the crystal structure and composition of calcium titanium oxide ($CaTiO_3$), named after Russian mineralogist Count Lev Alekseevich Perovski,[61] and are described by the formula ABX_3. Figure 1.6a shows a typical cubic unit cell of a perovskite, where cation A is in the middle of the box with twelve nearest neighbors anions X, and cation B neighbors six X. The formability of perovskite is estimated based on the Goldsmidt tolerance factor t (a geometric parameter calculated by $t = (R_A + R_X)/[\sqrt{2}(R_B + R_X)]$, where R_A, R_B and R_X are the radii of the corresponding ions).[62] Generally, the t has a value between 0.81 and 1.11 for the most-studied alkali metal halide perovskite,[63] where cation A is usually MA or FA, B is Pb or Sn; X is one of the halides (I, Br, Cl). For these perovskites, an ideal cubic perovskite is expected when $t = 1$, while symmetry decreases for $t < 1$, and is likely to give tetragonal or orthorhombic structures as shown in Figure 1.6b.[64]

Recently, the family of perovskite materials used for solar cells have been expanded extensively. Multi-compositional engineering has been demonstrated by mixing these A cations and/or other larger cations like guanidinium and ethylammonium to stabilize the perovskite structure and improve optoelectronic characteristics compared with the mono-cation perovskite materials.[65, 66] Meanwhile, X-site anion is also not limited to just halides. Pseudo-halides (univalent anions or functional groups which form hydracids with hydrogen), such as formate, azide, cyanate, or a mixture of these anions with the halides have also been applied to tune the optoelectronic properties of metal halide perovskites, such as the bandgap and defect density.[67, 68]

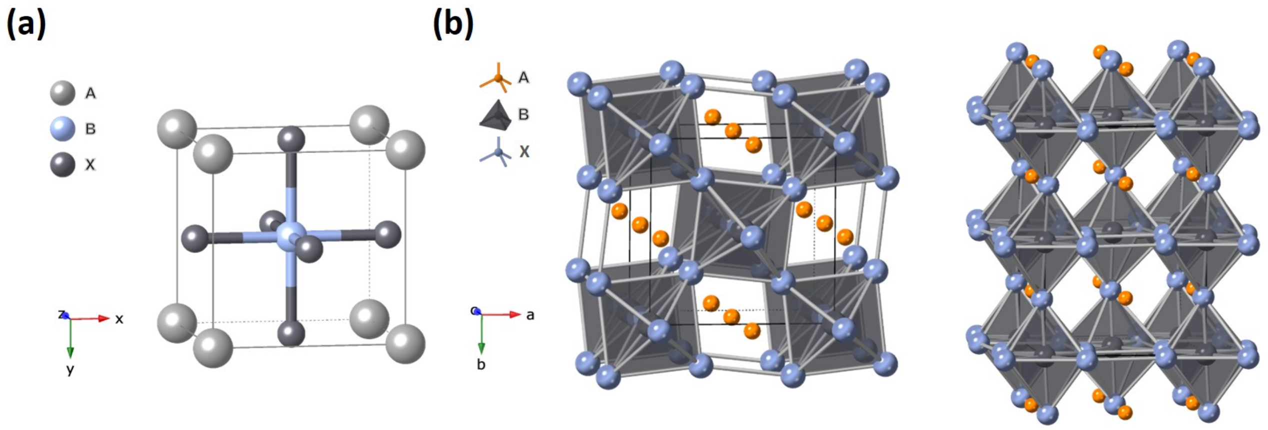

Figure 1.6: The crystal structure of a typical perovskite. (a) The ABX_3 crystal structure of a unit cell. (b) The crystal structure of the tetragonal phase (left) and orthorhombic phase (right) of $MAPbI_3$ with A=MA, B=Pb, X=I.

Despite the t value, the temperature also strongly impacts the crystal structure of perovskite, as phase transitions may occur across different temperature windows. For the typical perovskite $MAPbI_3$ as an example, at room temperature, it is stabilized in a tetragonal (β) phase; a reversible transition to the cubic (α) phase may occur at about 50 degrees, and a transition to orthorhombic (γ) phase can be detected at a much lower temperature of about 160K.[69, 70] The atomic structures for these three phases are shown in Figure 1.6b.[71] The temperature for the phase transition to occur may also vary significantly between perovskites with different compositions; for instance, $MAPbBr_3$ and $CsPbI_3$ demonstrate different phase transition temperatures compared with $MAPbI_3$.[72, 73, 74, 75]

1.3.3 History of perovskite solar cells

The first PV application of perovskite was presented by Kojima et al. in 2009 when perovskite was used as a liquid sensitizer in dye-sensitized solar cell (DSSC) configuration. PCEs of 3.81% and 3.2% were achieved using $MAPbI_3$ and $MAPbBr_3$, respectively.[45] However, the devices were extremely unstable, persisting only for a few seconds in the presence of liquid electrolytes. A potentially viable device was not achieved until 2012 when all-solid-state perovskite-based DSSC was developed. Kim et al. developed perovskite devices with PCEs of 9.7% and lifetimes of over 500 h without encapsulation.[76] At the same time, Lee et al. also fabricated similar devices PSC with a higher PCE of 10.9% and demonstrated that perovskite is acted as both an absorber and hole conducting layer.[77] These results stimulated further research and rapid development of more efficient devices. The remarkable progress made can be mainly attributed to the development of new perovskite deposition methods and novel device structures. A 2-step sequential deposition technique was implemented on planar-architectured PSCs by Burschka et al. in 2013, of which PCE reached 15%.[78] A similar method has also been applied by Im et al., to attain a higher performance of 17% the next year.[79] While most previous work used $MAPbI_3$, a breakthrough in PCE for over 20% was achieved by using FA-based perovskite in 2015.[80, 81] In 2021, a remarkable PCE over 25% was been reported using a passivation/interlayer modification strategy[37, 67] (see Figure 1.2 for comparison of effciency).

1.3.4 Progress in device architecture

The initial success of PSCs is built on the development of solid-state DSSCs. A big step was made by replacing liquid electrolytes with a solid hole transport layer (Spiro-OMeTAD).[76] This facilitates enhanced PSCs and st abilities of over 10% and 500 h respectively. This device structure has since been used to support efficiencies of over 25%. This structure (Figure 1.7a) is referred to as an n-i-p device and consists of five key components: (i) A transparent conductive oxide (TCO) bottom contact, such as indium tin oxide (ITO) and fluorine-doped tin oxide (FTO), (ii) an electron transport layer (ETL). This usually consists of metal oxides such as TiO_2, ZnO and SnO_2, (iii) a hole transport layer (HTL) such as Spiro-OMeTAD and Poly[bis(4-phenyl)(2,4,6-trimethylphenyl)amine] (PTAA), (iv) the perovskite absorber layer and (v) top metal electrode such as Au. For an HTL, its highest occupied molecular orbital (HOMO) or VB is generally higher or equal to the VB of the perovskite layer. Similarly, for an ETL, its lowest unoccupied molecular orbital (LUMO) or CB is normally lower than the CB of the perovskite layer, such that charges can be selectively collected through the charge transport layer (CTL) and finally to the electrodes. Specifically, the n-i-p structure requires all the ETLs to be highly transparent in the ultraviolet-visible (UV-Vis) wavelength range such that all photons can pass through it and be absorbed by the perovskite layer. Depending on the ETL, this n-i-p structure,

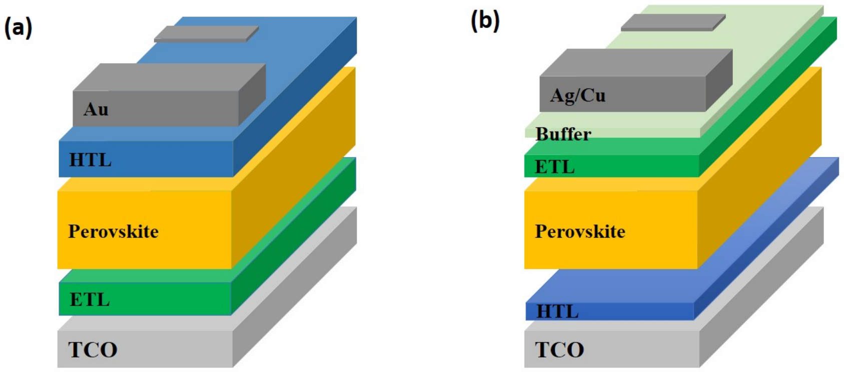

Figure 1.7: Typical device structures of PSCs. (a) n-i-p (conventional) structure and (b) p-i-n (inverted) structure.

also known as the conventional structure, is usually divided into two types: mesoscopic and planar, with the former using a mesoporous TiO_2 or Al_2O_3 as structure scaffold, and the later involving thin TiO_2 and SnO_2 as the transparent ETL. So far, devices using either of the two structures have successfully shown a recorded efficiency of over 25%.[37, 67]

Another widely used structure is the p-i-n structure commonly used in OPVs (also known as an inverted structure). This structure uses a TCO as the anode, a transparent HTL, a perovskite absorber layer, an ETL, and/or an ultra-thin buffer layer such as bathocuproine (BCP), and finally, a metal cathode such as Cu, Ag, and Au. In 2013, Jeng et al. demonstrated the first planar p-i-n PSC by sandwiching $MAPbI_3$ in between Poly (3,4-ethylenedioxythiophene): poly(styrene sulfonate) (PEDOT:PSS) as HTL and C60/BCP as ETL with a PCE of 1.6%, which was further improved to 3.9% by replacing C60 with phenyl-C61-butyric acid.[82] This result was improved to 9.8% by using $PC_{61}BM$ as the ETL in the same year.[83] The device structure is shown in Figure 1.7b. In 2014, PEDOT:PSS was replaced by other new HTLs such as NiO_x nanocrystals[84] and poly[N,N'-bis(4-butylphenyl)-N,N'-bis(phenyl)benzidine] (PTPD) [85] in this inverted structure with an efficiency of 7.8% and 15.3%, respectively. In addition, PTAA[86], CuSCN[87], CuI[88] were also introduced as a replacement for PEDOT:PSS in the inverted PSCs, which have been demonstrated as good HTLs. Whilst many other fullerenes and non-fullerenes have also been tried as the ETL,[89, 90], the state-of-art inverted PSCs is based on phenyl-C61-butyric acid methyl ester (PCBM) and C60.[91, 92] Recently, the p-i-n PSCs have received increasing attention due to their high reproducibility, low hysteresis, and suitability in tandem PV applications. They are also the primary focus of this thesis.

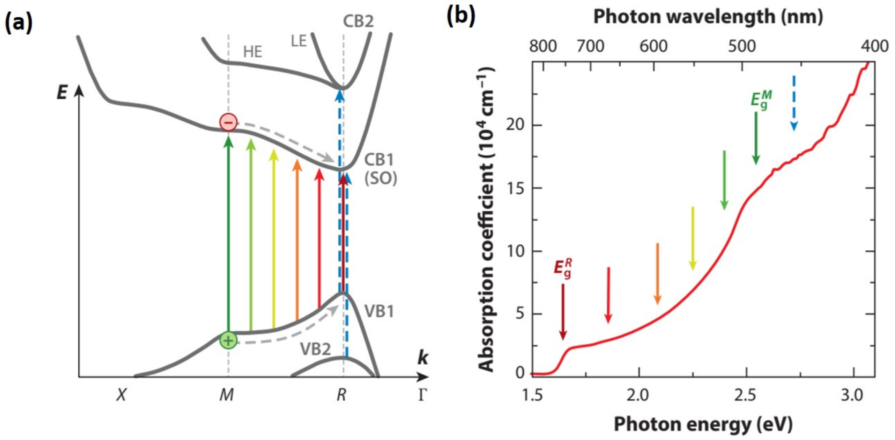

Figure 1.8: Electronic structure and the corresponding absorption spectrum of the typical perovskite $MAPbI_3$. (a) Electronic band structure of $MAPbI_3$. (b) Absorption spectrum of $MAPbI_3$. Copy right permission from reference [98].

1.4 Charge carrier dynamics in perovskite solar cells

1.4.1 Optoelectronic properties of perovskite

The electronic structures of different types of organic-inorganic hybrid lead halide perovskites have been widely studied by theoretical calculations.[93, 94, 95, 96, 97]. Figure 1.8a shows a example of calculated band structure of a typical perovskite: $MAPbI_3$. The minimum of the CB at the symmetry point R was formed by empty atomic 6p orbitals of lead, whereas the maximum of the VB is formed by the antibonding states of the hybridization of lead 6s orbitals and iodine 5p orbitals.[93, 95, 98, 99] A direct band gap with E_g = ~1.6 eV was calculated by estimating the difference between CB1 bottom and VB1 peak. As shown in Figure 1.8a (colourful arrows), in the reciprocal space, a clear and continuous connection of VB1 and CB1 between the M and R points allows photogeneration of electrons and holes across a wide range of wavelengths, leading to continuous absorption of photons with energy above E_g (see Figure 1.8b).[95, 98] Besides, it has been suggested that higher-energy absorption can also happen from transitions in between the higher or lower states in the R point, such as transitions from VB2 to CB1 or VB1 to CB2, shown as the blue dotted arrows in Figure 1.8a.[95, 98, 100]

The changes in band structure resulting from the compositional modification have also been examined by first-principles calculation and many other practical measurements.[101, 102, 103, 104] In the lead halide systems $APbX_3$, substitution of halide X along with Cl→ Br → I by increasing the atomic size leads to a decrease in E_g, likewise substitution of A cation along the line of increasing atomic size (Cs → MA → FA) decreases E_g, with gaps of 1.7, 1.6 and 1.5 eV across this series. Much lower E_g can be achieved by replacing Pb with Sn, with a shift of ∼1.6 eV to ∼1.2 eV from $MAPbI_3$ to $MASnI_3$.[105, 106] A comparison of such trends suggests many other factors, including structural distortion and spin-orbit coupling, affect E_g rather than just changes in ionic size.[101, 107]

1.4.2 Charge carrier recombination

In a PSC, absorption of photons with energy greater than E_g in the bulk perovskite produces bounded electron-hole pairs, known as excitons, or free electrons and holes in the range of femtoseconds to picoseconds.[108, 109, 110] Some carriers can be excited to energy positions higher than the minimum of CB and the maximum of VB or to high-energy sub-bands, forming hot carriers.[111, 112] These hot carriers will then relax through different processes towards the band edge on the sub-picosecond timescale.[98, 111, 112] After the early-stage relaxation processes, free charges are usually formed at the band edge in most typical organic-inorganic hybrid perovskites such as $MAPbI_3$ due to their relatively low exciton binding energy.[61, 98, 113, 114, 115] These charge carriers usually live much longer than the hot carriers and are the main contributors to photovoltage or photocurrent in solar cells. The lifetime of these carriers is widely discussed in PVs as it is one of the critical parameters that determine the time charges needed to be extracted to the contacts before recombination occurs. For recombination in a typical semiconductor, three processes have often been highlighted as determining the total recombination flux:

$$-\frac{dn}{dt} = k_1 n + k_2 n^2 + k_3 n^3 \tag{1.4}$$

where n is average free charge carrier density, assuming balanced electrons and holes; k_1 is a first-order rate constant, often physically interpreted as non-radiative charge-trapping and recombination process;[116, 117] k_2 is a second-order rate constant, typically describing the band-to-band radiative recombination process, though a few other reports have suggested the presence of second-order non-radiative processes;[117, 118, 119, 120] k_3 is the third-order Auger recombination (non-radiative process where the excess energy from the electron-hole recombination is transferred to electrons or holes that are subsequently excited to higher energy states within the same band instead of giving off photons) rate constant. In semiconductors, carrier lifetime (τ) is defined as the average time it takes for a minority carrier to recombine. Commonly, in a semiconductor with high trap densities or high doping levels, the lifetime usually refers to a time constant in an exponential decay defined under a first-order decay process with a lifetime equal to $1/k_1$. It is worth noting that where the density of photogenerated states is less than the background carrier density or when a minority population is present in the perovskite layer, this second term behaves in an exponential manner, as band-to-band recombination can be approximated to be pseudo-first-order, like in doped semiconductors.[116, 121, 122] In this case, a first-order minority carrier lifetime is used to describe the dominant recombination pathway. In the case of high excitation conditions, when the photoexcited carrier density is higher than the majority carrier concentration (especially common for high-quality, intrinsic semiconductors under solar or concentrated solar irradiation), the measured decay kinetics do not follow the exponential model but has to be described by the full rate equation shown above.

In typical metal halide perovskites, such as $MAPbI_3$, recombination has been reported to be dominated by Auger recombination with a rate of k_3 when the charge carrier density is over 10^{17} cm^{-3}, whereas k_1 and k_2 dominate the charge concentration of $<10^{15}$ cm^{-3} and 10^{15} cm^{-3} to 10^{17} cm^{-3}, respectively.[116, 123, 124, 125] In the condition of PV operating under AM1.5 illumination, typical charge-carrier concentrations are relatively low (10^{15} cm^{-3} to 10^{16} cm^{-3}).[116, 125, 126] Therefore, considering these conditions, the Auger recombination can be ignored, leading to mixed mono- and bi-molecular recombination. Solution-processed perovskite films have been reported to exhibit high trap densities ranging from 10^{14} cm^{-3} to 10^{17} cm^{-3}.[124, 127, 128] As such, strong competition between k_1 and k_2 is thought to occur under operation. This leads to current 3D perovskites usually reported to have low PL quantum yield ($PLQY$), a term that evaluates the radiative recombination efficiency, with values of less than 1% without passivation,[129, 130, 131] suggesting future work is still required to address these issues. It should be noted that for PV applications, a dominance of band-to-band radiative recombination is desired, while any other recombination pathways should be minimized. Considering this, k_1 should be as small as possible to favour the radiative recombination components in the rate equation. Strikingly, having such large trap densities, the lifetimes of carriers in the perovskite films have been shown to be over 100 ns - indicating significant tolerance to defects.[124, 132, 133] This unique character has been demonstrated both theoretically and experimentally and found in many of the organic-inorganic lead halide perovskites, where most of the intrinsic defects induced electronic states to reside either outside the bandgap or close to the edge of conduction or valence band.[132, 134] These states close to the band edges, namely so-called shallow traps, are less detrimental to device performance as these traps are suggested to be filled at solar fluences due to a kinetic competition between fast trapping and slow trap-mediated recombination.[135] Indeed, the lifetime can be improved to as long as over a few of μs by effective passivation,[121, 136] such slow decay kinetics are not expected compared to typical direct gap semiconductors.[137]

Understanding the origin of the detrimental non-radiative recombination is crucial to developing PSCs further and reaching their efficiency limits, though it is still a debated topic. Historically, the main focus was reducing trap-assisted recombination at defects in the perovskite bulk or at grain boundaries.[65, 138, 139] Remarkable improvements were achieved by putting much effort into advanced perovskite fabrication methodologies to enhance the crystallinity, increase the grain size, passivate the vacancies and grain boundaries, and form mulitcation and/or multihalide alloys.[67, 136, 140, 141, 142, 143] More recently, growing attention has been paid to recombination losses at the perovskite surface.[98, 135, 144, 145] These investigations showed that surface recombination is more important than recombination within the crystalline grains and at internal grain boundaries. For example, it has been demonstrated that longer lifetimes are observed in an unintentionally passivated polycrystalline perovskite film than in corresponding single-crystal samples.[146, 147] Another report showed that large $PLQY$ of around 20% and enhanced V_{OC} of 1.28 V was achieved by employing tri-n-octylphosphine oxide to passivate the top surface of $\mathrm{MAPbI_3}$ with bandgap of 1.6 eV.[147] Moreover, high $PLQYs$ have also been obtained in other perovskites such as KI passivated $\mathrm{Cs_{0.06}FA_{0.79}MA_{0.15}Pb(I_{0.85}Br_{0.15})_{0.3}}$ with recorded $PLQY$ of 66%,[148] However, among the most efficient PSCs, V_{OC} barely exceeds 1.2 V.[37, 67, 91] To understand this, an increasing number of studies have focused on understanding the recombination mechanisms behind this phenomena using absolute PL measurements.[130, 147, 149, 150, 151] This measurement allows one to measure the $PLQY$ and thus calculate the corresponding $QFLS$ under a steady-state condition close to the actual operating conditions, in contrast to the often employed transient measurements, such as transient absorption (TA) spectroscopy and time-resolved PL (TRPL). This measurement can also be applied to various structures, ranging from films to complete devices, which enable one to disentangle different recombination pathways. Taken together, these results strongly suggest that the recombination losses of highly efficient PSCs have their primary origin at the interfaces between the perovskite layer and its contacts.[130, 147, 152]

1.4.3 Charge carrier transport in perovskite

In addition to long charge carrier lifetimes, excellent charge transport is essential for achieving high-performance PVs. This is because photogenerated charges need to drift (move of these charges in response to an applied electric field) or diffuse (move of these charges from higher concentration to lower concentration) to the contact layers, depending on the operating conditions of a device, before they are finally collected by the electrodes. Consequently, charge transport in perovskites has been the subject of intensive study. Two key measures of charge transport in a semiconductor are the mobility (μ) and diffusion coefficient (D), which are ideally independent of charge carrier density (i.e. neglecting carrier–carrier scattering), have also been measured and discussed extensively. Current methodologies based on thin-film transistors, time of flight, and space-charge-limited current techniques have shown that perovskite single crystals exhibit similar electron and hole mobilities.[153, 154] First-principle calculations have suggested that this similarity could be attributed to an almost equally effective mass for electrons and holes.[155] Balanced transport behaviour can enhance charge collection as carriers can move away from one another and contribute to spatial separation of charge. This suppresses recombination and boosts performance. High mobility values of $\sim$ 100 $cm^2(V{*}s)^{-1}$ and diffusion coefficients of over 30 cm^2s^{-1} have been reported in perovskite single crystals,[156, 157, 158] indicating that transport properties in perovskites are potentially comparable to highly crystalline inorganic semiconductors with benchmark transport properties such as Si and GaAs,[159, 160]. Nevertheless, these values in solution-processed perovskite films for device fabrications are usually one or two orders of magnitudes lower.[108, 157, 161, 162, 163, 164]

Another important parameter, carrier diffusion length (L_D), is also used to describe the charge transport capability of the active layer in a practical solar cell, particularly when the internal electric field is weak, such as at OC. This is because L_D considers the effects from both carrier distribution and the recombination loss during the transport process, which is determined by the following equation:

$$L_D = \sqrt{\frac{\mu k_B T}{r(n) e}} \tag{1.5}$$

where μ is the mobility, $r(n)$ is the total recombination rate, k_B, T, and e are the Boltzmann constant, absolute temperature, and elementary charge, respectively. According to equation 1.4, the total recombination rate is expressed as $r(n) = k_1 + k_2 n + k_3 n^2$. Therefore, in a doped semiconductor or a semiconductor where first-order recombination dominates, $r(n)$ equals k_1, i.e. $1/\tau$, where τ is the first-order charge-carrier lifetime, as described in Section 1.4.2. In the case of an intrinsic semiconductor or a situation when the second-order recombination process is not negligible, such as a semiconductor with high charge carrier densities, the diffusion length is primarily impacted by the actual $r(n)$ value, which is often charge density dependent. Therefore, due to relatively long lifetimes and low recombination rates, perovskites were reported to have long diffusion lengths: over 175 μm in $MAPbI_3$ single crystals and 5.4 μm in solution-processed $MAPbI_3$ films under solar illumination densities, which are much longer than the thickness of the absorption layer in a typical PSC.[154, 165]. Diffusion lengths greater than the film thickness allow the majority of photogenerated charge carriers within the perovskite layer to be transported and collected by the contact layers. Nevertheless, in practice, the dynamic competition between charge transport to the interfaces to get collected versus charge recombination within the bulk as a loss limits the performance of most PSCs.

1.4.4 Charge carrier transfer from perovskite to its contacts

Rapid, irreversible charge transfer from the perovskite layer to its contact layer is critical to overall charge extraction efficiency. However, less attention has been paid to this process in comparison to recombination and charge transport behaviours within the perovskite layer. PL quenching, a method comparing the PL of a perovskite layer with/without CTL/quencher, is commonly used to measure charge transfer dynamics owing to its fast and straightforward operational advantage. This is because one can assume the quenching of PL is an assay of charge transfer, as PL is indicative of bulk charge carrier concentration. Whilst the steady-state PL can estimate the amount and percentage of transferred charges, TRPL can, in addition, probe the transfer kinetics, where fast charge transfer within ∼ns has been observed.[122, 166] Other measurements of transfer kinetics are also possible, such as the quenching of microwave photoconductivity (MWC) and absorption features from the absorption layer,[167, 168, 169] as well as the transient absorption (TA) arising from charge injection into the CTLs, a method which can exclude any surface recombination (non-radiative recombination at the perovskite/CTL interface) effect.[167, 170]

Attempts have been made during the past decade to probe the charge transfer kinetics across the perovskite/CTL interface. Varying charge transfer time constants have been reported, depending on the perovskite, CTL and measurement technique used. Marchioro et al. suggested that transfer for photogenerated charges from the perovskite to a mesoporous inorganic ETL (TiO_2) and HTL (2,2',7,7'-Tetrakis[N,N-di(4-ethoxyphenyl)amino]-9,9'-spirobifluorene (spiro-OMeTAD)) happens within tens to hundreds of picoseconds by using TA and MWC spectroscopy.[167] Later, Wang and his colleagues observed similar charge transfer time constants between 2 to 150 ps for both mesoporous/compact TiO_2 and compact TiO_2-only structured perovskite films by using the same technique of femtosecond TA spectroscopy.[168] However, much larger time scales of 0.7 ns for electron transfer from $CH_3NH_3PbCl_xI_{3-x}$ to TiO_2 and 1.8 ns to Y_2O_3 were also reported by Hayase and his colleagues.[171] Carlito et al. also studied the charge transfer dynamics at $MAPbI_3$/PCBM and $MAPbI_3$/spiro-OMeTAD interfaces, demonstrating lifetimes of injection with hundreds of picoseconds to several nanoseconds for PCBM, and subpicosecond for spiro-OMeTAD.[108] Apart from those most widely used CTLs above, the charge transfer kinetics from perovskite to many other materials has also been studied, such as a few nanoseconds for poly(3-hexylthiophene-2,5-diyl) (P3HT), a few hundreds of picoseconds for CuSCN, NiO_x and PTAA, and a few nanoseconds for C60 and indene-C60 bisadduct (ICBA).[84, 169, 172, 173, 174] These disagreements may be due to the variation of trap densities or charge transport abilities in the perovskite layer that may limit the measured kinetics, depending on the fabrication process, passivation effectiveness, or the quality of contacts.

1.5 The physics of ion migration

1.5.1 The origin of ion migration

Ions in metal halide perovskites can easily migrate in the lattice due to their low migration activation energy (E_A) (i.e., the energy required for the ion to hop from one equilibrium site to a neighbouring one). The activation energy for ion migration can be derived from both temperature-dependent electrical measurements and first-principle calculations.[175, 176, 177] Experimentally, the value of E_A can be extracted from the Arrhenius equation:[177]

$$\Gamma = \gamma_0 e^{\frac{-E_A}{k_B T}} \tag{1.6}$$

where k_B is the Boltzmann constant, T is the temperature, Γ is the individual jump rate of ions, and Γ_0 is a constant. Usually, A cation and X anion and their vacancies are more mobile than B cation because of their lower E_A. For a typical $\mathrm{MAPbI_3}$ as an example, the E_A of $\mathrm{I^-}$, $\mathrm{MA^+}$, and $\mathrm{Pb^{2+}}$ migration has been calculated with values of 0.1, 0.5, and 0.8 eV, respectively, although other values have also been reported due to different migration paths assumed.[175, 178, 179] Nevertheless, these calculations indicate that $\mathrm{I^-}$ is the most mobile ion.

Ion migration typically occurs via point defects in the perovskite layer,[176, 180, 181, 182, 183] though there are other possibilities for ion migration such as lattice distortion and strain-related effects.[184, 185] Point defects are easily formed in solution-processed perovskite crystals. These

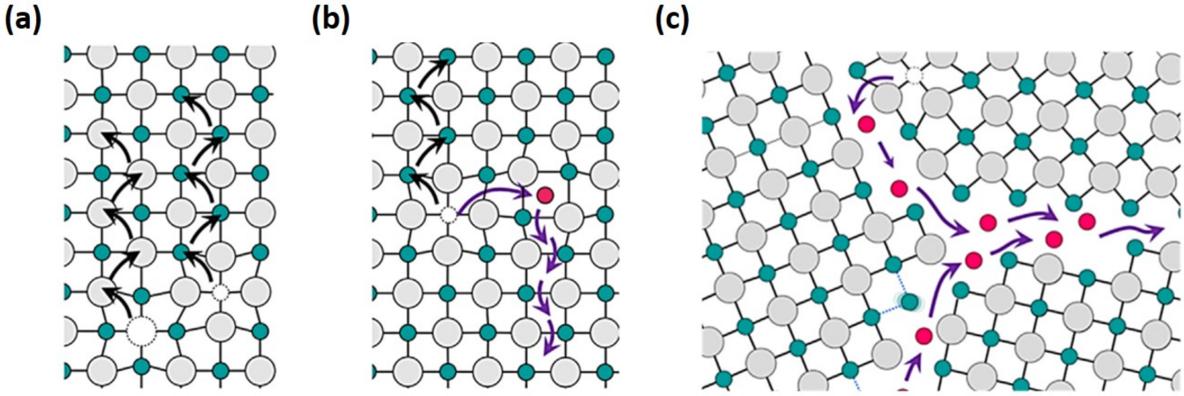

Figure 1.9: Main ion migration channels.(a) Schottky defects, (b) Frenkel defects, (c) grain boundaries. Copyright permission from reference [176].

.

include vacancies (e.g. V_A^-, V_B^{2-}, V_X^+), interstitials (e.g. A_i^+, B_i^{2+}, X_i^-) and defect pairs (e.g. Schottky defect, Frenkel defect).[180, 181, 182] These defects can act as a medium for ion migration in the perovskite crystal lattice, among which two major point defect pairs, the Schottky defect, and the Frenkel defect, are considered the primary migration channels, as shown in Figure 1.9a and b.[176, 186] The Schottky defect that comprises two vacancy sites with opposite charges (e.g., $V_{MA}^- + V_I^+$) involves the movement of an ion from one lattice site to another through the nearest vacancy, whereas the Frenkel defect that comprises a vacancy and its corresponding interstitial (e.g., $I_I^- + V_I^+$, $MA_i^+ + V_{MA}^-$) requires the diffusion of an ion through the interstitial space.[176] In both ion migration mechanisms, vacancies and interstitials with low formation energies can serve as ion migration channels.[181, 186] In solution-processed polycrystalline perovskite films, grain boundaries (GBs) and grain surfaces are also likely to be the primary channels for ion migration as they naturally have more defects and uncoordinated atoms, see Figure 1.9c.[187, 188]

1.5.2 The consequences of ion migration

Significant ion migration can accelerate the degradation of perovskite materials by causing unbalanced local stoichiometric variations.[186] These variations can change the defect chemistry and promote detrimental defects such as antisites (atoms of different type exchange positions) and metal interstitials (atoms that occupy a site in the crystal structure at which there is

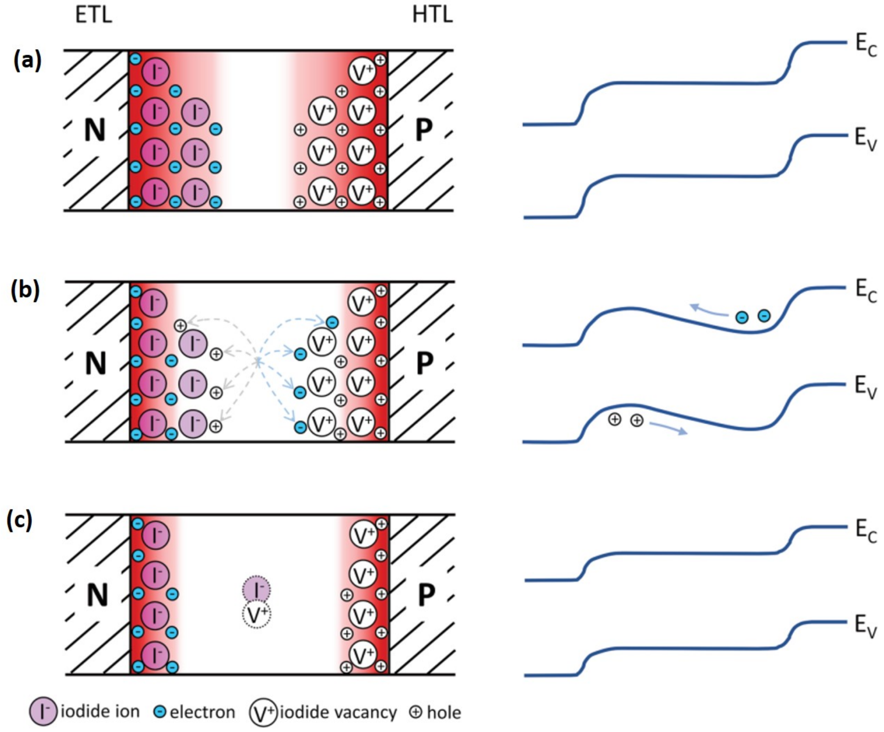

Figure 1.10: Schematics of ionic and electronic carrier distributions (left) and corresponding band diagrams (right) for three situations of interest: (a) the dark equilibrium, (b) immediately after the light turns on, and (c) after prolonged illumination. Copyright permission from reference [196].

.

usually not an atom) and eventually reduced the device performance.[189] For example, it has been demonstrated that metallic lead (Pb^0) is likely to form when Pb^{2+} ions lose their organic and halide ligands in the presence of light and heat, which will increase device shunt (leaking) current and non-radiative recombination.[189, 190, 191] Further, mobile I^- ions are susceptible oxidation into iodine (I^0). This triggers a chain of chemical reactions which drive degradation.[192] Moreover, ions from the perovskite layer may also migrate to the CTLs and cause unnecessary doping, leading to additional electronic losses.[193, 194, 195]

Another detrimental effect of ion migration on perovskite is light-induced dealloying.[197, 198] Particularly common in wide bandgap mixed halide perovskites (often used as the top absorber of tandem solar cells), halide segregation can occur when the mixed halogens form Br-rich and I-rich regions.[199, 200, 201] The origin of this phenomenon has been studied intensively and can be ascribed to the interaction between photoexcited charges and the soft and ionic perovskite lattice, including lattice strain induced by polaron formation, the existence of a miscibility gap between two perovskites under illumination, defect-induced halide mobility, and illumination-induced positive free energies of mixing.[202, 203, 204, 205] Upon illumination, charge carriers can be funnelled towards the lower bandgap I-rich phase leading to charge accumulation that would enhance localized recombination losses. Besides halides, cations can also segregate in mixed-cation perovskites,[206] such as the formation of Cs-rich clusters found in the aged FA-Cs-mixed-cation perovskite films, which can block the flow of current.[207]

Moreover, ion migration can also influence the electric field distribution within the PSCs, which leads to significant changes in charge carrier dynamics.[196, 208, 209, 210] As discussed in the last section, the transport and transfer of electrons and holes in a typical PSCs is usually on the time scale of <100 microseconds, which is fast compared to the timescale of ion migration (ms-s).[175, 211, 212] However, slow (10 ms to 100 s) electronic and optoelectronic dynamics are often observed in PSCs, such as J-V hysteresis, switchable PV behaviour, slow photocurrent transients, and massive apparent capacitances.[213, 214] The cause of these phenomena can be attributed to ion migration.[179, 215, 216, 217, 218] The effect of ion migration on device physics has been suggested by Barnes et al., with others drawing the similar conclusion.[218, 219] In the case of no external bias and light, i.e. dark equilibrium, ions can accumulate at interfaces to screen the built-in potential due to the difference in work functions of the contact materials (illustrated in Figure 1.10a). Therefore, assuming sufficiently mobile ions, only very narrow (compared to the thickness of the active layer of 300-500 nm) space-charge at the perovskite/CTL interface experience a significant electric field. In contrast, the bulk perovskite remains almost field-free. Upon illumination or under an applied bias, the electrical potential across the device is changed in relative to the dark equilibrium. Here an instantaneous electric field within the perovskite bulk is generated (see Figure 1.10b), which is subsequently screened over time with a time constant corresponding to the time-scale for ionic charge redistribution (see Figure 1.10c).[218, 220] These behaviours significantly influence device performance under equilibrium conditions by influencing both the recombination and extraction dynamics in cells. The field-free region that covers the majority of the perovskite layer leads to electrons and holes having to diffuse rather than drift to the contact layers, which could potentially result in charge accumulation in the bulk perovskite at low bias conditions or the introduction additional surface (interface) recombination due to the transferred charges in the contacts being able to approach one another.[221, 222, 223]

1.6 In this thesis

This thesis focuses on understanding the photogenerated charge carrier dynamics in differently processed PSCs. This includes charge recombination and charge transport within the perovskite layer, as well as charge recombination and charge transfer at the perovskite/CTL interface, and the effects of these on the overall charge extraction efficiency. To probe these physical processes, contactless optical spectroscopy is used, such as PL (photoluminescence), TRPL (time-resolved photoluminescence), TA (transient absorption), EL (electroluminescence) and UV-Vis (ultraviolet–visible) spectroscopies. A wide range of device structures was studied, with samples ranging from neat films to complete cells. A range of processing techniques and fabrication methodologies are also considered. By understanding the photophysical properties of these samples, commonly used device fabrication methodologies are linked to charge carrier dynamics in order to explain the measured solar cell performance. Strategies for improving PSC performance are also discussed.

Although a coherent picture of the underlying device physics in terms of charge carrier dynamics in PSCs is emerging, independent methods to interrogate physical processes within individual PSCs are needed to produce reliable qualitative estimates of key physical parameters. In particular, probes of the total charge extraction efficiency and the underlying charge recombination, transport, and transfer kinetics will help elucidate the loss mechanism and identify the limitation behind current state-of-the-art fabrication techniques. Previous literature on the parameters for evaluating these physical processes, especially on charge transport and transfer lifetimes, has been reported in a wide range of values, as discussed in Section 1.4. These variations may reflect the difference in the way of how samples are prepared and how they are measured. Thus, this thesis will explore the correlation between charge carrier dynamics and device performance by considering the factors of fabrication methodologies, sample structures, and measurement conditions, such as light intensity, external bias, etc.

Reducing non-radiative recombination losses either in the perovskite layer or at its interfaces is the key to exploring the total capacity of the PSCs. To address these issues, optimizing the perovskite layer quality through precursor engineering, annealing and defect passivation, and improving the contacting properties by developing new CTLs and surface modification, are the most effective and widely used methods.[149, 224, 225, 226] Whist enormous work has been dedicated to developing new materials and their deposition methodologies, discussions on the origin of their improvement or limitation are insufficient. This thesis focuses on revealing loss mechanisms by probing charge carrier dynamics and provides new insight into these passivation strategies.

Chapter 2 gives an outline of the methods by which the goals of this thesis are achieved. Chapter 3 discusses the charge carrier dynamics in three types of PSCs probed using a custom-built steady-state PL spectroscopy system. By comparing emissions at different light intensities ($<$ 1 sun, 1-sun and $>$ 1 sun), this optical measurement method provides insight into the dominant recombination mechanism close to the actual PV operation conditions. PL is a result of radiative recombination in the perovskite layer, reflecting the charge carrier concentration within this layer. Therefore, by measuring the PL of a device at its open circuit (OC) and short circuit (SC), the charges remained in the bulk and charges extracted to the external circuit can be compared. This measurement provides a probe of both recombination dynamics at OC in correlation to V_{OC} as well as the overall effective charge extraction efficiency of the PSCs in relation to J_{SC} and FF. It is then applied to study PSCs processed by three independent fabrication methods, including the control of perovskite layer thickness, defect passivation by precursor engineering and CTL modification by introducing nanomaterials. A particular focus lies on the material processing on total charge extraction.

In Chapter 4, the impacts of energetic alignment between the perovskite layer and its ETL on surface recombination and charge extraction are investigated. An operando PL system, which is based on but more advanced than the method used in Chapter 3, is developed. This system can measure real-time absolute PL spectra during a J-V scan under 1-sun equivalent illumination, allowing direct comparison between the internal performance (from recombination currents and $QFLS$) and the external performance (from J-V) of a PSC in operation. Four PSCs which have

ETLs with differing LUMOs are particularly studied. Additionally, this Chapter also discusses the impact of ion migration on both the optical and electrical characteristics, the analysis of which was based on an established Drift-diffusion simulation methodology: Driftfusion.

Whilst superior charge transport properties have been demonstrated in perovskite single crystals, [153, 227] Chapter 5 discussed the effect of spatial inhomogeneity, such as GBs and impurity, that influence the charge transport in solution-processed polycrystalline perovskite films. Meanwhile, comparisons between the ETL and HTL in terms of charge transfer kinetics are also compared. In this study, spatially localized TRPL was mainly used to monitor carrier populations generated adjacent to or on the opposite of perovskite/CTL interfaces. In this way, different processes determining extraction efficiency, namely charge carrier transport through the active layer, charge transfer from the active layer to a contact layer, and their competition with charge carrier trapping/recombination processes in the perovskite bulk and at the surface can be probed independently. In particular, the effect of different perovskite layer thicknesses and the presence of GBs on charge extraction and, thereby on device performance were discussed. Finally, a novel and universal post-deposition treatment were employed to eliminate those lateral GBs to improve the charge transport within the perovskite and to further enhance the overall device performance.

Chapter 2

Methods

This chapter introduces the experimental procedures, techniques and related characterisation methods used in this thesis, including materials preparation, device fabrication, and their corresponding characterisations. The set-up, operation method and data analysis of some main electrical and optical measurements used in the following chapters are also described. Further details specific to each research chapter can be found in the results section of these chapters.

2.1 Materials and device fabrication

Some samples and devices studied in this thesis were fabricated by myself, and some were by collaborators. More details are illustrated in each results chapter except for this subsection (Section 2.1), which demonstrates the sample and device preparation methods shared within the Durrant group used by Dr Tian Du and me.

2.1.1 Solution preparation

Perovskite precursor solutions

The standard $MAPbI_3$ precursor solution with a certain concentration (e.g. 1.5 M) was prepared by dissolving PbI_2 (TCI, 99.99 %) and CH_3NH_3I (MAI, Dyesol, 99.99 %) at a molar ratio of 1:1 in anhydrous N,N-dimethylformamide (DMF, Sigma)/dimethyl sulfoxide (DMSO, Sigma) (9 : 1.1 volume ratio).

The double cation perovskite precursor solution $FA_{0.95}Cs_{0.05}PbI_{2.7}Br_{0.3}$ of 1.35 M was prepared by dissolving formamidinium iodide (FAI, 99.99 % purity, Great Cell), cesium iodide (CsI, 99.9% purity, AlfaAesar), PbI_2 (99.99 % purity, TCI) and lead bromide ($PbBr_2$, 99.99 % purity, TCI) at a molar ratio of 0.95 : 0.05 : 0.9 : 0.1 in anhydrous DMF (Sigma)/DMSO (Sigma) (9 : 1.1 volume ratio).

Solution for the contact layers

The hole transport materials employed in this thesis include PEDOT:PSS (Ossila), PTPD (Ossila) and PTAA (Ossila). PEDOT:PSS is solution based and can be used instantly. PTAA and PTPD solutions were prepared by dissolving 2.5 mg powder in chlorobenzene (chlorobenzene). Due to the low wettability for perovskite precursor on PTAA and PTPD, in p-i-n structure Poly [(9,9-bis(3'-(N,N-dimethylamino)propyl)-2,7-fluorene)-alt-2,7-(9,9–dioctylfluorene)] (PFN -Br, 1-Material) were introduced and prepared by dissolving 1 mg powder in 20 mL methanol.

The electron transport materials employed in this thesis are organic fullerene derivatives, including ICBA, indene-C60-propionic acid hexyl ester (IPH), PCBM and KLOC-6. Solution of fullerene derivatives was prepared by dissolving 15 mg ICBA (Solenne, 99 %), 23 mg IPH (Solenne, 99 % purity), 23 mg PCBM (Solenne, 99.5 % purity) and 15 mg KLOC-6 (Solenne, 99 % purity) in 1 mL chlorobenzene, respectively. An additional thin BCP layer is also necessary for p-i-n PSC in between the CTL and cathode, acting as a blocking layer. The BCP solution was prepared by dissolving 5 mg BCP (Lumtec, 99.5 % purity) powder in 10 mL methanol.

2.1.2 Perovskite solar cell fabrication

Device fabrication

The p-i-n PSC studied in this thesis has the same structure as ITO/PTAA or PTPD/perovskite/CTL/BCP/metal electrode. The ITO substrate was sequentially cleaned in an ultrasonic bath in acetone, detergent solution (Decon 90), deionised water, acetone, and isopropanol for 5 min in each solvent. The ITO was then dried with a nitrogen blow and treated by oxygen plasma for 8 min. PTAA/PTPD solution was then spin-coated on the ITO at 5000 rpm with an acceleration of 5000 rpm for 20 s. To improve the wetting property, PFN-Br was subsequently spin-coated on top of the PTAA at 5000 rpm with an acceleration of 5000 rpm for 20 s. The substrate was transferred into an N_2 filled glove box afterwards. Perovskite precursor was spin-coated on the as-prepared substrates at 4000 rpm with an acceleration of 4000 rpm for 20 s, 0.4 mL of diethyl ether was rapidly dropped onto the substrate at 7 s for $MAPbI_3$ and 10 s for $FA_{0.95}Cs_{0.05}PbI_{2.7}Br_{0.3}$, respectively. The substrate was then immediately annealed at 65 °C for 2 min before further annealing at 100 °C, 1 h for $MAPI_3$, and 150 °C, 15 min for $FA_{0.95}Cs_{0.05}PbI_{2.7}Br_{0.3}$, respectively. After the substrates were cooled to room temperature, the fullerene derivative-based CTL solution was spin-coated on top of the as-prepared perovskite substrate at 2000 rpm with an acceleration of 4000 rpm for 20 s. BCP was immediately spin-coated on top of the PCBM layer at 5000 rpm with an acceleration of 5000 rpm for 20 s before the substrate was transferred into a thermal evaporator. Finally, 100 nm of Ag/Cu was thermally evaporated through a shadow mask onto the substrate as a top electrode of the device under a vacuum pressure of 5×10^6 mbar.

Aerosol-assisted solvent vapour annealing

This experiment is contributed by Dr Tian Du.

Aerosol-assisted solvent vapour annealing (AAS) treatments on perovskite films were carried out in an aerosol-assisted solvent vapour deposition system, with the schematic diagram shown in Figure 2.1. $MAPbI_3$ films of 750 nm were prepared with the same method as above in an N_2-

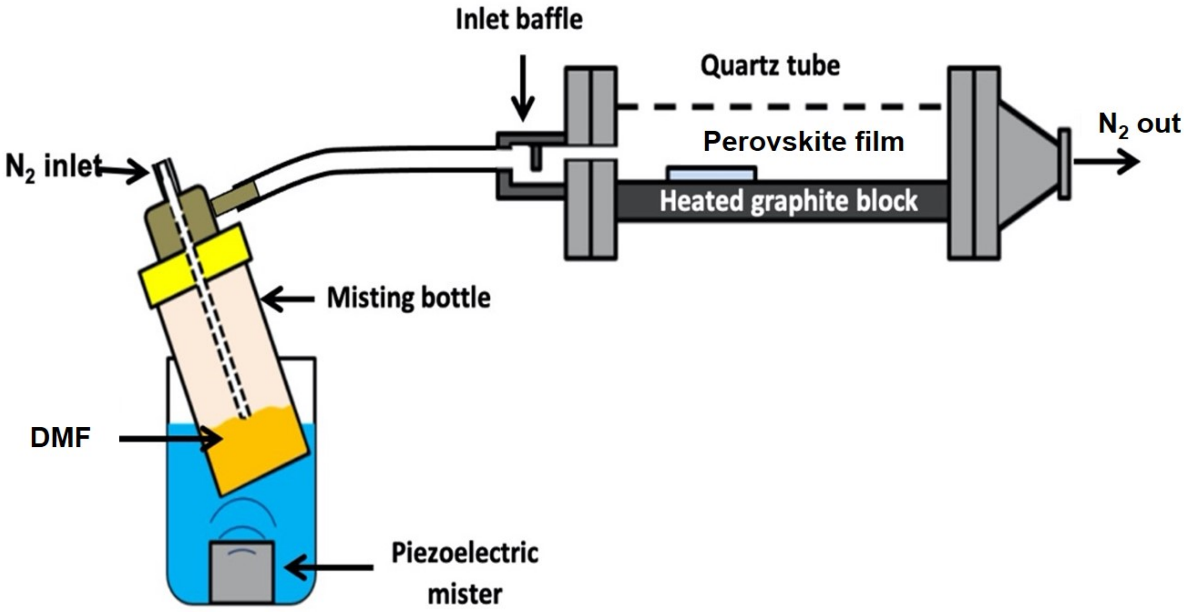

Figure 2.1: Schematic diagram of aerosol-assisted solvent vapour annealing treatment. This experiment is conducted by Dr Tian Du.

filled glove box and were annealed at 100 °C for 2 min to allow the films to turn black. The films were then transferred into the reactor chamber and placed on a graphite block heated at 100 °C. The aerosol of DMF was generated by ultrasonicating a bubbler containing DMF solvent with a piezoelectric generator and was carried by N_2 flow into the reactor with a flow rate of 0.5 $dm^3\ min^{-1}$ for 5 min. After switching off aerosol generation, N_2 flow was continuously carried out for another 5 min to remove the remaining DMF in the reactor chamber. At the same time, the heating was switched off, and the reactor chamber was cooled down to room temperature. Samples were then transferred back into an N_2-filled glove box for additional thermal annealing at 100 °C for 20 min.

2.2 Materials characterisation

2.2.1 Scanning electron microscopy

This measurement is conducted by Dr Tian Du.

SEM films were prepared using the same method as device fabrication with an ITO/HTL/

perovskite structure. All films are then coated with a thin chromium layer before measurement. The images were obtained using an LEO Gemini 1525 field emission gun scanning electron microscope. The acceleration voltage was set at 3–5 kV.

2.2.2 X-ray diffraction

The XRD samples were prepared by directly depositing perovskite on top of ITO substrates. XRD patterns were obtained using a Bruker D2 PHASER diffractometer Cu Ka (l = 1.5406 A°) source, samples were spun during measurement.

2.3 Electronic characterisation

The space charge-limited current (SCLC) measurement and analysis are conducted by Francesco Furlan; the thin film transistor (TFT) measurement and analysis are completed by Dr Julianna Panidi.

2.3.1 Space charge-limited current measurement

Electron-only devices were fabricated onto patterned ITO-coated glass, previously cleaned in detergent and water, and then ultrasonicated in acetone and isopropyl alcohol for 15 min each. The device structure employed is ITO/ZnO/PEIE/ETL/Ca/Al, where different ETLs are introduced with ICBA, IPH, PCBM and KLOC-6, respectively. Zinc oxide (ZnO) precursor solution was prepared from zinc acetate dihydrate (219.5 mg), ethanolamine (60 μL), and 2-methoxyethanol (2 mL). This ZnO precursor solution was filtered through a 0.45 μm Acrodisc filter, spin-coated onto the plasma-treated substrates at 4000 rpm for 40 s, and annealed at 180 °C for 15 min. This process is followed by a rinsing step with PEIE (polyethylenimine ethoxylated) (0.5% wt in 2-methoxyethanol) and further anneal at 100 °C for 10 min to dry. All active layer thin films are then deposited in inert conditions in chlorobenzene at a spin speed of 1000 rpm. Calcium (Ca 20 nm) and Aluminum (Al 100 nm) were then deposited by evaporation through a shadow mask with pixel areas of 0.045 cm^2.

To fit the J-V curves, a method following Blackesley et al. is used.[228] For $J \propto V^{\lambda}$, when the value of λ is close to 2, the Mott-Gurney equation is employed:

$$J = \frac{9}{8}\epsilon_0\epsilon_r\mu\frac{V^2}{d^3} \tag{2.1}$$

Here ϵ_r is the relative dielectric constant of the material (3 was assumed), ϵ_0 is the vacuum permittivity, μ_0 is the mobility, d is the film thickness, γ is the field activation factor of mobility, and V is the applied voltage.

In case the value of λ is higher than 3, the Mott–Gurney equation is modified to account for field-dependent mobility as follows:

$$J = \frac{9}{8}\epsilon_0\epsilon_r\mu_0\frac{(V - V_{bi})^2}{L^3}e^{0.89\gamma\sqrt{\frac{V-V_{bi}}{L}}} \tag{2.2}$$

where μ_0 is the zero-field mobility, V_{bi} is the built-in potential resulting from the work function difference of the electrodes, L is the film thickness, and V is the applied voltage corrected for the voltage drop across the series resistance due to contacts. When extracting the values of μ_0 and γ from the experimental data, the value of μ at any field E can be obtained by using the Poole–Frenkel expression:

$$\mu = \mu_0 e^{\gamma\sqrt{E}} \tag{2.3}$$

Figure 4.2 in Chapter 4 shows the J-V plots of the electron-only devices. Thicknesses of ETLs are measured with a dektak profilometer with 35 nm, 35 nm, 75 nm and 35 nm for ICBA, IPH, PCBM and KLOC-6, respectively. The mobilities extracted from these plots are $3\times10^{-5}cm^2V^{-1}s^{-1}$, $5\times10^{-6}cm^2V^{-1}s^{-1}$, $5\times10^{-6}cm^2V^{-1}s^{-1}$, and $1\times10^{-6}cm^2V^{-1}s^{-1}$ for ICBA, IPH, PCBM and KLOC-6, respectively.

2.3.2 Thin film transistor measurement

Bottom contact, top gate thin film transistors were fabricated in a nitrogen-filled glove box in order to evaluate the electron charge carrier mobility. Glass substrates were cleaned by sonication in a detergent solution (Decon 90), followed by sonication in acetone and isopropanol for 5 min respectively. Gold source and drain electrodes of 40 nm were deposited via thermal evaporation through shadow masks (device channel length 30 nm and width 1000 nm) in a high vacuum (5×10^{-6} mbar). The CTLs were spin-coated from a 20 mg ml^{-1} solution in chlorobenzene at 1500 rpm for 30 s, followed by 10 min of thermal annealing at 100 °C As the dielectric layer, 900 nm of CYTOP were used, and 40 nm of aluminium were thermally evaporated as the gate electrodes. An electrical characterisation by applying different source, drain and gate voltages as well as recording the corresponding current was conducted using a Keithley 4200 SCS.

Figure 4.3 in Chapter 4 shows the representative transfer (a-c) and output (d-f) characteristics of bottom contact, top gate (a,d) ICBA, (b,e) PCBM and (c,f) KLOC-6 TFTs. The electron charge carrier mobility in the linear regime was found 0.04 cm^{2}V^{-1}s^{-1} for ICBA, 0.08 cm^{2}V^{-1}s^{-1} for PCBM and 0.003 cm^{2}V^{-1}s^{-1} for KLOC-6, and in the saturation regime 0.05 cm^{2}V^{-1}s^{-1} for ICBA, 0.38 cm^{2}V^{-1}s^{-1} for PCBM and 0.005 cm^{2}V^{-1}s^{-1} for KLOC-6. IPH TFTs were also fabricated, but field effect was not observed.

The linear mobility was calculated by the following equation:

$$\mu_{Lin} = \frac{L}{WC_iV_D}(\frac{\partial I_{D,l}}{\partial V_G}) \tag{2.4}$$

where L and W are the channel length and width of the devices (30 and 1000 μm), C_i is the dielectric capacitance, $I_{D,l}$ is the drain current in the linear regime, V_D is the drain voltage, and V_G is the gate voltage. The saturation mobility was calculated by using equation:

$$\mu_{Sat} = \frac{L}{WC_iV_D}(\frac{\partial^2 I_{D,S}}{\partial {V_G}^2}) \tag{2.5}$$

where the second derivative of the $I_{D,S}$ (drain current in the saturation regime) versus V_G was extracted from the slope of the ${I_{D,S}}^{1/2}$ versus V_G.

2.4 Optical spectroscopy characterisation

For all the optical measurements in this study, samples and devices are encapsulated in an N_2 filled glove box prior to conducting the measurements to avoid any contact with the air.

2.4.1 Steady-state absorption spectroscopy

The ultraviolet-visible absorbance and reflectance spectra were acquired from a Shimadzu UV-1601 spectrophotometer. The reflectance was obtained by measuring the absolute reflected light from the sample through an integrating sphere compared to a reference light measured from a barium sulphate plate.

2.4.2 Time-resolved photoluminescence spectroscopy

TRPL experiments were carried out on a Delta Flex system (detector: PPD-900, Horiba scientific). Laser diodes with < 200 ps pulse duration (NanoLED, Horiba scientific) of 405 nm or 635 nm in wavelength were used for excitation with a repetition rate of 1 MHz and fluence of 0.4 nj/cm^2 and 0.1 nj/cm^2 per pulse were used respectively.

Specifically, for Chapter 4 another system of FLS1000 PL spectrometer from Edinburgh Instruments was used. Pulsed laser diodes with wavelengths of 637 nm and 405 nm were used as the excitation light source. The fluences are measured using an LED power meter with 5.3 mW/cm^2 (2.65 nJ/cm^2) for 637 nm and 6 mW/cm^2 (3 nJ/cm^2) for 405 nm at a frequency of 2 MHz. PL was recorded through a 700 nm long pass filter at a 778 nm peak wavelength.

2.4.3 Ultrafast transient absorption spectroscopy

Ultrafast TA spectroscopy measurement was carried out by using an amplified Ti:sapphire laser (Solstice, Spectra Physics), with a 800 nm laser pulse ($<$ 200 fs, 1 kHz repetition rate). The laser pulse is divided into the pump and the probe by using a beam splitter. The pump laser at the excitation wavelength used is generated through an optical parametric amplifier (TOPAS Prime, Light Conversion) and a frequency mixer (NirUVis, Light Conversion). The probe pulse at specific time delays is generated through a mechanical delay stage, which delays it by an adjustable period (maximum of 6 ns) relative to the pump pulse. The continuous white light probe in the 450-800 nm region is generated by focusing the probe pulse into a sapphire crystal. Then, the probe pulse is divided before the sample into two pulses, one is directed to the sample, and the other is used as the reference. Both pulses are directed to a separate multichannel spectrometer. The continuum probe pulse on the samples is spatially overlapped with the pump pulse. The pump pulse is chopped by a synchronized chopper with a frequency of 500 Hz. Pulse energies were measured using an energy meter (OPHIR Photonics, VEGA P/N 7Z01560) with a 500 μm diameter aperture.

2.4.4 Steady-state photoluminescence spectroscopy

The PL spectra used in Chapter 3 and Chapter 5 were collected by a Horiba Jobin–Yvon Fluorolog-3 spectrofluorometer. A continuous wavelength (CW) 635 nm laser module purchased from THORLABS with a power of 5 mW was used for excitation. After the sample, a long pass filter after 665 nm was used before the detectors to avoid scattered laser light going into the detector and causing high background. The set-up details are shown in Figure 2.2. For a device PL measurement, the device was held at either SC or OC conditions by connecting or disconnecting the top and bottom electrodes. A mask smaller than its pixel size was used to avoid the non-active area contributing to the PL. The laser beam is able to cover the whole mask area. The excitation intensity was adjusted to 1-sun equivalent by matching the J_{SC} of a device under both laser and solar simulator. The light-intensity-dependent PL measurement was achieved by passing the laser through variable neutral density filters and a lens to reduce

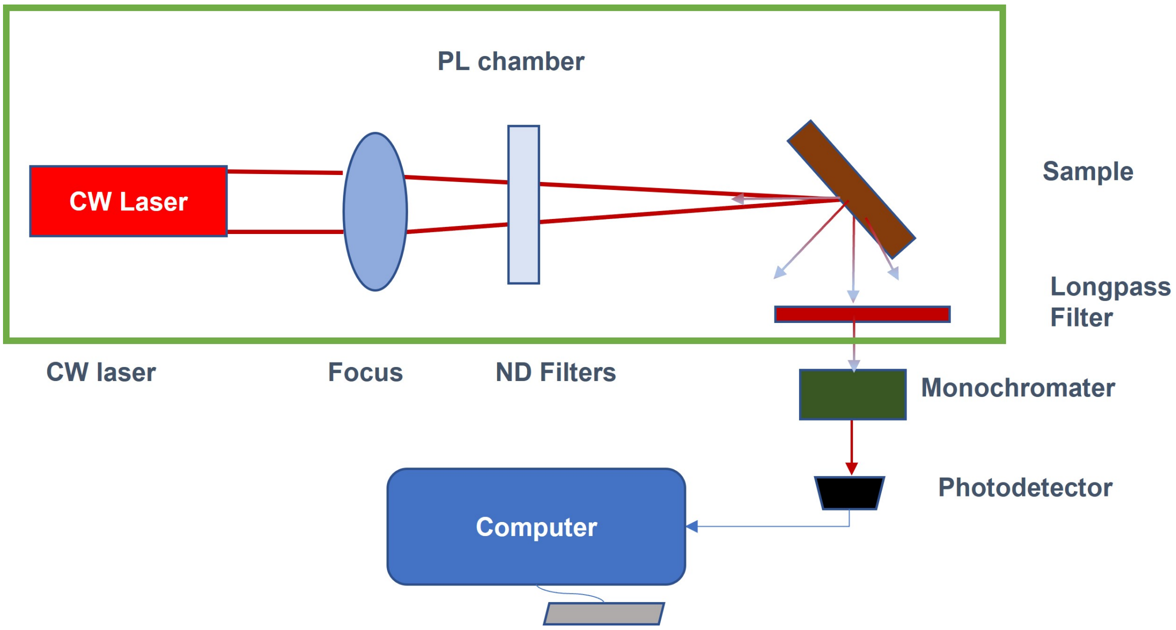

Figure 2.2: Set-up for the light intensity-dependent PL measurement. A 635 nm CW laser was employed for excitation.

or enhance the light intensity.

The film PL and light-intensity-dependent device PL spectra discussed in Chapter 4 were measured under a system with the same setting-up as the operando PL measurement, as discussed further below. Different excitation fluxes were achieved by passing a 532 nm laser through variable neutral density filters. The light intensity was measured via a digital power meter (THORLABS, PM100D) through a photodiode sensor (THORLABS, S120VC). In this measurement, no pre-illumination/ light soaking procedure was conducted before taking each spectrum, and the laser was immediately blocked right after each spectrum was taken with an exposure time of less than 2 s, where the device was kept in the dark for at least 30 s before taking the next spectrum. During the measurement under SC, photocurrents at each light intensity were recorded.

2.5 Optoelectric characterisation

Some of these measurements were conducted by myself, and others by collaborators. Further details are specified in each chapter.

2.5.1 Device performance characterisation

The performance of a solar cell was determined by recording its J-V scans by a Keithley 2400 source meter under one sun (AM 1.5) illumination from a calibrated solar simulator.

2.5.2 External quantum efficiency spectroscopy

The external quantum efficiency of a PSC EQE_{PV} measurements were conducted under a halogen lamp chopped to a frequency of 188 Hz through a Newport monochromator with a four-point probe in connection with a lock-in amplifier for data collection. A silicon photodiode was used for the reference calibration, and the data were analysed with Tracer 3.2 software (LOT) to produce the EQE_{PV} spectra.

2.5.3 Operando photoluminescence spectroscopy

System set-up and measurement procedures

Figure 2.3 shows the schematic drawing of operando PL setting up, where a home-built system by coupling an integrating sphere (AvaSphere-50-REFL, AVANTES), a spectrograph (Kymera 193i, Andor) and a CCD camera (DU420A-BEX2-DD, Andor) for the PL spectrum collection, a potentiostat (Ivium Vertex.100mA.EIS) for the voltage apply and current recording, a 532 nm laser diode module (THORLABS, CPS532b) for photoexcitation. A Labview code was specially developed for system control and data collection. A mercury light calibration source (AvaLight-CAL-MINI, AVANTES) was used for wavelength correction, while a halogen light source (AvaLight-HALCAL-ISP50-MINI, AVANTES) was used for the absolute photon flux calibration. The excitation intensity was adjusted to 1-sun equivalent by matching the J_{SC} of a PCBM device under both laser and solar simulator. A mask smaller than the pixel area was used during the measurement in order to make sure all exposure areas were covered with electrodes. All devices are encapsulated in the nitrogen-filled glove box prior to undertaking any measurements to avoid air exposure. All operando PL measurements were undertaken at

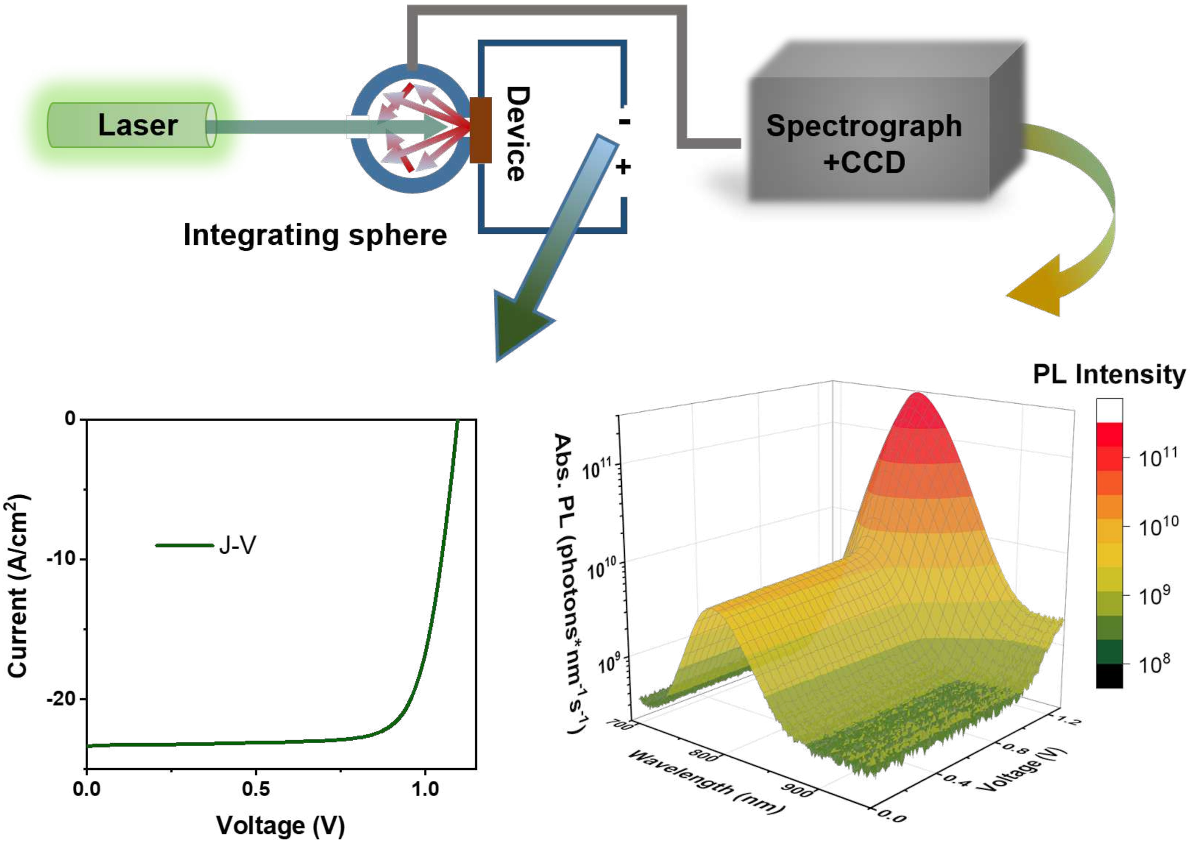

Figure 2.3: Schematic drawing of operando PL set-up. A CW laser diode with 532 nm is employed for excitation. An integrating sphere is used for collecting the total emission, which is delivered to a spectrograph and a CCD camera through a liquid light guide.

a scan rate of 7 mV/s, and all PSCs were soaked under the laser light for 5 min while being held at a bias voltage of 0.2 V before scanning.

Photoluminescence, electroluminescence quantum yield and quasi-Fermi-level-splitting determination

The system was calibrated by shining a halogen lamp of known spectrum and irradiance into the integrating sphere. A spectral correction factor was determined to ensure the detected spectrum of the lamp matched its known spectral irradiance. The spectral photon density of the corrected spectrum was then divided by the photon energy, followed by a numerical integration to obtain the absolute photon count for the excitation, PL, and EL. The $PLQY$ was determined by dividing the PL photon numbers by the excitation photon numbers, while the EQE_{EL} was determined by dividing the EL photon numbers by the injected electron-hole pairs calculated from the dark current. The calculation of $QFLS$ follows this equation

$$QFLS = k_B T \ln(\frac{J_{rad}}{J_{0,rad}}) = k_B T \ln(PLQY \frac{J_{gen}}{J_{0,rad}}) \tag{2.6}$$

where the radiative current (J_{rad}) and the generation current (J_{gen}) were calculated by converting the absolute emitted photon numbers and excitation photon numbers into the currents (photons per second multiplied by elementary charge), respectively. The dark radiative current ($J_{0,rad}$) was calculated by using a method the same as the previous reports.[150, 229] In brief, it was calculated by multiplying the black body radiation emission by the external quantum efficiency of the PCBM device,

$$J_{0,rad} = \int_0^\infty d\lambda EQE_{PV}(\lambda)\psi_{BB}(\lambda) \tag{2.7}$$

with a value of 2.3×10^{-24} A cm^{-2} used in this work.

2.6 Numerical simulation

This section below here is in support of the simulation discussion in Chapter 4. Lucy Hart conducted this simulation.

The simulations were performed using Driftfusion simulation, an open-source code for simulating ordered semiconductor devices with mixed ionic-electronic conducting materials in one dimension.[230] The simulation parameters used for the CTL, HTL and perovskite layers are provided below and were chosen to represent the PSCs used in the experimental measurements. However, this thesis does not assume the simulation results are not a fully accurate representation of the conditions within the PSC. Instead, it focuses its discussion on the trends found to be the most robust across a wide range of input parameters.

Table 2.1: Summary of the simulation parameters for the perovskite layer. This table is contributed by Lucy Hart.

Parameter	Value	Reference
Perovskite Bandgap	1.60 eV	[231]
Perovskite Valance Band Energy	-5.50 eV	[231]
Perovskite Fermi Level	-4.70 eV	Intrinsic
Perovskite Thickness	400 nm	Measured by Dektak
Perovskite Carrier Mobility	2.0 $cm^2V^{-1}s^{-1}$	[232]
Perovskite Ion Mobility	10^{-9} $cm^2V^{-1}s^{-1}$	[233]
Electron SRH Lifetime	300 ns	[234]
Hole SRH Lifetime	3 ns	[234]
SRH Trap State Energy Level	-4.7 eV	[234]
Radiative Recombination Rate	10^{-10} cm^{-3}	[116]
Perovskite Relative Permittivity	25	[235]
Perovskite Effective Density of States	10^{18} cm^{-3}	[135]
Cation Density	2×10^{17} cm^{-3}	[233, 235]

Table 2.2: Summary of the simulation parameters for the HTL. This table is contributed by Lucy Hart.

Parameter	Value	Reference
HTL Bandgap	3.00 eV	
HTL HOMO Energy	-5.20 eV	[236]
HTL Fermi Level	-4.70 eV	Intrinsic
Anode Work Function Thickness	-5.10 eV	
HTL Thickness	10 nm	[237]
HTL Mobility	5×10^{-5} cm^{2}V^{-1}s^{-1}	[236]
HTL Relative Permittivity	3.0	[238]
Electron Surface Recombination Velocity	25 cms^{-1}	
HTL Effective Density of States	10^{19} cm^{-3}	

Table 2.3: Summary of the simulation parameters for the different CTLs. This table is contributed by Lucy Hart.

Parameter	KLOC-6	PCBM	ICBA	Reference
CTL Bandgap	2 eV	2 eV	2 eV	[239]
CTL LUMO Energy	-4.25 eV	-3.95 eV	-3.75 eV	
CTL Fermi Level	-5.25 eV	-4.95 eV	-4.75 eV	
Cathode Work Function	-4.00 eV	-4.00 eV	-4.00 eV	
CTL Thickness	20 nm	30 nm	15 nm	
CTL Mobility	8×10^{-7} cm^{2}V^{-1}s^{-1}	5×10^{-4} cm^{2}V^{-1}s^{-1}	1×10^{-5} cm^{2}V^{-1}s^{-1}	
CTL Relative Permittivity	4.5	4.5	4.5	[240]
Hole Surface Recombination Velocity	500 cms^{-1}	250 cms^{-1}	250 cms^{-1}	
CTL Effective Density of States	10^{20} cm^{-3}	10^{20} cm^{-3}	10^{20} cm^{-3}	[241]

Chapter 3

Probing the Charge Recombination and Extraction in p-i-n Perovskite Solar Cells by Using Device Open Circuit to Short Circuit Photoluminescence Quenching Measurement

3.1 Declaration of contributions

The results presented in Section 3.4 contribute to the publication of the paper: Light-intensity and thickness dependent efficiency of planar perovskite solar cells: charge recombination versus extraction.[222]

The results presented in Section 3.5 contribute to the publication of the paper: Correlating active layer structure and composition with device performance and lifetime in amino acid-modified perovskite solar cells.[141]

The results presented in Section 3.6 contribute to the publication of the paper: Phosphorene nanoribbon-augmented optoelectronics for enhanced hole extraction.[242]

Dr Tian Du, Dr Chieh-Ting Lin, and Dr Thomas Macdonald carried out the thickness-dependent, amino-acid-additive-based and phosphorene nanoribbon-based device fabrication and their corresponding J-V characterisation for each section below, respectively. Apart from these, the optical transfer matrix analysis in Section 3.4 was conducted by Dr Shengda Xu.

3.2 Abstract

Developing high-quality perovskite layers and their ideal contacts is the key to achieving efficient PSCs. Whilst tremendous efforts have been devoted to reducing the defect density to improve V_{OC}, fewer studies looked into the impact of new emerging methods on charge extraction. The charge extraction process, including its underlying charge recombination, transport and transfer processes, is directly correlated to J_{SC} and FF and thus to the overall PCE. Therefore, understanding these processes is crucial to enhance the performance of current state-of-the-art PSCs further. In this chapter, several different material and device engineering methodologies for improving the PCE of p-i-n PSCs are introduced. These methodologies include controlling the perovskite layer thickness, defect passivation by additive engineering, and modification of hole transport contacts. Subsequently, the charge carrier dynamics of the devices fabricated by these new methodologies are discussed. PL is a consequence of radiative recombination, representing charge carrier concentration in the active layer of a PSC. Based on these fundamentals, one can estimate the charge extraction efficiency of these cells by comparing the PL of a device between its OC and SC, where PL is quenched when the device is switched from OC to SC. The quenching of the PL at SC relative to OC can be seen as a measure of the extraction efficiency at SC. The charge extraction processes are elucidated by combining this method with a variety of other optical spectroscopy techniques, and the losses and gains of these device processing methodologies are also discussed, which provides new guidance for designing and processing

future p-i-n PSCs.

3.3 Introduction

Recently, PSCs have been developed extensively, as discussed in Chapter 1, Section 1.3.[36, 243] However, the PCEs of present PSCs are still behind the radiative limit defined by the Shockley–Queisser (SQ) theory, which assumes that all recombination in a solar cell should be radiative.[244, 245] Therefore, minimizing all the other non-radiative losses is key to further improving the performances of current state-of-the-art PSCs towards the radiative limit.

On the one hand, tremendous strategies for suppressing non-radiative losses have been developed, as also discussed in Chapter 1, Section 1.3. These strategies include the control of perovskite crystallization, defect passivation and interface engineering, the formation of graded junctions, etc. Whilst most of them focused on reducing the defect densities of the perovskite layer, which has a significant effect on V_{OC} enhancement, fewer approaches were reported for improving the total charge extraction efficiency, which is more correlated with the J_{SC} and FF.

On the other hand, understanding the origin of non-radiative losses and their impact on PV performance is vital, whereby new strategies can be more effective in targeting specific issues. As discussed in Chapter 1, the major losses are thought to happen in the perovskite bulk and/or at the perovskite/CTL interfaces, i.e., trap-assisted bulk recombination and surface recombination. Various techniques have been employed to investigate these recombination dynamics, among which transient PL and pump-probe spectroscopy are widely used.[226, 246] The advantage of these transient techniques is that recombination rate constants, together with other physical properties such as mobility and diffusion length, can be extracted from their decay kinetics. However, parameters, like charge carrier lifetimes, determined from these measurements vary widely in the literature, which might be due to the different measurement conditions (e.g. excitation intensity).[98, 125] Besides, these techniques are limited to measuring film-structured samples (OC only), whereas a solar cell operates under lower biases. These uncertainties lead to many of the explanations in the literature being ambiguous and under debate. Key considerations of recombination versus extraction of photogenerated free carriers under operating conditions and how these dynamics correlate to device performance have rarely been addressed.

A particular PL system was designed by considering the effects of light intensity and bias to overcome the challenges in determining the charge extraction efficiency. Excitation with varying intensities can be achieved by using a tunable light source. For example, 1-sun equivalent illumination is performed to correlate the measured PL spectra to the PSC J-V parameters measured under AM 1.5. The detailed set-up is demonstrated in Figure 2.2 in Chapter 2, Section 2.4. Moreover, the PL spectra from a complete PSC can be measured while the device can be switched from OC to SC during the measurement. As PL is indicative of the charge carrier concentration in the active layer of a PSC, the charge extraction efficiency of these cells can be estimated by comparing the PL between OC and SC. This methodology was first demonstrated in a previous work of ours by studying a few p-i-n PSCs with varied HTMs,[221] where it allows one to investigate how photogenerated charge carriers recombine and are extracted in these cells. The results suggested that high open-circuit PL (PL_{OC}) indicative of minor non-radiative recombination and large $QFLS$, and low short-circuit PL (PL_{SC}) implying fewer charges accumulated in the bulk perovskite, are desired for an efficient cell. To evaluate the effective charge extraction efficiency, a figure of merit, device OC-to-SC PL quenching efficiency (PLQ_{OC-SC}), calculated by $(PL_{OC} - PL_{SC})/PL_{OC}$, was put forward. The related operation method and set-up are illustrated in Chapter 2, Section 2.4.

In this Chapter, three different fabrication approaches for improving device PCE are introduced, and the particularly designed device PL spectroscopy is applied to study their impacts on charge recombination and extraction dynamics. Thickness and light intensity variations are first considered to reveal the fundamental device physics behind the p-i-n PSCs, as discussed in Section 3.4. Charge distribution and charge extraction dynamics on changing the dominant recombination pathways (e.g. bulk and interface), and their effects on J-V parameters under different operating conditions were investigated. Section 3.5 demonstrates a new passivation method using amino acid-based additives with various carbon chain lengths and compares their impacts on device performance as well as charge extraction efficiency. Finally, In Section 3.6, devices with a phosphorene nanoribbon (PNR) modified HTL are studied. The influence of the PNR interlayer on improving J_{SC} and FF is revealed.

3.4 The impact of perovskite thickness and light intensity on charge recombination and extraction

3.4.1 Introduction

Optimising the photoactive layer thickness is usually the first step in maximising the performance of a solar cell. Due to the excellent absorption property of the perovskite material in a planar PSC, a photoactive layer thickness of over 200 nm is usually enough to absorb most of the light.[244, 247] Practically, the thickness of perovskite can be easily tuned over a broad range of between a few hundred nanometers to 1 micrometre, while their impact on device performance under 1-sun illumination is relatively small. In this thickness range, the main concern is the film morphology formed during deposition.[248, 249] Yet whether there are different optimum photoactive layer thicknesses for various applications. Also, the origin of this thickness insensitivity under 1-sun irradiation, remains largely unexplained. One of the key concerns in organic solar cells in terms of the active layer thickness is the competition between charge transport to the contacts versus bimolecular charge recombination in the bulk layer,[250, 251] an issue which has not been paid much attention to so far in PSCs. It is known that bulk recombination is one of the dominant recombination pathways in PSCs, which can limit charge extraction, therefore, the overall PCE.[116, 174] As trap filling and band-to-band recombination are both found in the perovskite and may strongly influence the recombination order, this suggests bulk recombination could also be light intensity-dependent.[117, 120, 125] This implies that the thickness-sensitivity of the PCE is likely to be light-intensity dependent, which will be the main focus of this section.

To standardize the device performance determination and allow a valid comparison, solar cells are routinely tested under AM 1.5 illumination with an intensity of 1 sun (100 mW/cm^2).

However, in actual applications, the solar cells will operate at intensities below 1 sun, such as at dawn and dusk, under cloudy weather, in high latitude regions, or in-door. On the contrary, devices for solar concentrators or space applications will operate under much higher irradiance. The PCE of a solar cell usually varies with light intensity; for example, silicon solar cells commonly exhibit reduced PCEs when light intensity is decreased.[252] Therefore, a systematic investigation of performance at varying intensities has practical significance in optimising the efficiency of PSCs for real-world operations.

To investigate the thickness dependence of device PCE and its variation with light intensity, p–i–n planar PSCs with optimised device structure were used, owing to their advantages of low J-V hysteresis and high reproducibility. This section explores the impact of perovskite thickness in p-i-n PSCs on charge extraction versus charge recombination and their correlation to the light-intensity dependent PCE.

3.4.2 Results and discussion

Thickness-dependent device performance

In this study, an optimised device architecture of glass/ITO/PTPD/$MAPbI_3$/PCBM/BCP/Ag was used, as shown in Figure 3.1a. The device fabrication method is the same as the general processes discussed in Chapter 2, except for the preparation of the perovskite precursors. Different concentrations over the range of 0.8-2 mol dm^{-3} were used to achieve 150 to 850 nm photoactive layers. Figure 3.1b shows the PCEs of these devices under 1-sun illumination. First, a sharp increase in PCE from 15.5% to 18.3% is observed as thickness increases from 150 to 250 nm. Analysis of the measured photovoltaic parameters reveals that this PCE increase is driven by improvements in J_{SC}, see Figure 3.1d, likely as a result of increased light absorption.[247, 253, 254] Beyond 250 nm, a steady increase in PCE is observed until the film thickness reaches 750 nm, and a sharp decrease is seen beyond 750 nm. This drop-off is mainly due to a dramatic reduction in FF, as shown in Figure 3.1f due to coarsened film surface.[255] Strikingly, for the PSCs with the perovskite thickness increasing from 250 to 750 nm (three-

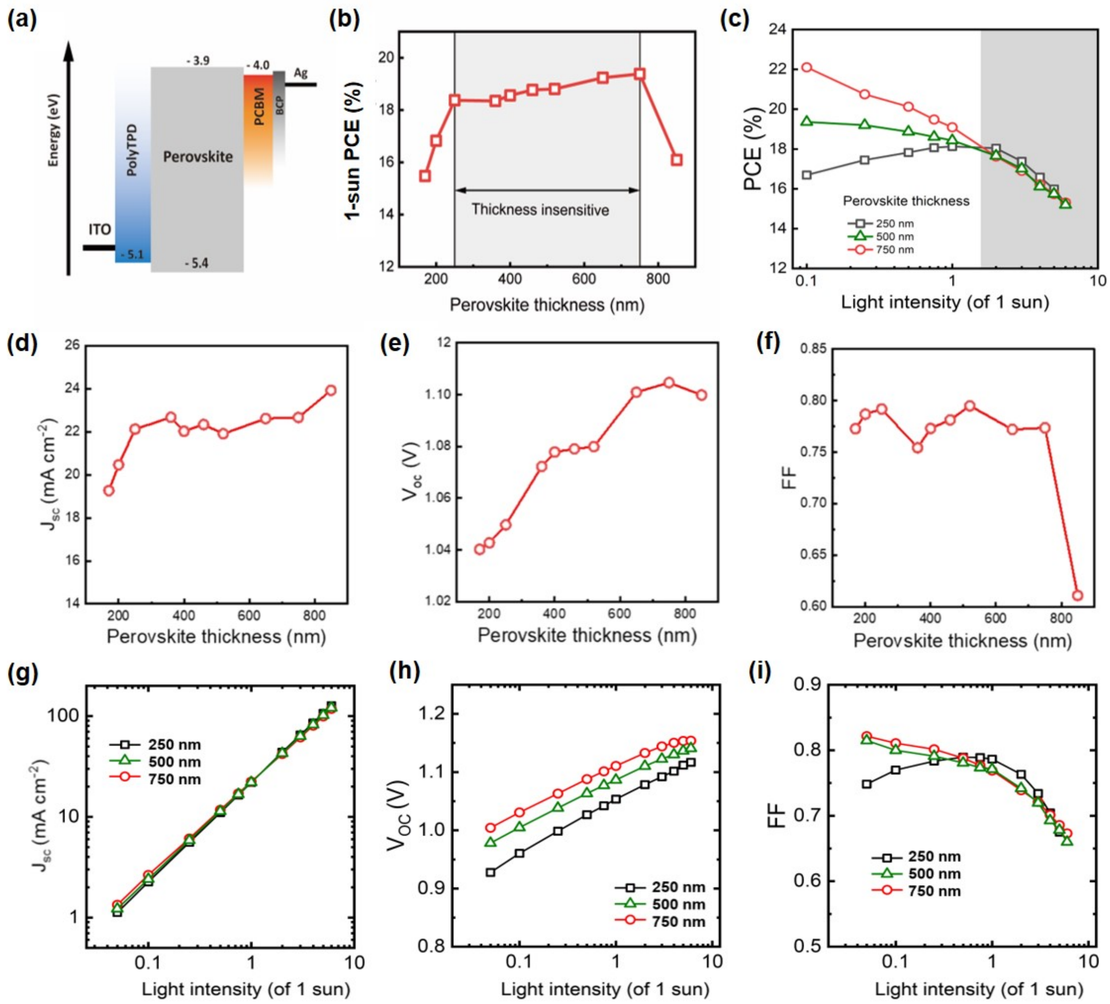

Figure 3.1: Thickness and light-intensity dependent performance of p–i–n PSCs. (a) Schematic drawing of a flat-band energy diagram of the planar PSC; (b) PCE, (d) J_{SC}, (e) V_{OC}, and (f) FF versus perovskite layer thickness (AM 1.5, 1 sun intensity). Dependence of (c) PCE, (g) J_{SC}, (h) V_{OC}, and (i) FF on light intensities of representative PSCs with 250, 500 and 750 nm $MAPbI_3$ active layer thicknesses. The data for (b-i) are contributed by Dr Tian Du.

fold, highlighted in grey), the PCE rises rather modestly from 18.3% to 19.2%. This highlights that PSCs are very tolerant to changes in the active layer thickness, which strongly contrasts with the trend in OPVs.[256] This is encouraging, considering the large-scale device fabrication process, where local variations of film thickness usually occur.[257]

Impact of thickness on device performance

To further investigate whether such thickness insensitivity is universal, devices with an active layer thickness of 250, 500 and 750 nm were studied. The performance of these devices measured under varying light intensities between 0.1-5 suns are shown in Figure 3.1c. The behaviour of these devices varies significantly: at 750 nm, PCE increases monotonically as light intensity is reduced, increasing from 15.7% at 5 suns to 22.1% at 0.1 suns. Over the same light intensity range, the 500 nm device exhibits a moderate increase in PCE with decreasing light intensity from 15.7% at 5 suns to 19.2% at 0.1 suns, whilst the PCE of the 250 nm device increases from 16.0% at 5 suns to 18.1% at 1 sun but then drops to 16.7% at 0.1 suns. These results suggest that the thickness dependence of PCE is strongly dependent upon light intensity: the thicker device performs better under low light intensities but poorer under high light intensities. Interestingly, the intermediate light intensities at 1-2 suns correspond to a switchover of the different thickness dependencies observed at 0.1 and 5 suns, resulting in all devices showing comparable PCEs. This may account for the strong thickness dependencies reported in this study being overlooked previously, as the perception that PSC performance is relatively insensitive to thickness was primarily derived from data measured under one sun irradiation.

The photovoltaic parameters plotted in Figure 3.1g show that below one sun, the 750 nm device exhibits a combination of greater J_{SC}, V_{OC} and FF than the 250 nm device, resulting in considerably higher PCE. The difference in J_{SC} and FF between the devices becomes less as light intensity increases and is almost identical under one sun. Above two suns, the trend is entirely inverted, such that the 250 nm device has greater J_{SC} and FF. Meanwhile, the difference of V_{OC} becomes smaller as light intensity increases. These results indicate that increasing perovskite thickness yields larger photocurrent and reduces non-radiative recombination below one sun, whereas above one sun, the variation of non-radiative recombination is limited, but a thick perovskite layer strongly reduces the photocurrent of the solar cell.

Impact of thickness on photocurrent generation

The impact of thickness on the photocurrent yield is initially considered. An optical transfer matrix analysis was used to model the optical field and charge generation rate (see details in reference [222]). From the analysis, the J_{SC} at different light intensities were predicted with 14% increase of J_{SC} as the perovskite thickness increases from 250 to 750 nm, regardless of light intensity. The measured J_{SC} is in good agreement with the calculated J_{SC} at 0.1 suns for

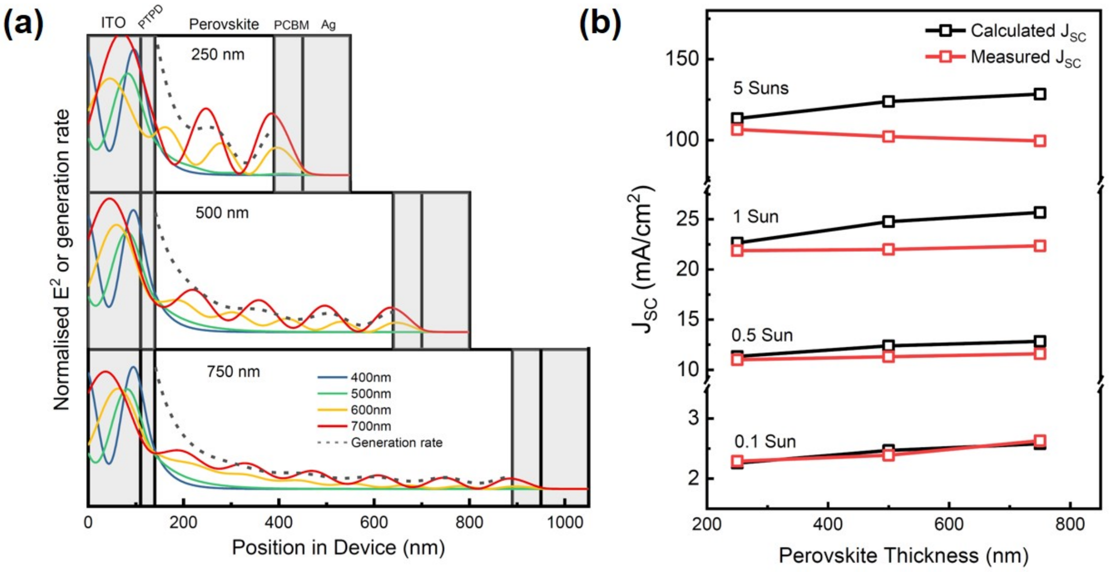

Figure 3.2: Thickness dependence of photocurrent generation. (a) Distribution of normalized optical field intensity for four wavelengths (400, 500, 600 and 700 nm), and the normalized charge generation rate in the solar cells. (b) The dependence of calculated J_{SC} and measured J_{SC} on perovskite thickness under four representative light intensities. These figures are produced by Dr Shengda Xu with copyright permission from reference [222].

all devices, while the difference becomes larger when light intensity is increased. However, at a light intensity over 0.1 suns, thicker films show larger current losses as shown in Figure 3.2. In addition, the light intensity-dependent linearity of J_{SC} with β, derived from $J_{SC} \propto I^{\beta}$, where I is the light intensity, is analysed. Figure 3.1g shows greater sub-linearity ($\beta < 1$) as thickness is increased, with 0.98 for 250 nm, 0.95 for 500 nm and 0.91 for 750 nm, respectively. These results indicate that thick devices suffer from greater recombination losses at high light intensities. These results also suggest efficient charge extraction under low-light conditions regardless of the active layer thickness. Therefore, photocurrent enhancement with increasing thickness is predominantly assigned to enhanced photo absorption. When the light intensity is elevated, the thicker devices exhibit stronger charge extraction losses than the thinner devices.[258]

Impact of perovskite thickness on charge extraction versus recombination

To further understand the limitation of charge extraction by the increase of active layer thickness, fs-TA spectroscopy was conducted on both neat perovskite and HTL/perovskite/ETL films probing the decay kinetics of band-edge PB. The HTL used is PTPD, and ETL is PCBM,

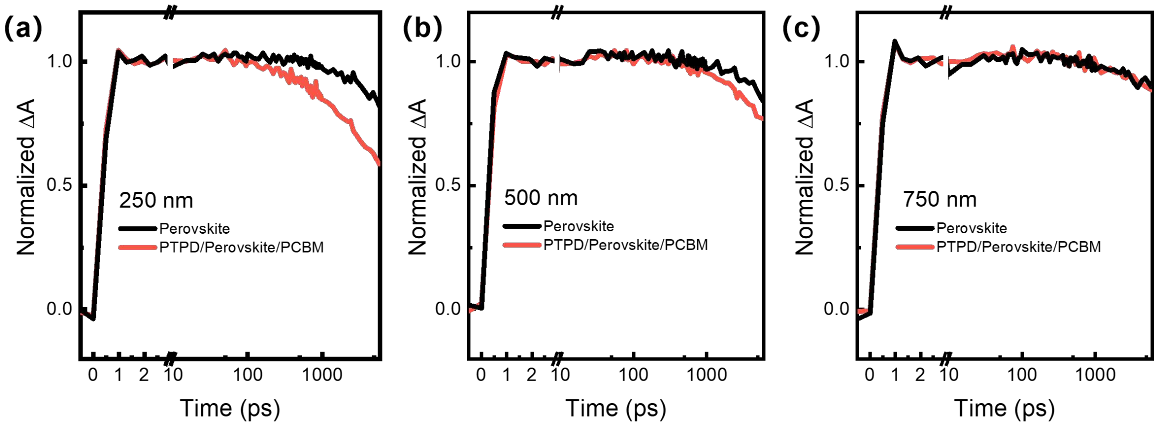

Figure 3.3: Thickness-dependent ultrafast TA kinetics of neat perovskite films and their stacks with structures of PTPD/perovskite/PCBM. The experiment was conducted under excitation of 635 nm pulsed laser with a density of 0.76 μj cm^{-2}, all decays were probed at the wavelength of 760 nm.

as shown in Figure 3.3. As the TA signals represent the population of photogenerated charges resident at the perovskite film band edges, the decay kinetics reflect the bulk charge recombination process or charge extraction process when measuring a neat perovskite film or a triple-layered film, respectively. The decays of the neat perovskite films show no significant changes though slightly slower kinetics are observed in thicker perovskite films, indicating a thicker perovskite film has lower trap densities. However, a much larger difference is observed when HTL and ETL are added: in the presence of CTLs, the TA decay is significantly accelerated for the 250 nm film, while for the 500 nm film, the change of decay dynamics is relatively smaller, the effect of which becomes negligible for 750 nm due to the limitation of the measurement time window. This implies the transport of the photogenerated charges from the bulk perovskite to the perovskite/CTL interface is slowed down as film thickness increases. Such a slowdown in charge transport may impede the charge extraction at higher light intensities, as shown in previous studies,[125] where the increased photo-generation yield and thus faster overall band-to-band recombination rate result in more severe recombination losses competing with charge extraction from the device.

Steady-state PL measurements were also performed on the devices at OC and SC to probe the competition between charge extraction versus bulk recombination.[141, 221, 259] PL from PSCs originates from the radiative component of bulk band-to-band recombination, with variations in the intensity of PL primarily resulting from variations in the rates of non-radiative processes,

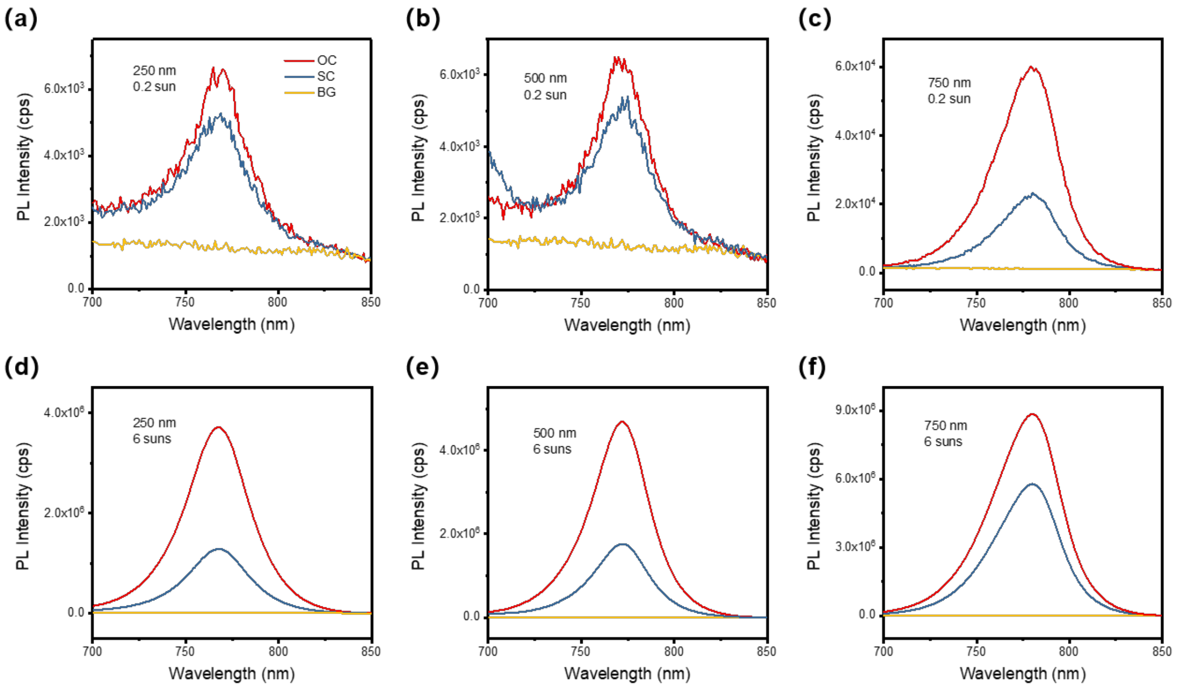

Figure 3.4: Steady-state PL spectra of complete perovskite solar cells with varied perovskite thickness, excited with 635 nm CW laser adjusted to (a-c) 0.2-sun, and (d-e) 6-sun equivalent intensities. Spectra labelled with red, blue and yellow represent OC, SC and background, respectively.

such as trap-mediated recombination or charge extraction (also see Chapter 1, Section 1.4). In this case, an efficient PSC should have weak PL emission at SC (PL_{SC}) due to efficient charge extraction but maximal PL emission at OC (PL_{OC}) due to the maximal QFLS resulting in charge accumulation in the perovskite layer.[221, 260] The PL spectra at OC and SC are shown in Figure 3.4 with excitation intensity equivalent to 0.2 suns, one sun, and 6 suns, respectively. The device OC-to-SC quenching efficiency (PLQ_{OC-SC}), describing the magnitude of the difference in PL emission intensity between OC and SC, is calculated and summarised in Table 3.1. It is evident that under all light intensities, based on the general photovoltaic device physics, a higher PL_{OC-SC} is usually correlated with good device performance.[221, 261] Under 0.2 suns, though enhanced PL_{SC} and PL_{OC} are observed with the increase of film thickness, the higher PLQ_{OC-SC} for the 750 nm device is mainly due to PL_{OC} enhancement, indicating suppression of non-radiative recombination at OC for these thicker devices, consistent with their higher V_{OC}. This is in good agreement with recent reports, where higher V_{OC} was correlated with higher PL emission or longer PL lifetimes at OC.[149, 262] The trend is reversed under 6 suns where band-to-band recombination starts to dominate, and the 750 nm device shows a lower PLQ_{OC-SC}, resulting from significantly intensified PL_{SC}. This trend indicates higher band-to-band recombination losses present in the perovskite layer during charge extraction, which is correlated with the reduced J_{SC} and FF for the thick devices under high light intensities. This is also analogous to the observation that poor PL quenching between MPP and OC correlates with lower FF, both suggesting PL quenching is an effective assay of efficient charge extraction.[260]

Table 3.1: PLQ_{OC-SC} of full PSCs with different perovskite film thickness.

	$PLQ_{OC-SC}/\%$	
Perovskite thickness (nm)	0.2 suns	6 suns
250	27	66
500	28	62
750	62	35

Origin of V_{OC} improvements

Finally, the V_{OC} increases with perovskite thickness are considered and discussed, in particular, the impact of perovskite thickness on the charge carrier distribution at OC.[263, 264] Figure 3.1h shows the light intensity dependence of V_{OC}, where the V_{OC} of the thinner devices exhibits a steeper voltage increase with increasing light intensity, leading to a larger V_{OC} difference between the thick and thin devices at lower light intensities, as reported previously.[139]

In order to understand the origin of these V_{OC} differences, light intensity-dependent PL measurements are employed. 250 nm and 750 nm perovskite-based samples with different structures, including neat perovskite, HTL/perovskite/ETL, and the complete device, were studied. The slope of the PL was analysed by using the power-law growth equation: $I_{PL}= I_{exc}^{\alpha}$, where I_{PL} is the PL intensity, I_{exc} is the excitation density, and α is a widely used parameter to estimate the recombination order in semiconductors: α equals 1, suggests second-order processes dominate; α equals 2, suggests first-order processes dominate; α is in between 1 and 2, indicates there is a competition between those two processes.[265, 266] Here, the α values are 1.4 and 1.3 for 250 nm and 750 nm perovskite films, respectively, as shown in Figure 3.5a. These values suggest suppression of first-order non-radiative recombination (monomolecular process) in the 750 nm perovskite film, consistent with the PL_{OC} and TA results. In the presence of CTLs, both 250 nm and 750 nm films show a dramatic reduction in the value of α, see Figure

3.5b. This reduction indicates that first-order processes become more significant and dominant in HTL/perovskite/ETL samples compared with the neat perovskite films,[265, 267, 268] attributed to a large amount of the photogenerated charge carriers being transferred into the contact layers irreversibly, as mentioned in Chapter 1, Section 1.4. Figure 3.5c shows that α decreases evenly towards 2 for the complete devices, further proving that the enhanced extraction of photogenerated charges to the contacts by the electrode-induced electric field reduces the band-to-band recombination (second-order process). In contrast to the 250 nm perovskite samples with high α values of 1.8 and 2.0 for HTL/perovskite/ETL and complete device structure, respectively, the 750 nm perovskite samples show relatively much lower values with 1.5 and 1.7 for the triple layer and the whole cell, respectively. This observation indicates PSCs with 250 nm perovskite have more charges extracted to their CTLs. These extracted charges are likely accumulated in the CTLs due to limited charge extraction at OC, such that they are more likely to cause surface recombination with electrons and holes in the perovskite layer.[130, 151, 226, 269, 270]

The PL quenching (PLQ) from a neat perovskite film to a complete device is also compared between the PSCs with two different thicknesses, as shown in Figure 3.5d. It is widely accepted that the PL intensity depends quadratically on charge carrier density in the perovskite layer and is exponential to the bulk QFLS, as discussed in Chapter 1, Section 1.4.[130, 147, 149, 150, 151] The PLQ shows a general trend for both devices with reduced values as light intensity increases. This indicates that as light intensity increases, fewer photogenerated charges are transferred to the CTLs, leading to more charges remaining in the perovskite layer and reduced surface recombination.[150, 151, 226, 270] Generally larger PLQ values observed in the 250 nm PSC compared to the 750 nm cell suggest that in the 250 nm PSCs, more free charges are extracted out of the perovskite layer, resulting in greater $QFLS$ losses.[130, 147, 149, 150, 151] These results suggest surface recombination becomes less significant in the PSCs when increasing the light intensity or perovskite layer thickness, consistent with the PL power-law analysis and TA data.

In addition, the slope of the device PL_{OC} in Figure 3.5c also explains the light intensity-dependent V_{OC} behaviours. Compared to the thick device, the thin device shows a steeper slope in PL_{OC}, indicating steeper growth of the $QFLS$ in the former, consistent with the V_{OC} data shown in Figure 3.1h. It is worth noting that compared to a 750 nm PSC, enhanced bulk and surface recombination can both lead to a lower V_{OC} in a 250 nm PSC. However, the impact from the bulk (α values in Figure 3.5a) is less dominant than the interface (α values in Figure 3.5 b and c) on the recombination order, as the α value is more sensitive to the thickness in the complete devices than neat films. This trend in α values suggests that surface recombination could be the dominant recombination pathway in thin 250 nm PSCs, whilst an increase in perovskite thickness can effectively reduce this loss, though the performance of thick devices may also benefit from the reduced defect states in its perovskite layer. This can be attributed to the thinner perovskite layer having faster and more efficient charge extraction, owing to more charges likely stored in the CTLs, as mentioned in this subsection before.

The results from the light intensity-dependent PL measurements demonstrate that thicker perovskite films have less substantial non-radiative recombination and reduced surface recombination weight, leading to larger V_{OC} values for their devices at any given light intensities, consistent with the TA and PL_{OC} measurement. However, the V_{OC} differences between the thick and thin PSCs become less significant as light intensity increases due to the reduced surface recombination at higher light intensities.

3.4.3 Summary

The above results show that the optimum PCE of p-i-n planar PSC varied with the perovskite thickness between 250-750 nm and depending on the intensity of the incident light. The thicker perovskite films absorb more light and have less bulk and surface non-radiative recombination at any given light intensities, leading to much greater V_{OC}.[125, 244, 253, 271] However, the thicker films also show more significant charge accumulation and band-to-band recombination losses at SC. This results in a continuous decrease in FF and PCE with increasing light intensity, especially at high-light illumination conditions (> 1 sun) when band-to-band recombination becomes more dominant.[233, 272] Surprisingly, the 750 nm PSCs still maintain comparable J_{SC} values except for a slight reduction at high light intensities. This may be due to the

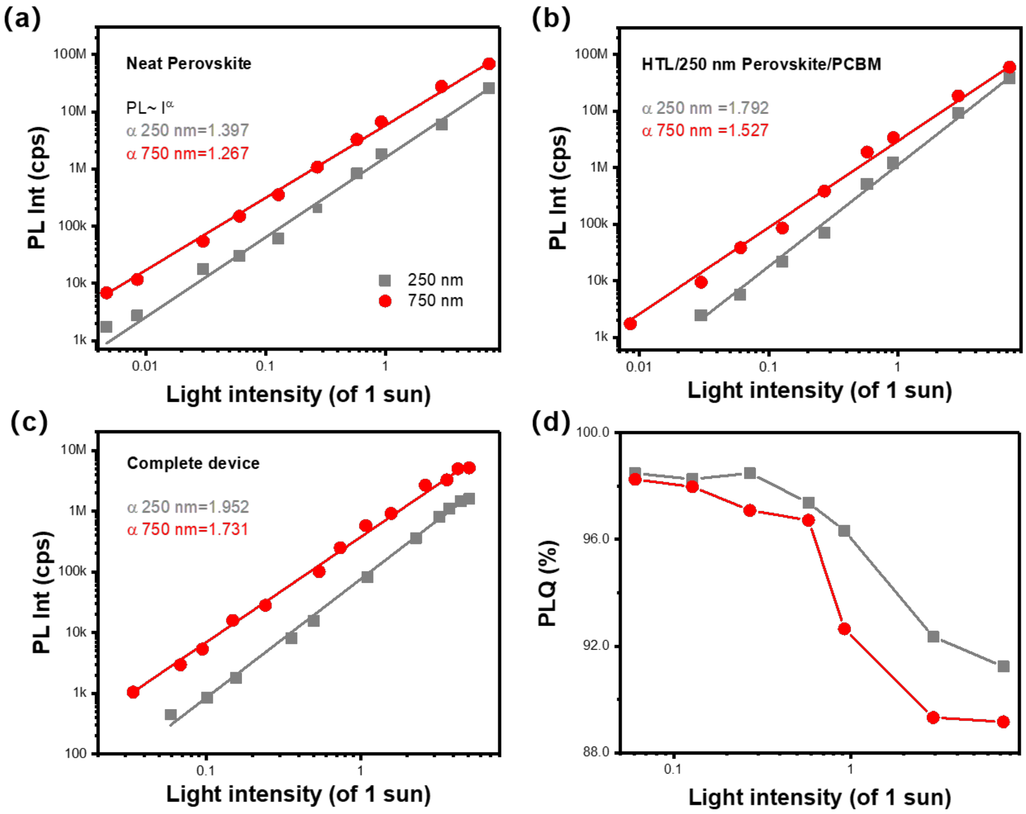

Figure 3.5: PL of 250 nm and 750 nm perovskite-based samples with the structure of (a) neat perovskite film, (b) HTL/perovskite/ETL, and (c) full device under varying light intensities (635 nm laser). (d) PL quenching from the neat perovskite films to their corresponding devices.

compensation by increased light absorption and reduced non-radiative recombination.[226, 244, 253] In contrast, despite the reduction in PCE above 1 sun, the 250 nm PSCs show better performance compared to the thicker devices, owing to their better charge extraction efficiency. Moreover, reducing light intensities below 1 sun actually leads to decreases in the PCE of thin PSCs, which is opposite to the trend observed in the thick ones. This phenomenon is attributed to the dominance of the surface recombination nature in the 250 nm PSCs. At low light intensities, in a PSC, when light intensity decreases, band-to-band recombination becomes less effective,[124, 125] whereas non-radiative trap-mediated recombination and surface recombination start to dominate the overall recombination.[125, 152] Therefore, compared to the 750 nm PSCs, in the 250 nm PSCs, as surface recombination is more pronounced, they have much lower FFs in the low-intensity range (< 1 sun) due to more considerable non-radiative losses, leading to poor low-light performance.[125]

The results of this study provide a key guide to the design of PSCs for optimum real-world performance. They show that a relatively thick perovskite layer can considerably improve the average PCE throughout the day under normal operational conditions, particularly in northern latitudes or shaded sites where light intensities are often less than AM 1.5.[273, 274, 275] Such thicker devices will also yield high performance for indoor light harvesting applications.[276] On the contrary, for concentrator PVs where high irradiance is implemented to achieve higher power outputs per unit area,[258, 277] PSCs with a relatively thin perovskite layer would yield higher PCEs.

3.5 Understanding the current loss in amino-acid modified perovskite solar cells

3.5.1 Introduction

In parallel to improving the PCE of PSCs, there has also been a tremendous research focus directed at addressing stability issues by proposing numerous sophisticated strategies, where additive engineering is often seen as one of the effective means of improving both stability and PCE.[278, 279, 280] Introducing bulky cations or amino acid derivatives has been shown to be promising for stabilizing PSCs. However, this method can also lead to a loss in photocurrent owing to the extended, saturated carbon chains of such additives.[142] Notably, incorporating low concentrations of aminovaleric acid (AVA) as a processing additive in screen-printed $MAPbI_3$ has demonstrated to improve the operational stability of the devices,[281, 282] while a reduced J_{SC} is usually observed.[51, 282, 283] Similar trend of J_{SC} reduction has also been reported with other bulky cation additives;[284, 285] however, the origin of this phenomenon is overlooked and remains unexplained.

The large variety of defects formed during the deposition of the perovskite layer can give rise to electronic trap states with a wide range of energies, where most of these defects are charged, which means they can be passivated by a variety of ionic bonding and coordinate bonding strategies.[286] The carboxylic and amine end groups of AVA are considered to be promising

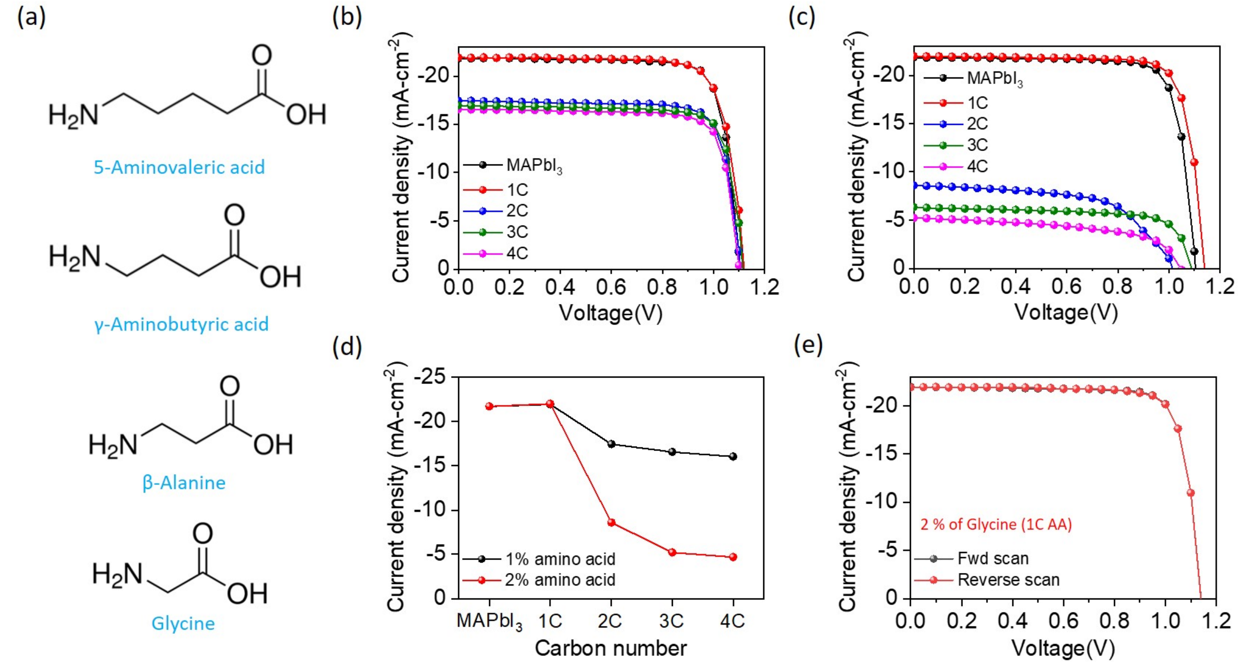

Figure 3.6: (a) Molecule structure of different amino acids. J-V performance of PSCs with (b) 1, and (c) 2 vol % of AAs added to the active layer during processing. (d) Average J_{SC} of devices with 1 and 2 vol % of AA additives. (e) Forward and reverse J-V scans of the champion device. These figures are provided by Dr Chieh-Ting Lin with copyright permission from published work [141].

for passivating these defects owing to their zwitterionic nature. The positive and negative terminal groups of the AVA molecule can form bonds and thus passivate surface cationic and anionic defects. This zwitterionic nature has been reported to contribute to a dual-passivation effect in perovskite quantum dots.[287] However, the aliphatic chain between the end groups may act as a barrier to charge extraction since the AVA is preferentially located on the surfaces and interfaces of perovskite grains, as demonstrated previously.[281] Here, four amino acids (AAs) with the same end groups but varying carbon chain lengths: AVA (4C), γ-aminobutyric acid (3C), β-alanine (2C), and glycine (1C), were investigated to explore the impact of the chain length of these molecules on the defect passivation and charge extraction properties as seen in Figure 3.6a

3.5.2 Results and discussion

Film deposition and device preparation

A device structure of glass/ITO/PTAA/$MAPbI_3$/PCBM/BCP/Cu was employed in this study, and full details are given in Chapter 2. Solutions of the AAs were prepared by dissolving AAs in deionized water, each to a concentration of 1.5 mol dm^{-3}. The 1.5 M $MAPbI_3$ solutions were prepared by adding 1-2 vol. % of the various amino acids, with the reference solution adding the same amount of deionized water.

Performance of amino-acid-modified perovskite solar cells

The device performance of PSCs with the amino acid additives added at a concentration of 1 vol. % is considered first, and the corresponding J-V characteristics are shown in Figure 3.6b. The performance of devices prepared with the addition of glycine (1C) is comparable to, if not subtly, better than, additive-free (reference) devices. However, the PCE of devices prepared with the longer carbon chain additives decrease with increased chain length due to significant reductions in J_{SC}. When the concentration of the amino acid additives is increased to 2 vol %, as shown in Figure 3.6c, unsurprisingly significant J_{SC} losses are observed in devices prepared with 2C-4C chain length amino acids, as shown in Figure 3.6d. Nevertheless, improved performance is shown in the devices prepared using glycine compared to the reference devices. Noticeably, the PCE of devices prepared with glycine improved from 18.9 %, to 19.5 % and finally reached 19.8 % in reference, 1 vol.% and 2 vol.% films, respectively. The PCE increase of the 2 vol.% devices is driven by an increase in V_{OC} from 1.10 V to 1.14 V compared to the reference, while J_{SC} is maintained. The champion cell, prepared with 2 vol.% glycine (1C), achieved a PCE of 20.2 % in both forward and reverse scan directions (0.1 V s^{-1}) and a stabilized PCE of 20.1 %. (Figure 3.6e). The J-V results suggest that optimisations of the AA concentration and carbon chain length improve device performance dramatically. This is consistent with many other reports using similar additives, such as widely used AVAs for enhancing device stability, indicating the robustness and generality of using this passivation method.[281, 282, 288, 289]

Photoluminescence quenching of perovskite films

To understand the passivation and charge extraction effect by AAs, steady-state PL measurements were first employed to study the perovskite films with and without interlayers. Figure 3.7a shows the PL spectra of neat perovskite films with a significant increase in the intensity (approx. 6-fold) for all 1 vol.% AA films compared with the AA-free reference films, confirming that the trap density facilitating non-radiative decay has been reduced in the AA films. This also explains the general V_{OC} increase in most of the PSCs prepared with AAs, indicating the generality of using these AAs for effective passivation, attributed to the effects from the carboxylic and amine end groups.[287, 290, 291] Figure 3.7b shows the PL spectra of ETL (PCBM)/perovskite/HTM (PTAA) films. It is well established that, under illumination, a large proportion of free charges are transferred from the perovskite to the CTLs, leading to strong PLQ from neat films to perovskite with CTLs,[125, 292, 293, 294] and indeed, significant quenching is observed in here. This PL quenching caused by the CTL (PLQ_{film}) is then calculated and summarised in Figure 3.7d, where the reference films and films with 1C AA show comparable values, around 90 %, while films with longer carbon chain length AAs obtain lower values of 70%. These behaviours indicate that the reference films and those prepared with 1C AA show similar charge transfer efficiencies, whereas the efficiency is significantly impeded when using longer carbon chain length (2-4C) AAs, resulting in greater radiative band-to-band recombination in bulk. Such impeded charge transfer phenomenon may be due to the barrier formed at the perovskite/CTL interfaces,[174, 295, 296, 297] potentially ascribed to the poor conductivity of these materials,[298] which impairs overall charge extraction and reduces device J_{SC}.

Photoluminescence quenching of devices at open circuit and short circuit conditions

Device OC to SC PL quenching measurements were then conducted on these PSCs to assess the operation charge collection efficiency, which has been demonstrated earlier in this chapter. Figure 3.8a-e shows the PL spectra of all devices at both OC and SC with intensities normalized to the peak point of PL_{OC}, and the corresponding PLQ_{OC-SC} values are calculated and plotted

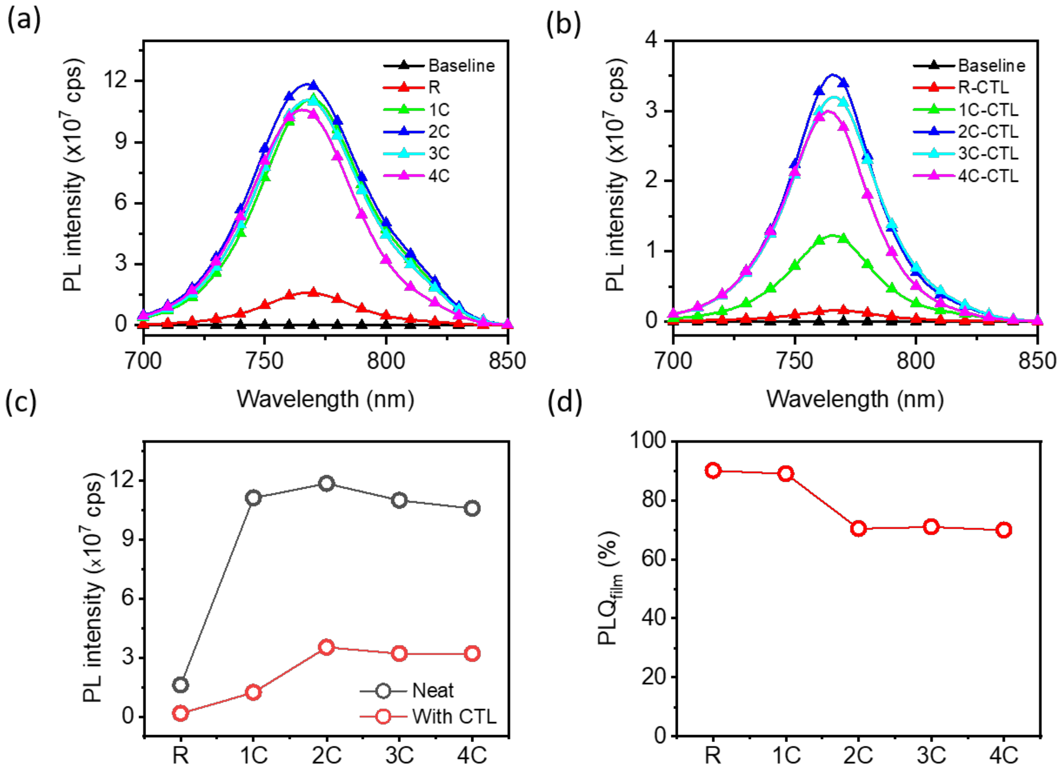

Figure 3.7: Steady-state PL emission spectra of additive-free and 1 vol % AA as an additive for (a) neat perovskite and (b) PTAA/perovskite/PCBM. (c) Summary of PL peak intensity from (a-b), and (d) the corresponding PLQ_{film}. A 635 nm CW laser light with 1-sun equivalent illumination intensity was used for excitation. Copyright permission of (a-b) from published work [141].

in Figure 3.8f. The PLQ_{OC-SC} gradually decreased from 92% to 46 % when the carbon chain length increased, indicating that the charge extraction to the out circuit becomes less efficient as the chain length increases. Again, the device incorporating 1C AA as an additive shows comparable PLQ_{OC-SC} behaviour to the reference cell, suggesting equally efficient charge extraction in the additive-based device. As expected, the trend of PLQ_{OC-SC} is inverse to that of device J_{SC}, where current density drops with increasing carbon chain length of the AA. This observation suggests that the loss of J_{SC} caused by increasing aliphatic chain length of the AAs results from inefficient charge extraction.[221, 260, 299, 300] This is mainly attributed to the hindered charge transfer from the perovskite to the interlayers, as discussed in the PLQ_{film} analysis. However, the device with 1C AA shows comparable PLQ_{OC-SC} to the reference cell, indicating reserved charge extraction efficiency. Such that, comparable J_{SC} is observed in the 1C AA PSC, and its outstanding PCE is attributed to the dramatic enhancement in V_{OC}.

3.5.3 Summary

This work has demonstrated that incorporating AA additives into the precursor solution is an effective way to passivate defect states and reduce non-radiative recombination in the PSCs, owing to their zwitterionic nature from the carboxylic and amine end groups.[287] Nevertheless, PSCs employing AAs with various aliphatic chain lengths yield dramatic differences in PCE. This change in PCE correlates with changes in the AA carbon chain length, where longer chain length significantly reduces the J_{SC} and thus the PCE. The device OC to SC PL quenching measurement results indicate this J_{SC} loss is due to substantial charge accumulation in the perovskite layer. Moreover, the PL data based on stand-alone thin films and films interfaced with CTLs implies that this charge accumulation is attributed to inefficient charge transfer from perovskite to the CTLs. Such accumulation effect could be attributed to the insulating effect or energetic barrier at the interface induced by the longer carbon chain-based AAs.[291, 296, 297, 301] Instead, using glycine (1C AA), as an additive leads to an improvement in V_{OC} from 1.10 V to 1.14 V due to defect passivation and no sacrifice in J_{SC} due to reserved charge extraction efficiency. This finally results in the device achieving a champion PCE of 20.2 %.

3.6 Enhanced hole extraction by introducing phosphorene nanoribbon in p-i-n perovskite solar cells

3.6.1 Introduction

PNRs are a distinct class of phosphorene materials with unique and exciting properties, including a tunable and direct bandgap, high-carrier mobility, and anisotropic characteristics, making them a promising candidate for a range of applications.[302, 303, 304, 305] The width-induced confinement nature of the PNRs could enable further tuning of properties and emergent exotic phenomena compared to the 2D sheet-formed phosphorene counterparts.[306, 307, 308, 309] Whilst PNRs have been predicted to offer transformative advantages in electronic applications, they are yet to be incorporated or studied in an optoelectronic device. Specifically, phosphorene-

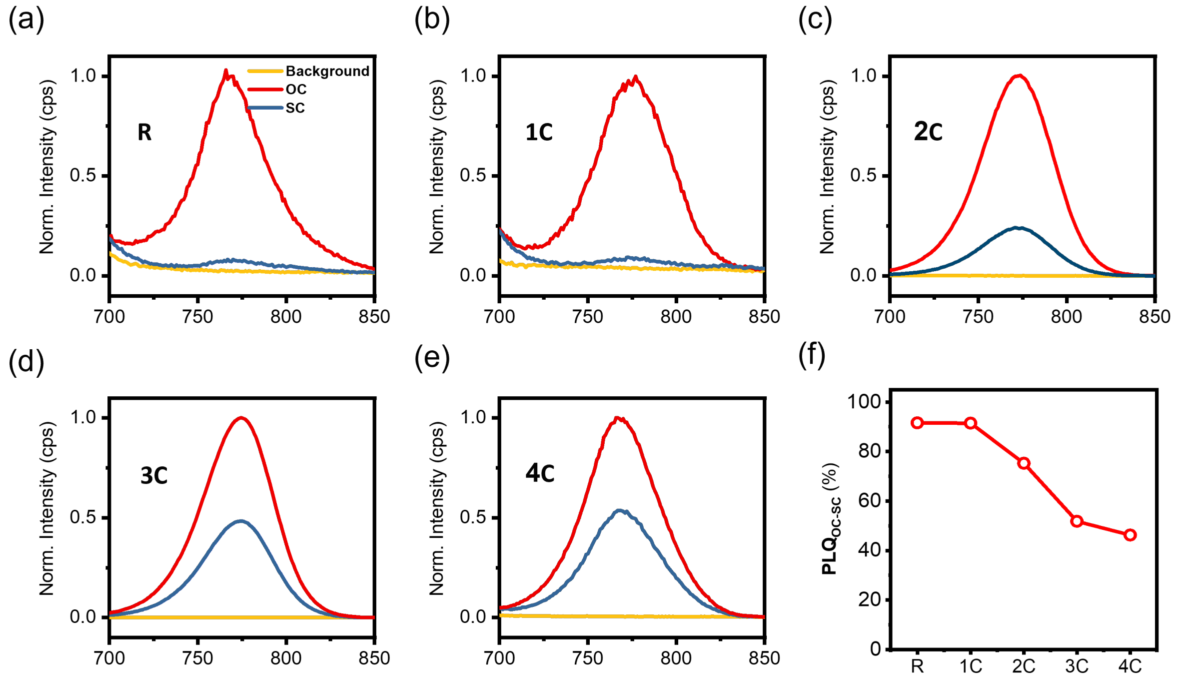

Figure 3.8: PL spectra of complete devices employing (a) additive-free MAPbI$_3$, and MAPbI$_3$ with 1 vol % (b) glycine, (c) β-alanine, (d) γ-aminobutyric acid, and (e) 5-AVA as an additive at OC and SC. Spectra labelled with red, blue and yellow represent OC, SC and background, respectively. (f) Calculated PLQ_{OC-SC}. A 635 nm CW laser light with 1-sun equivalent illumination intensity was used for excitation.

based materials exhibit holes as their majority carriers,[306] which gives PNRs great potential as novel HTMs in photovoltaic devices.

PSCs have rapidly emerged as one of the most promising candidates for PV due to their outstanding optoelectronic properties and solution processability (see Chapter 1). The most successful HTMs in PSCs are either small organic molecules or semiconducting polymers, and this has represented one of the major challenges for further enhancements in both device stability and efficiency.[236] However, these materials are not ideal, especially in the p-i-n PSCs, either causing non-negligible surface recombination or having a limited charge extraction efficiency.[122, 130] Owing to the superior electronic properties of phosphorene and its analogues, studies exploiting these materials in PSCs at both HTL/perovskite and ETL/perovskite interfaces have been demonstrated.[310, 311, 312, 313] Whilst most of the work was focused on black phosphorus quantum dots, black phosphorene was only reported once before: applying to n-i-p PSCs.[314] This work also demonstrated that enhanced charge transfer and charge collection are reached by better energetic alignments, achieved by tuning the thickness of the black phosphorene, leading to a PCE of 19.8%.[314] Despite this impressive result, no examples

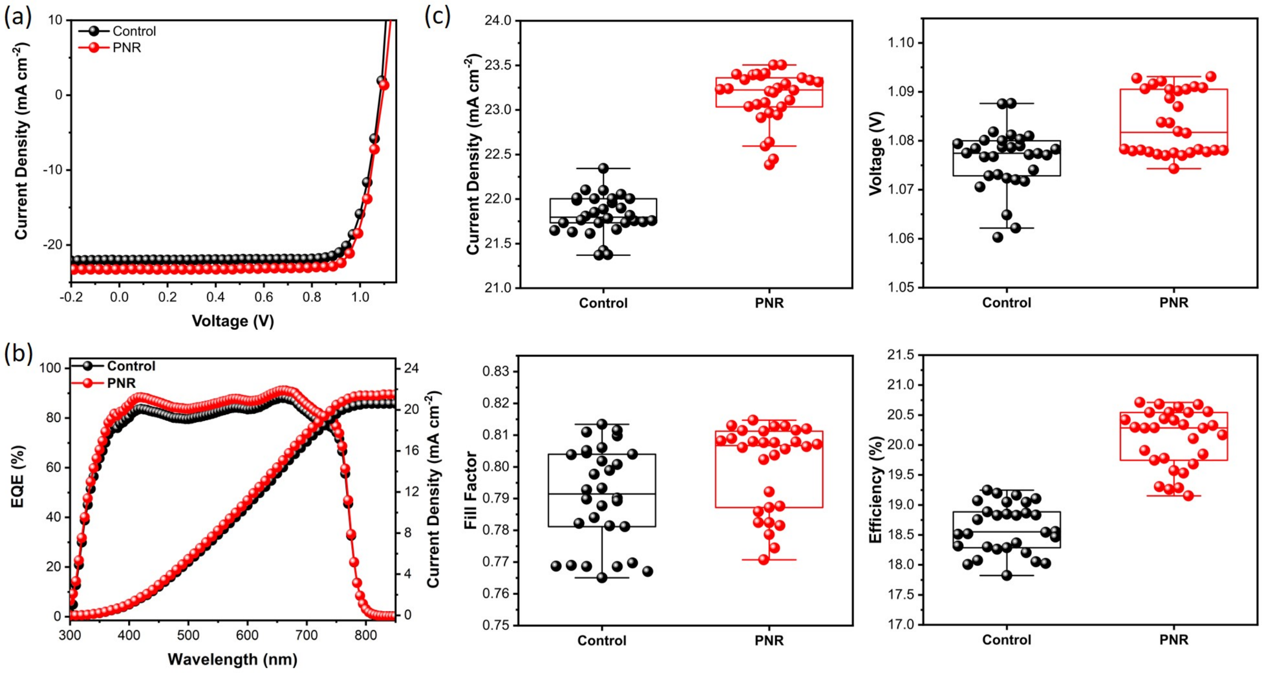

Figure 3.9: J-V performance of PSCs with and without PNRs. (a) J-V curve of champion PSCs with and without PNRs. (b) EQE and integrated current density of control and PNR PSCs. (c) PV parameters as statistical distribution for 70 PSCs with and without PNRs. These figures are contributed by Dr Thomas Macdonald.

of layered phosphorene have been studied in p-i-n PSCs.

Here, PNRs were employed as a hole-selective interlayer placed between the PTAA and $MAPbI_3$ in p-i-n planar PSCs with a device structure of glass/ITO/PTAA/$MAPbI_3$/PCBM/BCP /Cu. PNRs were optimised for device performance by controlling their layer thickness. Improved PCEs of over 21% were observed in the optimised PNR PSCs mainly due to the enhancement in J_{SC}. Finally, PL and ultrafast-TAS measurements were carried out to investigate the origin of these improvements by adding PNRs at the HTL/perovskite interface.

3.6.2 Results and discussion

Performance of the optimised phosphorene nanoribbons perovskite solar cells

The PNRs were produced and dispersed in DMF with a distribution in width of 5-50 nm and in lengths of 50 nm-10 μm, following the same protocol as reported previously.[309] The thickness of PNRs was tuned by controlling the number of spin-coated cycles of the PNR solution. More experimental details, including device fabrication, are shown in Chapter 2 and the previous report.[242] Figure 3.9a shows the J-V of champion PSCs with and without PNRs. Whilst the control devices demonstrate a PCE of 19.60%, J_{SC} of 22.30 mA cm^{-2}, V_{OC} of 1.089 V, and FF of 0.807, the PSCs incorporating the PNRs show improved device performances with PCE of 21.14%, J_{SC} of 23.33 mA cm^{-2}, V_{OC} of 1.093 V, and FF of 0.829. The integration of the EQE spectra shown in Figure 3.9b matches well with the corresponding J_{SC} values, ruling out any spectral mismatch issues. Figure 3.9c shows a statistical distribution of all photovoltaic parameters for 70 devices. Though all average photovoltaic parameters were improved for PSCs with PNRs, the most notable improvements were in the J_{SC} along with a slight improvement in V_{OC} and FF. The absorption spectra of ITO/HTL/MAPbI$_3$ films with and without PNRs are demonstrated in Figure 3.10a, where no differences were observed, excluding the possibility of J_{SC} is due to any optical enhancement effects. This implies that PSCs with PNRs show improved charge extraction efficiency compared to the control devices.

Evidence for improved charge extraction efficiency in PNR PSCs by optical measurements

Device OC to SC PL quenching measurements were carried out to understand the origin of the performance improvement in the PNR PSCs. Figure 3.10b shows the device OC to SC PL peak intensities of PNR and control PSCs under various intensities. Both devices exhibited similar PL_{OC} in terms of the intensity and slopes, indicating the same bulk recombination mechanisms and comparable $QFLS$ in these cells,[130, 149, 229, 315] as illustrated in the previous two sections in this chapter. This is in line with the J-V results where these two devices show similar V_{OC} values. However, compared with the control PSCs, devices with PNR have much lower values in PL_{SC} regardless of light intensities, indicating reduced band-to-band recombination and charge accumulation at SC.[272, 299] The PLQ_{OC-SC} under 1-sun equivalent illumination is then calculated and shown in Figure 3.10c, with 0.94 and 0.91 for the PNR and control PSCs, respectively. These results suggest that the enhancement of J_{SC} is due to the improved charge extraction efficiency at SC in the PNR-based PSCs.[141, 222] This improvement in charge extraction may also lead to the increase in the device FF, as indicated

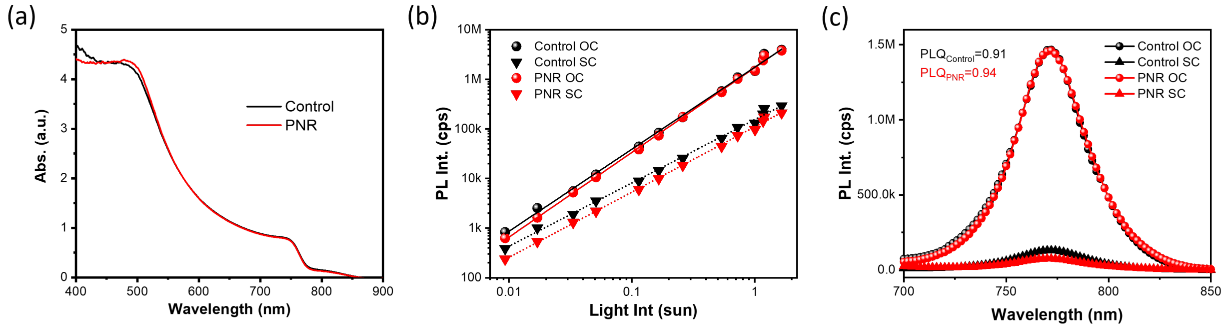

Figure 3.10: (a) UV-Vis results of films with the structure of ITO/HTL/MAPbI$_3$ and ITO/HTL/PNR/MAPbI$_3$. (b) Intensity-dependent device PL peak intensities of control and PNR PSCs at OC and SC. (c) Spectra of control and PNR devices at OC and SC under 1-sun equivalent illumination. A 635 nm CW laser was used for all the PL measurements.

in Chapter 3, Section 3.4.[141, 222, 259]

To understand the origin of the improvement in charge extraction efficiency, fs-TA spectroscopy is employed to study the charge transfer properties at the HTL/perovskite interface. The experimental details can be found in Chapter 2, Section 2.4. Figure 3.11 a and b represent the TA spectra, whereas c and d show the decay kinetics of the ITO/PTAA/MAPbI$_3$ (control) and ITO/PTAA/PNR/MAPbI$_3$ (PNR) films. The most prominent feature for both films is the negative optical density change (ΔOD) peaked at 758 nm, which is assigned to the photobleaching at the band edge of MAPbI$_3$.[168, 316] It is also worth noting on an early time scale ($<$ 450 fs), the noticeable kinetic features, a rise of a negative bleaching signal around higher energy (751 nm) along with a decrease of positive photo-induced absorption signal peaked around 777 nm, are attributed to hot carrier cooling at the band edge of MAPbI$_3$.[316, 317] Figure 3.11 c and d show the normalised (to an average between 2-3 ps after hot carrier cooling) decay kinetics of the band edge photobleaching for both films with two different excitation fluences. All decay kinetics show the same mono-exponential behaviour ascribed to the hole transfer from the MAPbI$_3$ to the HTL. Compared with the control sample, the PNR film shows more rapid decay kinetics consistently, regardless of the excitation fluence, demonstrating much faster hole transfer in this film.[167, 171] This indicates that the improved charge extraction efficiency in the PNR PSCs observed above may be attributed to the enhancement of hole extraction at the HTL/perovskite interface.

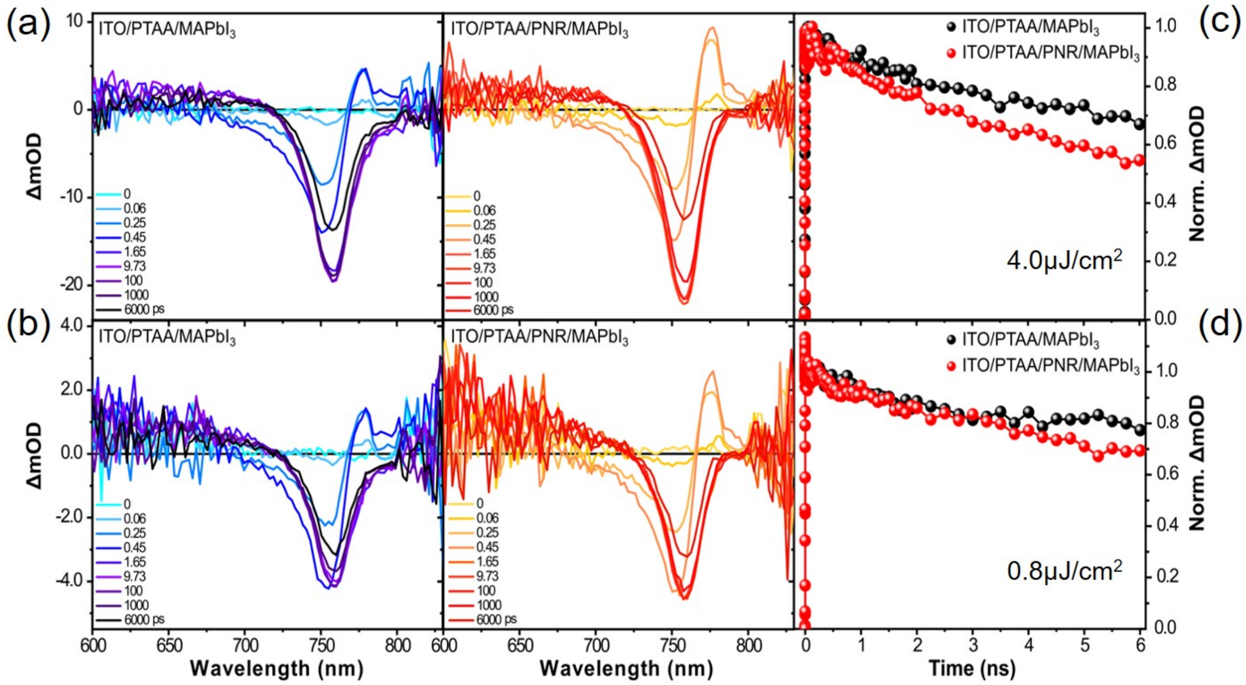

Figure 3.11: TA characterisation of ITO/PTAA/MAPbI$_3$ and ITO/PTAA/PNR/MAPbI$_3$ samples within 6 ns and measured under a 430 nm laser pump. The spectra evolution is shown in (a) and (b), with excitation fluence of 4 μJ/cm^2 and 0.8 μJ/cm^2, respectively. Normalised TA spectra of the band-edge transition in MAPbI$_3$ recorded at the maximum photobleaching signal are shown in (c) and (d) with pump excitation of 4 μJ/cm^2 and 0.8 μJ/cm^2, respectively.

3.6.3 Summary

In this work, PNRs have been successfully applied to p-i-n PSCs as a mediator layer between PTAA and the perovskite, leading to PSCs with enhanced PCE above 21%. This efficiency enhancement is mainly ascribed to a significantly improved J_{SC} and FF. Whilst the EQE and UV-Vis results have excluded that these improvements are due to increased light absorption, the device OC to SC PL quenching results demonstrated that the improved charge extraction efficiency at SC is the leading cause. This improvement can be mainly attributed to the accelerated hole transfer across the HTL/perovskite interface induced by the PNR intermediating, as indicated by the TA results. Previous reports have shown that the CB and VB of phosphorene are tunable by simply changing the layer thickness.[308] Thus, a better and graded energetic alignment (HOMO/VB) at the HTL/perovskite interface may be formed by introducing the PNR with optimised thickness to the best PCE. This graded bandgap concept is usually used as an efficient strategy to improve charge extraction in an optoelectronic device and has been demonstrated successfully in PSCs.[318, 319, 320] Moreover, the superior charge transport properties of the PNR layer could also assist in the charge transport through the HTL out to the anode by improving the conductivity of the HTL layer.[304]

3.7 Conclusion

To conclude, the unique device OC to SC PL quenching measurement, in combination with several other optical measurements, such as fs-TA, steady-state and time-resolved film-based PL spectroscopy, has been used as an effective tool to understand the recombination loss mechanism in p-i-n PSCs.[221, 259] The charge carrier dynamic processes, including bulk recombination, surface recombination and interface charge transfer, influenced by various materials and device processing methods, have been revealed extensively. In particular, three individual studies based on different solar cell fabrication approaches for optimizing the device PCE are introduced and discussed.

The results of the first study show that PSCs with thicker perovskite layers performed better under weak-light conditions due to enhanced absorption and suppressed non-radiative recombination, whereas their performance reduces with the increase of light intensity as there is a more significant charge extraction loss at SC due to a more substantial bulk band-to-band recombination. In contrast, the thinner PSCs show lower efficiency in weak light owing to less absorption and more dominating surface recombination, while their high-light performance is better due to more efficient charge extraction at SC, as photogenerated charges travel a shorter distance to be extracted. These results offer a guide for designing PSCs for different real-world applications when considering the actual solar irradiance.[273, 274]

Furthermore, an effective strategy for reducing defect states in the perovskite layer by incorporating AA derivatives as additives into the precursor has also been investigated. A champion PCE of over 20% was achieved by using glycine (1C AA), which is among the highest of PSCs using a similar method and active layer.[282, 287, 288, 290] This improvement is mainly due to the dramatic improvement in the V_{OC} of 40 mV. However, using AAs with longer carbon chain lengths decreases J_{SC} and, therefore, the PCE. This is attributed to their incorporation at interfaces where they obstruct charge transport and cause inefficient charge extraction from the perovskite layer to the CTLs. This work explains the limitation of using these AA-based additives, such as widely used AVA,[281, 282, 288, 289] which provides a physical and synthetic guide for future material and device engineering.

Finally, an interlayer modification strategy has also been demonstrated by inserting a nanomaterial, PNR, in between the PTAA and the perovskite layers. This strategy leads to a further boost of PCE up to over 21% due to the improved charge extraction efficiency contributing to improved J_{SC} and FF of the device. This charge extraction could be due to a gradient band alignment mediated by PNR that accelerates the charge transfer across the perovskite/HTL interface.[321, 322, 323] Moreover, this work is also the first demonstration of the PNR material in optoelectronic devices, which opens a new window for future application of these layered materials.[308, 309, 324]

Overall, this chapter demonstrated new strategies for the performance optimization of p-i-n planar PSCs and examples of using the device OC to SC PL quenching measurement to understand the charge carrier dynamics and loss mechanisms in these devices, providing new guides for future efficiency development.

Chapter 4

Impact of Interface Energetic Alignment and Mobile ions on Charge Carrier Accumulation and Recombination in Methylammonium-free p-i-n Perovskite Solar Cells

4.1 Declaration of contributions

Lucy Hart carried out the Driftfusion simulations.

Francesco Furlan and Dr Julianna Panidi conducted the SCLC and TFT measurements, respectively.

4.2 Abstract

Understanding the non-radiative loss mechanisms in PSCs is key to further improving their efficiency and moving towards their theoretical limit. Here, an operando PL system is built and applied to study four PSCs which have ETLs with differing LUMOs. This system can measure real-time PL spectra during a J-V scan under 1-sun equivalent illumination, which allows direct comparison between the internal performance (recombination currents and $QFLS$) and the external performance (J-V) of a PSC under operating conditions. The analysis reveals the impact of the energetic alignment between the LUMO of the ETL and the CB of the perovskite on charge transfer, recombination, and accumulation. The results demonstrate that a lower ETL LUMO reduces the V_{OC} by inducing strong surface recombination, while a higher LUMO impedes charge extraction owing to the energetic barrier for charge transfer from the perovskite to the ETL. Remarkably, a $QFLS$ of over 1 eV is observed at SC, even in cells with energetics that favour charge transfer. This indicates that charge accumulation in bulk perovskite is a common phenomenon in PSCs. Device simulations using Driftfusion, a software package which allows one to include a mobile ion population in the system's drift-diffusion equations, indicate that this can be ascribed to the mobile ions screening the internal electric field at SC. This field screening means that charge extraction is driven by diffusion, not drift, which can lead to a reduction in J_{SC}, suggesting mitigating ion migration is essential for developing more efficient solar cells.

4.3 Introduction

Over the past decade, organic-inorganic metal halide PSCs have made remarkable progress, achieving over 25% PCE in single-junction cells.[67, 325] This progress can be attributed to the rapid evolution of materials and device engineering techniques, which have allowed the field to obtain both high-quality bulk perovskites with low defect densities and desirable contacts which facilitate efficient charge-extraction. Nevertheless, the kinetics of charge extraction, including the role of charge transport within the perovskite layer versus transfer from the perovskite layer to its contacts, has received relatively little attention,[122, 130, 167, 170, 326] as discussed in Chapter 1, Section 1.4. In a PSC, photogenerated charges have to transport to the interfaces before being transferred to the interlayers and finally collected by the external circuit. During these processes, recombination, such as trap-assisted non-radiative recombination, band-to-band radiative recombination, and surface/interface non-radiative recombination, also occurs,[127, 225] which are also illustrated in Chapter 1, Section 1.4. As a result, the device performance is determined by a kinetic competition between these charge extraction processes versus the charge recombination processes. Therefore, understanding these processes is crucial to develop the PSCs further towards their theoretical limits. Whilst many studies focused on investigating these charge dynamics by measuring the samples at OC,[130, 149, 150, 167, 327] revealing them by considering the actual device operating conditions is unclear.

For charge extraction, a key factor to take into consideration is the screening of the built-in electric field by mobile ions, an effect which has been demonstrated both experimentally and using device simulations.[208, 209, 328] Indeed, this modulation of the internal electric field is thought to be one of the key factors causing J-V hysteresis and light soaking effect in PSCs,[208, 272, 329, 330, 331] and has been reported to reduce their stabilized photocurrent output,[233] as well as inducing inconsistencies between the measurement results and the actual device performance.[125] Herein, we use operando PL spectroscopy (described in Chapter 2, Section 2.5) to demonstrate a further consequence of ionic shielding; significant charge accumulation in the active layer, even under SC conditions. To investigate the universality of ion-induced charge accumulation in PSCs, we performed measurements on four p-i-n devices. These devices differ in their ETLs, which were selected to cover a range of LUMO values. This allowed us to elucidate the impact of energetic alignment at the perovskite/ETL interface on charge accumulation, transfer and extraction and verify that the charge accumulation observed at SC is not solely a consequence of the ETL's properties.

Among the many possible choices of ETLs, TiO_2 and SnO_2 are promising n-type materials used in the most efficient n-i-p structured PSCs.[37, 67, 325] Unfortunately, these materials are unsuitable for use in p-i-n PSCs due to their depositional incompatibility; high-temperature annealing is necessary for both ETL materials, but is detrimental to the perovskite layer deposited underneath. Instead, fullerene derivatives, such as PCBM and C60, are widely used as the best ETLs in p-i-n devices.[91, 92, 332] However, these materials are not ideal, either causing non-negligible surface recombination or contributing to high series resistance.[333, 334] Particularly, in state-of-the-art wide-bandgap PSCs (which are used as the top cells in tandem solar cells), the energetics of the ETL's LUMO and the perovskite's CB are not well matched, which leads to additional surface recombination.[229]

Although it is well known that p-i-n PSCs perform worse than n-i-p devices, there is still debate about which CTL properties are most responsible for this and the mechanisms linking CTL properties to a device's J-V parameters: V_{OC}, FF, and J_{SC}. Therefore, to answer these questions and realise further improvements in PCE for p-i-n devices, it is necessary to understand the loss mechanisms both inside the perovskite and at the perovskite/CTL interface.

Steady-state PL spectroscopy has been widely used to examine the properties of perovskites by monitoring their radiative recombination. A high PL yield obtained from the perovskite bulk demonstrates that there are low defect densities in the perovskite. Moreover, once the absolute PL spectrum is measured, it is possible to calculate the $PLQY$, radiative recombination current (J_{rad}) and $QFLS$ using Equation 2.6. This method allows one to compare the internal bulk $QFLS$ to the external V_{OC}, and has been used extensively to indicate the dominant recombination loss mechanisms in PSCs.[130, 150, 229] While many studies are focused on understanding the origin of V_{OC} losses, the performance of a PSC is determined by recording its current at multiple voltages, including the information of FF and J_{SC}. Hence, developing new methodologies to quantify the $QFLS$ across the J-V curve and use this to quantify the impact of charge accumulation and charge extraction on FF and J_{SC} is necessary.

The previous chapter has shown three examples of using the quenching of device PL from OC to SC to identify recombination pathways and assess charge extraction efficiency in a variety of PSCs. Additionally, other reports have demonstrated the correlation between voltage-dependent PL and PSC performance.[260, 300, 335] This work builds on these insights and introduces an operando PL measurement, similar to that used by Stolterfoht et al.,[260] but focused more on the operating conditions, which can measure the absolute PL spectrum while

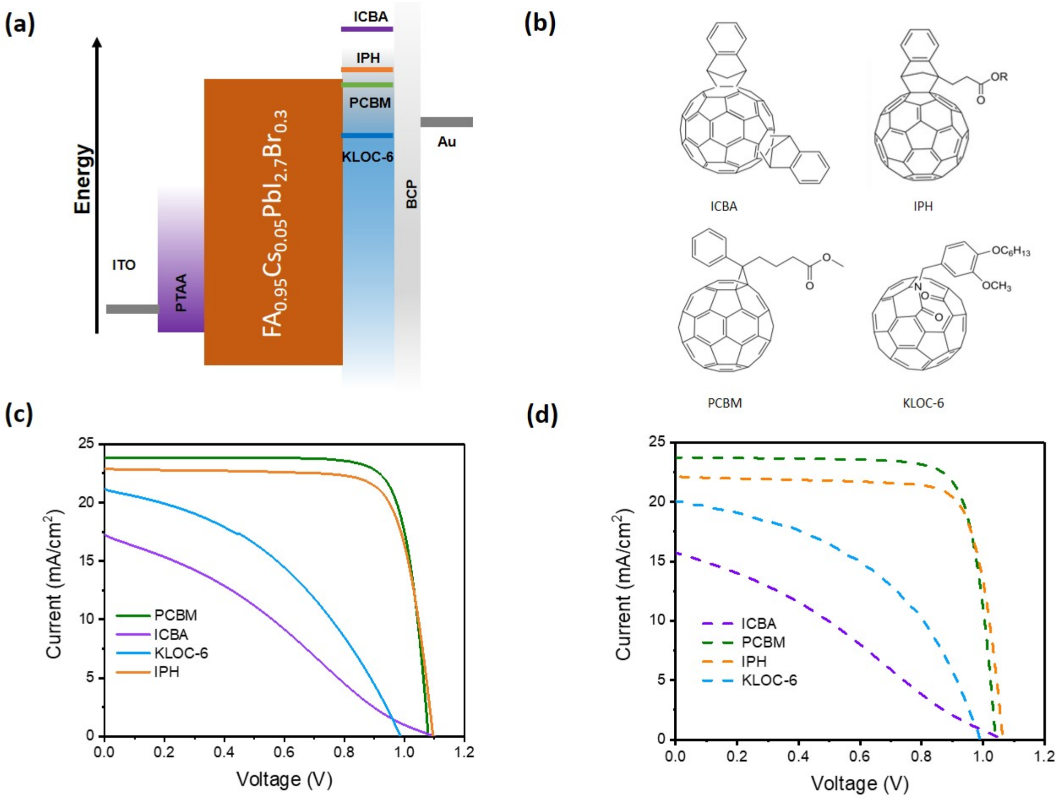

Figure 4.1: (b) Flat-band energy alignment of p-i-n PSCs with different ETLs; (b) chemical structures of all fullerene-based ETL materials; device J-V performances obtained from (c) the operando PL measurement (532 nm CW laser 1-sun equivalent illumination) and (d) solar simulator (AM 1.5).

simultaneously performing a J-V scan under 1-sun equivalent illumination, as shown in Figure 2.3 in Chapter 2, Section 2.5. By calculating the $QFLS$ and the various recombination currents, this technique can monitor and compare the recombination and extraction rates of photogenerated charge carriers at different operating voltages.

In this work, significant charge accumulation at low voltages in all the devices measured is observed, irrespective of the energetic alignment at the perovskite/ETL interface. The results also show that a negative energy offset from the perovskite's CB to the ETL's LUMO results in strong surface recombination, which reduces V_{OC}, while a positive energy offset leads to a reduction in charge extraction efficiency, limiting J_{SC} and FF. Device modelling indicates that this occurs due to ionic screening of the built-in electric field, which causes charge transport to be driven by diffusion rather than drift. Overall, these results suggest that the loss mechanisms in these devices are strongly influenced by both the perovskite/ETL interface properties and the effects of ion migration.

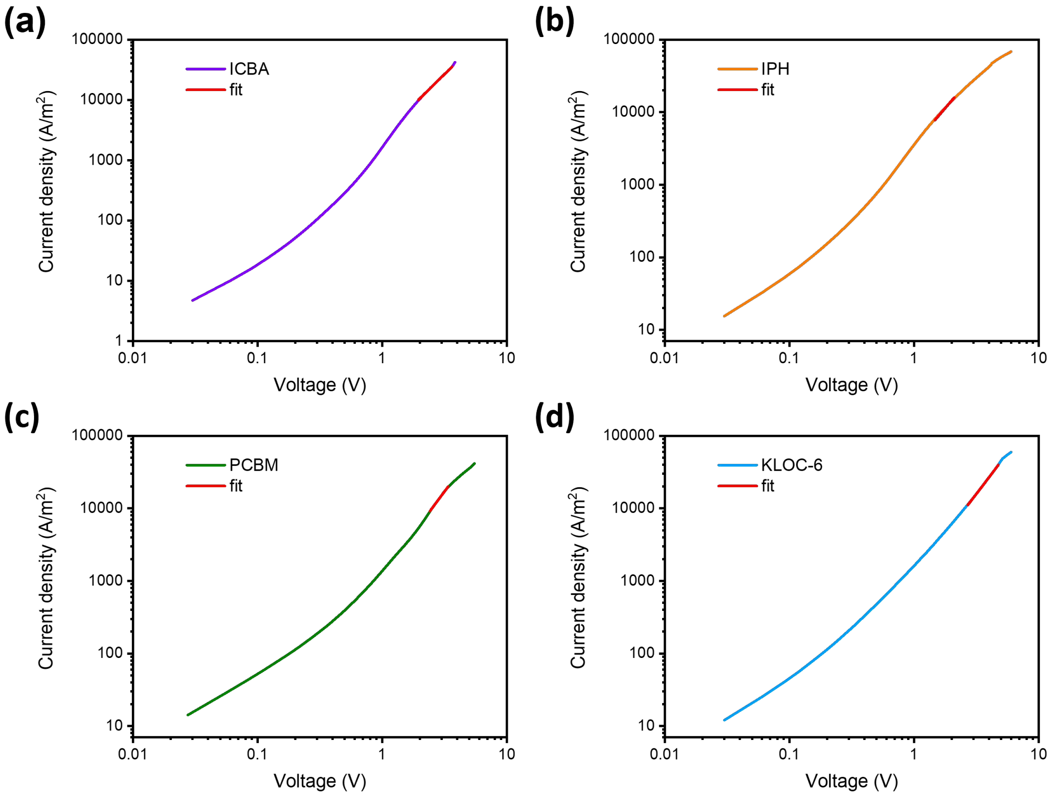

Figure 4.2: J-V curves from the SCLC measurement with electron-only devices. A device structure of ITO/ZnO/PEIE/ETL/Ca/Al is employed, with ETL of ICBA, IPH, PCBM and KLOC-6, respectively. These data were contributed by Francesco Furlan.

4.4 Results and discussion

4.4.1 Experimental

Device structure

Four p-i-n PSCs with the same device structure but varied ETLs were studied using operando PL spectroscopy, with experimental procedures given in Chapter 2, Section 2.5. Figure 4.1a shows the flat-band energy alignment of these devices, which have the geometric structure ITO/PTAA/perovskite/ETL/BCP/Au, where the perovskite is $FA_{0.95}Cs_{0.05}PbI_{2.7}Br_{0.3}$, and four ETLs used were ICBA, IPH, PCBM, and KLOC-6. Their chemical structures are shown in Figure 4.1b, and typical values of their electron affinity/LUMO are summarised in Table 4.1 (row 10). We note that the absolute values of the electron affinity/LUMO vary across the literature as different measurements may give variable absolute values. Additionally, other factors, such as aggregation and tail states, may also make these energy levels hard to determine.[336, 337] These uncertainties thus suggest that measuring the absolute LUMO values of these ETLs is challenging, as it will vary depending on both the chosen measurement technique and the method of sample preparation. Nevertheless, it is consistently found that ICBA has the shallowest LUMO of the chosen ETL materials, followed by IPH, then PCBM and lastly, KLOC-6.[338, 339, 340, 341, 342] An example for determining the LUMOs of these ETLs using the same method has been demonstrated by Willems et al., consistent with this trend.[338] Furthermore, it is usually recognized that the LUMO of PCBM has been measured to lie slightly below the perovskite CB, meaning that this device should have the smallest barrier to charge extraction and injection at the perovskite/ETL interface.[89, 338, 343]

Charge transport property of ETLs

The mobilities of the ETLs were examined. The method of SCLC was first employed, in which the mobilities of the ETLs are determined by fitting their J-V data from the electron-only devices, as shown in Figure 4.2 and illustrated in Chapter 2, Section 2.3. The results follow a trend of PCBM > ICBA $\geq$ IPH > KLOC-6 with values of 3×10^{-5}cm^{2}V^{-1}s^{-1}, 5×10^{-6}cm^{2}V^{-1}s^{-1}, 5×10^{-6}cm^{2}V^{-1}s^{-1}, and 1×10^{-6}cm^{2}V^{-1}s^{-1}, respectively. This trend was further verified by the mobilities obtained from TFT measurements shown in Figure 4.3 with experimental and analysis details demonstrated in Chapter 2, Section 2.3. Though much larger values were obtained from the TFT measurements due to their high operation voltages, the same trend was observed.

PV performance

J-V curves and their parameters of the four PSCs obtained from the operando PL measurement are first discussed, as shown in Figure 4.1c and summarised in Table 4.1. PCBM shows the best PCE, the highest J_{SC} of 23.9 mA/cm^2, a V_{OC} of 1.08 V and an FF of 0.79. Though ICBA and IPH show the highest V_{OC} of 1.10 V, compared to PCBM, they have lower PCEs due to their lower J_{SC} values (22.9 mA/cm^2 for IPH, 17.2 mA/cm^2 for ICBA) and FFs (0.77 for IPH, 0.30

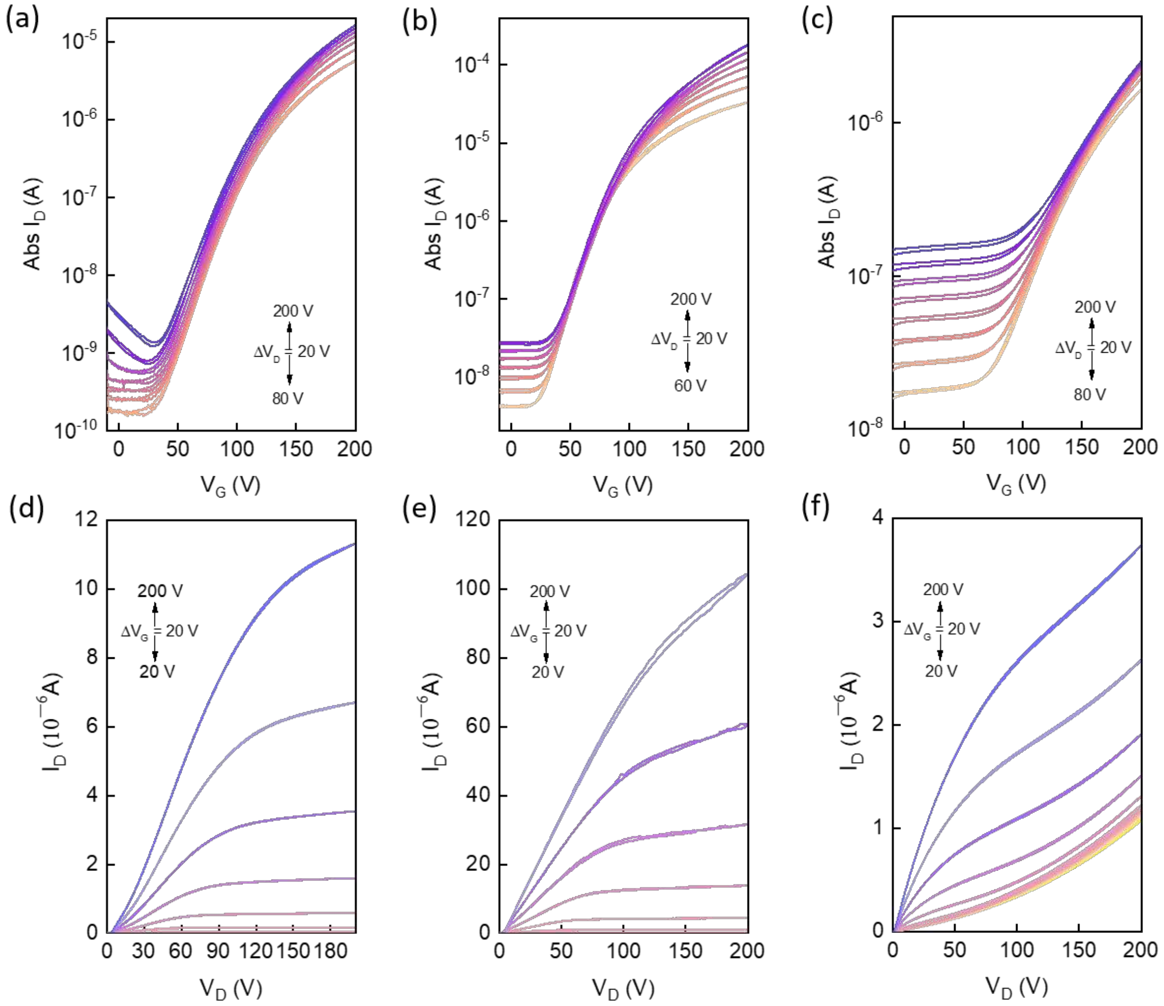

Figure 4.3: Characterisations of TFTs with ICBA, PCBM and KLOC-6. Gold source and drain electrodes and glass substrates are used in these devices. These data were provided by Dr Julianna Panidi.

for ICBA). The KLOC-6 device has the lowest V_{OC} of 0.99 V, a reduced J_{SC} and FF of 21.2 mA/cm^2 and 0.41, respectively. However, compared to ICBA, KLOC-6 shows a higher PCE due to its higher J_{SC} and FF. These parameters are comparable with the data measured under AM 1.5 from a solar simulator, as shown in Figure 4.1d and summarised in Table 4.1. Devices measured from the operando PL system show slightly better PCEs, which might be due to the 532 nm laser having a spatially shallower photogeneration profile than that of the broad solar spectrum. Nevertheless, both data show the same trends in the device J-V parameters.

Table 4.1: Summary of device J-V parameters under 532 nm CW laser and solar simulator from Figure 1c and Figure 1d.

Illumination condition	Parameter	ICBA	IPH	PCBM	KLOC-6
Laser	J_{SC} (mA cm^{-2})	17.24	22.91	23.87	21.17
	V_{OC} (V)	1.10	1.10	1.08	0.99
	FF	0.30	0.77	0.79	0.41
	PCE (%)	5.68	19.40	20.37	8.59
AM 1.5	J_{SC} (mA cm^{-2})	15.72	22.14	23.73	20.06
	V_{OC} (V)	1.06	1.06	1.04	0.99
	FF	0.30	0.78	0.79	0.46
	PCE (%)	5.02	18.37	19.52	9.14
	LUMO (eV)	-3.70	-3.79	-3.82	-4.04
	ΔLUMO (meV)	120	30	0	-220

Charge transfer kinetics at the perovskite/ETL interface

In order to understand the impact of energetic alignment on charge transfer at the perovskite/ETL interface, TRPL and steady-state PL spectroscopy were performed on neat perovskite and perovskite/ETL films. Figure 4.4a shows the TRPL decay kinetics of the five samples. All the decay kinetics exhibit a similar, fast first phase but varied, slower second phases. Considering the second phase, ICBA shows the slowest decay, followed by IPH, while PCBM and KLOC-6 decay the fastest. As all the films were excited from the side opposite to the perovskite/ETL interface and a low excitation fluence of 0.4 nJ/cm^2 was used, we attribute the fast phase to bulk trapping, in line with previous results in the literature.[119, 122] The slow phase of the neat perovskite film is due to bulk transport and/or recombination kinetics, while the slow phase of the other films is determined not only by bulk transport and recombination but also by the subsequent charge transfer from the perovskite to the ETL.[122] Therefore, the fast decay of the second phase observed in the samples with PCBM and KLOC-6 is indicative of rapid charge transfer at the perovskite/ETL interface, while the slow decay of the second phase observed in IPH and ICBA suggests a lower rate of charge transfer. This is corroborated by the fs transient absorption spectroscopy results in Figure 4.4b, where the band-edge photobleaching kinetics demonstrate a similar trend in decay rates as the TPRL kinetics. Additionally, steady-state $PLQY$ measurements (shown in Figure 4.4c) demonstrate that ETLs with lower

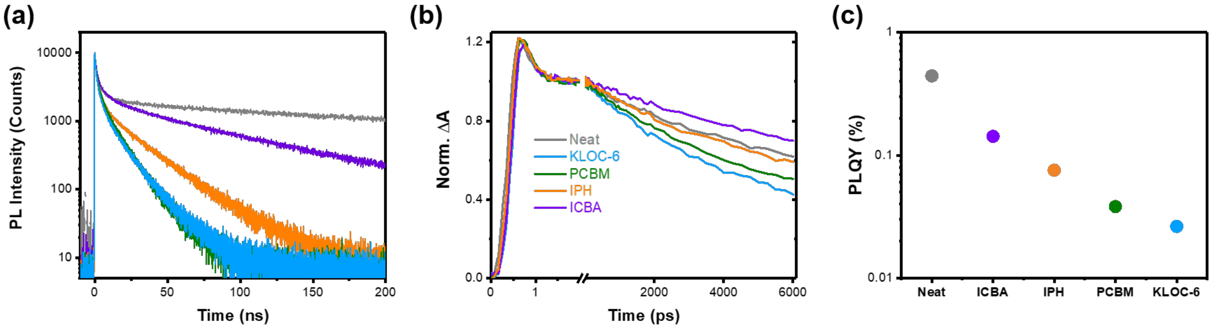

Figure 4.4: (a) TRPL decay kinetics, (b) ultrafast TA spectroscopy band-edge photobleaching decay kinetics, and (c) steady-state $PLQY$ measurement of perovskite films with or without ETLs. For all the measurements, samples are excited from the glass/perovskite interface. The PL signals were all probed from the glass/perovskite interface, whilst the TA signals were obtained from the transmitted light. In the TRPL measurements, 1 MHz 405 nm laser pulses with a fluence of 0.4 nJ/cm^2 per pulse and duration of $<$ 200 ps per pulse were used for excitation, and the decay kinetics were probed at the PL peak wavelength of 790 nm. For the TA measurements, 500 Hz 635 nm laser pulses with a pulse duration of $<$ 200 fs and flux of 2.3 $\mu J/cm^2$ per pulse were used for excitation, and the decay was probed at 770 nm. In the $PLQY$ measurements, a 532 nm CW laser light with 1-sun equivalent illumination intensity was used for excitation.

LUMO levels have greater PL quenching versus the neat perovskite film, indicative of a lower charge density in the perovskite layer and greater charge transfer to the ETL. Thus, when taken together, these results provide strong evidence that lowering the LUMO of the ETL increases the rate of charge transfer from the perovskite to the ETL and reduces the bulk carrier density.

Operando PL and QFLS

The operando PL spectra of the full devices are investigated. Figures 4.5a-d show the absolute PL spectra of the devices as the voltage is scanned from 0 V to 1.3 V under 1-sun equivalent illumination, with the overall $PLQY$ for each device plotted versus voltage in Figure 4.5e (right-y-axis). None of the spectra shows a peak shift indicating that there are no significant effects of halide segregation. For most devices, the $PLQY$ increases dramatically for V $>$ MPP, indicative of enhancing charge accumulation in the perovskite layer, while it is nearly voltage-independent for V $<$ MPP, ascribed to charge extraction to the contact layers.

For the $PLQY$ at voltages near V_{OC}, there is little current extraction, and a high carrier accumulation in the bulk perovskite is expected, meaning a high rate of PL. At V_{OC}, the KLOC-6 device has by far the lowest $PLQY$, followed by the PCBM device and finally the IPH and ICBA devices. This trend is consistent with the steady-state $PLQY$ results and indicates that

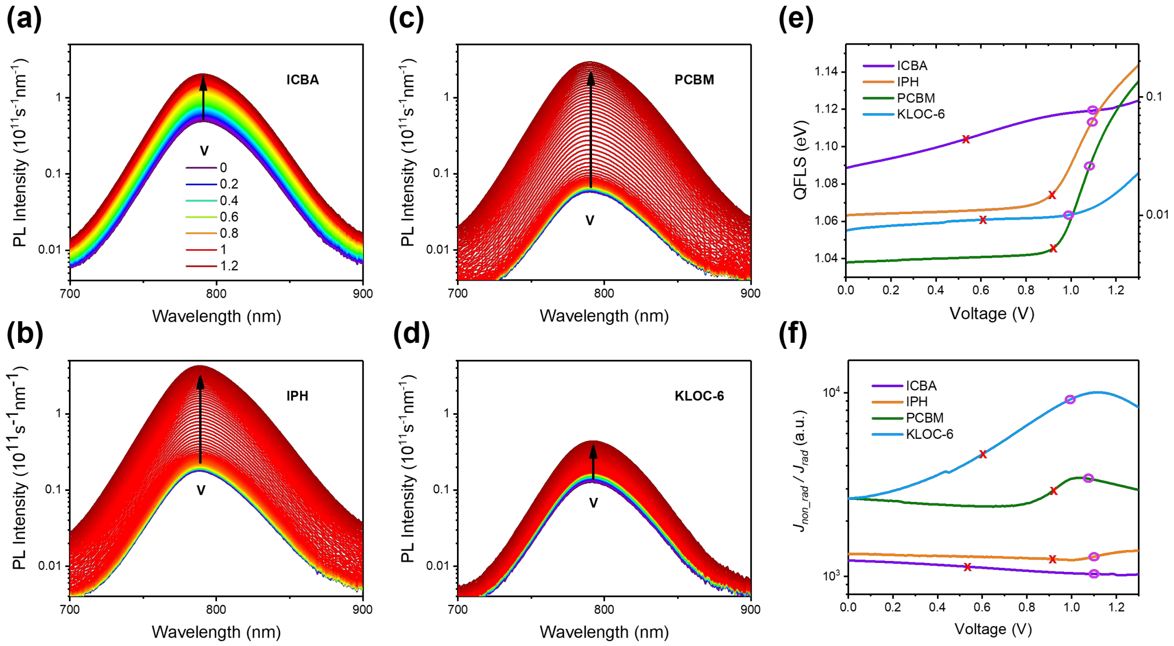

Figure 4.5: (a-d) Operando PL spectra of (a) ICBA, (b) IPH, (c) PCBM, and (d) KLOC-6. The voltage increases from 0 V to 1.3 V, as is indicated by the colour change from blue to red, and the corresponding legend is shown in (a). (e) $PLQY$, $QFLS$ and (f) $J_{non-rad}/J_{rad}$ of all devices Measurements were carried out under 1-sun equivalent 532 nm CW laser illumination, and all devices were illuminated under these conditions for 5 min prior to measurement. The values at V_{OC} and MPP for each device are marked as circles and crosses in (e) and (f), respectively.

the low LUMO of KLOC-6 limits the bulk carrier density at OC, attributed to enhanced surface recombination losses. As the applied voltage (V_{app}) is decreased, the concomitant reduction in $PLQY$ is indicative of the charge extraction efficiency.[221, 222] In both the IPH and PCBM devices, the $PLQY$ decreases by one order of magnitude when V_{app} decreases from V $\geq V_{OC}$ to the MPP, indicative of efficient charge extraction, with the largest decrease observed for PCBM device, consistent with it exhibiting the highest J_{SC}. The KLOC-6 device only shows a modest $PLQY$ reduction, attributed to its low charge accumulation even at OC, as commented above. Most strikingly, the ICBA device has a high $PLQY$ across the entire voltage range, indicative of its poor charge extraction efficiency resulting in substantial charge accumulation in the perovskite bulk even at SC, as discussed in Chapter 2.[141, 222, 299, 300] This is consistent with the energy barrier presented by the high LUMO of ICBA, the effects of which can also be seen in the low J_{SC} and FF of the ICBA device.[141]

Using Equation 2.6, the $PLQY$ values were used to calculate the $QFLS$ in each device at each voltage and this is shown in Figure 4.5e (left-hand y-axis), with the calculation details

Table 4.2: Summary of OC and SC device $PLQY$, $QFLS$ from operando PL measurements.

ETL	V_{OC} (V)	$QFLS_{OC}$ (eV)	$QFLS_{OC} - qV_{OC}$ (meV)	J_{SC} (mA cm^{-2})	$QFLS_{SC}$ (eV)	$\Delta QFLS_{OC-SC}$ (meV)
ICBA	1.10	1.13	30	17.2	1.10	30
IPH	1.10	1.12	20	22.9	1.07	50
PCBM	1.08	1.10	20	23.9	1.05	50
KLOC-6	0.99	1.07	80	21.2	1.06	10

described in the experiment section. We first compare the OC $QFLS$ ($QFLS_{OC}$) measured from the PL data to the device qV_{OC}'s, as summarised in Table 4.2. As expected, $QFLS_{OC}$ shows the same trend as the qV_{OC} values, namely ICBA $\geq$ IPH > PCBM > KLOC-6. However, it is striking that the differences between $QFLS_{OC}$ and qV_{OC} are all 20-30 meV for ICBA, IPH and PCBM but significantly higher (80 meV) for KLOC-6 (See Column 4 in Table 4.2). This larger mismatch between $QFLS_{OC}$ and qV_{OC} for the KLOC-6 device is indicative of larger surface recombination losses for this device at OC. This can be attributed to greater electron accumulation in the KLOC-6 ETL resulting from its lower LUMO level, accelerating interfacial recombination losses with perovskite holes.[152] We note that surface recombination at the PTAA/perovskite interface may also contribute to $QFLS_{OC} - qV_{OC}$.[315]

The SC $QFLS$ ($QFLS_{SC}$) of these devices and the $QFLS$ reduction from OC to SC ($\Delta QFLS_{OC-SC}$) are now considered, as summarised in Table 4.2. Surprisingly, all the devices show high values of $QFLS_{SC}$ (>1 eV), regardless of the ETL LUMO level, indicating that there is significant charge accumulation in the perovskite layer, even under SC conditions. As a result, small values of $\Delta QFLS_{OC-SC}$ are observed, with all the devices having a value $\leq$ 50 meV. It is apparent that the PCBM device had the lowest $QFLS_{SC}$, largest $\Delta QFLS_{OC-SC}$, and highest J_{SC}, followed by IPH and then ICBA. This can be attributed to the improvement in charge extraction efficiency, which occurs as the LUMO of the ETL is decreased and agrees with the trend in the charge transfer rates observed in the fs-TA and PL results. However, the device using KLOC-6, which has the lowest LUMO among the ETLs, is an exception to this trend as it has a higher $QFLS_{SC}$ (by 10 meV) and a lower J_{SC} (by 2.7 mAcm^{-2}) than the PCBM, and the smallest $\Delta QFLS_{OC-SC}$ (10 meV) of all the devices. This low $\Delta QFLS_{OC-SC}$ value can be attributed to two factors: first, the low LUMO of KLOC-6 leads to enhanced surface recombination and a reduced $QFLS_{OC}$ (as discussed in the previous paragraph) and second, the low mobility of the KLOC-6 (one order of magnitude lower than that of PCBM as measured in the SCLC and TFT measurements presented in Figure 4.2) reduces charge extraction efficiency to the external circuit under SC conditions. This leads to charge accumulation in the device at SC, which enhances $QFLS_{SC}$ and reduces J_{SC}.[141, 222, 300, 299]

It is striking that compared to less efficient technologies, such as DSSC and OPVs, which have reported OC to SC charge density reduction of over one order of magnitude,[223, 344, 345] the best-performing PCBM PSC (PCE of ∼20%) demonstrates a relatively small $\Delta QFLS_{OC-SC}$ ($\leq$ 50 meV), corresponding to a low reduction in charge density. This is because, for classic intrinsic semiconductors with sharp band edges, $QFLS$ can be determined using the equation:

$$QFLS = k_B T \times ln(\frac{n}{n_0}) \tag{4.1}$$

, where n is the charge density under photoexcitation and n_0 is the background charge density under dark equilibrium. Assuming that the perovskite satisfies these assumptions, the value of $\Delta QFLS_{OC-SC}$ corresponds to a ∼7-fold reduction in charge density between OC and SC conditions. This small $\Delta QFLS_{OC-SC}$ can be mainly attributed to its large $QFLS_{SC}$ (1.05 eV with bandgap of ∼1.55 eV). Similar high values of $QFLS_{SC}$ (1.03 eV with a bandgap of ∼1.60 eV) have also been observed in other more efficient p-i-n PSCs reported in the literature.[260, 299] The $QFLS_{SC}$ here from the operando PL measurement is attributed to the light-soaking effect as much smaller $QFLS_{SC}$, and thus larger $\Delta QFLS_{OC-SC}$ (e.g., $QFLS_{SC}$ = 1.03 eV and $\Delta QFLS_{OC-SC}$ = 80 meV for PCBM device under 1-sun equivalent illumination), are observed in a light-intensity-dependent OC and SC PL measurement without pre-illumination, as shown in Figure 4.6. This is because the PL of PSCs at a low voltage will increase under continuous illumination, as reported previously and attributed to ion migration.[233, 272] The sensitivity of $QFLS_{SC}$ to prior illumination suggests that its high value is not solely due to contact material properties but is also determined by an intrinsic property of the perovskite. This is most likely the presence of mobile ions, as will be discussed further below.

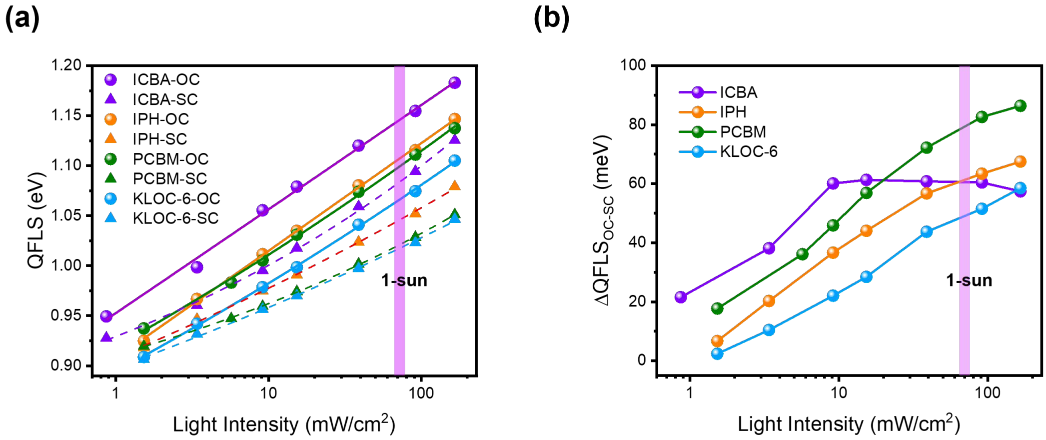

Figure 4.6: Light intensity-dependent PL measurement of PSCs with ICBA, IPH, PCBM and KLOC-6 as ETL at OC and SC. (a) Calculated $QFLS$ of those devices at OC and SC. (b) Calculated $\Delta QFLS_{OC-SC}$ of these devices under different light illuminations. No pre-illumination was applied and the laser was blocked right after each measurement. A 532 nm CW laser is used as the light source. The pink stripe area demonstrates the excitation fluence is equivalent to 1-sun illumination.

Light intensity-dependent device PL and QFLS

In order to confirm that the results of the operando PL measurement are valid over a wide range of illumination conditions, light intensity-dependent PL measurements were performed on the same devices under both OC and SC conditions without pre-illumination/light soaking. The corresponding $QFLS$s were calculated via Equation 4.1, and the results are shown in Figure 4.6a. In general, the $QFLS$ increases with light intensity since a higher incident photon flux leads to a greater density of photogenerated charges. For any given incident light intensity, the $QFLS_{OC}$ values follow the same trend as was observed under 1-sun conditions in the operando PL measurement (i.e., ICBA $>$ IPH $>$ PCBM $>$ KLOC-6) and are higher than the $\Delta QFLS_{OC-SC}$ values, as is expected due to charge extraction to the external circuit at SC. Surprisingly, the $QFLS_{OC}$ values also follow this trend, which is counter to the operando PL results where the KLOC-6 had a larger $QFLS_{OC}$ than the PCBM. This demonstrates the importance of considering the light soaking effect and the implementation of PL measurements under operating conditions.

Figure 4.6b shows $\Delta QFLS_{OC-SC}$, a parameter indicative of the reduction in charge density in the perovskite layer between OC and SC, to be compared between the four devices such that differences in their behaviour can be distinguished easily. In the IPH, PCBM and KLOC-6

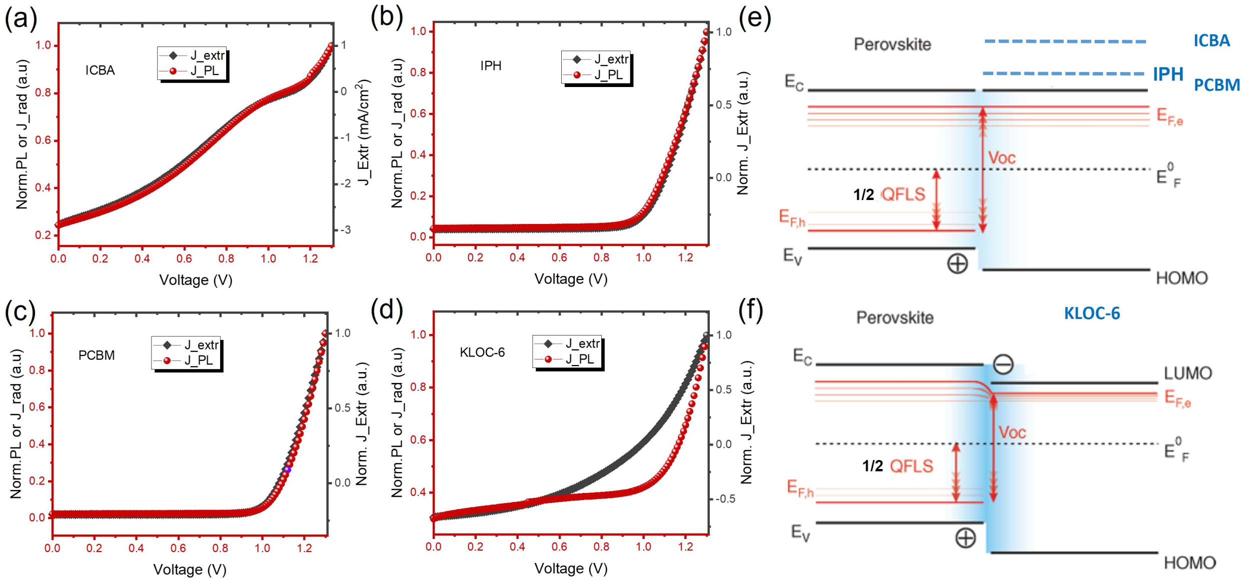

Figure 4.7: (a-d)PL or radiative current comparing with the extracted current by matching their first and the last points. Each curve is normalised to its maximum value with the data from Figure 4.1c and 4.5e. (e-f) Schematic drawing of different quasi-Fermi level distributions at the perovskite/ETL interface with varied ETLs

devices, $\Delta QFLS_{OC-SC}$ increases with light intensity, while for ICBA, it is nearly intensity independent for excitation fluence greater than 0.1-sun equivalent illumination. As the difference in gradient between OC and SC conditions (which is what causes the increase in $\Delta QFLS_{OC-SC}$ with intensity) is due to charge extraction to the external circuit at SC, the fact that no increase in $\Delta QFLS_{OC-SC}$ is observed for ICBA indicates that the presence of charge extraction does not significantly influence the dominant recombination pathways in the device. Thus, this measurement confirms that ICBA has inefficient charge extraction under SC conditions due to its high LUMO and relatively low mobility, which means that most of the photogenerated charges accumulate in the perovskite layer and create conditions in the device similar to those at OC.

Operando PL-V versus J-V

A direct comparison between the operando J-V and PL-V is made in Figure 4.7a-d by normalising both curves to their values at 1.3 V and 0 V. These plots allow us to easily compare the voltage dependence of the extracted current and the rate of bulk, radiative recombination.[260, 223, 346] A discrepancy between the shapes of these curves indicates that these two currents

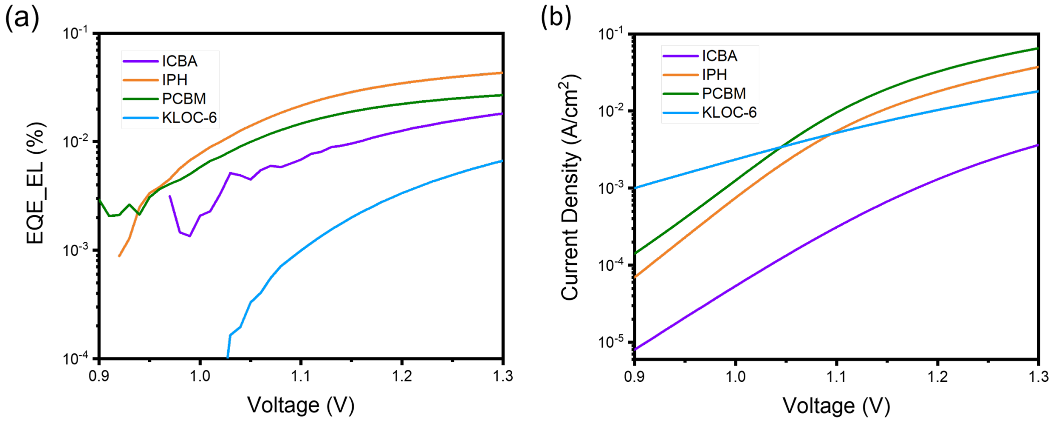

Figure 4.8: Dark measurements of PSCs with different ETLs: (a) EQE_{EL}, (b) dark J-V. These measurements were conducted using the same set-up as the operando PL measurement but without laser illumination. The scan window is 0-1.3 V and a scan speed of 7 mV/s was used.

have a different functional dependence upon the applied voltage, which would be expected if the voltage across the device is not an accurate probe of its QFLS. It is evident in Figure 4.7a-d that the PL-V and J-V curves are very well matched for ICBA, IPH and PCBM, whereas the curves for KLOC-6 diverge noticeably, suggesting that in this device, there is a significant reduction in the QFLS between the bulk of the perovskite and the external contacts, in agreement with the larger value of $QFLS_{OC}$-qV_{OC} measured above, as is illustrated schematically in Figures 4.7e-f. This difference in behaviour between the IPH, PCBM and IBCA devices on the one hand and the KLOC-6 device on the other suggests that non-radiative recombination in the latter device is dominated by a different mechanism to that in the other three devices, namely surface recombination at the perovskite/ETM interface, which is greater in KLOC-6 due to its low LUMO, as is discussed further below.

Electroluminescence measurement

EQE_{EL} measurements were also performed to further examine the perovskite/ETL interface, with the results shown in Figure 4.8a. As EL is measured by running the device in the dark, i.e., the device is acting like a LED, EQE_{EL} measurements evaluate the efficiency of charge injection from the transport layers into the perovskite, including the effects of surface interfaces. In Figure 4.8a, PSCs with IPH and PCBM as the ETL show good EL performance. This indicates excellent charge injection from the ETL, which can be attributed to their good energetic alignment with the perovskite CB. Noticeably, compared with PCBM, IPH has a higher EQE_{EL}, despite its injection current being lower (see Figure 4.8b), which indicates that non-radiative recombination at the IPH/perovskite interface is reduced in the voltage range 0.9-1.3 V. As expected, the KLOC-6 device shows the lowest EQE_{EL}, attributed to the injection barrier at ETL/perovskite interface, where this injection barrier leads to unbalance charge injection and thus to enhance surface recombination at the interface.[347, 348, 349, 350] Unexpectedly, the ICBA has a lower EQE_{EL} than the IPH and PCBM, despite having ETL/perovskite energetics which is more favourable for electron injection. This could be attributed to a larger barrier for electron injection from the Au electrode to the ICBA layer, as suggested by its lower injection current (see Figure 4.8b).[351, 352] In summary, the EQE_{EL} results have offered another insight into the quality of the ETL/perovskite interface, with non-radiative recombination losses being the most significant for KLOC-6.[353] This is consistent with the J-V and PL observations that the device with KLOC-6 has the lowest V_{OC} and $QFLS_{OC}$.

Non-radiative recombination versus radiative recombination

To quantify the weight between the non-radiative recombination versus radiative recombination, the ratio between their corresponding currents ($J_{non-rad}/J_{rad}$) was compared, as shown in Figure 4.9a. Although the correlation between the J-V characters and the radiative recombination behaviours has been shown in Figure 4.7, a discrepancy is also observed, limiting us from understanding the origin of the loss in photocurrent, especially at SC and MPP, as non-radiative recombination could also play a role in. Since photogenerated charges recombine either radiatively or non-radiatively, calculating the ratio ($J_{non-rad}/J_{rad}$) allows one to better understand the recombination loss mechanisms in these devices under different operating voltages. Here, the radiative recombination current (J_{rad}) can be calculated directly from the measured emission flux, assuming that each photon originated from a single electron-hole pair; the non-radiative recombination current ($J_{non-rad}$) can't be accessed directly, but can be determined by $J_{gen} - J_{rad} - J_{extr}$. Here, J_{gen} is the generation current, a constant, calculated from the incident laser flux by excluding the total reflection of the device and the absorption of the substrate (glass/ITO/PTAA), see Figure 4.9d; J_{extr} is the extraction current collected directly from the electrodes. Figure 4.10 summarises all recombination currents. As $J_{non-rad-bulk}$ is the total non-radiative loss current, which is a sum of both the bulk, non-radiative recombination current ($J_{non-rad-bulk}$)) and the surface recombination current ($J_{surface}$), the ratio $J_{non-rad}/J_{rad}$ can be written as

$$\frac{J_{non-rad}}{J_{rad}} = \frac{J_{non-rad-bulk} + J_{surface}}{J_{rad}} \tag{4.2}$$

According to Equation 4.2, each of these currents has a different dependence on the carrier density and distribution within the device, such that variable ratios are expected to be observed if the dominant recombination pathway is changed from the bulk to the interface. Here, we consider $J_{non-rad-bulk}$ to be proportional to n^{α}, where n is the average number density of carriers in the perovskite layer and α lies in the range 1-2, depending on the precise mechanism of the bulk recombination. For Shockley-Read-Hall recombination with balanced carrier lifetimes and densities, $\alpha = 1$, while for non-radiative bi-molecular recombination (as suggested by a few groups [117, 120]), $\alpha = 2$. For surface recombination at the ETL/perovskite interface, $J_{surface}$ is proportional to the product of the minority (hole) population at the interface, n_h, and the number of electrons in the ETL, n_{ETL}. Finally, J_{rad} is proportional to n^2. Thus, by examining how the ratio $J_{non-rad}/J_{rad}$ changes with applied voltage, we can learn how the dominant recombination mechanism within the device depends upon the applied voltage.

In the case when $J_{surface}$ is much less than $J_{non-rad-bulk}$, the ratio can be written as $J_{non-rad}/J_{rad} \propto n^{\alpha-2}$. This would decrease the ratio as the applied voltage increases due to the concurrent increase in n (as $1 \leq \alpha \leq 2$). Alternatively, in the case when $J_{surface}$ is comparable to or greater than $J_{non-rad-bulk}$, the ratio is proportional to n_{ETL}/n_e, and thus its voltage dependence will depend on which of these two quantities is larger at a given voltage.

Although it may seem unexpected for n_{ETL} to be larger than n_e, there are two factors which could contribute to this. First, the ETLs used in these devices have an effective density of states at the conduction band edge $\sim$ 100x greater than that of the perovskite, implying a greater electron density for the same electron quasi-Fermi level.[241, 354] Secondly, the electron density in semiconductors increases exponentially as the energetic offset between the electron Fermi level and the conduction band decreases. As this quantity will be smaller in the ETLs

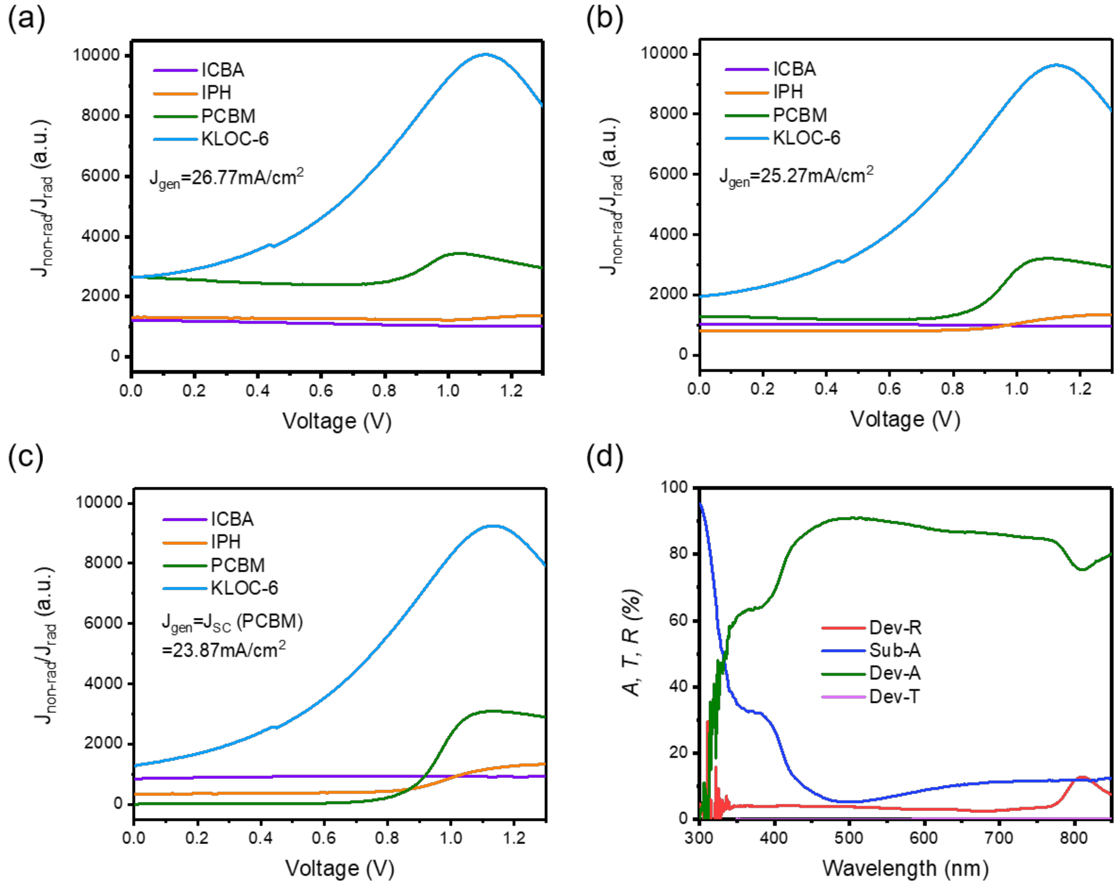

Figure 4.9: (a-c)$J_{non-rad}/J_{rad}$ using three different J_{gen} values; (d) absorptance, transmittance and reflectance measurements of the substrate (glass/ITO/PTAA) and a complete PCBM device for J_{gen} estimation.

with LUMO levels that lie below the perovskite CB than it is in the perovskite bulk, we would expect it to be the case that n_{ETL} is greater than n_e.

Figure 4.9a shows the ratio $J_{non-rad}/J_{rad}$ for each device, normalised to its value at 0 V. Here, this ratio, and the conclusions drawn from it, are not sensitive to the absolute value of J_{gen}, as illustrated in Figure 4.9a-c. Considering the solar cell operating voltage range (0 - V_{OC}), the ratio of $J_{non-rad}/J_{rad}$ decreases monotonically in the ICBA and IPH devices as the applied voltage (V_{app}) increases, which implies that surface recombination is a less significant loss mechanism than bulk, non-radiative recombination in these devices. The same phenomenon is also observed in the PCBM device at lower applied voltages, but the ratio then starts to increase until it reaches a maximum near the V_{OC} point, implying that surface recombination is negligible near J_{SC} but becomes significant around V_{OC}. For KLOC-6, the ratio continuously increases from 0 V to V_{OC}, indicating that surface recombination is the dominant recombination

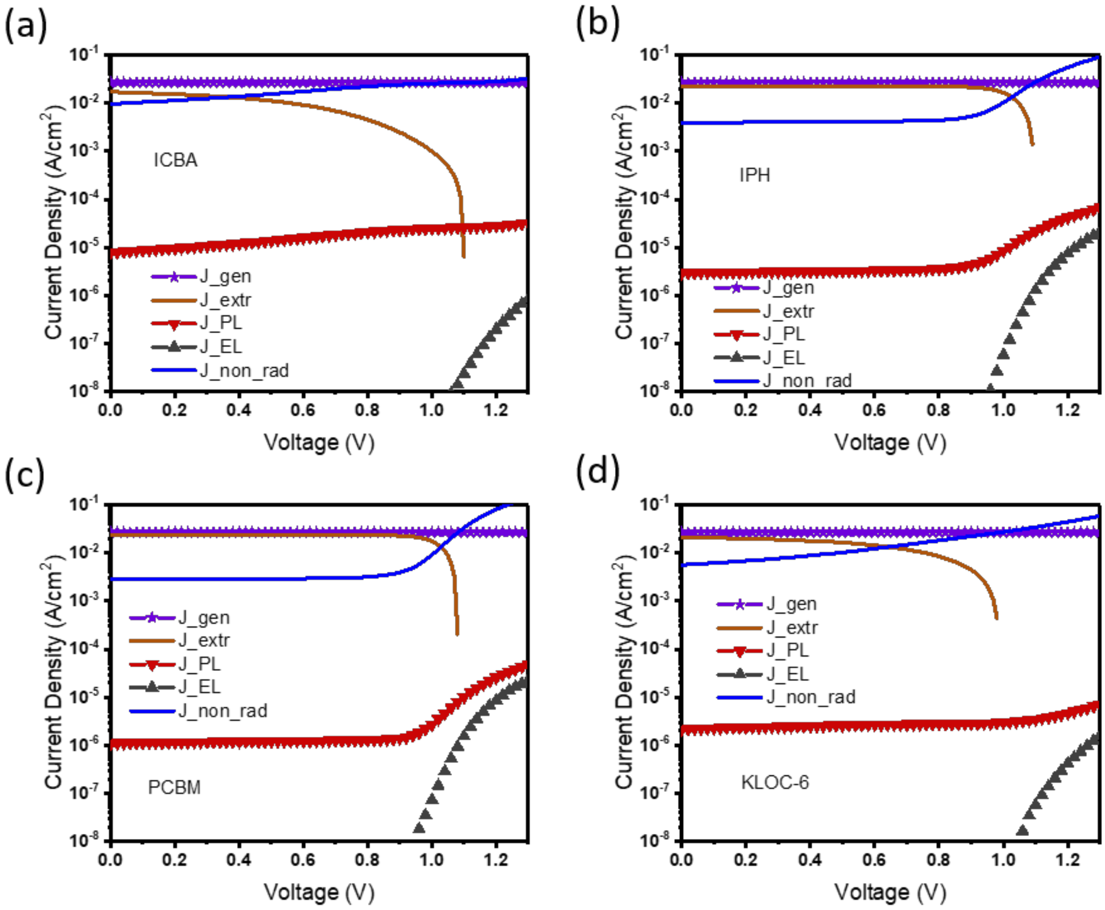

Figure 4.10: Summary of different recombination currents of devices with (a) ICBA, (b) IPH), (c) PCBM and (d) KLOC-6. These plots are based on the data from operando PL measurement from Figure 4.5e and absorption measurement from Figure 4.9d.

process at all voltages. These data are consistent with the PL and EQE_{EL} results, where they demonstrate the primacy of bulk recombination in the ICBA and IPH devices due to their high LUMO ETLs, while also showing that KLOC-6 exhibits strong surface recombination losses, which can be attributed to excess charges accumulated in the ETL due to its low mobility and deep LUMO.

This analysis shows that the ratio of $J_{non-rad}/J_{rad}$ not only provides an effective way to quantify the balance between radiative and non-radiative recombination but also gives information about the source of the non-radiative recombination. In these devices, we find that bulk non-radiative recombination is the dominant cause of charge carrier losses at low voltages. However, at voltages near V_{OC}, surface recombination may become more significant due to charge accumulation on the ETL.[333] Compared with other devices, the results of the V-dependent $J_{non-rad}/J_{rad}$

further explain the J-V characters of the PCBM device, where higher J_{SC} but lower V_{OC} were observed due to less surface recombination at SC but more pronounced this phenomenon at OC. This suggests that the PCBM device has the highest extraction efficiency at SC. However, these results still can't explain its high $QFLS_{SC}$.

Summary of the experimental results

Overall, the J-V and operando PL results demonstrate that ETLs with shallower LUMOs tend to have higher values of V_{OC}. This agrees well with these ETL materials used in the OPVs.[338] The absolute PL data measured from both the films and devices at OC reveal this trend is due to the enhancement of $QFLS$ within the perovskite layer. However, if the LUMO level is too far above the perovskite CB, it can create an energetic barrier to slow the charge transfer from the perovskite to the ETL, as indicated by the kinetic measurements.[169, 174, 355] Consequently, this hindered charge transfer reduces overall charge extraction by observing small values of $\Delta QFLS_{OC-SC}$, which results in a lower FF and J_{SC}. Conversely, ETMs with LUMOs too far below the perovskite CB can introduce additional surface recombination, leading to small $QFLS_{OC}$ and reducing V_{OC}.[130, 152, 229] Such considerable surface recombination phenomena induced by the energy offsets have also been reported in other p-i-n PSCs using a different CTL, such as P3HT and C60.[152, 315, 333] Figure 4.7f demonstrates the mechanisms of this surface recombination, where excess charges in the ETL recombine with the opposite charges in the perovskite layer. This surface recombination can be mainly attributed to photogenerated charges in the perovskite layer tend to transfer into these ETLs with lower LUMOs due to increased charge transfer rates. It is also worth noting that this surface recombination is voltage-dependent and becomes less pronounced as Vapp approaches 0 V, as indicated by the analysis of the $J_{non-rad}/J_{rad}$. This could be attributed to charges accumulated at the ETL [333] at OC but extracted to the external circuit at SC. Moreover, ETLs with much lower mobility, such as KLOC-6, can also cause charge accumulation in the device and decrease FF and J_{SC} by introducing additional series resistance.[356, 357]

Additionally, the results demonstrate significant charge accumulation at SC ($QFLS_{SC} > 1$ eV) in all the measured devices, including those with the highest J_{SC} values. As this is observed for all four ETMs, even those which show the fastest rates of charge transfer from the perovskite to the ETM, it appears that this charge accumulation is not solely the result of transport layer properties. Therefore, it seems that the significant SC charge accumulation reported here is a result of transport limitations within the perovskite layer. Further evidence that this charge accumulation is a result of perovskite layer properties comes from the inconsistency of the $QFLS_{SC}$ values measured in operando PL and light intensity-dependent PL. This inconsistency indicates that SC charge accumulation and the consequent high values of $QFLS_{SC}$ are associated with the light soaking effect, a phenomenon which has been previously linked to ion migration in the perovskite layer.[233, 272]

4.4.2 Drift diffusion simulation

In order to understand the origin of the charge accumulation (high $QFLS$) under low voltage conditions, drift-diffusion simulations were performed using Driftfusion, a software package which can accurately model PSCs due to its inclusion of the effects of mobile ionic species in the drift-diffusion equations.[230] The simulation results obtained by including and not including mobile ions are contrasted in Figure 4.12, with the simulation parameters summarised in Table 2.1-2.3 in Chapter 2, Section 2.5. When mobile ions are included in the simulation, the trends shown in the measured J-V and $PLQY/QFLS$ results have been successfully reconstructed and are qualitatively consistent with the measured results in Figure 4.1 and Figure 4.2, respectively. Specifically, as shown in Figure 4.12a, all the devices modelled while neglecting simulated with no ion motion all have equal J_{SC} values, which are consistently higher than those measured experimentally. Additionally, the simulation results also suggest that these devices always exhibit lower V_{OC} values if the mobile ions are excluded. Similarly, in Figure 4.12b, it is observed that neglecting the presence of mobile ions leads to all the devices demonstrating low $PLQY_{SC}$, which is one or two orders of magnitude lower than those measured experimentally. This also leads to the $QFLS_{SC}$ values of ~ 0.9 eV for all the devices without mobile ions, while the inclusion of mobile ions leads to values which are in better agreement with the experiment,

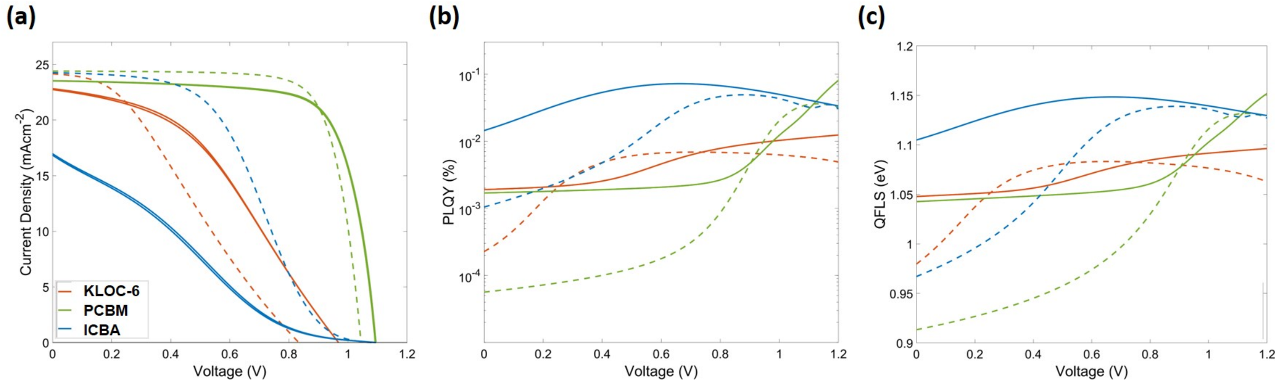

Figure 4.11: (a) J-V curves of the simulated devices with (solid lines) and without (dotted lines) the effects of mobile ions. The ions impact the current hugely, especially under low biases. Simulated (b) $PLQY$ (c) $QFLS$ results with/without mobile ions. Lucy Hart produced these figures.

as shown in Figure 4.12c and summarised in Table 4.3. It is worth noting that this simulation is dependent upon mobile ion density and other properties of the perovskite layer, such as the carriers' mobilities and bulk recombination lifetimes. By contrast, the choice of ETM mobility and LUMO has a less significant impact on the value of $PLQY_{SC}$.

All these observations can be explained by the redistribution of the ions in response to the device's internal electric field. As introduced by Chapter 1, Section 1.5, a large population of mobile ions, exists in most metal halide perovskites,[209, 218, 358] which screens the electric field throughout the perovskite layer, thus, leading to photogenerated charges must diffuse, not drift, to the interfaces to be extracted.[208, 209, 233] The impact of this is especially pronounced at SC,[208, 209, 218, 359] where it leads to charges accumulating in the perovskite, as illustrated in Figures 4.12d-f. Consequently, there is a reduction in J_{SC} (see the second column in Table 4.3) since a greater fraction of the photogenerated charges recombine in both bulk and surface before they can be extracted out as current.[222, 233]

However, the presence of ions is not wholly detrimental to device performance. The simulated J-V curves indicate that the devices which included mobile ions also had higher V_{OC} values. The reason for this can be seen in Figures 4.12d-e; the inclusion of mobile ions reduces the density of the minority carrier at the counter interlayer surface when compared to the case with no ionic motion.[360] This effect occurs as it is largely the ionic, not electronic, charge distribution which determines the electrical field within these devices.[235] Thus, it is the redistribution of the ions in response to the change in applied voltage which is responsible for the shielding of the internal

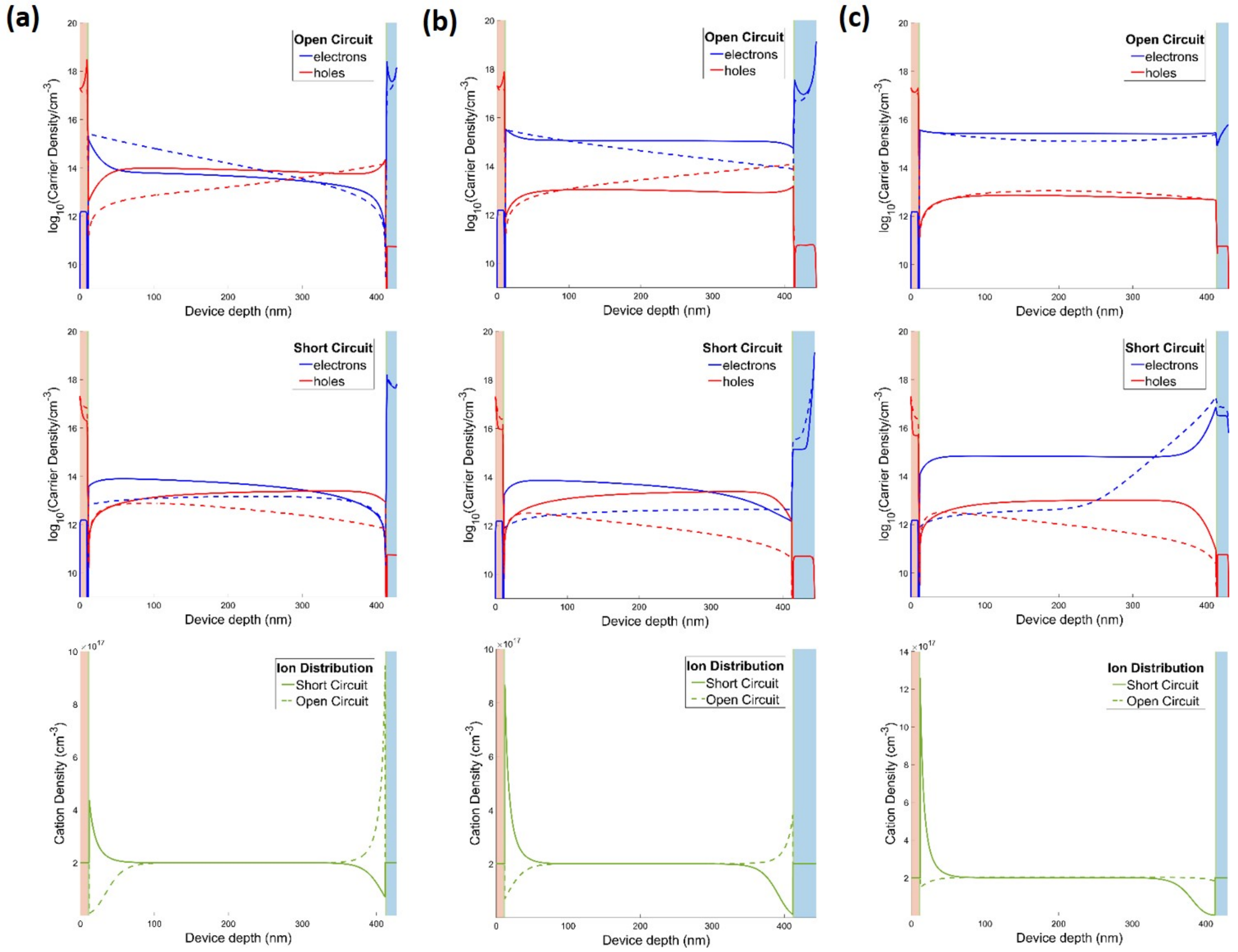

Figure 4.12: Simulation results of charge carrier distributions at OC (top) and SC (middle) conditions with (solid lines) and without (dashed lines) mobile ions of (a) KLOC-6, (b) PCBM and (c) ICBA, respectively. The bottom figures show the mobile ion distribution. Lucy Hart produced these figures.

electrical field, removing the need for minority carrier accumulation near the counter interface as the applied voltage approaches the built-in voltage. This reduces the surface recombination rate at the perovskite/ETL interface for a given applied voltage and improves the value of V_{OC}. Nevertheless, the PCE gain from the enhanced V_{OC} value cannot compensate for the losses due to the reduction in J_{SC}.

To summarise, regardless of the properties of the ETM, the simulation results suggest that the inclusion of mobile ions leads to lower J_{SC} values and higher values of $QFLS_{SC}$, consistent with the observation in other perovskite solar cells.[233, 361] It was found that values of $QFLS_{SC}$ comparable to those measured experimentally could not be simulated unless the effects of mobile ions were included, demonstrating the necessity of incorporating ionic effects to accurately model the electric field and carrier distributions in PSCs.[209, 218, 219] Additionally, the results demonstrated that the low values of $\Delta QFLS_{OC-SC}$ measured in PSCs are a direct consequence of charge accumulation in the perovskite layer at SC, a phenomenon which occurs due to the screening of the internal electric field by mobile ions, resulting in slower, diffusion-driven current extraction at SC.[218, 219]

Table 4.3: Simulation results of device $QFLS$ under OC and SC conditions with and without mobile ions. Lucy Hart provided the original data.

	ETL	J_{SC} (mA cm^{-2})	$QFLS_{SC}$ (eV)	$QFLS_{OC}$ (eV)	$\Delta QFLS_{OC-SC}$ (eV)
No mobile ions	KLOC-6	24.2	0.98	1.09	110
	PCBM	24.4	0.91	1.11	200
	ICBA	24.3	0.97	1.14	170
Including mobile ions	KLOC-6	22.8	1.05	1.09	40
	PCBM	23.5	1.04	1.12	80
	ICBA	16.8	1.10	1.14	40

4.5 Conclusion

To conclude, this chapter has demonstrated a method using operando PL spectroscopy as a tool to quantify the radiative and non-radiative recombination of four p-i-n PSCs under operating conditions. Combined with the results of light intensity-dependent device PL measurements and Driftfusion simulation, the operando PL data suggest that the large $QFLS$, observed at SC in all the PSCs, regardless of ETL properties, is mainly due to ion migration, an effect which may be enhanced by light soaking. This is because, at low applied voltages, mobile ions located at the perovskite/contact layer interfaces screen the internal electric field, impeding charge extraction, and reducing J_{SC}.[208, 209, 218, 359] Our results also suggest that, in addition to choosing an ETL with good charge transport properties (e.g., mobility),[356, 357] it is necessary to optimise the energetic alignment at the perovskite/ETL interface to achieve the highest device performance.[130, 152, 362] Whilst a low LUMO favours charge transfer from the perovskite to the ETL, it can result in increased non-radiative recombination at the perovskite/ETL interface, which limits the PSC's FF and V_{OC}.[130, 152, 229] On the contrary, though a high LUMO benefits the $QFLS$ in the bulk perovskite, it impedes charge extraction under low voltage conditions (when V < V_{OC}, leading to the accumulation of photogenerated charges in the bulk.[141, 174] This results in a device with a low J_{SC} and/or FF. Moreover, by analysing the ratio of non-radiative to radiative recombination currents as a function of applied voltage, the evidence shows that surface recombination is more severe at voltages close to V_{OC} than it is under low voltage conditions. However, it is only the dominant recombination process in devices which use ETLs whose LUMO lies beneath the perovskite's CB, which can be attributed to the formation of a non-ohmic contact at the ETL/perovskite interface.[362, 363] This work suggests that, in order to achieve more efficient p-i-n PSCs and move towards the theoretical limit, it is necessary both to optimise the energetic alignment at the perovskite/ETL interface and to mitigate the effects of ion migration in the bulk perovskite.

Chapter 5

Asymmetric Charge Transfer and Charge Transport in Planar Lead Halide Perovskite Solar Cells

5.1 Declaration of contributions

The results presented in this chapter led to the publication of the paper: Asymmetric charge carrier transfer and transport in planar lead halide perovskite solar cells. [122]

Dr Tian Du is responsible for the fabrication of the samples and devices in this Chapter.

5.2 Abstract

Efficient charge extraction from the perovskite layer is crucial to the design of high-performed PSCs. Here, this chapter demonstrates a simple TRPL method to probe charge transfer from perovskite to its contacts and charge transport across the perovskite layer individually, based on asymmetric and spatially localized excitation. The effects of perovskite layer thickness, GBs, and interlayers on these dynamics are revealed. The results indicate that both film thickness

and GBs impact the asymmetry between the electron and hole charge transport across the perovskite layer and charge transfer from the perovskite layer to its contacts.

5.3 Introduction

The photon-to-electricity conversion in the PSCs is driven by processes with dynamics ranging from fs to ms.[108, 115, 163, 164, 364] Thus, elucidating these charge carrier dynamics is the key to optimizing materials fabrication and device engineering. In the last decade, charge carrier dynamics in the perovskites have been investigated extensively. Particularly, the ultrafast dynamics, probed by transient pump-probe techniques, on charge generation and charge relaxation in the perovskites have received intensive attention,[61, 98, 108, 163, 365] with increasing agreement on the understanding of these processes.[61, 108, 156, 366, 367] However, there is less consensus on subsequent charge carrier recombination, transport and transfer processes, which typically occur in ns and μs.[115, 163, 164, 368] These processes are strongly dependent on material processing and device architecture and can be critical to device performance.[98, 236, 366, 369] In a PSC under operation, photogenerated charges have to travel through the bulk perovskite to reach the perovskite/CTL interface, and then be transferred to the CTLs and ultimately be collected by the electrodes. This series of steps is often referred to as charge extraction, which is in kinetic competition with recombination processes in the device. This competition is often considered a key determinant of device performance. Kinetics of fast charge transport and charge transfer, and slow charge recombination are essential for efficient charge extraction. Whilst extensive attention has been paid to the kinetics of charge recombination,[116, 119, 370, 371] less has been paid to charge transport and transfer kinetics and their impact on the overall charge extraction efficiency as a function of material processing,[115, 222] which is the primary focus of this manuscript.

A range of measurement techniques has been developed to study charge transport, transfer and recombination kinetics within PSCs. Pump-probe TA spectroscopy is one of the commonly used methods for probing charge transfer dynamics within ns.[167, 170, 326, 327, 372] However, the high pump fluxes used in such measurements are remote from the actual working conditions of the solar cell. Charge recombination kinetics are typically studied by transient PL or absorption studies in bare perovskite films, or by impedance or transient photovoltage analysis in complete cells to reveal the recombination processes in between ns and ms.[123, 126, 163, 164, 221, 222] Charge transport kinetics have also been studied by various methods. However, consensus on them is difficult to achieve as physical parameters such as mobilities and diffusion coefficients have been reported to vary over several orders of magnitudes.[227] It is suggested that charge mobilities measured from most contact measurements, such as space-charge-limited-current, time-of-flight, and Hall effect, may be overestimated due to ion migration.[73, 153, 154, 373] Contactless measurements such as transient THz conductivity and microwave conductivity typically measure local mobilities, and are unable to separate electron or hole mobilities.[108, 157, 161, 162, 374] Instead, steady-state and time-resolved PL methods of perovskite films with and without CTLs have been used to measure both electron and hole extraction kinetics,[164, 375, 376] where the surface-quenching TRPL approach has recently been shown to be applicable to probing charge carrier mobilities.[375, 376] However, this approach has not yet been employed to compare electron and hole mobilities or the impact of perovskite film processing.

In this study, surface quenching TRPL analyses were employed as the primary tool to investigate the electron and hole transport and transfer kinetics dependent on perovskite film thickness, GB, and the presence/absence CTLs. To distinguish charge transfer and charge transport processes, a blue (405 nm) light source with a short penetration depth of 30 nm was used to achieve spatial-localized photogeneration, along with employing front and back excitation. This allows charge generation either adjacent to, or on the opposite side of, the perovskite/CTL interface. This results in more pronounced charge transfer dynamics if the charges are generated adjacent to the interface, and more dominant charge transport dynamics when charges are generated on the opposite side.[163, 376] Thus, this approach can be applied to measure both electron and hole transport kinetics within the photoactive layer by employing either an ETL or HTL.

Achieving compact and continuous perovskite films is always challenging, especially in large-scale commercial fabrication processes.[42, 377, 378, 379] In this work, the impact of perovskite

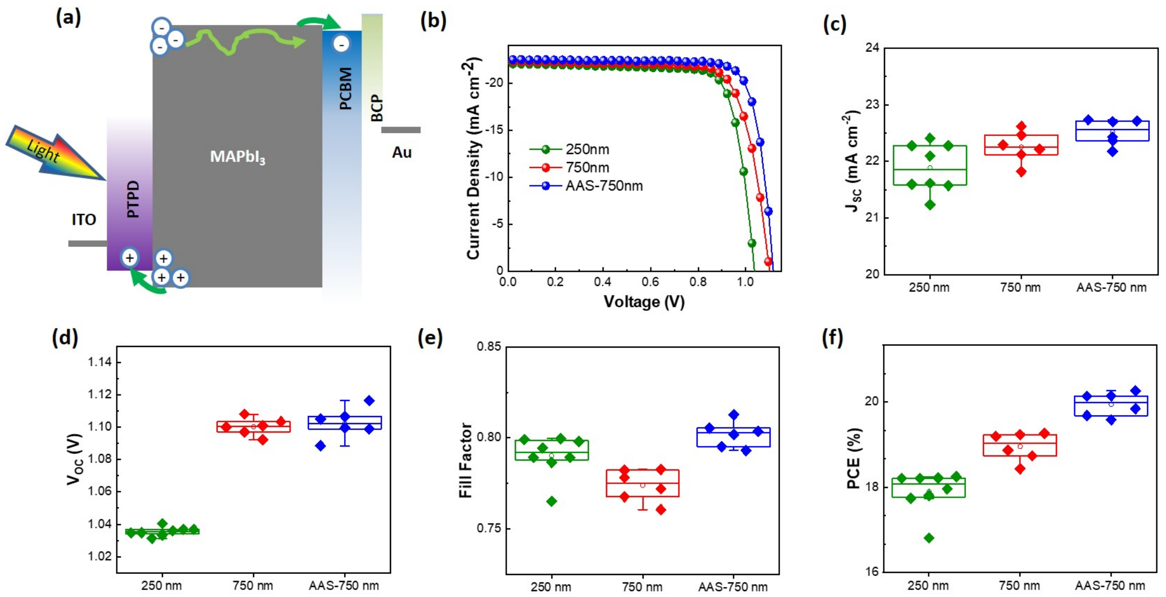

Figure 5.1: 250 nm, 750 nm and AAS-750 nm perovskite based device structure (a), J-V curves (b) and their corresponding parameters in statistics, with J_{SC} in (c), V_{OC} in (d), FF in (e) and PCE in (f). The J-V data and parameters were obtained by Dr Tian Du.

film thickness and crystallinity on electron and hole transfer and transport kinetics were investigated. The impact of these parameters on the overall charge extraction dynamics is an important consideration for device efficiency. Three $MAPbI_3$ based perovskites were investigated, including a thin 250 nm layer, a thicker 750 nm, and a 750 nm thick film that was AAS treated with enhanced film crystallinity and reduced GBs.[140, 380] Perovskite films with three different types of structures were studied: neat $MAPbI_3$ film on glass, ITO/PTPD/$MAPbI_3$, glass/$MAPbI_3$/PCBM, and ITO/PTPD/$MAPbI_3$/PCBM. TRPL measurements and a simple numerical model are employed to determine charge transfer and transport kinetics and the underlying electron and hole mobilities, and their correlation with device performance are also discussed.

5.4 Results and discussion

5.4.1 Film processing and solar cell performance

This study focuses on charge extraction dynamics for films and devices employing three different perovskite absorber layers: 250 nm $MAPbI_3$, 750 nm $MAPbI_3$ and AAS treated 750 nm (AAS-750 nm) $MAPbI_3$. The device performance of the PSCs using these absorbers was first investigated, where a device structure of ITO/PTPD /$MAPbI_3$/PCBM/BCP/Au is employed, as shown in Figure 5.1a. A commonly used anti-solvent dripping spin-coating and annealing process was used for the deposition of the perovskite layer, with different thicknesses controlled by varying the precursor concentration between 1 M and 1.85 M for the 250 nm $MAPbI_3$ and 750 nm $MAPbI_3$, respectively.[222] The AAS-750 nm $MAPI_3$ was fabricated with the same procedure but with an additional AAS post-deposition treatment.[140] Further details of the fabrication process are given in Chapter 2. Figure 5.1b shows the J-V curves of the measured devices with their respective performance statistics summarised in Table 5.1 and plotted in Figure 5.1c-f. When the $MAPbI_3$ thickness increases from 250 nm to 750 nm, there is a large enhancement in the V_{OC} from 1.036 V to 1.100 V, and a small increase in J_{SC} from 21.9 mA cm^{-2} to 22.3 mA cm^{-2}. These increases are however partially offset by a loss in FF from 0.79 to 0.77, resulting in a small net increase in the PCE from 17.9% to 19.0%. The device PCE further goes up to 19.9% after AAS treatment which is mainly attributed to an increase in FF of 0.80, as well as increased J_{SC} of 22.52 mA cm^{-2} and V_{OC} of 1.11 V.

Table 5.1: Device performance with 8 for 250 nm, 6 each for 750 nm and AAS-750 nm PSCs. These parameters were contributed by Dr Tian Du.

Perovskite	J_{SC} (mA cm^{-2})	V_{OC} (V)	FF (V)	PCE (%)
250 nm	21.88±0.43	1.036±0.003	0.790±0.011	17.90±0.48
750 nm	22.25±0.28	1.100±0.005	0.774±0.009	18.96±0.33
AAS-750 nm	22.52±0.23	1.103±0.009	0.802±0.007	18.96±0.33

The absorption and PL characters of $MAPbI_3$ films were also investigated. Figure 5.2a shows the UV-Vis absorption spectrum of the neat $MAPbI_3$ films. Compared with the 250 nm $MAPbI_3$ film, both the 750 nm and AAS-750nm films show the expected increase in absorption with

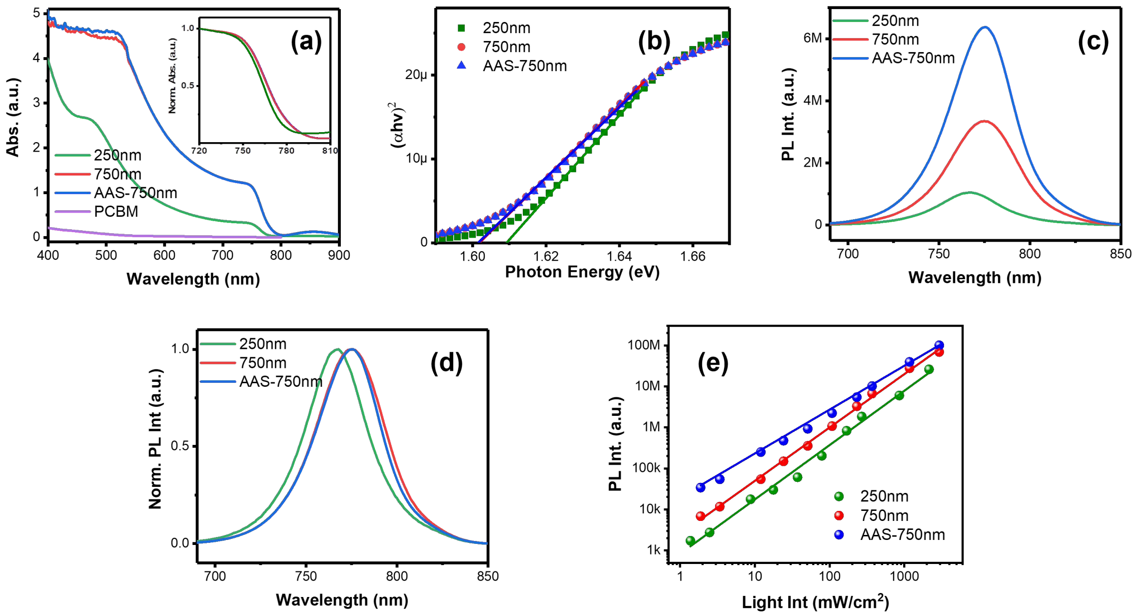

Figure 5.2: (a) UV-Vis absorbance, (b) Tauc plot of the band edge absorption, (c) steady-state PL and its (d) normalized spectra, and (e) excitation density dependent PL measurement of 250 nm, 750 nm and AAS-750 nm $MAPbI_3$ on a glass substrate. For PL measurement, a 635 nm CW laser was used to excite the samples from the glass substrate side with probing from the same side.

film thickness, as well as a small (7 meV) redshift of their band edge absorption onset (determined from Tauc plots, Figure 5.2b). A red shift for the thicker films is also observed in PL spectra (Figure 5.2c and 5.2d), though this shift, 16 meV is large than for the absorption onset, most likely due to the effect of additional photon recycling.[381] Figure 5.2e demonstrated the fluence-dependent PL results of the three films with normalized PL intensity to match the densities of absorbed photons. The PL yield increases from 250 nm $MAPbI_3$ to 750 nm $MAPbI_3$ and further to AAS-750 nm $MAPbI_3$ (see Figure 5.2d), indicating that non-radiative loss is greatest for the 250 nm film, and least for the AAS-750 nm. As variations in the PL intensity of $MAPbI_3$ are typically attributed to charge trapping (monomolecular) into non-radiative states, the presence of such trapping process can also be analysed by fitting the PL against the excitation fluence using the equation: I_{PL}= ${I_{PL}}^{\alpha}$, as plotted in Figure 1c. Here, α is a parameter to estimate recombination order in perovskites,[265, 266] as illustrated in Chapter 3, Section 3.4. The calculated α values are 1.4, 1.3 and 1.1 for the 250 nm, 750 nm and AAS-750 nm films, respectively, indicating suppression of monomolecular recombination (e.g.: charge trapping into non-radiative states) with increasing the film thickness and is more so when AAS treatment is employed, consistent with the trend in PL intensity between films. A smaller full-

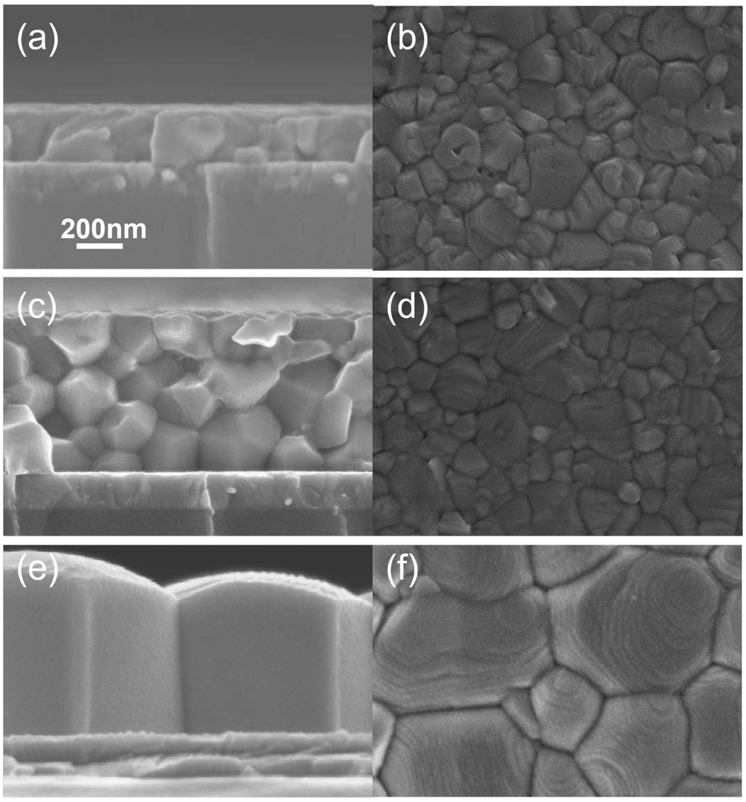

Figure 5.3: Cross-sectional SEM images of 250 nm $MAPbI_3$ (a), 750 nm $MAPbI_3$ (c) and AAS-750 nm $MAPbI_3$ (e). Surface SEM images of 250 nm $MAPbI_3$ (b), 750 nm $MAPbI_3$ (d) and AAS-750 nm $MAPbI_3$ (f). These SEM figures are contributed by Dr Tian Du.

width half-maximum (FWHM) PL peak is also observed in the AAS-750 nm $MAPbI_3$, further demonstrating higher uniformity of emission energies, consistent with a higher film uniformity of the AAS-750nm film, compared with 750 nm $MAPbI_3$ (Figure 5.2d). These results indicate that the 250 nm $MAPbI_3$ exhibits the most inferior semiconductor property whilst the AAS-750 nm $MAPbI_3$ the best, with the highest PL intensity and an α -value of near unity indicative of near ideal behaviour. These trends are consistent with the trend in the V_{OC} of these devices, with the 250 nm device yielding the lowest V_{OC} due to stronger non-radiative recombination and the AAS-750nm device being the highest.

The film morphology of the three perovskite absorbers was further investigated. Figures 5.3 a-d shows the cross-sectional and surface scanning SEM images of the 250 nm and 750 nm $MAPbI_3$ films. Both films exhibit grain sizes of around 250 nm, with the stacking of multiple grains in the vertical direction only observed in the 750 nm $MAPbI_3$. This results in the presence of additional GBs between the top and bottom surfaces in this film, which may influence vertical charge transport by blocking or scattering charge carriers. On the contrary, in Figure 5.3e and f, AAS-750 nm $MAPbI_3$ shows monolithic grains with diameters of around 750 nm, which extend through the whole film thickness; no GBs parallel to the substrate are observed. The absence of lateral internal GBs in the 250 nm $MAPbI_3$ and AAS-750 nm $MAPbI_3$ films is correlated with their device performance by showing higher FFs compared with the 750 nm $MAPbI_3$ PSCs, as discussed further below.

The crystallinity of different $MAPbI_3$ films was studied by XRD with the results shown in Figure 5.4. Comparing Figures 5.4 a and b, the diffraction intensity of 750 nm $MAPbI_3$ film is higher than the 250 nm $MAPbI_3$ film due to the greater thickness of the former. Similar FWHMs of the (110) peak were observed with 0.135° and 0.137° for 250 nm and 750 nm films, respectively, as shown in Figures 5.4(e-g) and summarised in Table 5.2. This suggests that both films have similar grain sizes, consistent with the SEM results in Figure 5.3. By contrast, the highest intensity and smallest (110) FWHM of 0.113° were observed for the AAS-750 nm $MAPbI_3$ demonstrating the strongest orientation along <110> direction and crystallinity among all the films, in good agreement with our analyses of the optical data above. It is also noticeable in Figure 5.4c that a small PbI_2 peak is only present for the 250 nm film. This PbI_2 may be associated with a great proportion of volatilization of methylammonium during annealing due to its larger surface area to volume ratio. The emergence of PbI_2 in the 250 nm film may also be associated with the higher defect density observed for it, with these defects possibly generated by photolysis of PbI_2,[382] consistent with our optical data that the 250 nm film is likely to own the highest proportion of non-radiative, monomolecular recombination.

Table 5.2: Gaussian fit of (110) phase of the XRD patterns from Figure 5.4.

Perovskite	Centre 2 theta (°)	Amplitude (V)	FWHM
250 nm	14.185	25.780	0.137
750 nm	14.184	52.770	0.135
AAS-750 nm	14.190	68.163	0.113

5.4.2 Photoluminescence analysis of charge extraction dynamics

TRPL measurements were carried out to address the charge carrier dynamics of the three $MAPbI_3$ films. Here, 405 nm laser pulses with penetration depth (1/e absorption) of ~30 nm

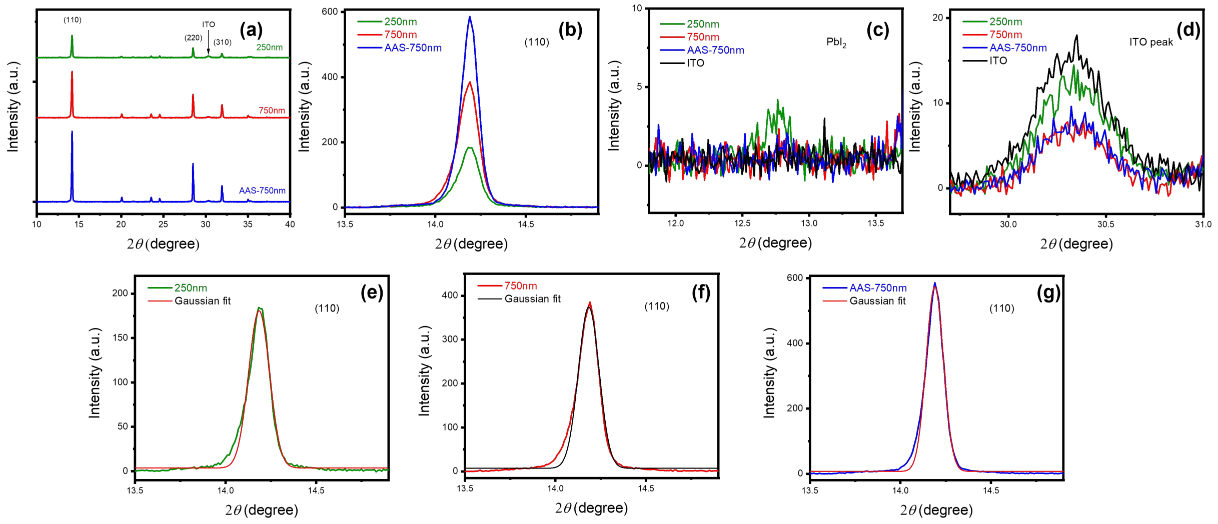

Figure 5.4: (a) XRD patterns of 250 nm, 750 nm and AAS-750 nm neat MAPI$_3$ on ITO substrate with zoomed-in pattern for (110) phase (b) and PbI$_2$ peak (c). The peak position is adjusted to the ITO peak in (d), and no peak shift is observed in all perovskites. (e-g) Gaussian fit results of (110) phase peaks.

were employed to excite these samples from either side, to ensure the initial charge generation is near either surface. An excitation fluence of 3 nJ cm^{-2} per pulse (6.8×10^{14} cm^{-3}), slightly lower than 1-sun illumination (10^{15} cm^{-3}-10^{16} cm^{-3}) reported previous, was used.[125] In comparison, 637 nm laser pulses were employed for control data, which excites relatively uniformly throughout the film as the penetration depth is of ∼200 nm. Decays of films without and with HTL/ETL layers from 405 nm excitation are shown in Figure 5.5.

The TRPL decays for the three bare MAPbI$_3$ films were compared first, as shown in Figure 5.5a-c. All decays appear in two decay phases, with a fast (few ns) one followed by a slow (hundreds of ns) one. The fast phase is most pronounced in the 250 nm film and significantly suppressed in the AAS-750 nm film. As reported previously, this fast phase is assigned to monomolecular charge trapping into non-radiative trap states.[119, 383] This assignment is further supported by light intensity dependent TRPL results, shown in Figure 5.6 a and b, where the amplitude of this fast phase is suppressed at higher excitation densities, which has been assigned previously to the effect of trap filling.[119, 125, 383] The trend in the amplitude of this fast phase between films indicates the density of non-radiative trap states is at its highest in the 250 nm film and at its lowest in the AAS-750 nm film, consistent with steady-state optical data discussed above. Again, following literature assignments,[119, 383], the second phase is assigned to band-

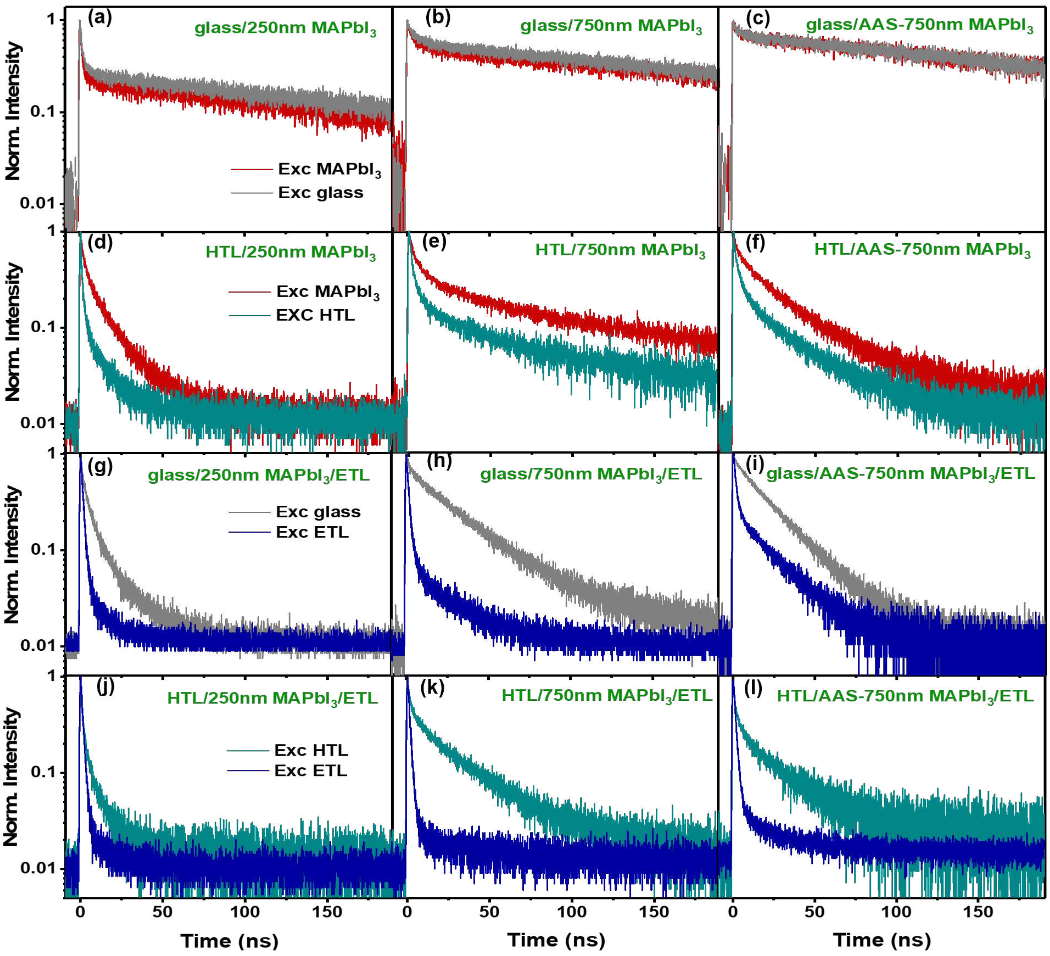

Figure 5.5: TRPL decays of 250, 750, and AAS-750 nm $MAPbI_3$ films under 3 nJ cm^{-2} $pulse^{-1}$ 405 nm laser excitation from either side with a structure of (a–c) glass/$MAPbI_3$, (d–f) HTL/$MAPbI_3$, (g–i) glass/$MAPbI_3$/ETL, (j–l) HTL/$MAPbI_3$/ETL.

to-band recombination. The exponential nature of this slow phase is attributed to the fact that the density of free (untrapped) carriers generated at this low excitation fluence (3 nj cm^{-2}) is lower than the dark doping density of the film, resulting in pseudo-first-order (exponential) band-to-band recombination.[116, 383, 267] Consistent with this assignment, the decay kinetics of the second phase accelerate and become more a power-law behaviour at higher excitation densities, which is attributed to the photogenerated free carrier density increasingly exceeding the doping density, as shown in Figure 5.6a-b. Thus, due to the low excitation densities used for Figure 5.5, all decay kinetics were fitted by a simple and widely used [65, 346, 384] biexponential equation $y = y_0 + A_1 e^{-\frac{x}{t_1}} + A_2 e^{-\frac{x}{t_2}}$, with fitting results summarised in table 5.3. These fittings are based on a general assumption: The system has two different decay components, which have a short lifetime of τ_1, and a long lifetime of τ_2, respectively. The assignment of these decay components follows the same discussion of assigning the decay phases, where τ_1 is the short lifetime with an amplitude of A_1 and τ_2 is the long lifetime with an amplitude of A_2. In the fitting of TRPL decays of bare $MAPbI_3$ films, τ_1 is the lifetime of the first order charge trapping process while τ_2 is the lifetime of the pseudo-first-order band-to-band recombination process, as discussed above. A comparison with the decay kinetics observed from 637 nm excitation, shown in Figures 5.7, which results in more bulk excitation rather than surface excitation, indicates that the fast decay phase is more dominant for surface (405 nm) rather than bulk (637 nm) excitation, suggesting that monomolecular charge trapping is most severe at the film surfaces. This conclusion agrees with previous studies which emphasized the importance of surface recombination losses in perovskite films and solar cells.[385, 386, 387] Comparison between the 405 nm excitation methods through glass versus through $MAPI_3$ (Figure 5.5a, b, c) suggests this trapping is enhanced at both film surfaces, but slightly more noticeable at the $MAPI_3$ top surface. Overall, these data of bare perovskite films indicate the dominance of non-radiative charge trapping follows the trend 250 nm > 750 nm > AAS-750 nm, consistent with the steady-state optical data and the trend in V_{OC} discussed above. Additionally, these data also suggest that charge trapping is most significant at the film surfaces.

The employment of ITO/PTPD and/or PCBM as hole and electron transport layers (HTL and ETL) respectively to the three bare perovskite films leads to a substantial acceleration of the TRPL decay kinetics of these films, indicating charge transfer from the perovskite layer to the CTL (Figures 5.5d-l). These transferred charge carriers in the CTLs would subsequently recombine with opposite charges within the perovskite layer, primarily through the interfaces, known as the surface recombination in longer timescales due to the absence of an external circuit. The inclusion of ITO is to avoid excessive charge accumulation in the PTPD layer(less than 20 nm thick),[221] which would limit further charge transfer during the TRPL measurements, as illustrated in Figure 5.6c-d. As these decay kinetics were probed under 405 nm excitation for achieving spatially localized charge generation on either side of the perovskite layer, this method allows one to probe the impact of photoexciting adjacent to, or on the opposite side from, the CTL.

Now, the TRPL decay kinetics for the perovskite/CTL (ETL or HTL) films and with photoex-

Table 5.3: Lifetime fitting results of decays from Figure 5.5 by the bi-exponential fitting equation: $y = y_0 + A_1 e^{-\frac{x}{t_1}} + A_2 e^{-\frac{x}{t_2}}$. Here y_0 is fixed to zero for neat film fittings but equals to its tail background for all other fittings.

Sample name	A_1	τ_1 (ns)	A_2 (V)	τ_2 (ns)	y_0
glass/250nm-Exc glass	0.73	1.3	0.25	193.9	0
glass/250nm-Exc $MAPbI_3$	0.71	1.1	0.20	190.9	0
glass/750nm-Exc glass	0.34	4.7	0.56	241.5	0
glass/750nm-Exc $MAPbI_3$	0.42	4.2	0.48	254.4	0
glass/AAS-750nm-Exc glass	0.21	2.9	0.68	237.1	0
glass/AAS-750nm-Exc $MAPbI_3$	0.23	3.5	0.68	239.1	0
HTL/250nm-Exc HTL	0.79	0.7	0.15	8.6	0.003
HTL/250nm-Exc $MAPbI_3$	0.53	1.9	0.39	14.1	0.004
HTL/750nm-Exc HTL	0.76	2.3	0.16	76.1	0.01
HTL/750nm-Exc $MAPbI_3$	0.60	5.0	0.28	100.7	0.01
HTL/AAS-750nm-Exc HTL	0.64	2.0	0.26	25.2	0.006
HTL/AAS-750nm-Exc $MAPbI_3$	0.36	3.9	0.49	32.5	0.01
glass/250nm/ETL-Exc ETL	0.98	1.4	0.03	11.4	0.001
glass/250nm/ETL-Exc glass	0.55	1.7	0.39	10.5	0.002
glass/750nm/ETL-Exc ETL	0.92	1.5	0.07	21.0	0.002
glass/750nm/ETL-Exc glass	0.27	2.3	0.67	30.7	0.006
glass/AAS-750nm/ETL-Exc ETL	0.91	1.4	0.14	16.4	0.001
glass/AAS-750nm/ETL-Exc glass	0.20	2.5	0.74	16.7	0.001
HTL/250nm/PCBM-Exc HTL	1.05	1.3	0.01	25.2	0.003
HTL/250nm/PCBM-Exc ETL	0.99	1.3	0.03	6.7	0.002
HTL/750nm/PCBM-Exc HTL	0.50	1.9	0.38	27.7	0.008
HTL/750nm/PCBM-Exc ETL	0.70	0.8	0.26	6.8	0.006
HTL/AAS-750nm/PCBM-Exc HTL	0.57	1.7	0.26	25.3	0.015
HTL/AAS-750nm/PCBM-Exc ETL	1.02	1.4	0.02	19.9	0.002

citation through the CTL to achieve spatial-localized charge generation in the perovskite layer near the CTL, shown as the cyan traces in Figures 5.5d-f and blue traces in Figures 5.5g-i. In general, all the TRPL decay kinetics begin with a dominant fast phase with τ_1 (< 3 ns), followed by a subsequent slow phase with relatively small amplitude ($A_2 < 0.3$) and variable τ_2 (~8 - 80 ns). Compared with the corresponding bare perovskite films, all films here exhibit increased amplitude in their fast phases, such that this fast phase is assigned primarily to direct charge transfer across the perovskite/CTL interface. Therefore, τ_1 can be assigned to the transfer time of charges from the perovskite into the CTL. These transfer times were found to be independent of perovskite film thickness and AAS treatment, with ~1.4 ns for electron transfer and ~2 ns

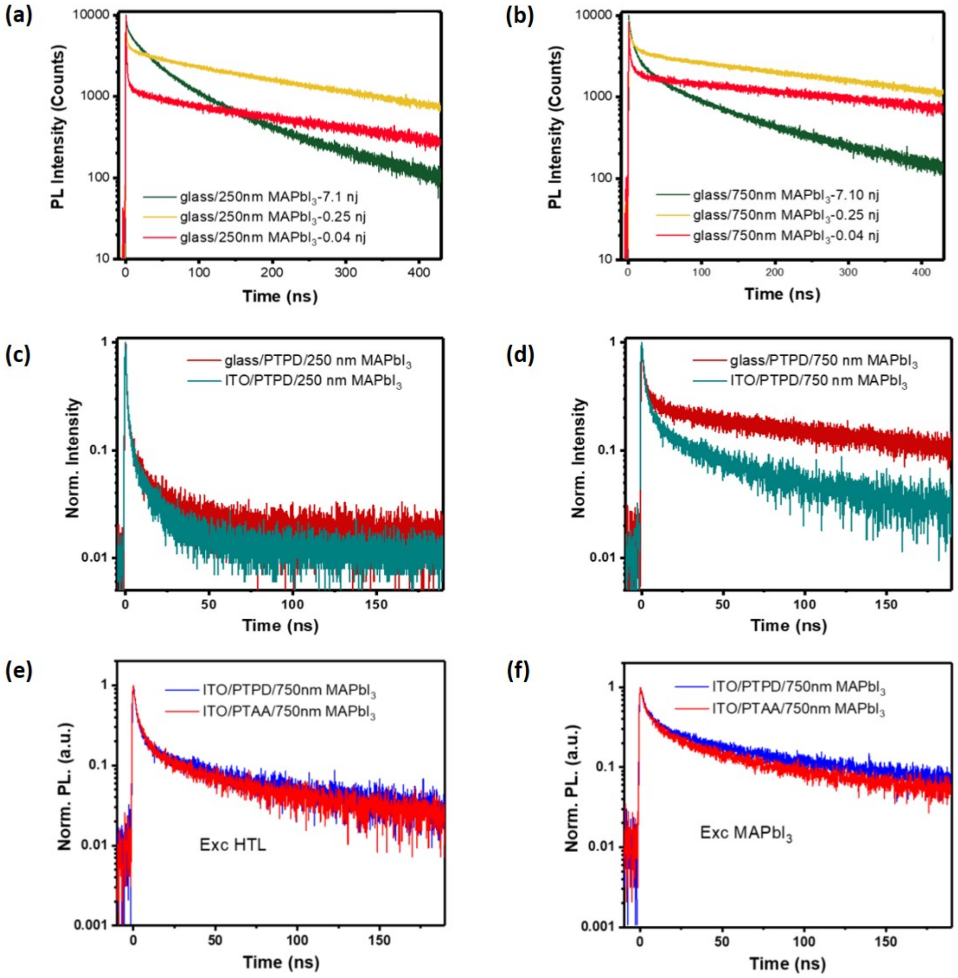

Figure 5.6: (a-b) TRPL of bare 250 nm and 750 nm MAPbI$_3$ films under three excitation fluences of 7.1 nj cm^{-2} pulse^{-1}, 0.25 nj cm^{-2} pulse^{-1} and 0.04 nj cm^{-2} pulse^{-1}, where 467 nm laser was used. (c-d) TRPL decays of 250 nm and 750 nm (b) MAPbI$_3$ based PTPD/MAPbI$_3$ films with/without ITO substrate. 405 nm laser with excitation fluence of 3 nJ cm^{-2} per pulse was used. The decays show a larger amplitude in PL quenching for ITO-based samples than glass-based, demonstrating charge accumulation in PTPD-only samples. (e-f) Comparison of TRPL decays between ITO/PTAA/750 nm MAPbI$_3$ and ITO/PTPD/750 nm MAPbI$_3$ under the same excitation conditions as c and d.

for hole transfer, comparable with the result from other reports measured by TRMC.[174] It is worth noting that exception is found on the data for HTL/250 nm MAPbI$_3$, ascribed to additional contributions from charge trapping, as observed for bare 250 nm MAPbI$_3$ discussed above. The faster time constant for electron transfer is also in good agreement with the larger amplitude (A_1) of this fast decay phase in MAPI$_3$/ETL films compared to HTL/MAPI$_3$ films. The second, slower phase here is primarily assigned to charges diffusing into the perovskite bulk but not directly transferred to the CTL, as illustrated in Figure 5.8a. Consistent with this assignment, the second phase of these films is pronounced for the thicker 750 nm MAPbI$_3$, and is more significant for the AAS-750 nm MAPbI$_3$. This indicates faster and more dominant

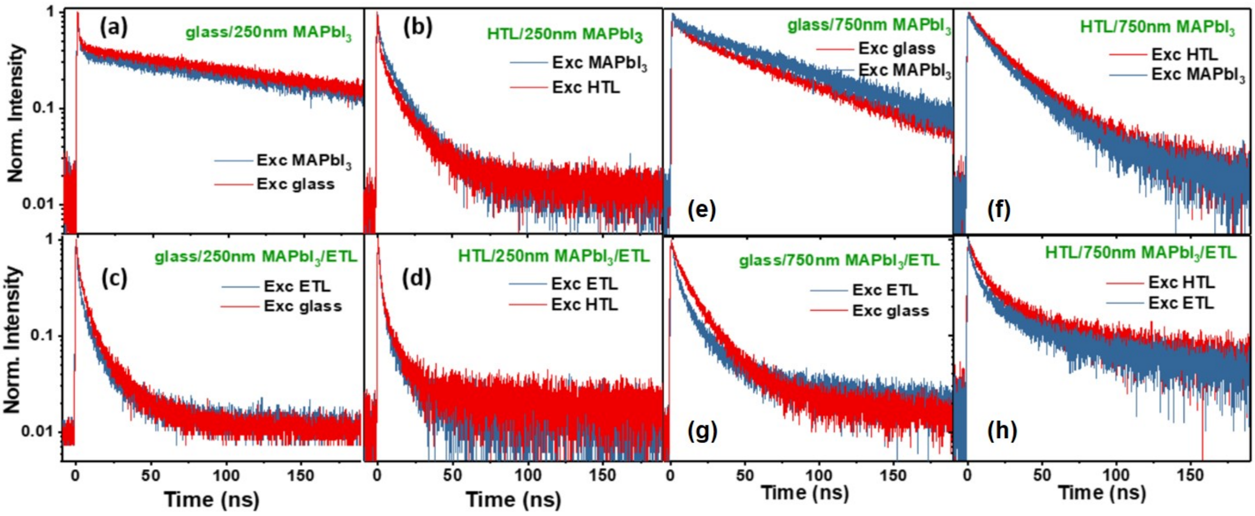

Figure 5.7: Two-side excited TRPL decays of 250 nm and 750 nm $MAPbI_3$ films with varied sample structures under 2.7 nJ cm^{-2} per pulse 637 nm excitation.

charge diffusion kinetics away from the $MAPI_3$/CTL interface were introduced by this treatment, as discussed further below. In summary, localized photoexcitation adjacent to the CTL allows the determination of electron transfer time of ∼1.4 ns and hole transfer time of ∼ 2 ns, the values of which are independent of perovskite thickness or processing.

The TRPL decays kinetics with photoexcitation from the opposite side to the perovskite/CTL interface are discussed, shown as the red traces in Figures 5.5d-f and grey traces in Figures 5.5g-i. Again, the decay kinetics can be fit to two decay phases. The fast phase shows similar lifetimes and amplitudes as they are from the bare $MAPbI_3$ films. It is therefore assigned to charge trapping at the CTL free $MAPbI_3$ surface. By contrast, the second, slower decay phase exhibits faster decay kinetics than bare films. It is assigned to a combined effect of charge diffusion across the perovskite film to the perovskite/CTL interface and subsequent charge transfer to the CTL. Figure 5.8b presents a schematic drawing of these processes. This second phase slows down when $MAPbI_3$ increases from 250 nm to 750 nm, and then become faster after AAS treatment, as demonstrated by the time constants shown in Table 5.3. Similar trends are also observed for the second decay phase with photoexcitation through the CTLs. These trends can be assigned to differences in charge transport times across the perovskite film, which is fastest for the 250 nm film, but also accelerated after AAS treatment, consistent with the improved perovskite quality (higher crystallinity and reduced vertical GBs) after this

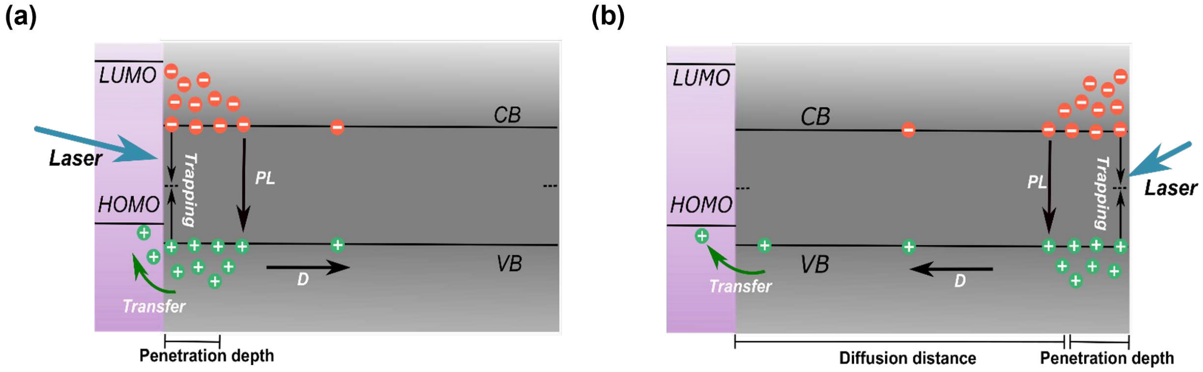

Figure 5.8: Schematic diagram of charge carrier dynamics in an HTL/MAPbI$_3$ sample with (a) excited from HTL side and (b) excited from the MAPbI$_3$ side. The purple layer represents the HTL and the grey layer represents MAPbI$_3$. The laser is pulsed with a duration of $<$ 200 ps and a wavelength of 405 nm. Copyright permission from published work.[122]

treatment. As such, the time constant of this second phase can be used as an indicator of the charge diffusion kinetics across the perovskite films, which will be discussed more quantitatively below.

Finally, TRPL decay kinetics for the full layer stack HTL/MAPbI$_3$/ETL (Figures 5.5j-l) were considered. It is apparent that all decays show a fast phase with a large amplitude followed by a slow phase with a small amplitude, consistent with the trend of bilayers exited at each CTL side. These data are also in good agreement with the assignments above that the first phase represents charge transfer to CTL while the second one represents charge diffusion away from the interface with excitation.

Following excitation through the HTL, the TRPL decay kinetics for the full stack are almost indistinguishable from those of the HTL/MAPbI$_3$ bilayer, consistent with our analyses above. We note that, for excitation through the ETL in the full stack, the slow decay phase is suppressed in amplitude, indicative of enhanced direct electron transfer to the ETL relative to MAPbI$_3$/ETL bilayers, tentatively assigned to the impact of the HTL on band bending in the perovskite. For excitation through the HTL, similar decay kinetics are observed between the TRPL decay kinetics from the full stack and from the HTL/MAPbI$_3$ bilayer, consistent with the analysis on the bilayer above. However, following excitation through the ETL, compared with the data from MAPbI$_3$/ETL films, the slower decay phase from the full layer stacks is suppressed in amplitude, suggesting enhanced electron transfer to the ETL. This could be attributed to the impact of the HTL on band bending in the perovskite. Notably, if a laser with a longer wavelength is used, achieving deeper penetration and more uniform charge generation in the perovskite layer, PL decay kinetics show less noticeable changes between excitation from either side, highlighting the importance of confining charge generation close to the perovskite/CTL interface to differentiate charge transfer versus transport. These results agree with the bilayer analysis that decreasing the thickness or removing vertical GBs can accelerate hole extraction.

Using bulk (637 nm) photoexcitation, TRPL decay kinetics exhibits a much less pronounced fast phase compared to the data from surface (405 nm) excitation, as shown in Figure 5.7. This is consistent with the assignment of this phase representing direct charge transfer through the perovskite/CTL interface or charge trapping close to the perovskite surface, depending on excitation direction, as detailed above. Under 637 nm excitation, it is apparent that a slow decay phase dominates the total TRPL decay kinetics, with the decay phase assigned primarily to charge diffusion to the interfaces. In summary, these results demonstrate the utility of using surface-localized photoexcitation to probe the charge trapping, transport and transfer kinetics in perovskite-based samples with CTLs.

5.4.3 Transport dynamics and mobility determination

Here, to further quantify the transport capability of these films, a simplified 1-D diffusion equation was introduced to estimate the charge carrier mobilities from their TRPL decays in Figure 5.5. In this model, only the decays of $MAPbI_3$/CTL films excited at the opposite side from the CTL interface were considered. Additionally, the following assumptions are made: charges are photogenerated and distributed homogenously within the optical penetration depth δ_p at time zero and then diffuse toward the $MAPbI_3$/CTL interface at the other side; charges are transferred immediately without any delay once they have reached the interface. The slower time constant τ_2 from the bi-exponential fitting results is used as a measure of the transport time of carriers across the film. The transport time $\tau_{transport}$ can be calculated from:

$$\frac{1}{\tau_{transport}} = \frac{1}{\tau_2} - \frac{1}{\tau_{recom}} \tag{5.1}$$

where τ_{recom} is the charge recombination time determined from the second decay phase for bare $MAPI_3$ films. The charge carrier mobility μ can then be calculated from:

$$\mu = \frac{qD}{k_B T} \times \frac{L^2}{2\tau_{transport}} \tag{5.2}$$

Here, the diffusion distance $L = d - \delta_p$, d is the film thickness, q is the elemental charge of an electron, D is diffusion coefficient, δ_p is the optical penetration depth, k_B is the Boltzmann constant, and T is the room temperature. More details regarding the derivation of this equation are given below.

Mobilities of the three different $MAPbI_3$ films obtained from this analysis are summarised in Table 5.4, showing different impacts of film thickness and morphology (GBs) on electron and hole transport. The 250 nm film shows the lowest mobilities, with μ_e and μ_h of $\sim$ 0.8 and 0.6 cm^2 V^{-1} s^{-1}, respectively, in agreement with the thinnest film having the highest defect density. The 750 nm film shows an over 3-fold higher μ_e but retained μ_h, suggesting the higher trap density in the 250 nm film primarily impacts electron transport rather than hole transport. It is likely that the lower μ_h in the 750 nm $MAPbI_3$, and the asymmetry between μ_e and μ_h (μ_e/μ_h = 4.8), is the origin of the lower FFs of its devices. A further enhancement of the mobilities was achieved by the AAS treatment, in particular with μ_h increasing more than 4 folds. Given a key effect of this treatment is the removal of vertical GBs, this result suggests that μ_h is more sensitive to GBs than μ_e, consistent with the literature that GBs can form shallow traps close to VBM that are benign to recombination but decrease μ_h.[116, 383] The results of μ_e = 11.2 cm^2 V^{-1} s^{-1} and μ_h = 5.3 cm^2 V^{-1} s^{-1} are comparable to the values obtained via other measurements in the literature.[108, 157, 161, 373] Though we note that these values measured under low-light excitation may be relatively smaller than the others measured under 1-sun equivalent illumination, these higher and more balanced mobilities are most likely the primary cause for the high FFs observed for the AAS PSCs.

Table 5.4: Mobility and diffusion coefficient summary of different $MAPbI_3$ films

Perovskite	Bilayer τ_2 (ns)	Bare film second lifetime τ_2 (ns)	μ_e ($cm^2V^{-1}s^{-1}$)	μ_h ($cm^2V^{-1}s^{-1}$)	μ_e/μ_h	D (cm^2s^{-1})
250 nm	10.5	193.9	0.8			0.02
	14.1	190.9		0.6	1.3	0.02
750 nm	30.5	241.5	2.7			0.07
	100.7	254.4		0.6	4.8	0.02
AAS-750 nm	16.7	237.1	5.6			0.14
	32.5	239.1		2.9	1.9	0.07

These differences in charge carrier dynamics discussed above are also reflected in the device performance. The PSCs with 250 nm $MAPbI_3$ show higher FFs due to short transport distance, which contributes to fast extraction in total, and similar μ_e and μ_h, which contributes to symmetric transport. However, these devices also show lower V_{OC} due to a combination of increased trap states and surface recombination. In contrast, by increasing the perovskite thickness to 750 nm, the PSCs with thicker $MAPbI_3$ show a considerably reduced trap density, leading to a significant enhancement in V_{OC}. However, these devices have a lower μ_h compared with μ_e, which results in asymmetric electron and hole transport, and therefore poorer charge extraction and FFs compared with 250 nm PSCs. As thicker perovskite layer is preferable for producing scaled-up[379, 388] and more efficient PSCs,[389, 390] a new post-deposition treatment: AAS treatment was employed to remove the lateral GBs. This treatment increased the device FF up to 0.802 ± 0.007 owning to improved symmetry of electron and hole transport and their mobility values. A further improvement of J_{SC} is also observed in the AAS-treated PSCs indicative of enhanced charge extraction. Nevertheless, our champion PCE still lags behind other state-of-the-art n-i-p-based devices, which could be attributed to the relatively slow hole transfer from $MAPbI_3$ to the HTL, limiting overall charge extraction in the complete cell. It is worth mentioning that this slow hole transfer is also observed for PTAA-based devices, with similar TRPL decay kinetics observed in both PTAA- and PTPD-based ITO/HTL/$MAPbI_3$ samples.

5.4.4 Derivation of mobility equation

To derive equation 5.2 for mobility calculation, the time-dependent 1-D diffusion equation from Fick's second law was solved as below. First, the charge distribution $n(x,t)$ can be expressed as:

$$\frac{\partial n(x,t)}{\partial t} = D\frac{\partial^2 n(x,t)}{\partial x^2} \tag{5.3}$$

Here, x is the position, t is the time, n is the charge concentration, and N_0 is the initial distribution approximated with a square pulse of negligible width. Therefore,[391]

$$n(x,t) = \frac{{N_0}^2}{\sqrt{4\pi Dt}} e^{\frac{-x^2}{4Dt}} \tag{5.4}$$

As the PL intensity (counts) $I(x,t)$ is proportional to the carrier concentration $n(x,t)$ and pseudo-first-order recombination kinetics are observed in the TRPL data above, a simple relationship of $n(x,t) = c \times I(x,t)$ is assumed. Here c is a constant describing the proportionality of total emitted PL photons collected by the detector. Thus,

$$c \times I(x,t) = \frac{{N_0}^2}{\sqrt{4\pi Dt}} e^{\frac{-x^2}{4Dt}} \tag{5.5}$$

Assuming all charges are quenched once reaching the MAPbI$_3$/CTL interface ($x = L$), a boundary condition of $dI(L,t)/dt = 0$ is applied to equation 5.5. As a result,

$$D = \frac{L^2}{2t} \tag{5.6}$$

where again t is the transport time, i.e. the time carriers take to diffuse over the distance L. As described above, the transport time $t = \tau_{transport}$ is obtained from the τ_2 of the exponential fit by using equation 5.1. Since $D = \mu k_B T$, one can calculate the mobility through equation 5.2.

5.5 Conclusion

In summary, the asymmetric surface localized photoexcitation method offers an approach to probe the trapping, transport and transfer kinetics of electrons and holes in PSC by deconstructing it into different layers. The results suggest that lateral GBs can reduce hole mobility but has less impact on electron mobility, which results in asymmetric charge transport within the perovskite layer such that reduced FF in PSCs. A post-deposition treatment (AAS treatment) was employed to remove the vertical GBs and was found to profoundly increase the hole mobility and thus FF of the PSC. Our results elucidate the role of vertical GBs impairing balanced charge transport, highlighting the importance of monolithic grains in the perovskite active layer, and putting forward an effective method to further improve the PSC performance. Though fast and balanced charge transport is achieved in these PSCs, they still suffer from asymmetric charge extraction with slow hole transfer at the perovskite/HTL interface with respect to electron transfer at the perovskite/ETL interface. Previous studies have shown that PTPD and PTAA are excellent HTLs for p-i-n PSCs as they can effectively suppress surface recombination,[130, 221] whilst the slow hole extraction observed here may still be a factor limiting the FF and potentially the J_{SC} of the devices. It suggests that developing a new HTL with improved hole extraction capability whilst retaining minimized surface recombination is the key to achieving more efficient p-i-n PSCs.

Chapter 6

Conclusion and Perspective

6.1 Summary

In this thesis, steady-state and time-resolved PL, in combination with many other optical spectroscopic methods, have been used to probe the charge carrier dynamics and to understand the device physics in various p-i-n PSCs. In a particular focus, this thesis has studied the dynamic competition between charge recombination, which is a loss, and charge extraction, which contributes to the power output. To achieve precise control of these optical measurements close to the actual solar cell working environments, this thesis has introduced a few new measurement techniques by considering illumination flux and biases, including light and voltage-dependent PL spectroscopy as well as spatial-localized surface quenching TRPL spectroscopy. These unique techniques have been successfully applied to investigate the individual charge trapping, charge transport, charge transfer and charge recombination processes in a range of different-processed PSCs. Based on these measurements, this thesis has not only compared various materials and device engineering methods, but also revealed their physical mechanisms for improving or limiting the performance of the p-i-n PSCs.

6.1.1 Measurement techniques

Steady-state PL is one of the most used techniques in this thesis. Probing the PL of perovskite-based samples or cells at OC condition is a crucial determinant of the bulk recombination correlated to device V_{OC}; measuring the PL_{SC} and thus calculating the quenching efficiency (PL_{OC-SC}) are also an assessment of charge extraction efficiency corresponding to FF and J_{SC}.[141, 221, 222, 242, 259] These measurements demonstrate that to achieve an efficient PSC, PL_{OC} needs to be maximized, whereas a small PL_{SC} and a large PL_{OC-SC} are desired. In other words, both large V_{OC} with minimized non-radiative recombination at OC and efficient charge extraction at low-biased conditions are crucial for achieving highly-efficient PSCs. Chapter 3 demonstrated the applications of this device OC to SC PL quenching method to three types of p-i-n PSCs with their variations in perovskite layer thickness, passivation additive and HTL structure.

To further quantify the losses at each operating voltage of a PSC in correlation to its J-V curve, Chapter 4 introduces an improved PL system: operando PL. This system measures real-time and absolute PL spectra during a J-V scanning under 1-sun equivalent illumination, allowing quantification of recombination currents and $QFLS$ under a series of biases.[260] In Chapter 4, this method is applied to study four p-i-n devices that differed in their ETLs selected to cover a range of LUMO values.

To distinguish the charge transport (a process within the perovskite layer) and the transfer process (a process across the perovskite/CTL interface), Chapter 5 introduces a unique TRPL measurement to study perovskite films with and without CTLs.[122, 164] Using spatial-localized and front and back excitation, charges are generated either adjacent to, or on the opposite side of, the perovskite/CTL interface. Under these excitation conditions, the TRPL decays obtained from the perovskite layer with an ETL/HTL reflect the individual electron/hole transfer or transport kinetics, where the individual electron and hole mobilities are quantified. Using this analysis, Chapter 5 compared charge transport properties between different-processed perovskite films, as well as charge transfer lifetimes between the ETL and HTL.

6.1.2 Device physics

6.1.3 Bulk effect

The perovskite layer thickness is first considered and investigated, as discussed at the beginning of Chapter 3. Compared to the thicker thin film, the thin thicker film absorbs more light and has lower defect densities, with minor trap-mediated and surface recombination. These characteristics are mainly revealed by the steady-state PL measurements performed on neat perovskite films and their devices at OC. These advantages lead to a greater V_{OC} in thicker PSCs regardless of light intensities, which is further confirmed in Chapter 5 using TRPL measurements. Nevertheless, charge extraction in a thicker perovskite-based solar cell is less efficient than in a thin one. This is attributed to two main factors. First, there is enhanced band-to-band recombination in the thicker perovskite film because photogenerated charge carriers must travel a longer distance before being transferred. This effect can become more pronounced when considerable mobile ions are present, which leads to charge transport in the PSC will be mainly diffusion rather than drift due to the field screening effect, as illustrated in Chapter 4.[208, 209] Another factor demonstrated in Chapter 5 is the GBs that reduce charge carrier mobility, especially for the holes, and cause asymmetric charge extraction. These factors result in the thicker PSCs having lower FFs and more substantial current losses under high illumination ($\geq$ 1-sun). However, an opposite trend is observed under low illuminations ($<$ 1 sun), where thinner PSCs demonstrated much lower FFs. This can be ascribed to the dominance of first-order non-radiative recombination in the thinner devices. Under these light intensities, second-order band-to-band recombination becomes less effective, whilst first-order trap-mediated and surface recombination becomes more significant in the device.[124, 125, 145, 223] Overall, the results show that the photoactive layer thickness of p–i–n planar perovskite solar cells for optimum photovoltaic PCE depends upon the incident light intensity, and that this behaviour depends particularly upon the light intensity dependence of the kinetic competition between charge extraction and bulk recombination.

Additive engineering using AAs (amino acids) is an effective method to passivate defect states in the perovskite layer and improve the V_{OC} of a PSC, as demonstrated in Chapter 3. Whilst 1-C AA has boosted the device PCE dramatically, other additives with longer carbon chain length (2-4C) reduce device performance, especially the J_{SC}. The analysis reveals that charge extraction efficiency in these AAs (2-4C) PSCs is reduced, though all AAs show effective passivation. This is attributed to the impeded charge transfer from the perovskite layer to the CTL, likely due to a barrier formed by these additives at the perovskite surfaces.[174, 295, 297]

Ion migration is also a vital factor considered in PSCs. Chapter 4 discusses the impact of the mobile ion on charge carrier recombination and extraction corresponding to the device performance. At low applied voltages, mobile ions located at the perovskite/CTL interfaces screen the internal electric field, resulting in slower, diffusion-driven charge extraction and reduced J_{SC}.[208, 209, 233] Though the ions accumulated at the perovskite/CTL interface repel the opposite charge carriers close to the interface, which decreases the surface recombination velocity and improves the V_{OC},[360] this contribution to the overall PCE is minor compared to the J_{SC} loss. Thus, ion migration is still an issue considering device performance.

6.1.4 Charge transport layer effect

The CTL plays a crucial role in affecting charge extraction efficiency in a p-i-n PSC. In Chapter 5, slow charge transfer is observed from the perovskite layer to PTAA/PTPD layer through spatial-localized surface quenching TRPL measurement. This results in asymmetric charge extraction, limiting device FF and J_{SC}. A strategy targeting this issue is illustrated in Chapter 3, where a new methodology is introduced by inserting a 1-dimensional nanomaterial, PNR, in between the HTL and perovskite. The TA results suggest that PNR accelerates hole transfer at the PTAA/perovskite interface. This improved charge transfer results in a significant enhancement of total charge extraction in the device, as indicated by the device PL measurement, finally leading to improved device performance. This suggests that inserting a low-dimensional nanomaterial between the PTAA and the perovskite may be an effective strategy to improve charge extraction efficiency and enhance device FF and J_{SC}.

Another important concern in the PSC is the energetic offsets between the LUMO of the ETL and the CB of the perovskite layer. Chapter 4 discusses how ETLs with different LUMO levels impact the charge carrier dynamics in the methylammonium-free p-i-n PSCs. Most of the optical measurements used in the previous chapters are employed during this study. Analysis of these optical and many other optoelectric data suggest that in addition to choosing an ETL with good charge transport properties (e.g., mobility), it is necessary to optimise the energy alignment at the perovskite interface to achieve the highest device performance. Whilst a low LUMO favours charge transfer from the perovskite to the ETL, it causes Fermi-level deflection and non-radiative recombination at the perovskite/ETL interface, which consequently leads to reduced FF and V_{OC} in the PSC. On the contrary, despite the benefits for $QFLS$, a high LUMO impedes charge extraction at low voltages (V < V_{OC}), leading to photogenerated charges accumulating in bulk and decreased J_{SC} and FF. Moreover, quantifying different recombination currents also suggests that surface recombination is more severe at high voltages (near V_{OC}) than under low-voltage conditions. These analyses imply that matching the energetic alignment at the perovskite/CTL interface is essential for minimising surface recombination and avoiding charge accumulation.

6.2 Outlook

This thesis has also pointed out several vital concerns existing in current p-i-n PSCs, which are due to be addressed.

First, slow hole transfer at the perovskite/HTL interface could limit the efficiency developing of current-stage p-i-n PSCs, as most studies are still focused on PTAA-based cells. To tackle this problem, using a self-assembled monolayer to replace PTAA,[392, 393] or modifying the PTAA/perovskite interface with an ultra-thin intermedia layer may be promising.[394, 395]

Second, considerable surface recombination at the perovskite/ETL side is still observed in many efficient solar cells with PCE > 20%, such as devices using PCBM. For those devices using wide bandgap perovskites, this becomes even more severe due to the much higher CB of the perovskite layer.[229] Thus, developing new ETLs with matchable LUMOs and excellent mobilities, or modifying the perovskite/ETL interface by inserting a thin buffer layer, could be future strategies.

Third, ion migration is general in all PSCs, which may induce charge accumulation at SC to reduce device J_{SC} and FF.[233] To fully explore the solar conversion potential of the PSCs, mitigating ion migration in these devices is essential.

Despite those issues, this thesis has extended and developed several new measurement techniques and analysis methods to understand charge recombination and charge extraction in PSCs. The three chapters in this thesis have offered several detailed examples of using these techniques and methods, demonstrating their accessibility and adaptability for other researchers and technicians. These simple and easily adapted PL-based techniques and methods are also likely to be widely used in both research and industrial communities. In addition, the fundamental scientific finding from these studies has also illustrated the benefit and limitations of various device processing methods and provided guides for developing more efficient PSCs in the future.

Bibliography

[1] IEA. Global energy review 2021. 2021.

[2] Andrea Franco, Marjan Shaker, Dikolela Kalubi, and Silvia Hostettler. A review of sustainable energy access and technologies for healthcare facilities in the global south. *Sustainable Energy Technologies and Assessments*, 22:92–105, 2017.

[3] Chian-Woei Shyu. Energy poverty alleviation in southeast asian countries: policy implications for improving access to electricity. *Journal of Asian Public Policy*, 15(1):97–121, 2022.

[4] Peter J Hotez, Alan Fenwick, and David Molyneux. The new covid-19 poor and the neglected tropical diseases resurgence, 2021.

[5] Christophe McGlade and Paul Ekins. The geographical distribution of fossil fuels unused when limiting global warming to 2 c. *Nature*, 517(7533):187–190, 2015.

[6] Nicholas Bloom. Fluctuations in uncertainty. *Journal of Economic Perspectives*, 28(2):153–76, 2014.

[7] Ibrahim Dincer. Renewable energy and sustainable development: a crucial review. *Renewable and sustainable energy reviews*, 4(2):157–175, 2000.

[8] John Houghton. Global warming. *Reports on progress in physics*, 68(6):1343, 2005.

[9] Samer Fawzy, Ahmed I Osman, John Doran, and David W Rooney. Strategies for mitigation of climate change: a review. *Environmental Chemistry Letters*, 18(6):2069–2094, 2020.

[10] Dario Maradin. Advantages and disadvantages of renewable energy sources utilization. *670216917*, 2021.

[11] Daryl M Chapin, Calvin S Fuller, and Gerald L Pearson. A new silicon p-n junction photocell for converting solar radiation into electrical power. *Journal of applied physics*, 25(5):676–677, 1954.

[12] Vignesh Ramasamy, David Feldman, Jal Desai, and Robert Margolis. Us solar photovoltaic system and energy storage cost benchmarks: Q1 2021. Technical report, National Renewable Energy Lab.(NREL), Golden, CO (United States), 2021.

[13] David Feldman, Vignesh Ramasamy, Ran Fu, Ashwin Ramdas, Jal Desai, and Robert Margolis. Us solar photovoltaic system and energy storage cost benchmark (q1 2020). Technical report, National Renewable Energy Lab.(NREL), Golden, CO (United States), 2021.

[14] Armin Richter, Ralph Müller, Jan Benick, Frank Feldmann, Bernd Steinhauser, Christian Reichel, Andreas Fell, Martin Bivour, Martin Hermle, and Stefan W Glunz. Design rules for high-efficiency both-sides-contacted silicon solar cells with balanced charge carrier transport and recombination losses. *Nature Energy*, 6(4):429–438, 2021.

[15] F Meillaud, Arvind Shah, C Droz, Evelyne Vallat-Sauvain, and C Miazza. Efficiency limits for single-junction and tandem solar cells. *Solar energy materials and solar cells*, 90(18-19):2952–2959, 2006.

[16] Alexis De Vos. Detailed balance limit of the efficiency of tandem solar cells. *Journal of Physics D: Applied Physics*, 13(5):839, 1980.

[17] Matthew O Reese, Stephen Glynn, Michael D Kempe, Deborah L McGott, Matthew S Dabney, Teresa M Barnes, Samuel Booth, David Feldman, and Nancy M Haegel. Increasing markets and decreasing package weight for high-specific-power photovoltaics. *Nature Energy*, 3(11):1002–1012, 2018.

[18] Masafumi Yamaguchi, Ryo Ozaki, Kyotaro Nakamura, Kan-Hua Lee, Nobuaki Kojima, Yoshio Ohshita, Taizo Masuda, Kenichi Okumura, Akinori Satou, Takashi Nakado, et al. Development of high-efficiency solar cell modules for photovoltaic-powered vehicles. *Solar RRL*, 6(5):2100429, 2022.

[19] Guanqi Tang and Feng Yan. Recent progress of flexible perovskite solar cells. *Nano Today*, 39:101155, 2021.

[20] Yongguang Tu, Jiang Wu, Guoning Xu, Xiaoyu Yang, Rong Cai, Qihuang Gong, Rui Zhu, and Wei Huang. Perovskite solar cells for space applications: progress and challenges. *Advanced Materials*, 33(21):2006545, 2021.

[21] Jenny A Nelson. *The physics of solar cells*. World Scientific Publishing Company, 2003.

[22] C Riordan and R Hulstron. What is an air mass 1.5 spectrum?(solar cell performance calculations). In *IEEE Conference on Photovoltaic Specialists*, pages 1085–1088. IEEE, 1990.

[23] J Meier, R Flückiger, H Keppner, and Arvind Shah. Complete microcrystalline p-i-n solar cell—crystalline or amorphous cell behavior? *Applied Physics Letters*, 65(7):860–862, 1994.

[24] Peter V Meyers. Design of a thin film cdte solar cell. *Solar cells*, 23(1-2):59–67, 1988.

[25] Yasufumi Tsunomura, Yukihiro Yoshimine, Mikio Taguchi, Toshiaki Baba, Toshihiro Kinoshita, Hiroshi Kanno, Hitoshi Sakata, Eiji Maruyama, and Makoto Tanaka. Twenty-two percent efficiency hit solar cell. *Solar Energy Materials and Solar Cells*, 93(6-7):670–673, 2009.

[26] Kenji Yamamoto, Kunta Yoshikawa, Hisashi Uzu, and Daisuke Adachi. High-efficiency heterojunction crystalline si solar cells. *Japanese Journal of Applied Physics*, 57(8S3):08RB20, 2018.

[27] Priyanka Roy, Numeshwar Kumar Sinha, Sanjay Tiwari, and Ayush Khare. A review on perovskite solar cells: Evolution of architecture, fabrication techniques, commercialization issues and status. *Solar Energy*, 198:665–688, 2020.

[28] Nam-Gyu Park and Kai Zhu. Scalable fabrication and coating methods for perovskite solar cells and solar modules. *Nature Reviews Materials*, 5(5):333–350, 2020.

[29] Zhanhua Wei, Haining Chen, Keyou Yan, and Shihe Yang. Inkjet printing and instant chemical transformation of a ch3nh3pbi3/nanocarbon electrode and interface for planar perovskite solar cells. *Angewandte Chemie International Edition*, 53(48):13239–13243, 2014.

[30] Xiaojin Peng, Jian Yuan, Shirley Shen, Mei Gao, Anthony SR Chesman, Hong Yin, Jinshu Cheng, Qi Zhang, and Dechan Angmo. Perovskite and organic solar cells fabricated by inkjet printing: progress and prospects. *Advanced Functional Materials*, 27(41):1703704, 2017.

[31] Yehao Deng, Edwin Peng, Yuchuan Shao, Zhengguo Xiao, Qingfeng Dong, and Jinsong Huang. Scalable fabrication of efficient organolead trihalide perovskite solar cells with doctor-bladed active layers. *Energy & Environmental Science*, 8(5):1544–1550, 2015.

[32] Yehao Deng, Qi Wang, Yongbo Yuan, and Jinsong Huang. Vividly colorful hybrid perovskite solar cells by doctor-blade coating with perovskite photonic nanostructures. *Materials Horizons*, 2(6):578–583, 2015.

[33] Rahul Patidar, Daniel Burkitt, Katherine Hooper, David Richards, and Trystan Watson. Slot-die coating of perovskite solar cells: An overview. *Materials Today Communications*, 22:100808, 2020.

[34] Mingzhen Liu, Michael B Johnston, and Henry J Snaith. Efficient planar heterojunction perovskite solar cells by vapour deposition. *Nature*, 501(7467):395–398, 2013.

[35] Matthew R Leyden, Luis K Ono, Sonia R Raga, Yuichi Kato, Shenghao Wang, and Yabing Qi. High performance perovskite solar cells by hybrid chemical vapor deposition. *Journal of Materials Chemistry A*, 2(44):18742–18745, 2014.

[36] Hanul Min, Do Yoon Lee, Junu Kim, Gwisu Kim, Kyoung Su Lee, Jongbeom Kim, Min Jae Paik, Young Ki Kim, Kwang S Kim, Min Gyu Kim, et al. Perovskite solar cells with atomically coherent interlayers on sno2 electrodes. *Nature*, 598(7881):444–450, 2021.

[37] Jason J Yoo, Gabkyung Seo, Matthew R Chua, Tae Gwan Park, Yongli Lu, Fabian Rotermund, Young-Ki Kim, Chan Su Moon, Nam Joong Jeon, Juan-Pablo Correa-Baena, et al. Efficient perovskite solar cells via improved carrier management. *Nature*, 590(7847):587–593, 2021.

[38] Minyong Du, Xuejie Zhu, Likun Wang, Hui Wang, Jiangshang Feng, Xiao Jiang, Yuexian Cao, Youming Sun, Lianjie Duan, Yuxiao Jiao, et al. High-pressure nitrogen-extraction and effective passivation to attain highest large-area perovskite solar module efficiency. *Advanced Materials*, 32(47):2004979, 2020.

[39] Yuanhang Yang, Zexu Xue, Long Chen, Cho Fai Jonathan Lau, and Zhiping Wang. Large-area perovskite films for pv applications: A perspective from nucleation and crystallization. *Journal of Energy Chemistry*, 59:626–641, 2021.

[40] Sanjay Sahare, Hong Duc Pham, Dechan Angmo, Prachi Ghoderao, Jennifer MacLeod, Sadaf Bashir Khan, Shern-Long Lee, Samareandra P Singh, and Prashant Sonar. Emerging perovskite solar cell technology: Remedial actions for the foremost challenges. *Advanced Energy Materials*, 11(42):2101085, 2021.

[41] Yehao Deng, Xiaopeng Zheng, Yang Bai, Qi Wang, Jingjing Zhao, and Jinsong Huang. Surfactant-controlled ink drying enables high-speed deposition of perovskite films for efficient photovoltaic modules. *Nature Energy*, 3(7):560–566, 2018.

[42] Shi Tang, Yehao Deng, Xiaopeng Zheng, Yang Bai, Yanjun Fang, Qingfeng Dong, Haotong Wei, and Jinsong Huang. Composition engineering in doctor-blading of perovskite solar cells. *Advanced Energy Materials*, 7(18):1700302, 2017.

[43] Francesco Di Giacomo, Santhosh Shanmugam, Henri Fledderus, Bardo J Bruijnaers, Wiljan JH Verhees, Maarten S Dorenkamper, Sjoerd C Veenstra, Weiming Qiu, Robert Gehlhaar, Tamara Merckx, et al. Up-scalable sheet-to-sheet production of high efficiency perovskite module and solar cells on 6-in. substrate using slot die coating. *Solar Energy Materials and Solar Cells*, 181:53–59, 2018.

[44] Martin Green, Ewan Dunlop, Jochen Hohl-Ebinger, Masahiro Yoshita, Nikos Kopidakis, Karsten Bothe, David Hinken, Michael Rauer, and Xiaojing Hao. Solar cell efficiency tables (version 60). *Progress in photovoltaics: research and applications*, 30(7):687–701, 2022.

[45] Akihiro Kojima, Kenjiro Teshima, Yasuo Shirai, and Tsutomu Miyasaka. Organometal halide perovskites as visible-light sensitizers for photovoltaic cells. *Journal of the american chemical society*, 131(17):6050–6051, 2009.

[46] Dian Wang, Matthew Wright, Naveen Kumar Elumalai, and Ashraf Uddin. Stability of perovskite solar cells. *Solar Energy Materials and Solar Cells*, 147:255–275, 2016.

[47] Guangda Niu, Xudong Guo, and Liduo Wang. Review of recent progress in chemical stability of perovskite solar cells. *Journal of Materials Chemistry A*, 3(17):8970–8980, 2015.

[48] Nengxu Li, Xiuxiu Niu, Qi Chen, and Huanping Zhou. Towards commercialization: the operational stability of perovskite solar cells. *Chemical Society Reviews*, 49(22):8235–8286, 2020.

[49] Hui-Seon Kim, Ja-Young Seo, and Nam-Gyu Park. Material and device stability in perovskite solar cells. *ChemSusChem*, 9(18):2528–2540, 2016.

[50] Fei Zhang and Kai Zhu. Additive engineering for efficient and stable perovskite solar cells. *Advanced Energy Materials*, 10(13):1902579, 2020.

[51] Giulia Grancini, C Roldán-Carmona, Iwan Zimmermann, E Mosconi, X Lee, D Martineau, S Narbey, Frédéric Oswald, F De Angelis, Michael Graetzel, et al. One-year stable perovskite solar cells by 2d/3d interface engineering. *Nature communications*, 8(1):1–8, 2017.

[52] Randi Azmi, Esma Ugur, Akmaral Seitkhan, Faisal Aljamaan, Anand S Subbiah, Jiang Liu, George T Harrison, Mohamad I Nugraha, Mathan K Eswaran, Maxime Babics, et al. Damp heat–stable perovskite solar cells with tailored-dimensionality 2d/3d heterojunctions. *Science*, 376(6588):73–77, 2022.

[53] Junming Li, Hai-Lei Cao, Wen-Bin Jiao, Qiong Wang, Mingdeng Wei, Irene Cantone, Jian Lü, and Antonio Abate. Biological impact of lead from halide perovskites reveals the risk of introducing a safe threshold. *Nature communications*, 11(1):1–5, 2020.

[54] Nicole Moody, Samuel Sesena, Dane W deQuilettes, Benjia Dak Dou, Richard Swartwout, Joseph T Buchman, Anna Johnson, Udochukwu Eze, Roberto Brenes, Matthew Johnston, et al. Assessing the regulatory requirements of lead-based perovskite photovoltaics. *Joule*, 4(5):970–974, 2020.

[55] Aslihan Babayigit, Anitha Ethirajan, Marc Muller, and Bert Conings. Toxicity of organometal halide perovskite solar cells. *Nature materials*, 15(3):247–251, 2016.

[56] Bin-Bin Yu, Zhenhua Chen, Yudong Zhu, Yiyu Wang, Bing Han, Guocong Chen, Xusheng Zhang, Zheng Du, and Zhubing He. Heterogeneous 2d/3d tin-halides perovskite solar cells with certified conversion efficiency breaking 14%. *Advanced Materials*, 33(36):2102055, 2021.

[57] Zihao Zhu, Xianyuan Jiang, Danni Yu, Na Yu, Zhijun Ning, and Qixi Mi. Smooth and compact fasni3 films for lead-free perovskite solar cells with over 14% efficiency. *ACS Energy Letters*, 7:2079–2083, 2022.

[58] Xun Li, Fei Zhang, Haiying He, Joseph J Berry, Kai Zhu, and Tao Xu. On-device lead sequestration for perovskite solar cells. *Nature*, 578(7796):555–558, 2020.

[59] Xun Xiao, Meixiang Wang, Shangshang Chen, Yihang Zhang, Hangyu Gu, Yehao Deng, Guang Yang, Chengbin Fei, Bo Chen, Yuze Lin, et al. Lead-adsorbing ionogel-based encapsulation for impact-resistant, stable, and lead-safe perovskite modules. *Science advances*, 7(44):eabi8249, 2021.

[60] Andreas Binek, Michiel L Petrus, Niklas Huber, Helen Bristow, Yinghong Hu, Thomas Bein, and Pablo Docampo. Recycling perovskite solar cells to avoid lead waste. *ACS applied materials & interfaces*, 8(20):12881–12886, 2016.

[61] Atsuhiko Miyata, Anatolie Mitioglu, Paulina Plochocka, Oliver Portugall, Jacob Tse-Wei Wang, Samuel D Stranks, Henry J Snaith, and Robin J Nicholas. Direct measurement of the exciton binding energy and effective masses for charge carriers in organic–inorganic tri-halide perovskites. *Nature Physics*, 11(7):582–587, 2015.

[62] Hui-Seon Kim, Sang Hyuk Im, and Nam-Gyu Park. Organolead halide perovskite: new horizons in solar cell research. *The Journal of Physical Chemistry C*, 118(11):5615–5625, 2014.

[63] Chonghea Li, Xionggang Lu, Weizhong Ding, Liming Feng, Yonghui Gao, and Ziming Guo. Formability of abx3 (x= f, cl, br, i) halide perovskites. *Acta Crystallographica Section B: Structural Science*, 64(6):702–707, 2008.

[64] Martin A Green, Anita Ho-Baillie, and Henry J Snaith. The emergence of perovskite solar cells. *Nature photonics*, 8(7):506–514, 2014.

[65] Woon Seok Yang, Byung-Wook Park, Eui Hyuk Jung, Nam Joong Jeon, Young Chan Kim, Dong Uk Lee, Seong Sik Shin, Jangwon Seo, Eun Kyu Kim, Jun Hong Noh, et al. Iodide management in formamidinium-lead-halide–based perovskite layers for efficient solar cells. *Science*, 356(6345):1376–1379, 2017.

[66] Michael Saliba, Taisuke Matsui, Ji-Youn Seo, Konrad Domanski, Juan-Pablo Correa-Baena, Mohammad Khaja Nazeeruddin, Shaik M Zakeeruddin, Wolfgang Tress, Antonio Abate, Anders Hagfeldt, et al. Cesium-containing triple cation perovskite solar cells: improved stability, reproducibility and high efficiency. *Energy & environmental science*, 9(6):1989–1997, 2016.

[67] Jaeki Jeong, Minjin Kim, Jongdeuk Seo, Haizhou Lu, Paramvir Ahlawat, Aditya Mishra, Yingguo Yang, Michael A Hope, Felix T Eickemeyer, Maengsuk Kim, et al. Pseudo-halide anion engineering for α-fapbi3 perovskite solar cells. *Nature*, 592(7854):381–385, 2021.

[68] Pei-Ying Lin, Aswaghosh Loganathan, Itaru Raifuku, Ming-Hsien Li, Yueh-Ya Chiu, Shao-Tung Chang, Azhar Fakharuddin, Chen-Fu Lin, Tzung-Fang Guo, Lukas Schmidt-Mende, et al. Pseudo-halide perovskite solar cells. *Advanced Energy Materials*, 11(28):2100818, 2021.

[69] Yukihiko Kawamura, Hiroyuki Mashiyama, and Katsuhiko Hasebe. Structural study on cubic-tetragonal transition of ch 3 nh 3 pbi 3. *Journal of the Physical Society of Japan*, 71(7):1694–1697, 2002.

[70] Tom Baikie, Nathan S Barrow, Yanan Fang, Philip J Keenan, Peter R Slater, Ross O Piltz, Matthias Gutmann, Subodh G Mhaisalkar, and Tim J White. A combined single crystal neutron/x-ray diffraction and solid-state nuclear magnetic resonance study of the hybrid perovskites ch 3 nh 3 pbx 3 (x= i, br and cl). *Journal of Materials Chemistry A*, 3(17):9298–9307, 2015.

[71] Yixin Zhao and Kai Zhu. Organic–inorganic hybrid lead halide perovskites for optoelectronic and electronic applications. *Chemical Society Reviews*, 45(3):655–689, 2016.

[72] Albrecht Poglitsch and Daniel Weber. Dynamic disorder in methylammoniumtrihalogenoplumbates (ii) observed by millimeter-wave spectroscopy. *The Journal of chemical physics*, 87(11):6373–6378, 1987.

[73] Constantinos C Stoumpos, Christos D Malliakas, and Mercouri G Kanatzidis. Semiconducting tin and lead iodide perovskites with organic cations: phase transitions, high mobilities, and near-infrared photoluminescent properties. *Inorganic chemistry*, 52(15):9019–9038, 2013.

[74] DM Trots and SV Myagkota. High-temperature structural evolution of caesium and rubidium triiodoplumbates. *Journal of Physics and Chemistry of Solids*, 69(10):2520–2526, 2008.

[75] Zhaohua Zhu, Qian Sun, Zhipeng Zhang, Jie Dai, Guichuan Xing, Shaozhou Li, Xiao Huang, and Wei Huang. Metal halide perovskites: stability and sensing-ability. *Journal of Materials Chemistry C*, 6(38):10121–10137, 2018.

[76] Hui-Seon Kim, Chang-Ryul Lee, Jeong-Hyeok Im, Ki-Beom Lee, Thomas Moehl, Arianna Marchioro, Soo-Jin Moon, Robin Humphry-Baker, Jun-Ho Yum, Jacques E Moser, et al. Lead iodide perovskite sensitized all-solid-state submicron thin film mesoscopic solar cell with efficiency exceeding 9%. *Scientific reports*, 2(1):1–7, 2012.

[77] Michael M Lee, Joël Teuscher, Tsutomu Miyasaka, Takurou N Murakami, and Henry J Snaith. Efficient hybrid solar cells based on meso-superstructured organometal halide perovskites. *Science*, 338(6107):643–647, 2012.

[78] Julian Burschka, Norman Pellet, Soo-Jin Moon, Robin Humphry-Baker, Peng Gao, Mohammad K Nazeeruddin, and Michael Grätzel. Sequential deposition as a route to high-performance perovskite-sensitized solar cells. *Nature*, 499(7458):316–319, 2013.

[79] Jeong-Hyeok Im, In-Hyuk Jang, Norman Pellet, Michael Grätzel, and Nam-Gyu Park. Growth of ch3nh3pbi3 cuboids with controlled size for high-efficiency perovskite solar cells. *Nature nanotechnology*, 9(11):927–932, 2014.

[80] Woon Seok Yang, Jun Hong Noh, Nam Joong Jeon, Young Chan Kim, Seungchan Ryu, Jangwon Seo, and Sang Il Seok. High-performance photovoltaic perovskite layers fabricated through intramolecular exchange. *Science*, 348(6240):1234–1237, 2015.

[81] Xiong Li, Dongqin Bi, Chenyi Yi, Jean-David Décoppet, Jingshan Luo, Shaik Mohammed Zakeeruddin, Anders Hagfeldt, and Michael Grätzel. A vacuum flash–assisted solution process for high-efficiency large-area perovskite solar cells. *Science*, 353(6294):58–62, 2016.

[82] Jun-Yuan Jeng, Yi-Fang Chiang, Mu-Huan Lee, Shin-Rung Peng, Tzung-Fang Guo, Peter Chen, and Ten-Chin Wen. Ch3nh3pbi3 perovskite/fullerene planar-heterojunction hybrid solar cells. *Advanced Materials*, 25(27):3727–3732, 2013.

[83] Pablo Docampo, James M Ball, Mariam Darwich, Giles E Eperon, and Henry J Snaith. Efficient organometal trihalide perovskite planar-heterojunction solar cells on flexible polymer substrates. *Nature communications*, 4(1):1–6, 2013.

[84] Jun-Yuan Jeng, Kuo-Cheng Chen, Tsung-Yu Chiang, Pei-Ying Lin, Tzung-Da Tsai, Yun-Chorng Chang, Tzung-Fang Guo, Peter Chen, Ten-Chin Wen, and Yao-Jane Hsu. Nickel oxide electrode interlayer in ch3nh3pbi3 perovskite/pcbm planar-heterojunction hybrid solar cells. *Advanced materials*, 26(24):4107–4113, 2014.

[85] Dewei Zhao, Michael Sexton, Hye-Yun Park, George Baure, Juan C Nino, and Franky So. High-efficiency solution-processed planar perovskite solar cells with a polymer hole transport layer. *Advanced Energy Materials*, 5(6):1401855, 2015.

[86] Deying Luo, Wenqiang Yang, Zhiping Wang, Aditya Sadhanala, Qin Hu, Rui Su, Ravichandran Shivanna, Gustavo F Trindade, John F Watts, Zhaojian Xu, et al. Enhanced photovoltage for inverted planar heterojunction perovskite solar cells. *Science*, 360(6396):1442–1446, 2018.

[87] Senyun Ye, Weihai Sun, Yunlong Li, Weibo Yan, Haitao Peng, Zuqiang Bian, Zhiwei Liu, and Chunhui Huang. Cuscn-based inverted planar perovskite solar cell with an average pce of 15.6%. *Nano letters*, 15(6):3723–3728, 2015.

[88] Wei-Yi Chen, Lin-Long Deng, Si-Min Dai, Xin Wang, Cheng-Bo Tian, Xin-Xing Zhan, Su-Yuan Xie, Rong-Bin Huang, and Lan-Sun Zheng. Low-cost solution-processed copper iodide as an alternative to pedot: Pss hole transport layer for efficient and stable inverted planar heterojunction perovskite solar cells. *Journal of Materials Chemistry A*, 3(38):19353–19359, 2015.

[89] Lin-Long Deng, Su-Yuan Xie, and Feng Gao. Fullerene-based materials for photovoltaic applications: Toward efficient, hysteresis-free, and stable perovskite solar cells. *Advanced Electronic Materials*, 4(10):1700435, 2018.

[90] Daizhe Wang, Tengling Ye, and Yong Zhang. Recent advances of non-fullerene organic electron transport materials in perovskite solar cells. *Journal of Materials Chemistry A*, 8(40):20819–20848, 2020.

[91] Xiaodong Li, Wenxiao Zhang, Xuemin Guo, Chunyan Lu, Jiyao Wei, and Junfeng Fang. Constructing heterojunctions by surface sulfidation for efficient inverted perovskite solar cells. *Science*, 375(6579):434–437, 2022.

[92] Zhen Li, Bo Li, Xin Wu, Stephanie A Sheppard, Shoufeng Zhang, Danpeng Gao, Nicholas J Long, and Zonglong Zhu. Organometallic-functionalized interfaces for highly efficient inverted perovskite solar cells. *Science*, 376(6591):416–420, 2022.

[93] Laurent Pedesseau, Jean-Marc Jancu, Alain Rolland, Emmanuelle Deleporte, Claudine Katan, and Jacky Even. Electronic properties of 2d and 3d hybrid organic/inorganic perovskites for optoelectronic and photovoltaic applications. *Optical and Quantum Electronics*, 46(10):1225–1232, 2014.

[94] Aron Walsh. Atomistic models of metal halide perovskites. *Matter*, 4(12):3867–3873, 2021.

[95] Jacky Even, Laurent Pedesseau, and Claudine Katan. Analysis of multivalley and multibandgap absorption and enhancement of free carriers related to exciton screening in hybrid perovskites. *The Journal of Physical Chemistry C*, 118(22):11566–11572, 2014.

[96] Masaki Shirayama, Hideyuki Kadowaki, Tetsuhiko Miyadera, Takeshi Sugita, Masato Tamakoshi, Masato Kato, Takemasa Fujiseki, Daisuke Murata, Shota Hara, Takurou N Murakami, et al. Optical transitions in hybrid perovskite solar cells: ellipsometry, density functional theory, and quantum efficiency analyses for ch 3 nh 3 pbi 3. *Physical Review Applied*, 5(1):014012, 2016.

[97] Jeremy L Knutson, James D Martin, and David B Mitzi. Tuning the band gap in hybrid tin iodide perovskite semiconductors using structural templating. *Inorganic chemistry*, 44(13):4699–4705, 2005.

[98] Laura M Herz. Charge-carrier dynamics in organic-inorganic metal halide perovskites. *Annual review of physical chemistry*, 67:65–89, 2016.

[99] YH Chang, Chul Hong Park, and Kiyoto Matsuishi. First-principles study of the structural and the electronic properties of the lead-halide-based inorganic-organic perovskites (ch˜ 3nh˜ 3) pbx˜ 3 and cspbx˜ 3 (x= cl, br, i). *Journal-Korean Physical Society*, 44:889–893, 2004.

[100] Joseph S Manser, Jeffrey A Christians, and Prashant V Kamat. Intriguing optoelectronic properties of metal halide perovskites. *Chemical reviews*, 116(21):12956–13008, 2016.

[101] Anna Amat, Edoardo Mosconi, Enrico Ronca, Claudio Quarti, Paolo Umari, Md K Nazeeruddin, Michael Gratzel, and Filippo De Angelis. Cation-induced band-gap tuning in organohalide perovskites: interplay of spin–orbit coupling and octahedra tilting. *Nano letters*, 14(6):3608–3616, 2014.

[102] Naresh K Kumawat, Amrita Dey, Aravindh Kumar, Sreelekha P Gopinathan, KL Narasimhan, and Dinesh Kabra. Band gap tuning of ch3nh3pb (br1–x cl x) 3 hybrid perovskite for blue electroluminescence. *ACS Applied Materials & Interfaces*, 7(24):13119–13124, 2015.

[103] Giles E Eperon, Samuel D Stranks, Christopher Menelaou, Michael B Johnston, Laura M Herz, and Henry J Snaith. Formamidinium lead trihalide: a broadly tunable perovskite for efficient planar heterojunction solar cells. *Energy & Environmental Science*, 7(3):982–988, 2014.

[104] Edoardo Mosconi, Anna Amat, Md K Nazeeruddin, Michael Gratzel, and Filippo De Angelis. First-principles modeling of mixed halide organometal perovskites for photovoltaic applications. *The Journal of Physical Chemistry C*, 117(27):13902–13913, 2013.

[105] Nakita K Noel, Samuel D Stranks, Antonio Abate, Christian Wehrenfennig, Simone Guarnera, Amir-Abbas Haghighirad, Aditya Sadhanala, Giles E Eperon, Sandeep K Pathak, Michael B Johnston, et al. Lead-free organic–inorganic tin halide perovskites for photovoltaic applications. *Energy & Environmental Science*, 7(9):3061–3068, 2014.

[106] Feng Hao, Constantinos C Stoumpos, Duyen Hanh Cao, Robert PH Chang, and Mercouri G Kanatzidis. Lead-free solid-state organic–inorganic halide perovskite solar cells. *Nature photonics*, 8(6):489–494, 2014.

[107] Claudine Katan, Laurent Pedesseau, Mikaël Kepenekian, Alain Rolland, and Jacky Even. Interplay of spin–orbit coupling and lattice distortion in metal substituted 3d tri-chloride hybrid perovskites. *Journal of Materials Chemistry A*, 3(17):9232–9240, 2015.

[108] Carlito S Ponseca Jr, Tom J Savenije, Mohamed Abdellah, Kaibo Zheng, Arkady Yartsev, Tobjorn Pascher, Tobias Harlang, Pavel Chabera, Tonu Pullerits, Andrey Stepanov, et al. Organometal halide perovskite solar cell materials rationalized: ultrafast charge generation, high and microsecond-long balanced mobilities, and slow recombination. *Journal of the American Chemical Society*, 136(14):5189–5192, 2014.

[109] CS Ponseca Jr and Villy Sundström. Revealing the ultrafast charge carrier dynamics in organo metal halide perovskite solar cell materials using time resolved thz spectroscopy. *Nanoscale*, 8(12):6249–6257, 2016.

[110] Jagdeep Shah. *Ultrafast spectroscopy of semiconductors and semiconductor nanostructures*, volume 115. Springer Science & Business Media, 2013.

[111] Mingjie Li, Jianhui Fu, Qiang Xu, and Tze Chien Sum. Slow hot-carrier cooling in halide perovskites: prospects for hot-carrier solar cells. *Advanced Materials*, 31(47):1802486, 2019.

[112] Jianhui Fu, Qiang Xu, Guifang Han, Bo Wu, Cheng Hon Alfred Huan, Meng Lee Leek, and Tze Chien Sum. Hot carrier cooling mechanisms in halide perovskites. *Nature communications*, 8(1):1–9, 2017.

[113] Ye Yang, Mengjin Yang, Zhen Li, Ryan Crisp, Kai Zhu, and Matthew C Beard. Comparison of recombination dynamics in ch3nh3pbbr3 and ch3nh3pbi3 perovskite films: influence of exciton binding energy. *The journal of physical chemistry letters*, 6(23):4688–4692, 2015.

[114] Krzysztof Galkowski, Anatolie Mitioglu, Atsuhiko Miyata, Paulina Plochocka, Oliver Portugall, Giles E Eperon, Jacob Tse-Wei Wang, Thomas Stergiopoulos, Samuel D Stranks, Henry J Snaith, et al. Determination of the exciton binding energy and effective masses for methylammonium and formamidinium lead tri-halide perovskite semiconductors. *Energy & Environmental Science*, 9(3):962–970, 2016.

[115] Jiangjian Shi, Yiming Li, Yusheng Li, Dongmei Li, Yanhong Luo, Huijue Wu, and Qingbo Meng. From ultrafast to ultraslow: charge-carrier dynamics of perovskite solar cells. *Joule*, 2(5):879–901, 2018.

[116] Dane W deQuilettes, Kyle Frohna, David Emin, Thomas Kirchartz, Vladimir Bulovic, David S Ginger, and Samuel D Stranks. Charge-carrier recombination in halide perovskites: Focus review. *Chemical reviews*, 119(20):11007–11019, 2019.

[117] Alan R Bowman, Stuart Macpherson, Anna Abfalterer, Kyle Frohna, Satyawan Nagane, and Samuel D Stranks. Extracting decay-rate ratios from photoluminescence quantum efficiency measurements in optoelectronic semiconductors. *Physical Review Applied*, 17(4):044026, 2022.

[118] Luis M Pazos-Outón, T Patrick Xiao, and Eli Yablonovitch. Fundamental efficiency limit of lead iodide perovskite solar cells. *The Journal of Physical Chemistry Letters*, 9(7):1703–1711, 2018.

[119] Michael J Trimpl, Adam D Wright, Kelly Schutt, Leonardo RV Buizza, Zhiping Wang, Michael B Johnston, Henry J Snaith, Peter Müller-Buschbaum, and Laura M Herz. Charge-carrier trapping and radiative recombination in metal halide perovskite semiconductors. *Advanced Functional Materials*, 30(42):2004312, 2020.

[120] Angelica Simbula, Riccardo Pau, Fang Liu, Luyan Wu, Stefano Lai, Alessandra Geddo-Lehmann, Alessio Filippetti, Maria A Loi, Daniela Marongiu, Francesco Quochi, et al. Direct measurement of radiative decay rates in metal halide perovskites. *Energy & Environmental Science*, 15(3):1211–1221, 2022.

[121] Dane W DeQuilettes, Susanne Koch, Sven Burke, Rajan K Paranji, Alfred J Shropshire, Mark E Ziffer, and David S Ginger. Photoluminescence lifetimes exceeding 8 μs and quantum yields exceeding 30% in hybrid perovskite thin films by ligand passivation. *ACS Energy Letters*, 1(2):438–444, 2016.

[122] Weidong Xu, Tian Du, Michael Sachs, Thomas J Macdonald, Ganghong Min, Lokeshwari Mohan, Katherine Stewart, Chieh-Ting Lin, Jiaying Wu, Richard Pacalaj, et al. Asymmetric charge carrier transfer and transport in planar lead halide perovskite solar cells. *Cell Reports Physical Science*, 3(5):100890, 2022.

[123] Johannes M Richter, Mojtaba Abdi-Jalebi, Aditya Sadhanala, Maxim Tabachnyk, Jasmine PH Rivett, Luis M Pazos-Outón, Karl C Gödel, Michael Price, Felix Deschler, and Richard H Friend. Enhancing photoluminescence yields in lead halide perovskites by photon recycling and light out-coupling. *Nature communications*, 7(1):1–8, 2016.

[124] Samuel D Stranks. Nonradiative losses in metal halide perovskites. *ACS Energy Letters*, 2(7):1515–1525, 2017.

[125] Jinhyun Kim, Robert Godin, Stoichko D Dimitrov, Tian Du, Daniel Bryant, Martyn A McLachlan, and James R Durrant. Excitation density dependent photoluminescence quenching and charge transfer efficiencies in hybrid perovskite/organic semiconductor bilayers. *Advanced Energy Materials*, 8(35):1802474, 2018.

[126] Scot Wheeler, Daniel Bryant, Joel Troughton, Thomas Kirchartz, Trystan Watson, Jenny Nelson, and James R Durrant. Transient optoelectronic analysis of the impact of material energetics and recombination kinetics on the open-circuit voltage of hybrid perovskite solar cells. *The Journal of Physical Chemistry C*, 121(25):13496–13506, 2017.

[127] Gert-Jan AH Wetzelaer, Max Scheepers, Araceli Miquel Sempere, Cristina Momblona, Jorge Ávila, and Henk J Bolink. Trap-assisted non-radiative recombination in organic–inorganic perovskite solar cells. *Advanced Materials*, 27(11):1837–1841, 2015.

[128] Samuel D Stranks, Victor M Burlakov, Tomas Leijtens, James M Ball, Alain Goriely, and Henry J Snaith. Recombination kinetics in organic-inorganic perovskites: excitons, free charge, and subgap states. *Physical Review Applied*, 2(3):034007, 2014.

[129] Guichuan Xing, Bo Wu, Xiangyang Wu, Mingjie Li, Bin Du, Qi Wei, Jia Guo, Edwin KL Yeow, Tze Chien Sum, and Wei Huang. Transcending the slow bimolecular recombination in lead-halide perovskites for electroluminescence. *Nature communications*, 8(1):1–9, 2017.

[130] Martin Stolterfoht, Pietro Caprioglio, Christian M Wolff, José A Márquez, Joleik Nordmann, Shanshan Zhang, Daniel Rothhardt, Ulrich Hörmann, Yohai Amir, Alex Redinger, et al. The impact of energy alignment and interfacial recombination on the internal and external open-circuit voltage of perovskite solar cells. *Energy & environmental science*, 12(9):2778–2788, 2019.

[131] Pietro Caprioglio, Sebastian Caicedo-Davila, Terry Chien-Jen Yang, Christian M Wolff, Francisco Pena-Camargo, Peter Fiala, Bernd Rech, Christophe Ballif, Daniel Abou-Ras, Martin Stolterfoht, et al. Nano-emitting heterostructures violate optical reciprocity and enable efficient photoluminescence in halide-segregated methylammonium-free wide bandgap perovskites. *ACS Energy Letters*, 6(2):419–428, 2021.

[132] K Xerxes Steirer, Philip Schulz, Glenn Teeter, Vladan Stevanovic, Mengjin Yang, Kai Zhu, and Joseph J Berry. Defect tolerance in methylammonium lead triiodide perovskite. *ACS Energy Letters*, 1(2):360–366, 2016.

[133] Guan-Woo Kim and Annamaria Petrozza. Defect tolerance and intolerance in metal-halide perovskites. *Advanced Energy Materials*, 10(37):2001959, 2020.

[134] Jun Kang and Lin-Wang Wang. High defect tolerance in lead halide perovskite cspbbr3. *The journal of physical chemistry letters*, 8(2):489–493, 2017.

[135] Tomas Leijtens, Giles E Eperon, Alex J Barker, Giulia Grancini, Wei Zhang, James M Ball, Ajay Ram Srimath Kandada, Henry J Snaith, and Annamaria Petrozza. Carrier trapping and recombination: the role of defect physics in enhancing the open circuit voltage of metal halide perovskite solar cells. *Energy & Environmental Science*, 9(11):3472–3481, 2016.

[136] Weidong Xu, John A McLeod, Yingguo Yang, Yimeng Wang, Zhongwei Wu, Sai Bai, Zhongcheng Yuan, Tao Song, Yusheng Wang, Junjie Si, et al. Iodomethane-mediated organometal halide perovskite with record photoluminescence lifetime. *ACS Applied Materials & Interfaces*, 8(35):23181–23189, 2016.

[137] AW Walker, S Heckelmann, C Karcher, O Höhn, C Went, M Niemeyer, AW Bett, and D Lackner. Nonradiative lifetime extraction using power-dependent relative photoluminescence of iii-v semiconductor double-heterostructures. *Journal of Applied Physics*, 119(15):155702, 2016.

[138] Wolfgang Tress. Perovskite solar cells on the way to their radiative efficiency limit–insights into a success story of high open-circuit voltage and low recombination. *Advanced Energy Materials*, 7(14):1602358, 2017.

[139] Wolfgang Tress, Mozhgan Yavari, Konrad Domanski, Pankaj Yadav, Bjoern Niesen, Juan Pablo Correa Baena, Anders Hagfeldt, and Michael Graetzel. Interpretation and evolution of open-circuit voltage, recombination, ideality factor and subgap defect states during reversible light-soaking and irreversible degradation of perovskite solar cells. *Energy & Environmental Science*, 11(1):151–165, 2018.

[140] Tian Du, Sinclair R Ratnasingham, Felix U Kosasih, Thomas J Macdonald, Lokeshwari Mohan, Adriana Augurio, Huda Ahli, Chieh-Ting Lin, Shengda Xu, Weidong Xu, et al. Aerosol assisted solvent treatment: a universal method for performance and stability enhancements in perovskite solar cells. *Advanced Energy Materials*, 11(33):2101420, 2021.

[141] Chieh-Ting Lin, Weidong Xu, Thomas J Macdonald, Jonathan Ngiam, Ju-Hyeon Kim, Tian Du, Shengda Xu, Pabitra Shakya Tuladhar, Hongkyu Kang, Kwanghee Lee, et al. Correlating the active layer structure and composition with the device performance and lifetime of amino-acid-modified perovskite solar cells. *ACS applied materials & interfaces*, 13(36):43505–43515, 2021.

[142] Chieh-Ting Lin, Jinho Lee, Jinhyun Kim, Thomas J Macdonald, Jonathan Ngiam, Bob Xu, Matyas Daboczi, Weidong Xu, Sebastian Pont, Byoungwook Park, et al. Origin of open-circuit voltage enhancements in planar perovskite solar cells induced by addition of bulky organic cations. *Advanced Functional Materials*, 30(7):1906763, 2020.

[143] Nam Joong Jeon, Jun Hong Noh, Woon Seok Yang, Young Chan Kim, Seungchan Ryu, Jangwon Seo, and Sang Il Seok. Compositional engineering of perovskite materials for high-performance solar cells. *Nature*, 517(7535):476–480, 2015.

[144] Dongqin Bi, Chenyi Yi, Jingshan Luo, Jean-David Décoppet, Fei Zhang, Shaik Mohammed Zakeeruddin, Xiong Li, Anders Hagfeldt, and Michael Grätzel. Polymer-templated nucleation and crystal growth of perovskite films for solar cells with efficiency greater than 21%. *Nature Energy*, 1(10):1–5, 2016.

[145] Tejas S Sherkar, Cristina Momblona, Lidon Gil-Escrig, Jorge Avila, Michele Sessolo, Henk J Bolink, and L Jan Anton Koster. Recombination in perovskite solar cells: significance of grain boundaries, interface traps, and defect ions. *ACS energy letters*, 2(5):1214–1222, 2017.

[146] Ye Yang, Yong Yan, Mengjin Yang, Sukgeun Choi, Kai Zhu, Joseph M Luther, and Matthew C Beard. Low surface recombination velocity in solution-grown ch3nh3pbbr3 perovskite single crystal. *Nature communications*, 6(1):1–6, 2015.

[147] Ian L Braly, Dane W DeQuilettes, Luis M Pazos-Outón, Sven Burke, Mark E Ziffer, David S Ginger, and Hugh W Hillhouse. Hybrid perovskite films approaching the radiative limit with over 90% photoluminescence quantum efficiency. *Nature Photonics*, 12(6):355–361, 2018.

[148] Mojtaba Abdi-Jalebi, Zahra Andaji-Garmaroudi, Stefania Cacovich, Camille Stavrakas, Bertrand Philippe, Johannes M Richter, Mejd Alsari, Edward P Booker, Eline M Hutter, Andrew J Pearson, et al. Maximizing and stabilizing luminescence from halide perovskites with potassium passivation. *Nature*, 555(7697):497–501, 2018.

[149] Martin Stolterfoht, Christian M Wolff, José A Márquez, Shanshan Zhang, Charles J Hages, Daniel Rothhardt, Steve Albrecht, Paul L Burn, Paul Meredith, Thomas Unold, et al. Visualization and suppression of interfacial recombination for high-efficiency large-area pin perovskite solar cells. *Nature Energy*, 3(10):847–854, 2018.

[150] Pietro Caprioglio, Martin Stolterfoht, Christian M Wolff, Thomas Unold, Bernd Rech, Steve Albrecht, and Dieter Neher. On the relation between the open-circuit voltage and quasi-fermi level splitting in efficient perovskite solar cells. *Advanced Energy Materials*, 9(33):1901631, 2019.

[151] Martin Stolterfoht, Max Grischek, Pietro Caprioglio, Christian M Wolff, Emilio Gutierrez-Partida, Francisco Peña-Camargo, Daniel Rothhardt, Shanshan Zhang, Meysam Raoufi, Jakob Wolansky, et al. How to quantify the efficiency potential of neat perovskite films: Perovskite semiconductors with an implied efficiency exceeding 28%. *Advanced Materials*, 32(17):2000080, 2020.

[152] Christian M Wolff, Pietro Caprioglio, Martin Stolterfoht, and Dieter Neher. Nonradiative recombination in perovskite solar cells: the role of interfaces. *Advanced Materials*, 31(52):1902762, 2019.

[153] Dong Shi, Valerio Adinolfi, Riccardo Comin, Mingjian Yuan, Erkki Alarousu, Andrei Buin, Yin Chen, Sjoerd Hoogland, Alexander Rothenberger, Khabiboulakh Katsiev, et al. Low trap-state density and long carrier diffusion in organolead trihalide perovskite single crystals. *Science*, 347(6221):519–522, 2015.

[154] Qingfeng Dong, Yanjun Fang, Yuchuan Shao, Padhraic Mulligan, Jie Qiu, Lei Cao, and Jinsong Huang. Electron-hole diffusion lengths¿ 175 μm in solution-grown ch3nh3pbi3 single crystals. *Science*, 347(6225):967–970, 2015.

[155] Yu-Che Hsiao, Ting Wu, Mingxing Li, Qing Liu, Wei Qin, and Bin Hu. Fundamental physics behind high-efficiency organo-metal halide perovskite solar cells. *Journal of Materials Chemistry A*, 3(30):15372–15385, 2015.

[156] David A Valverde-Chávez, Carlito S Ponseca, Constantinos C Stoumpos, Arkady Yartsev, Mercouri G Kanatzidis, Villy Sundström, and David G Cooke. Intrinsic femtosecond charge generation dynamics in single crystal ch 3 nh 3 pbi 3. *Energy & Environmental Science*, 8(12):3700–3707, 2015.

[157] Rebecca L Milot, Giles E Eperon, Henry J Snaith, Michael B Johnston, and Laura M Herz. Temperature-dependent charge-carrier dynamics in ch3nh3pbi3 perovskite thin films. *Advanced Functional Materials*, 25(39):6218–6227, 2015.

[158] Dong Hoe Kim, Jaehong Park, Zhen Li, Mengjin Yang, Ji-Sang Park, Ik Jae Park, Jin Young Kim, Joseph J Berry, Garry Rumbles, and Kai Zhu. 300% enhancement of carrier mobility in uniaxial-oriented perovskite films formed by topotactic-oriented attachment. *Advanced Materials*, 29(23):1606831, 2017.

[159] GW Ludwig and RL Watters. Drift and conductivity mobility in silicon. *Physical Review*, 101(6):1699, 1956.

[160] SM Sze and JC Irvin. Resistivity, mobility and impurity levels in gaas, ge, and si at 300 k. *Solid-State Electronics*, 11(6):599–602, 1968.

[161] Eline M Hutter, Giles E Eperon, Samuel D Stranks, and Tom J Savenije. Charge carriers in planar and meso-structured organic–inorganic perovskites: mobilities, lifetimes, and concentrations of trap states. *The journal of physical chemistry letters*, 6(15):3082–3090, 2015.

[162] Obadiah G Reid, Mengjin Yang, Nikos Kopidakis, Kai Zhu, and Garry Rumbles. Grain-size-limited mobility in methylammonium lead iodide perovskite thin films. *ACS Energy Letters*, 1(3):561–565, 2016.

[163] Guichuan Xing, Nripan Mathews, Shuangyong Sun, Swee Sien Lim, Yeng Ming Lam, Michael Grätzel, Subodh Mhaisalkar, and Tze Chien Sum. Long-range balanced electron-and hole-transport lengths in organic-inorganic ch3nh3pbi3. *Science*, 342(6156):344–347, 2013.

[164] Samuel D Stranks, Giles E Eperon, Giulia Grancini, Christopher Menelaou, Marcelo JP Alcocer, Tomas Leijtens, Laura M Herz, Annamaria Petrozza, and Henry J Snaith. Electron-hole diffusion lengths exceeding 1 micrometer in an organometal trihalide perovskite absorber. *Science*, 342(6156):341–344, 2013.

[165] Yiming Li, Yusheng Li, Jiangjian Shi, Huiyin Zhang, Jionghua Wu, Dongmei Li, Yanhong Luo, Huijue Wu, and Qingbo Meng. High quality perovskite crystals for efficient film photodetectors induced by hydrolytic insulating oxide substrates. *Advanced Functional Materials*, 28(10):1705220, 2018.

[166] Dong Zhong, Bing Cai, Xiuli Wang, Zhou Yang, Yedi Xing, Shu Miao, Wen-Hua Zhang, and Can Li. Synthesis of oriented tio2 nanocones with fast charge transfer for perovskite solar cells. *Nano Energy*, 11:409–418, 2015.

[167] Arianna Marchioro, Joël Teuscher, Dennis Friedrich, Marinus Kunst, Roel Van De Krol, Thomas Moehl, Michael Grätzel, and Jacques-E Moser. Unravelling the mechanism of photoinduced charge transfer processes in lead iodide perovskite solar cells. *Nature photonics*, 8(3):250–255, 2014.

[168] Lili Wang, Christopher McCleese, Anton Kovalsky, Yixin Zhao, and Clemens Burda. Femtosecond time-resolved transient absorption spectroscopy of ch3nh3pbi3 perovskite films: evidence for passivation effect of pbi2. *Journal of the American Chemical Society*, 136(35):12205–12208, 2014.

[169] Katarzyna Pydzińska, Jerzy Karolczak, Ivet Kosta, Ramon Tena-Zaera, Anna Todinova, Jesus Idígoras, Juan A Anta, and Marcin Ziółek. Determination of interfacial charge-transfer rate constants in perovskite solar cells. *ChemSusChem*, 9(13):1647–1659, 2016.

[170] Robert JE Westbrook, Thomas J Macdonald, Weidong Xu, Luis Lanzetta, Jose M Marin-Beloqui, Tracey M Clarke, and Saif A Haque. Lewis base passivation mediates charge transfer at perovskite heterojunctions. *Journal of the American Chemical Society*, 143(31):12230–12243, 2021.

[171] Qing Shen, Yuhei Ogomi, Jin Chang, Syota Tsukamoto, Kenji Kukihara, Takuya Oshima, Naoya Osada, Kenji Yoshino, Kenji Katayama, Taro Toyoda, et al. Charge transfer and recombination at the metal oxide/ch 3 nh 3 pbcli 2/spiro-ometad interfaces: uncovering the detailed mechanism behind high efficiency solar cells. *Physical Chemistry Chemical Physics*, 16(37):19984–19992, 2014.

[172] Jan C Brauer, Yong Hui Lee, Mohammad Khaja Nazeeruddin, and Natalie Banerji. Charge transfer dynamics from organometal halide perovskite to polymeric hole transport materials in hybrid solar cells. *The Journal of Physical Chemistry Letters*, 6(18):3675–3681, 2015.

[173] Dong Hun Sin, Hyomin Ko, Sae Byeok Jo, Min Kim, Geun Yeol Bae, and Kilwon Cho. Decoupling charge transfer and transport at polymeric hole transport layer in perovskite solar cells. *ACS applied materials & interfaces*, 8(10):6546–6553, 2016.

[174] Eline M Hutter, Jan-Jaap Hofman, Michiel L Petrus, Michiel Moes, Ruben D Abellón, Pablo Docampo, and Tom J Savenije. Charge transfer from methylammonium lead iodide perovskite to organic transport materials: Efficiencies, transfer rates, and interfacial recombination. *Advanced Energy Materials*, 7(13):1602349, 2017.

[175] Jon M Azpiroz, Edoardo Mosconi, Juan Bisquert, and Filippo De Angelis. Defect migration in methylammonium lead iodide and its role in perovskite solar cell operation. *Energy & Environmental Science*, 8(7):2118–2127, 2015.

[176] Yongbo Yuan and Jinsong Huang. Ion migration in organometal trihalide perovskite and its impact on photovoltaic efficiency and stability. *Accounts of chemical research*, 49(2):286–293, 2016.

[177] Cheng Li, Steffen Tscheuschner, Fabian Paulus, Paul E Hopkinson, Johannes Kießling, Anna Köhler, Yana Vaynzof, and Sven Huettner. Iodine migration and its effect on hysteresis in perovskite solar cells. *Advanced Materials*, 28(12):2446–2454, 2016.

[178] Moritz H Futscher, Ju Min Lee, Lucie McGovern, Loreta A Muscarella, Tianyi Wang, Muhammad Irfan Haider, Azhar Fakharuddin, Lukas Schmidt-Mende, and Bruno Ehrler. Quantification of ion migration in ch 3 nh 3 pbi 3 perovskite solar cells by transient capacitance measurements. *Materials Horizons*, 6(7):1497–1503, 2019.

[179] Christopher Eames, Jarvist M Frost, Piers RF Barnes, Brian C O'regan, Aron Walsh, and M Saiful Islam. Ionic transport in hybrid lead iodide perovskite solar cells. *Nature communications*, 6(1):1–8, 2015.

[180] Wolfgang Tress. Metal halide perovskites as mixed electronic–ionic conductors: Challenges and opportunities from hysteresis to memristivity. *The journal of physical chemistry letters*, 8(13):3106–3114, 2017.

[181] Wan-Jian Yin, Tingting Shi, and Yanfa Yan. Unusual defect physics in ch3nh3pbi3 perovskite solar cell absorber. *Applied Physics Letters*, 104(6):063903, 2014.

[182] Tingting Shi, Hai-Shan Zhang, Weiwei Meng, Qiang Teng, Meiyue Liu, Xiaobao Yang, Yanfa Yan, Hin-Lap Yip, and Yu-Jun Zhao. Effects of organic cations on the defect physics of tin halide perovskites. *Journal of Materials Chemistry A*, 5(29):15124–15129, 2017.

[183] Weike Zhu, Shurong Wang, Xin Zhang, Aili Wang, Cheng Wu, and Feng Hao. Ion migration in organic–inorganic hybrid perovskite solar cells: Current understanding and perspectives. *Small*, 18(15):2105783, 2022.

[184] Joshua J Choi, Xiaohao Yang, Zachariah M Norman, Simon JL Billinge, and Jonathan S Owen. Structure of methylammonium lead iodide within mesoporous titanium dioxide: active material in high-performance perovskite solar cells. *Nano letters*, 14(1):127–133, 2014.

[185] Qingfeng Dong, Jingfeng Song, Yanjun Fang, Yuchuan Shao, Stephen Ducharme, and Jinsong Huang. Lateral-structure single-crystal hybrid perovskite solar cells via piezoelectric poling. *Advanced Materials*, 28(14):2816–2821, 2016.

[186] Enbing Bi, Zhaoning Song, Chongwen Li, Zhifang Wu, and Yanfa Yan. Mitigating ion migration in perovskite solar cells. *Trends in Chemistry*, 3(7):575–588, 2021.

[187] Yuchuan Shao, Yanjun Fang, Tao Li, Qi Wang, Qingfeng Dong, Yehao Deng, Yongbo Yuan, Haotong Wei, Meiyu Wang, Alexei Gruverman, et al. Grain boundary dominated ion migration in polycrystalline organic–inorganic halide perovskite films. *Energy & Environmental Science*, 9(5):1752–1759, 2016.

[188] Jae S Yun, Jan Seidel, Jincheol Kim, Arman Mahboubi Soufiani, Shujuan Huang, Jonathan Lau, Nam Joong Jeon, Sang Il Seok, Martin A Green, and Anita Ho-Baillie. Critical role of grain boundaries for ion migration in formamidinium and methylammonium lead halide perovskite solar cells. *Advanced Energy Materials*, 6(13):1600330, 2016.

[189] Ligang Wang, Huanping Zhou, Junnan Hu, Bolong Huang, Mingzi Sun, Bowei Dong, Guanghaojie Zheng, Yuan Huang, Yihua Chen, Liang Li, et al. A eu3+-eu2+ ion redox shuttle imparts operational durability to pb-i perovskite solar cells. *Science*, 363(6424):265–270, 2019.

[190] Youzhen Li, Xuemei Xu, Congcong Wang, Ben Ecker, Junliang Yang, Jinsong Huang, and Yongli Gao. Light-induced degradation of ch3nh3pbi3 hybrid perovskite thin film. *The Journal of Physical Chemistry C*, 121(7):3904–3910, 2017.

[191] Bertrand Philippe, T Jesper Jacobsson, Juan-Pablo Correa-Baena, Naresh K Jena, Amitava Banerjee, Sudip Chakraborty, Ute B Cappel, Rajeev Ahuja, Anders Hagfeldt, Michael Odelius, et al. Valence level character in a mixed perovskite material and determination of the valence band maximum from photoelectron spectroscopy: variation with photon energy. *The Journal of Physical Chemistry C*, 121(48):26655–26666, 2017.

[192] Caleb C Boyd, Rongrong Cheacharoen, Tomas Leijtens, and Michael D McGehee. Understanding degradation mechanisms and improving stability of perovskite photovoltaics. *Chemical reviews*, 119(5):3418–3451, 2018.

[193] Xiaodong Li, Sheng Fu, Shiyu Liu, Yulei Wu, Wenxiao Zhang, Weijie Song, and Junfeng Fang. Suppressing the ions-induced degradation for operationally stable perovskite solar cells. *Nano Energy*, 64:103962, 2019.

[194] Yanbo Wang, Tianhao Wu, Julien Barbaud, Weiyu Kong, Danyu Cui, Han Chen, Xudong Yang, and Liyuan Han. Stabilizing heterostructures of soft perovskite semiconductors. *Science*, 365(6454):687–691, 2019.

[195] Shenghao Wang, Yan Jiang, Emilio J Juarez-Perez, Luis K Ono, and Yabing Qi. Accelerated degradation of methylammonium lead iodide perovskites induced by exposure to iodine vapour. *Nature Energy*, 2(1):1–8, 2016.

[196] Dongchen Lan. The physics of ion migration in perovskite solar cells: Insights into hysteresis, device performance, and characterization. *Progress in Photovoltaics: Research and Applications*, 28(6):533–537, 2020.

[197] Michael C Brennan, Anthony Ruth, Prashant V Kamat, and Masaru Kuno. Photoinduced anion segregation in mixed halide perovskites. *Trends in Chemistry*, 2(4):282–301, 2020.

[198] Seog Joon Yoon, Sergiu Draguta, Joseph S Manser, Onise Sharia, William F Schneider, Masaru Kuno, and Prashant V Kamat. Tracking iodide and bromide ion segregation in mixed halide lead perovskites during photoirradiation. *ACS Energy Letters*, 1(1):290–296, 2016.

[199] Zhaoning Song, Cong Chen, Chongwen Li, Rasha A Awni, Dewei Zhao, and Yanfa Yan. Wide-bandgap, low-bandgap, and tandem perovskite solar cells. *Semiconductor Science and Technology*, 34(9):093001, 2019.

[200] Dewei Zhao, Yue Yu, Changlei Wang, Weiqiang Liao, Niraj Shrestha, Corey R Grice, Alexander J Cimaroli, Lei Guan, Randy J Ellingson, Kai Zhu, et al. Low-bandgap mixed tin–lead iodide perovskite absorbers with long carrier lifetimes for all-perovskite tandem solar cells. *Nature Energy*, 2(4):1–7, 2017.

[201] David P McMeekin, Golnaz Sadoughi, Waqaas Rehman, Giles E Eperon, Michael Saliba, Maximilian T Hörantner, Amir Haghighirad, Nobuya Sakai, Lars Korte, Bernd Rech, et al. A mixed-cation lead mixed-halide perovskite absorber for tandem solar cells. *Science*, 351(6269):151–155, 2016.

[202] Connor G Bischak, Craig L Hetherington, Hao Wu, Shaul Aloni, D Frank Ogletree, David T Limmer, and Naomi S Ginsberg. Origin of reversible photoinduced phase separation in hybrid perovskites. *Nano letters*, 17(2):1028–1033, 2017.

[203] Prashant V Kamat and Masaru Kuno. Halide ion migration in perovskite nanocrystals and nanostructures. *Accounts of Chemical Research*, 54(3):520–531, 2021.

[204] Alexander J Knight and Laura M Herz. Preventing phase segregation in mixed-halide perovskites: a perspective. *Energy & Environmental Science*, 13(7):2024–2046, 2020.

[205] Sergiu Draguta, Onise Sharia, Seog Joon Yoon, Michael C Brennan, Yurii V Morozov, Joseph S Manser, Prashant V Kamat, William F Schneider, and Masaru Kuno. Rationalizing the light-induced phase separation of mixed halide organic–inorganic perovskites. *Nature communications*, 8(1):1–8, 2017.

[206] Juan-Pablo Correa-Baena, Yanqi Luo, Thomas M Brenner, Jordan Snaider, Shijing Sun, Xueying Li, Mallory A Jensen, Noor Titan Putri Hartono, Lea Nienhaus, Sarah Wieghold, et al. Homogenized halides and alkali cation segregation in alloyed organic-inorganic perovskites. *Science*, 363(6427):627–631, 2019.

[207] Nengxu Li, Yanqi Luo, Zehua Chen, Xiuxiu Niu, Xiao Zhang, Jiuzhou Lu, Rishi Kumar, Junke Jiang, Huifen Liu, Xiao Guo, et al. Microscopic degradation in formamidinium-cesium lead iodide perovskite solar cells under operational stressors. *Joule*, 4(8):1743–1758, 2020.

[208] Philip Calado, Andrew M Telford, Daniel Bryant, Xiaoe Li, Jenny Nelson, Brian C O'Regan, and Piers RF Barnes. Evidence for ion migration in hybrid perovskite solar cells with minimal hysteresis. *Nature communications*, 7(1):1–10, 2016.

[209] Rebecca A Belisle, William H Nguyen, Andrea R Bowring, Philip Calado, Xiaoe Li, Stuart JC Irvine, Michael D McGehee, Piers RF Barnes, and Brian C O'Regan. Interpretation of inverted photocurrent transients in organic lead halide perovskite solar cells: proof of the field screening by mobile ions and determination of the space charge layer widths. *Energy & Environmental Science*, 10(1):192–204, 2017.

[210] Biao Li, Minshen Lin, Chenxia Kan, Pengjie Hang, Yuxin Yao, Zechen Hu, Ying Wang, Yiqiang Zhang, Wenxing Zhong, Deren Yang, et al. Revealing the correlation of light soaking effect with ion migration in perovskite solar cells. *Solar RRL*, page 2200050, 2022.

[211] Brian C O'Regan, Piers RF Barnes, Xiaoe Li, Chunhung Law, Emilio Palomares, and Jose M Marin-Beloqui. Optoelectronic studies of methylammonium lead iodide perovskite solar cells with mesoporous tio2: separation of electronic and chemical charge storage, understanding two recombination lifetimes, and the evolution of band offsets during j–v hysteresis. *Journal of the American Chemical Society*, 137(15):5087–5099, 2015.

[212] Adam Pockett, Giles E Eperon, Nobuya Sakai, Henry J Snaith, Laurence M Peter, and Petra J Cameron. Microseconds, milliseconds and seconds: deconvoluting the dynamic behaviour of planar perovskite solar cells. *Physical Chemistry Chemical Physics*, 19(8):5959–5970, 2017.

[213] Henry J Snaith, Antonio Abate, James M Ball, Giles E Eperon, Tomas Leijtens, Nakita K Noel, Samuel D Stranks, Jacob Tse-Wei Wang, Konrad Wojciechowski, and Wei Zhang. Anomalous hysteresis in perovskite solar cells. *The journal of physical chemistry letters*, 5(9):1511–1515, 2014.

[214] Isaac Zarazua, Juan Bisquert, and Germà Garcia-Belmonte. Light-induced space-charge accumulation zone as photovoltaic mechanism in perovskite solar cells. *The journal of physical chemistry letters*, 7(3):525–528, 2016.

[215] Tae-Youl Yang, Giuliano Gregori, Norman Pellet, Michael Grätzel, and Joachim Maier. The significance of ion conduction in a hybrid organic–inorganic lead-iodide-based perovskite photosensitizer. *Angewandte Chemie*, 127(27):8016–8021, 2015.

[216] Alessandro Senocrate, Igor Moudrakovski, Gee Yeong Kim, Tae-Youl Yang, Giuliano Gregori, Michael Grätzel, and Joachim Maier. The nature of ion conduction in methylammonium lead iodide: a multimethod approach. *Angewandte Chemie International Edition*, 56(27):7755–7759, 2017.

[217] Davide Moia and Joachim Maier. Ion transport, defect chemistry, and the device physics of hybrid perovskite solar cells. *ACS Energy Letters*, 6(4):1566–1576, 2021.

[218] Davide Moia, Ilario Gelmetti, Philip Calado, Yinghong Hu, Xiaoe Li, Pablo Docampo, John de Mello, Joachim Maier, Jenny Nelson, and Piers RF Barnes. The dynamics of internal electric field screening in hybrid perovskite solar cells probed using electroabsorption. *arXiv preprint arXiv:2201.02175*, 2022.

[219] Davide Moia, Ilario Gelmetti, Phil Calado, William Fisher, Michael Stringer, Onkar Game, Yinghong Hu, Pablo Docampo, David Lidzey, Emilio Palomares, et al. Ionic-to-electronic current amplification in hybrid perovskite solar cells: ionically gated transistor-interface circuit model explains hysteresis and impedance of mixed conducting devices. *Energy & Environmental Science*, 12(4):1296–1308, 2019.

[220] Xiaoning Zhao, Haiyang Xu, Zhongqiang Wang, Ya Lin, and Yichun Liu. Memristors with organic-inorganic halide perovskites. *InfoMat*, 1(2):183–210, 2019.

[221] Tian Du, Weidong Xu, Matyas Daboczi, Jinhyun Kim, Shengda Xu, Chieh-Ting Lin, Hongkyu Kang, Kwanghee Lee, Martin J Heeney, Ji-Seon Kim, et al. p-doping of organic hole transport layers in p–i–n perovskite solar cells: correlating open-circuit voltage and photoluminescence quenching. *Journal of Materials Chemistry A*, 7(32):18971–18979, 2019.

[222] Tian Du, Weidong Xu, Shengda Xu, Sinclair R Ratnasingham, Chieh-Ting Lin, Jinhyun Kim, Joe Briscoe, Martyn A McLachlan, and James R Durrant. Light-intensity and thickness dependent efficiency of planar perovskite solar cells: charge recombination versus extraction. *Journal of Materials Chemistry C*, 8(36):12648–12655, 2020.

[223] Jiaying Wu, Hyojung Cha, Tian Du, Yifan Dong, Weidong Xu, Chieh-Ting Lin, and James R Durrant. A comparison of charge carrier dynamics in organic and perovskite solar cells. *Advanced Materials*, 34(2):2101833, 2022.

[224] Albertus A Sutanto, Pietro Caprioglio, Nikita Drigo, Yvonne J Hofstetter, Ines Garcia-Benito, Valentin IE Queloz, Dieter Neher, Mohammad Khaja Nazeeruddin, Martin Stolterfoht, Yana Vaynzof, et al. 2d/3d perovskite engineering eliminates interfacial recombination losses in hybrid perovskite solar cells. *Chem*, 7(7):1903–1916, 2021.

[225] Jiangzhao Chen and Nam-Gyu Park. Causes and solutions of recombination in perovskite solar cells. *Advanced Materials*, 31(47):1803019, 2019.

[226] Deying Luo, Rui Su, Wei Zhang, Qihuang Gong, and Rui Zhu. Minimizing non-radiative recombination losses in perovskite solar cells. *Nature Reviews Materials*, 5(1):44–60, 2020.

[227] Laura M Herz. Charge-carrier mobilities in metal halide perovskites: fundamental mechanisms and limits. *ACS Energy Letters*, 2(7):1539–1548, 2017.

[228] James C Blakesley, Fernando A Castro, William Kylberg, George FA Dibb, Caroline Arantes, Rogério Valaski, Marco Cremona, Jong Soo Kim, and Ji-Seon Kim. Towards reliable charge-mobility benchmark measurements for organic semiconductors. *Organic Electronics*, 15(6):1263–1272, 2014.

[229] Robert DJ Oliver, Pietro Caprioglio, Francisco Peña-Camargo, Leonardo RV Buizza, Fengshuo Zu, Alexandra J Ramadan, Silvia G Motti, Suhas Mahesh, Melissa M McCarthy, Jonathan H Warby, et al. Understanding and suppressing non-radiative losses in methylammonium-free wide-bandgap perovskite solar cells. *Energy & Environmental Science*, 15(2):714–726, 2022.

[230] Philip Calado, Ilario Gelmetti, Benjamin Hilton, Mohammed Azzouzi, Jenny Nelson, and Piers RF Barnes. Driftfusion: an open source code for simulating ordered semiconductor devices with mixed ionic-electronic conducting materials in one dimension. *Journal of Computational Electronics*, pages 1–32, 2022.

[231] Shibing Leng, Luyao Wang, Xin Wang, Zhanfei Zhang, Jianghu Liang, Yiting Zheng, Jinkun Jiang, Zhiang Zhang, Xiao Liu, Yuankun Qiu, et al. Bottom interfacial engineering for methylammonium-free regular-structure planar perovskite solar cells over 21%. *Solar RRL*, 5(8):2100285, 2021.

[232] Jongchul Lim, Manuel Kober-Czerny, Yen-Hung Lin, James M Ball, Nobuya Sakai, Elisabeth A Duijnstee, Min Ji Hong, John G Labram, Bernard Wenger, and Henry J Snaith. Long-range charge carrier mobility in metal halide perovskite thin-films and single crystals via transient photo-conductivity. *Nature communications*, 13(1):1–9, 2022.

[233] Jarla Thiesbrummel, Vincent M Le Corre, Francisco Peña-Camargo, Lorena Perdigón-Toro, Felix Lang, Fengjiu Yang, Max Grischek, Emilio Gutierrez-Partida, Jonathan Warby, Michael D Farrar, et al. Universal current losses in perovskite solar cells due to mobile ions. *Advanced Energy Materials*, 11(34):2101447, 2021.

[234] Tiarnan AS Doherty, Andrew J Winchester, Stuart Macpherson, Duncan N Johnstone, Vivek Pareek, Elizabeth M Tennyson, Sofiia Kosar, Felix U Kosasih, Miguel Anaya, Mojtaba Abdi-Jalebi, et al. Performance-limiting nanoscale trap clusters at grain junctions in halide perovskites. *Nature*, 580(7803):360–366, 2020.

[235] Luca Bertoluzzi, Caleb C Boyd, Nicholas Rolston, Jixian Xu, Rohit Prasanna, Brian C O'Regan, and Michael D McGehee. Mobile ion concentration measurement and open-access band diagram simulation platform for halide perovskite solar cells. *Joule*, 4(1):109–127, 2020.

[236] Florine M Rombach, Saif A Haque, and Thomas J Macdonald. Lessons learned from spiro-ometad and ptaa in perovskite solar cells. *Energy & Environmental Science*, 2021.

[237] Qian Zhao, Runsheng Wu, Zheling Zhang, Jian Xiong, Zhen He, Baojin Fan, Zhongjun Dai, Bingchu Yang, Xiaogang Xue, Ping Cai, et al. Achieving efficient inverted planar perovskite solar cells with nondoped ptaa as a hole transport layer. *Organic Electronics*, 71:106–112, 2019.

[238] Michael Sendner, Jens Trollmann, and Annemarie Pucci. Dielectric function and degradation process of poly (triarylamine)(ptaa). *Organic Electronics*, 15(11):2959–2963, 2014.

[239] Jiupeng Cao and Feng Yan. Recent progress in tin-based perovskite solar cells. *Energy & Environmental Science*, 14(3):1286–1325, 2021.

[240] Michael P Hughes, Katie D Rosenthal, Niva A Ran, Martin Seifrid, Guillermo C Bazan, and Thuc-Quyen Nguyen. Determining the dielectric constants of organic photovoltaic materials using impedance spectroscopy. *Advanced Functional Materials*, 28(32):1801542, 2018.

[241] Heinz Bässler, Daniel Kroh, Franz Schauer, Vojtech Nádaždy, and Anna Köhler. Mapping the density of states distribution of organic semiconductors by employing energy resolved–electrochemical impedance spectroscopy. *Advanced Functional Materials*, 31(9):2007738, 2021.

[242] Thomas J Macdonald, Adam J Clancy, Weidong Xu, Zhongyao Jiang, Chieh-Ting Lin, Lokeshwari Mohan, Tian Du, Daniel D Tune, Luis Lanzetta, Ganghong Min, et al. Phosphorene nanoribbon-augmented optoelectronics for enhanced hole extraction. *Journal of the American Chemical Society*, 143(51):21549–21559, 2021.

[243] Sai Bai, Peimei Da, Cheng Li, Zhiping Wang, Zhongcheng Yuan, Fan Fu, Maciej Kawecki, Xianjie Liu, Nobuya Sakai, Jacob Tse-Wei Wang, et al. Planar perovskite solar cells with long-term stability using ionic liquid additives. *Nature*, 571(7764):245–250, 2019.

[244] Wei EI Sha, Xingang Ren, Luzhou Chen, and Wallace CH Choy. The efficiency limit of ch3nh3pbi3 perovskite solar cells. *Applied Physics Letters*, 106(22):221104, 2015.

[245] William Shockley and Hans J Queisser. Detailed balance limit of efficiency of p-n junction solar cells. *Journal of applied physics*, 32(3):510–519, 1961.

[246] Jinsong Huang, Yongbo Yuan, Yuchuan Shao, and Yanfa Yan. Understanding the physical properties of hybrid perovskites for photovoltaic applications. *Nature Reviews Materials*, 2(7):1–19, 2017.

[247] Qianqian Lin, Ardalan Armin, Ravi Chandra Raju Nagiri, Paul L Burn, and Paul Meredith. Electro-optics of perovskite solar cells. *Nature Photonics*, 9(2):106–112, 2015.

[248] Juan-Pablo Correa-Baena, Miguel Anaya, Gabriel Lozano, Wolfgang Tress, Konrad Domanski, Michael Saliba, Taisuke Matsui, Tor Jesper Jacobsson, Mauricio E Calvo, Antonio Abate, et al. Unbroken perovskite: interplay of morphology, electro-optical properties, and ionic movement. *Advanced Materials*, 28(25):5031–5037, 2016.

[249] David Kiermasch, Lidón Gil-Escrig, Andreas Baumann, Henk J Bolink, Vladimir Dyakonov, and Kristofer Tvingstedt. Unravelling steady-state bulk recombination dynamics in thick efficient vacuum-deposited perovskite solar cells by transient methods. *Journal of Materials Chemistry A*, 7(24):14712–14722, 2019.

[250] Thomas Kirchartz, Tiziano Agostinelli, Mariano Campoy-Quiles, Wei Gong, and Jenny Nelson. Understanding the thickness-dependent performance of organic bulk heterojunction solar cells: the influence of mobility, lifetime, and space charge. *The journal of physical chemistry letters*, 3(23):3470–3475, 2012.

[251] Davide Bartesaghi, Irene Del Carmen Pérez, Juliane Kniepert, Steffen Roland, Mathieu Turbiez, Dieter Neher, and L Koster. Competition between recombination and extraction of free charges determines the fill factor of organic solar cells. *Nature communications*, 6(1):1–10, 2015.

[252] Erdem Cuce, Pinar Mert Cuce, and Tulin Bali. An experimental analysis of illumination intensity and temperature dependency of photovoltaic cell parameters. *Applied Energy*, 111:374–382, 2013.

[253] Feng Liu, Jun Zhu, Junfeng Wei, Yi Li, Mei Lv, Shangfeng Yang, Bing Zhang, Jianxi Yao, and Songyuan Dai. Numerical simulation: toward the design of high-efficiency planar perovskite solar cells. *Applied Physics Letters*, 104(25):253508, 2014.

[254] James M Ball, Samuel D Stranks, Maximilian T Hörantner, Sven Hüttner, Wei Zhang, Edward JW Crossland, Ivan Ramirez, Moritz Riede, Michael B Johnston, Richard H Friend, et al. Optical properties and limiting photocurrent of thin-film perovskite solar cells. *Energy & Environmental Science*, 8(2):602–609, 2015.

[255] Jiehuan Chen, Lijian Zuo, Yingzhu Zhang, Xiaomei Lian, Weifei Fu, Jielin Yan, Jun Li, Gang Wu, Chang-Zhi Li, and Hongzheng Chen. High-performance thickness insensitive perovskite solar cells with enhanced moisture stability. *Advanced Energy Materials*, 8(23):1800438, 2018.

[256] Guichuan Zhang, Kai Zhang, Qingwu Yin, Xiao-Fang Jiang, Zaiyu Wang, Jingming Xin, Wei Ma, He Yan, Fei Huang, and Yong Cao. High-performance ternary organic solar cell enabled by a thick active layer containing a liquid crystalline small molecule donor. *Journal of the American Chemical Society*, 139(6):2387–2395, 2017.

[257] Francesca De Rossi, Jenny A Baker, David Beynon, Katherine EA Hooper, Simone MP Meroni, Daniel Williams, Zhengfei Wei, Amrita Yasin, Cecile Charbonneau, Eifion H Jewell, et al. All printable perovskite solar modules with 198 cm2 active area and over 6% efficiency. *Advanced Materials Technologies*, 3(11):1800156, 2018.

[258] Qianqian Lin, Zhiping Wang, Henry J Snaith, Michael B Johnston, and Laura M Herz. Hybrid perovskites: prospects for concentrator solar cells. *Advanced Science*, 5(4):1700792, 2018.

[259] Yong Li, Weidong Xu, Nursultan Mussakhanuly, Yongyoon Cho, Jueming Bing, Jianghui Zheng, Shi Tang, Yang Liu, Guozheng Shi, Zeke Liu, et al. Homologous bromides treatment for improving the open-circuit voltage of perovskite solar cells. *Advanced Materials*, 34(6):2106280, 2022.

[260] Martin Stolterfoht, Vincent M Le Corre, Markus Feuerstein, Pietro Caprioglio, L Jan Anton Koster, and Dieter Neher. Voltage-dependent photoluminescence and how it correlates with the fill factor and open-circuit voltage in perovskite solar cells. *ACS Energy Letters*, 4(12):2887–2892, 2019.

[261] Kristofer Tvingstedt, Olga Malinkiewicz, Andreas Baumann, Carsten Deibel, Henry J Snaith, Vladimir Dyakonov, and Henk J Bolink. Radiative efficiency of lead iodide based perovskite solar cells. *Scientific reports*, 4(1):1–7, 2014.

[262] Zhifa Liu, Lisa Kruckemeier, Benedikt Krogmeier, Benjamin Klingebiel, José A Márquez, Sergiu Levcenko, Senol Oz, Sanjay Mathur, Uwe Rau, Thomas Unold, et al. Open-circuit voltages exceeding 1.26 v in planar methylammonium lead iodide perovskite solar cells. *ACS energy letters*, 4(1):110–117, 2018.

[263] Florent Deledalle, Pabitra Shakya Tuladhar, Jenny Nelson, James R Durrant, and Thomas Kirchartz. Understanding the apparent charge density dependence of mobility and lifetime in organic bulk heterojunction solar cells. *The Journal of Physical Chemistry C*, 118(17):8837–8842, 2014.

[264] Ilario Gelmetti, Lydia Cabau, Núria F Montcada, and Emilio Palomares. Selective organic contacts for methyl ammonium lead iodide (mapi) perovskite solar cells: influence of layer thickness on carriers extraction and carriers lifetime. *ACS Applied Materials & Interfaces*, 9(26):21599–21605, 2017.

[265] Sergiu Draguta, Siddharatha Thakur, Yurii V Morozov, Yuanxing Wang, Joseph S Manser, Prashant V Kamat, and Masaru Kuno. Spatially non-uniform trap state densities in solution-processed hybrid perovskite thin films. *The journal of physical chemistry letters*, 7(4):715–721, 2016.

[266] Sergiu Draguta, Jeffrey A Christians, Yurii V Morozov, Anselme Mucunzi, Joseph S Manser, Prashant V Kamat, Joseph M Luther, and Masaru Kuno. A quantitative and spatially resolved analysis of the performance-bottleneck in high efficiency, planar hybrid perovskite solar cells. *Energy & Environmental Science*, 11(4):960–969, 2018.

[267] Sascha Feldmann, Stuart Macpherson, Satyaprasad P Senanayak, Mojtaba Abdi-Jalebi, Jasmine PH Rivett, Guangjun Nan, Gregory D Tainter, Tiarnan AS Doherty, Kyle Frohna, Emilie Ringe, et al. Photodoping through local charge carrier accumulation in alloyed hybrid perovskites for highly efficient luminescence. *Nature Photonics*, 14(2):123–128, 2020.

[268] Conrad Spindler, Thomas Galvani, Ludger Wirtz, Germain Rey, and Susanne Siebentritt. Excitation-intensity dependence of shallow and deep-level photoluminescence transitions in semiconductors. *Journal of Applied Physics*, 126(17):175703, 2019.

[269] Jinane Haddad, Benedikt Krogmeier, Benjamin Klingebiel, Lisa Krückemeier, Stephanie Melhem, Zhifa Liu, Jürgen Hüpkes, Sanjay Mathur, and Thomas Kirchartz. Analyzing interface recombination in lead-halide perovskite solar cells with organic and inorganic hole-transport layers. *Advanced materials interfaces*, 7(16):2000366, 2020.

[270] Benedikt Krogmeier, Florian Staub, David Grabowski, Uwe Rau, and Thomas Kirchartz. Quantitative analysis of the transient photoluminescence of ch 3 nh 3 pbi 3/pc 61 bm heterojunctions by numerical simulations. *Sustainable Energy & Fuels*, 2(5):1027–1034, 2018.

[271] Gede WP Adhyaksa, Eric Johlin, and Erik C Garnett. Nanoscale back contact perovskite solar cell design for improved tandem efficiency. *Nano letters*, 17(9):5206–5212, 2017.

[272] Xiaofan Deng, Xiaoming Wen, Jianghui Zheng, Trevor Young, Cho Fai Jonathan Lau, Jincheol Kim, Martin Green, Shujuan Huang, and Anita Ho-Baillie. Dynamic study of the light soaking effect on perovskite solar cells by in-situ photoluminescence microscopy. *Nano Energy*, 46:356–364, 2018.

[273] Wolfgang Tress, Konrad Domanski, Brian Carlsen, Anand Agarwalla, Essa A Alharbi, Michael Graetzel, and Anders Hagfeldt. Performance of perovskite solar cells under simulated temperature-illumination real-world operating conditions. *Nature energy*, 4(7):568–574, 2019.

[274] Vasil Stoichkov, Noel Bristow, J Troughton, F De Rossi, TM Watson, and Jeffrey Kettle. Outdoor performance monitoring of perovskite solar cell mini-modules: diurnal performance, observance of reversible degradation and variation with climatic performance. *Solar Energy*, 170:549–556, 2018.

[275] Yegraf Reyna, Manuel Salado, Samrana Kazim, Amador Perez-Tomas, Shahzada Ahmad, and Monica Lira-Cantu. Performance and stability of mixed fapbi3 (0.85) mapbbr3 (0.15) halide perovskite solar cells under outdoor conditions and the effect of low light irradiation. *Nano Energy*, 30:570–579, 2016.

[276] Ian Mathews, Sai Nithin Kantareddy, Tonio Buonassisi, and Ian Marius Peters. Technology and market perspective for indoor photovoltaic cells. *Joule*, 3(6):1415–1426, 2019.

[277] Priyabrata Sadhukhan, Anurag Roy, Payal Sengupta, Sachindranath Das, Tapas K Mallick, Mohammad Khaja Nazeeruddin, and Senthilarasu Sundaram. The emergence of concentrator photovoltaics for perovskite solar cells. *Applied Physics Reviews*, 8(4):041324, 2021.

[278] Lijian Zuo, Hexia Guo, Dane W deQuilettes, Sarthak Jariwala, Nicholas De Marco, Shiqi Dong, Ryan DeBlock, David S Ginger, Bruce Dunn, Mingkui Wang, et al. Polymer-modified halide perovskite films for efficient and stable planar heterojunction solar cells. *Science advances*, 3(8):e1700106, 2017.

[279] Xiong Li, M Ibrahim Dar, Chenyi Yi, Jingshan Luo, Manuel Tschumi, Shaik M Zakeeruddin, Mohammad Khaja Nazeeruddin, Hongwei Han, and Michael Grätzel. Improved performance and stability of perovskite solar cells by crystal crosslinking with alkylphosphonic acid ω-ammonium chlorides. *Nature chemistry*, 7(9):703–711, 2015.

[280] Xiaopeng Zheng, Bo Chen, Jun Dai, Yanjun Fang, Yang Bai, Yuze Lin, Haotong Wei, Xiao Cheng Zeng, and Jinsong Huang. Defect passivation in hybrid perovskite solar cells using quaternary ammonium halide anions and cations. *Nature Energy*, 2(7):1–9, 2017.

[281] Chieh-Ting Lin, Francesca De Rossi, Jinhyun Kim, Jenny Baker, Jonathan Ngiam, Bob Xu, Sebastian Pont, Nicholas Aristidou, Saif A Haque, Trystan Watson, et al. Evidence for surface defect passivation as the origin of the remarkable photostability of unencapsulated perovskite solar cells employing aminovaleric acid as a processing additive. *Journal of Materials Chemistry A*, 7(7):3006–3011, 2019.

[282] Anyi Mei, Xiong Li, Linfeng Liu, Zhiliang Ku, Tongfa Liu, Yaoguang Rong, Mi Xu, Min Hu, Jiangzhao Chen, Ying Yang, et al. A hole-conductor–free, fully printable mesoscopic perovskite solar cell with high stability. *science*, 345(6194):295–298, 2014.

[283] Yue Hu, Si Si, Anyi Mei, Yaoguang Rong, Huawei Liu, Xiong Li, and Hongwei Han. Stable large-area (10× 10 cm2) printable mesoscopic perovskite module exceeding 10% efficiency. *Solar Rrl*, 1(2):1600019, 2017.

[284] Tao Ye, Annalisa Bruno, Guifang Han, Teck Ming Koh, Jia Li, Nur Fadilah Jamaludin, Cesare Soci, Subodh G Mhaisalkar, and Wei Lin Leong. Efficient and ambient-air-stable solar cell with highly oriented 2d@ 3d perovskites. *Advanced Functional Materials*, 28(30):1801654, 2018.

[285] Yang Bai, Shuang Xiao, Chen Hu, Teng Zhang, Xiangyue Meng, He Lin, Yinglong Yang, and Shihe Yang. Dimensional engineering of a graded 3d–2d halide perovskite interface enables ultrahigh voc enhanced stability in the p-i-n photovoltaics. *Advanced Energy Materials*, 7(20):1701038, 2017.

[286] Bo Chen, Peter N Rudd, Shuang Yang, Yongbo Yuan, and Jinsong Huang. Imperfections and their passivation in halide perovskite solar cells. *Chemical Society Reviews*, 48(14):3842–3867, 2019.

[287] Donglin Jia, Jingxuan Chen, Mei Yu, Jianhua Liu, Erik MJ Johansson, Anders Hagfeldt, and Xiaoliang Zhang. Dual passivation of cspbi3 perovskite nanocrystals with amino acid ligands for efficient quantum dot solar cells. *Small*, 16(24):2001772, 2020.

[288] Yingjie Hu, Lili Gao, Hang Su, Xinyi Du, Ningyi Yuan, Jianning Ding, Jing Zhang, and Shengzhong Liu. Amino acid-based low-dimensional management for enhanced perovskite solar cells. *Solar RRL*, page 2200168, 2022.

[289] Feng Gao, Yang Zhao, Xingwang Zhang, and Jingbi You. Recent progresses on defect passivation toward efficient perovskite solar cells. *Advanced Energy Materials*, 10(13):1902650, 2020.

[290] Yue Hu, Zhihui Zhang, Anyi Mei, Youyu Jiang, Xiaomeng Hou, Qifei Wang, Kai Du, Yaoguang Rong, Yinhua Zhou, Gengzhao Xu, et al. Improved performance of printable perovskite solar cells with bifunctional conjugated organic molecule. *Advanced Materials*, 30(11):1705786, 2018.

[291] Wenjing Li, Deng Wang, Weizhi Hou, Ruoshui Li, Zibao Wu, Weihai Sun, Jihuai Wu, and Zhang Lan. High efficiency and stability of perovskite solar cells from π-conjugated 5-(fmoc-amino) valeric acid modification. *Organic Electronics*, 87:105982, 2020.

[292] Zelin Lu, Xujie Pan, Yingzhuang Ma, Yu Li, Lingling Zheng, Danfei Zhang, Qi Xu, Zhijian Chen, Shufeng Wang, Bo Qu, et al. Plasmonic-enhanced perovskite solar cells using alloy popcorn nanoparticles. *RSC Advances*, 5(15):11175–11179, 2015.

[293] Bo Wu, Kunwu Fu, Natalia Yantara, Guichuan Xing, Shuangyong Sun, Tze Chien Sum, and Nripan Mathews. Charge accumulation and hysteresis in perovskite-based solar cells: An electro-optical analysis. *Advanced Energy Materials*, 5(19):1500829, 2015.

[294] Gon Namkoong, Abdullah A Mamun, and Tanzila Tasnim Ava. Impact of pcbm/c60 electron transfer layer on charge transports on ordered and disordered perovskite phases and hysteresis-free perovskite solar cells. *Organic Electronics*, 56:163–169, 2018.

[295] Bat-El Cohen, Malgorzata Wierzbowska, and Lioz Etgar. High efficiency quasi 2d lead bromide perovskite solar cells using various barrier molecules. *Sustainable Energy & Fuels*, 1(9):1935–1943, 2017.

[296] Jialong Duan, Yudi Wang, Xiya Yang, and Qunwei Tang. Alkyl-chain-regulated charge transfer in fluorescent inorganic cspbbr3 perovskite solar cells. *Angewandte Chemie International Edition*, 59(11):4391–4395, 2020.

[297] Seid Yimer Abate, Ding-Chi Huang, and Yu-Tai Tao. Surface modification of tio2 layer with phosphonic acid monolayer in perovskite solar cells: Effect of chain length and terminal functional group. *Organic Electronics*, 78:105583, 2020.

[298] Gunzi Saito and Yukihiro Yoshida. Development of conductive organic molecular assemblies: Organic metals, superconductors, and exotic functional materials. *Bulletin of the Chemical Society of Japan*, 80(1):1–137, 2007.

[299] Akash Dasgupta, Suhas Mahesh, Pietro Caprioglio, Yen-Hung Lin, Karl-Augustin Zaininger, Robert DJ Oliver, Philippe Holzhey, Suer Zhou, Melissa M McCarthy, Joel A Smith, et al. Visualizing macroscopic inhomogeneities in perovskite solar cells. *ACS Energy Letters*, 7(7):2311–2322, 2022.

[300] Lukas Wagner, Patrick Schygulla, Jan Philipp Herterich, Mohamed Elshamy, Dmitry Bogachuk, Salma Zouhair, Simone Mastroianni, Uli Würfel, Yuhang Liu, Shaik M Zakeeruddin, et al. Revealing fundamentals of charge extraction in photovoltaic devices through potentiostatic photoluminescence imaging. *Matter*, 2022.

[301] Gilbert Teyssedre and Christian Laurent. Charge transport modeling in insulating polymers: from molecular to macroscopic scale. *IEEE Transactions on Dielectrics and Electrical Insulation*, 12(5):857–875, 2005.

[302] Likai Li, Yijun Yu, Guo Jun Ye, Qingqin Ge, Xuedong Ou, Hua Wu, Donglai Feng, Xian Hui Chen, and Yuanbo Zhang. Black phosphorus field-effect transistors. *Nature nanotechnology*, 9(5):372–377, 2014.

[303] Jingsi Qiao, Xianghua Kong, Zhi-Xin Hu, Feng Yang, and Wei Ji. High-mobility transport anisotropy and linear dichroism in few-layer black phosphorus. *Nature communications*, 5(1):1–7, 2014.

[304] Han Liu, Adam T Neal, Zhen Zhu, Zhe Luo, Xianfan Xu, David Tománek, and Peide D Ye. Phosphorene: an unexplored 2d semiconductor with a high hole mobility. *ACS nano*, 8(4):4033–4041, 2014.

[305] Zhifang Liu, Yilin Sun, Huaqiang Cao, Dan Xie, Wei Li, Jiaou Wang, and Anthony K Cheetham. Unzipping of black phosphorus to form zigzag-phosphorene nanobelts. *Nature communications*, 11(1):1–10, 2020.

[306] Alexandra Carvalho, Min Wang, Xi Zhu, Aleksandr S Rodin, Haibin Su, and Antonio H Castro Neto. Phosphorene: from theory to applications. *Nature Reviews Materials*, 1(11):1–16, 2016.

[307] Esmaeil Taghizadeh Sisakht, Mohammad H Zare, and Farhad Fazileh. Scaling laws of band gaps of phosphorene nanoribbons: A tight-binding calculation. *Physical Review B*, 91(8):085409, 2015.

[308] J Zhang, HJ Liu, L Cheng, J Wei, JH Liang, DD Fan, J Shi, XF Tang, and QJ Zhang. Phosphorene nanoribbon as a promising candidate for thermoelectric applications. *Scientific reports*, 4(1):1–8, 2014.

[309] Mitchell C Watts, Loren Picco, Freddie S Russell-Pavier, Patrick L Cullen, Thomas S Miller, Szymon P Bartuś, Oliver D Payton, Neal T Skipper, Vasiliki Tileli, and Christopher A Howard. Production of phosphorene nanoribbons. *Nature*, 568(7751):216–220, 2019.

[310] Munkhbayar Batmunkh, Kasturi Vimalanathan, Congcong Wu, Abdulaziz SR Bati, LePing Yu, Sherif Abdulkader Tawfik, Michael J Ford, Thomas J Macdonald, Colin L Raston, Shashank Priya, et al. Efficient production of phosphorene nanosheets via shear stress mediated exfoliation for low-temperature perovskite solar cells. *Small Methods*, 3(5):1800521, 2019.

[311] Wei Chen, Kaiwen Li, Yao Wang, Xiyuan Feng, Zhenwu Liao, Qicong Su, Xinnan Lin, and Zhubing He. Black phosphorus quantum dots for hole extraction of typical planar hybrid perovskite solar cells. *The Journal of Physical Chemistry Letters*, 8(3):591–598, 2017.

[312] Nianqing Fu, Chun Huang, Peng Lin, Mingshan Zhu, Tao Li, Mao Ye, Shenghuang Lin, Guoge Zhang, Jun Du, Chang Liu, et al. Black phosphorus quantum dots as dual-functional electron-selective materials for efficient plastic perovskite solar cells. *Journal of Materials Chemistry A*, 6(19):8886–8894, 2018.

[313] Subas Kumar Muduli, Eswaraiah Varrla, Sneha Avinash Kulkarni, Guifang Han, Krishnamoorthy Thirumal, Ovadia Lev, Subodh Mhaisalkar, and Nripan Mathews. 2d black phosphorous nanosheets as a hole transporting material in perovskite solar cells. *Journal of Power Sources*, 371:156–161, 2017.

[314] Meng Zhang, Meidan Ye, Wenlong Wang, Chunyuan Ma, Shun Wang, Qiliang Liu, Tianquan Lian, Jinsong Huang, and Zhiqun Lin. Perovskite solar cells: Synergistic cascade carrier extraction via dual interfacial positioning of ambipolar black phosphorene for high-efficiency perovskite solar cells (adv. mater. 28/2020). *Advanced Materials*, 32(28):2070211, 2020.

[315] Pietro Caprioglio, Christian M Wolff, Oskar J Sandberg, Ardalan Armin, Bernd Rech, Steve Albrecht, Dieter Neher, and Martin Stolterfoht. On the origin of the ideality factor in perovskite solar cells. *Advanced Energy Materials*, 10(27):2000502, 2020.

[316] Michael B Price, Justinas Butkus, Tom C Jellicoe, Aditya Sadhanala, Anouk Briane, Jonathan E Halpert, Katharina Broch, Justin M Hodgkiss, Richard H Friend, and Felix Deschler. Hot-carrier cooling and photoinduced refractive index changes in organic–inorganic lead halide perovskites. *Nature communications*, 6(1):1–8, 2015.

[317] P O'keeffe, D Catone, A Paladini, F Toschi, S Turchini, L Avaldi, F Martelli, A Agresti, S Pescetelli, AE Del Rio Castillo, et al. Graphene-induced improvements of perovskite solar cell stability: effects on hot-carriers. *Nano letters*, 19(2):684–691, 2019.

[318] Kyung Taek Cho, Sanghyun Paek, Giulia Grancini, Cristina Roldán-Carmona, Peng Gao, Yonghui Lee, and Mohammad Khaja Nazeeruddin. Highly efficient perovskite solar cells with a compositionally engineered perovskite/hole transporting material interface. *Energy & Environmental Science*, 10(2):621–627, 2017.

[319] Mojtaba Abdi-Jalebi, M Ibrahim Dar, Satyaprasad P Senanayak, Aditya Sadhanala, Zahra Andaji-Garmaroudi, Luis M Pazos-Outón, Johannes M Richter, Andrew J Pearson, Henning Sirringhaus, Michael Grätzel, et al. Charge extraction via graded doping of hole transport layers gives highly luminescent and stable metal halide perovskite devices. *Science advances*, 5(2):eaav2012, 2019.

[320] Ziru Huang, Mingyang Wei, Andrew Harald Proppe, Hao Chen, Bin Chen, Yi Hou, Zhijun Ning, and Edward Sargent. Band engineering via gradient molecular dopants for csfa perovskite solar cells. *Advanced Functional Materials*, 31(18):2010572, 2021.

[321] Pengyang Wang, Renjie Li, Bingbing Chen, Fuhua Hou, Jie Zhang, Ying Zhao, and Xiaodan Zhang. Gradient energy alignment engineering for planar perovskite solar cells with efficiency over 23%. *Advanced Materials*, 32(6):1905766, 2020.

[322] Hong Wei Qiao, Shuang Yang, Yun Wang, Xiao Chen, Tian Yu Wen, Li Juan Tang, Qilin Cheng, Yu Hou, Huijun Zhao, and Hua Gui Yang. A gradient heterostructure based on tolerance factor in high-performance perovskite solar cells with 0.84 fill factor. *Advanced Materials*, 31(5):1804217, 2019.

[323] Xiu Gong, Qiang Sun, Shuangshuang Liu, Peizhe Liao, Yan Shen, Carole Gratzel, Shaik M Zakeeruddin, Michael Gratzel, and Mingkui Wang. Highly efficient perovskite solar cells with gradient bilayer electron transport materials. *Nano Letters*, 18(6):3969–3977, 2018.

[324] Wei Yu, Jinlin Yang, Jing Li, Kun Zhang, Haomin Xu, Xin Zhou, Wei Chen, and Kian Ping Loh. Facile production of phosphorene nanoribbons towards application in lithium metal battery. *Advanced Materials*, 33(35):2102083, 2021.

[325] Minjin Kim, Jaeki Jeong, Haizhou Lu, Tae Kyung Lee, Felix T Eickemeyer, Yuhang Liu, In Woo Choi, Seung Ju Choi, Yimhyun Jo, Hak-Beom Kim, et al. Conformal quantum dot–sno2 layers as electron transporters for efficient perovskite solar cells. *Science*, 375(6578):302–306, 2022.

[326] Jing Leng, Junxue Liu, Jun Zhang, and Shengye Jin. Decoupling interfacial charge transfer from bulk diffusion unravels its intrinsic role for efficient charge extraction in perovskite solar cells. *The Journal of Physical Chemistry Letters*, 7(24):5056–5061, 2016.

[327] Robert JE Westbrook, Weidong Xu, Xinxing Liang, Thomas Webb, Tracey M Clarke, and Saif A Haque. 2d phase purity determines charge-transfer yield at 3d/2d lead halide perovskite heterojunctions. *The Journal of Physical Chemistry Letters*, 12(13):3312–3320, 2021.

[328] Luca Bertoluzzi, Rebecca A Belisle, Kevin A Bush, Rongrong Cheacharoen, Michael D McGehee, and Brian C O'Regan. In situ measurement of electric-field screening in hysteresis-free ptaa/fa0. 83cs0. 17pb (i0. 83br0. 17) 3/c60 perovskite solar cells gives an ion mobility of 3× 10–7 cm2/(v s), 2 orders of magnitude faster than reported for metal-oxide-contacted perovskite cells with hysteresis. *Journal of the American Chemical Society*, 140(40):12775–12784, 2018.

[329] Teng Zhang, Haining Chen, Yang Bai, Shuang Xiao, Lei Zhu, Chen Hu, Qingzhong Xue, and Shihe Yang. Understanding the relationship between ion migration and the anomalous hysteresis in high-efficiency perovskite solar cells: A fresh perspective from halide substitution. *Nano Energy*, 26:620–630, 2016.

[330] Bo Chen, Mengjin Yang, Xiaojia Zheng, Congcong Wu, Wenle Li, Yongke Yan, Juan Bisquert, Germà Garcia-Belmonte, Kai Zhu, and Shashank Priya. Impact of capacitive effect and ion migration on the hysteretic behavior of perovskite solar cells. *The journal of physical chemistry letters*, 6(23):4693–4700, 2015.

[331] Chen Zhao, Bingbing Chen, Xianfeng Qiao, Lin Luan, Kai Lu, and Bin Hu. Revealing underlying processes involved in light soaking effects and hysteresis phenomena in perovskite solar cells. *Advanced Energy Materials*, 5(14):1500279, 2015.

[332] Matteo Degani, Qingzhi An, Miguel Albaladejo-Siguan, Yvonne J Hofstetter, Changsoon Cho, Fabian Paulus, Giulia Grancini, and Yana Vaynzof. 23.7% efficient inverted perovskite solar cells by dual interfacial modification. *Science Advances*, 7(49):eabj7930, 2021.

[333] Jonathan Warby, Fengshuo Zu, Stefan Zeiske, Emilio Gutierrez-Partida, Lennart Frohloff, Simon Kahmann, Kyle Frohna, Edoardo Mosconi, Eros Radicchi, Felix Lang, et al. Understanding performance limiting interfacial recombination in pin perovskite solar cells. *Advanced Energy Materials*, 12(12):2103567, 2022.

[334] Yanjun Fang, Cheng Bi, Dong Wang, and Jinsong Huang. The functions of fullerenes in hybrid perovskite solar cells. *ACS Energy Letters*, 2(4):782–794, 2017.

[335] Chris Dreessen, Daniel Pérez-del Rey, Pablo P Boix, and Henk J Bolink. Radiative and non-radiative losses by voltage-dependent in-situ photoluminescence in perovskite solar cell current-voltage curves. *Journal of Luminescence*, 222:117106, 2020.

[336] Fiona C Jamieson, Ester Buchaca Domingo, Thomas McCarthy-Ward, Martin Heeney, Natalie Stingelin, and James R Durrant. Fullerene crystallisation as a key driver of charge separation in polymer/fullerene bulk heterojunction solar cells. *Chemical Science*, 3(2):485–492, 2012.

[337] Yuchuan Shao, Yongbo Yuan, and Jinsong Huang. Correlation of energy disorder and open-circuit voltage in hybrid perovskite solar cells. *Nature Energy*, 1(1):1–6, 2016.

[338] Robin EM Willems, Stefan CJ Meskers, Martijn M Wienk, and René AJ Janssen. Effect of charge-transfer state energy on charge generation efficiency via singlet fission in pentacene–fullerene solar cells. *The Journal of Physical Chemistry C*, 123(16):10253–10261, 2019.

[339] Yuze Lin, Bo Chen, Fuwen Zhao, Xiaopeng Zheng, Yehao Deng, Yuchuan Shao, Yanjun Fang, Yang Bai, Chunru Wang, and Jinsong Huang. Matching charge extraction contact for wide-bandgap perovskite solar cells. *Advanced materials*, 29(26):1700607, 2017.

[340] CG Wu, CH Chiang, and SH Chang. Moderate temperature processed solar cell with record-high-v oc of 1.61 v and ff of 0.77 based on solvent annealed ch 3 nh 3 pbbr 3/icba active layer. *Nanoscale*, 8:4077–4085, 2016.

[341] Lidón Gil-Escrig, Cristina Momblona, Michele Sessolo, and Henk J Bolink. Fullerene imposed high open-circuit voltage in efficient perovskite based solar cells. *Journal of Materials Chemistry A*, 4(10):3667–3672, 2016.

[342] Michelle S Vezie, Mohammed Azzouzi, Andrew M Telford, Thomas R Hopper, Alexander B Sieval, Jan C Hummelen, Kealan Fallon, Hugo Bronstein, Thomas Kirchartz, Artem A Bakulin, et al. Impact of marginal exciton–charge-transfer state offset on charge generation and recombination in polymer: fullerene solar cells. *ACS energy letters*, 4(9):2096–2103, 2019.

[343] Hang Hu, Somayeh Moghadamzadeh, Raheleh Azmi, Yang Li, Milian Kaiser, Jan C Fischer, Qihao Jin, Julia Maibach, Ihteaz M Hossain, Ulrich W Paetzold, et al. Sn-pb mixed perovskites with fullerene-derivative interlayers for efficient four-terminal all-perovskite tandem solar cells. *Advanced Functional Materials*, 32(12):2107650, 2022.

[344] Brian C O'Regan, James R Durrant, Paul M Sommeling, and Nicolaas J Bakker. Influence of the ticl4 treatment on nanocrystalline tio2 films in dye-sensitized solar cells. 2. charge density, band edge shifts, and quantification of recombination losses at short circuit. *The Journal of Physical Chemistry C*, 111(37):14001–14010, 2007.

[345] Christopher G Shuttle, Richard Hamilton, Jenny Nelson, Brian C O'Regan, and James R Durrant. Measurement of charge-density dependence of carrier mobility in an organic semiconductor blend. *Advanced Functional Materials*, 20(5):698–702, 2010.

[346] Xufeng Ling, Hongwei Zhu, Weidong Xu, Cheng Liu, Linfeng Pan, Dan Ren, Jianyu Yuan, Bryon W Larson, Carole Grätzel, Ahmad R Kirmani, et al. Combined precursor engineering and grain anchoring leading to ma-free, phase-pure, and stable α-formamidinium lead iodide perovskites for efficient solar cells. *Angewandte Chemie*, 133(52):27505–27512, 2021.

[347] Liuqi Zhang, Xiaolei Yang, Qi Jiang, Pengyang Wang, Zhigang Yin, Xingwang Zhang, Hairen Tan, Yang Michael Yang, Mingyang Wei, Brandon R Sutherland, et al. Ultra-bright and highly efficient inorganic based perovskite light-emitting diodes. *Nature communications*, 8(1):1–8, 2017.

[348] Huiyuan Cheng, Yaomiao Feng, Yu Fu, Yifan Zheng, Yuchuan Shao, and Yang Bai. Understanding and minimizing non-radiative recombination losses in perovskite light emitting diodes. *Journal of Materials Chemistry C*, 2022.

[349] Lei Meng, En-Ping Yao, Ziruo Hong, Huajun Chen, Pengyu Sun, Zhanlue Yang, Gang Li, and Yang Yang. Pure formamidinium-based perovskite light-emitting diodes with high efficiency and low driving voltage. *Advanced Materials*, 29(4):1603826, 2017.

[350] Min-Ho Park, Su-Hun Jeong, Hong-Kyu Seo, Christoph Wolf, Young-Hoon Kim, Hobeom Kim, Jinwoo Byun, Joo Sung Kim, Himchan Cho, and Tae-Woo Lee. Unravelling additive-based nanocrystal pinning for high efficiency organic-inorganic halide perovskite light-emitting diodes. *Nano Energy*, 42:157–165, 2017.

[351] Wan Ki Bae, Sergio Brovelli, and Victor I Klimov. Spectroscopic insights into the performance of quantum dot light-emitting diodes. *MRS bulletin*, 38(9):721–730, 2013.

[352] Haoran Wang, Xiwen Gong, Dewei Zhao, Yong-Biao Zhao, Sheng Wang, Jianfeng Zhang, Lingmei Kong, Bin Wei, Rafael Quintero-Bermudez, Oleksandr Voznyy, et al. A multi-functional molecular modifier enabling efficient large-area perovskite light-emitting diodes. *Joule*, 4(9):1977–1987, 2020.

[353] Wolfgang Tress, Nevena Marinova, Olle Inganäs, Mohammad K Nazeeruddin, Shaik M Zakeeruddin, and Michael Graetzel. Predicting the open-circuit voltage of ch3nh3pbi3 perovskite solar cells using electroluminescence and photovoltaic quantum efficiency spectra: the role of radiative and non-radiative recombination. *Advanced Energy Materials*, 5(3):1400812, 2015.

[354] Giacomo Giorgi, Jun-Ichi Fujisawa, Hiroshi Segawa, and Koichi Yamashita. Small photocarrier effective masses featuring ambipolar transport in methylammonium lead iodide perovskite: a density functional analysis. *The journal of physical chemistry letters*, 4(24):4213–4216, 2013.

[355] Robert JE Westbrook, Dr Irene Sanchez-Molina, Dr Jose Manuel Marin-Beloqui, Dr Hugo Bronstein, and Dr Saif A Haque. Effect of interfacial energetics on charge transfer from lead halide perovskite to organic hole conductors. *The Journal of Physical Chemistry C*, 122(2):1326–1332, 2018.

[356] Nicola E Courtier, James M Cave, Jamie M Foster, Alison B Walker, and Giles Richardson. How transport layer properties affect perovskite solar cell performance: insights from a coupled charge transport/ion migration model. *Energy & Environmental Science*, 12(1):396–409, 2019.

[357] Qianqian Zhu, Xichang Bao, Jianhua Yu, Dangqiang Zhu, Meng Qiu, Renqiang Yang, and Lifeng Dong. Compact layer free perovskite solar cells with a high-mobility hole-transporting layer. *ACS applied materials & interfaces*, 8(4):2652–2657, 2016.

[358] Ilka M Hermes, Yi Hou, Victor W Bergmann, Christoph J Brabec, and Stefan AL Weber. The interplay of contact layers: How the electron transport layer influences interfacial recombination and hole extraction in perovskite solar cells. *The journal of physical chemistry letters*, 9(21):6249–6256, 2018.

[359] Phil Calado, Dan Burkitt, Jizhong Yao, Joel Troughton, Trystan M Watson, Matt J Carnie, Andrew M Telford, Brian C O'Regan, Jenny Nelson, and Piers RF Barnes. Identifying dominant recombination mechanisms in perovskite solar cells by measuring the transient ideality factor. *Physical Review Applied*, 11(4):044005, 2019.

[360] Naeimeh Mozaffari, Daniel Walter, Thomas P White, Anh D Bui, Grace Dansoa Tabi, Klaus Weber, and Kylie R Catchpole. Unraveling the role of energy band alignment and mobile ions on interfacial recombination in perovskite solar cells. *Solar RRL*, page 2101087, 2022.

[361] Vincent M Le Corre, Jonas Diekmann, Francisco Peña-Camargo, Jarla Thiesbrummel, Nurlan Tokmoldin, Emilio Gutierrez-Partida, Karol Pawel Peters, Lorena Perdigón-Toro, Moritz H Futscher, Felix Lang, et al. Quantification of efficiency losses due to mobile ions in perovskite solar cells via fast hysteresis measurements. *Solar RRL*, 6(4):2100772, 2022.

[362] Shuyan Shao and Maria Antonietta Loi. The role of the interfaces in perovskite solar cells. *Advanced Materials Interfaces*, 7(1):1901469, 2020.

[363] Oskar J Sandberg and Ardalan Armin. On the effect of surface recombination in thin film solar cells, light emitting diodes and photodetectors. *Synthetic Metals*, 254:114–121, 2019.

[364] Zhengguo Xiao, Qingfeng Dong, Cheng Bi, Yuchuan Shao, Yongbo Yuan, and Jinsong Huang. Solvent annealing of perovskite-induced crystal growth for photovoltaic-device efficiency enhancement. *Advanced Materials*, 26(37):6503–6509, 2014.

[365] Joseph S Manser and Prashant V Kamat. Band filling with free charge carriers in organometal halide perovskites. *Nature Photonics*, 8(9):737–743, 2014.

[366] Christian Wehrenfennig, Giles E Eperon, Michael B Johnston, Henry J Snaith, and Laura M Herz. High charge carrier mobilities and lifetimes in organolead trihalide perovskites. *Advanced materials*, 26(10):1584–1589, 2014.

[367] Ye Yang, David P Ostrowski, Ryan M France, Kai Zhu, Jao Van De Lagemaat, Joseph M Luther, and Matthew C Beard. Observation of a hot-phonon bottleneck in lead-iodide perovskites. *Nature Photonics*, 10(1):53–59, 2016.

[368] Chengbo Li, Aili Wang, Xiaoyu Deng, Shurong Wang, Yuan Yuan, Liming Ding, and Feng Hao. Insights into ultrafast carrier dynamics in perovskite thin films and solar cells. *Acs Photonics*, 7(8):1893–1907, 2020.

[369] Yixin Zhao and Kai Zhu. Ch3nh3cl-assisted one-step solution growth of ch3nh3pbi3: structure, charge-carrier dynamics, and photovoltaic properties of perovskite solar cells. *The Journal of Physical Chemistry C*, 118(18):9412–9418, 2014.

[370] Handong Jin, Elke Debroye, Masoumeh Keshavarz, Ivan G Scheblykin, Maarten BJ Roeffaers, Johan Hofkens, and Julian A Steele. It's a trap! on the nature of localised states and charge trapping in lead halide perovskites. *Materials Horizons*, 7(2):397–410, 2020.

[371] Christopher L Davies, Marina R Filip, Jay B Patel, Timothy W Crothers, Carla Verdi, Adam D Wright, Rebecca L Milot, Feliciano Giustino, Michael B Johnston, and Laura M Herz. Bimolecular recombination in methylammonium lead triiodide perovskite is an inverse absorption process. *Nature communications*, 9(1):1–9, 2018.

[372] Meng Zhou, Julio S Sarmiento, Chengbin Fei, and He Wang. Charge transfer and diffusion at the perovskite/pcbm interface probed by transient absorption and reflection. *The Journal of Physical Chemistry C*, 123(36):22095–22103, 2019.

[373] Ayan A Zhumekenov, Makhsud I Saidaminov, Md Azimul Haque, Erkki Alarousu, Smritakshi Phukan Sarmah, Banavoth Murali, Ibrahim Dursun, Xiao-He Miao, Ahmed L Abdelhady, Tom Wu, et al. Formamidinium lead halide perovskite crystals with unprecedented long carrier dynamics and diffusion length. *ACS Energy Letters*, 1(1):32–37, 2016.

[374] Yaxin Zhai, Kang Wang, Fei Zhang, Chuanxiao Xiao, Aaron H Rose, Kai Zhu, and Matthew C Beard. Individual electron and hole mobilities in lead-halide perovskites revealed by noncontact methods. *ACS Energy Letters*, 5(1):47–55, 2019.

[375] Peng Zeng, Guanqun Feng, Xiang Cui, and Mingzhen Liu. Revealing the role of interfaces in photocarrier dynamics of perovskite films by alternating front/back side excitation time-resolved photoluminescence. *The Journal of Physical Chemistry C*, 124(11):6290–6296, 2020.

[376] Oskar Blaszczyk, Lethy Krishnan Jagadamma, Arvydas Ruseckas, Muhammad T Sajjad, Yiwei Zhang, and Ifor DW Samuel. Interface limited hole extraction from methylammonium lead iodide films. *Materials Horizons*, 7(3):943–948, 2020.

[377] Benjia Dou, James B Whitaker, Karsten Bruening, David T Moore, Lance M Wheeler, John Ryter, Nicholas J Breslin, Joseph J Berry, Sean M Garner, Frank S Barnes, et al. Roll-to-roll printing of perovskite solar cells. *ACS Energy Letters*, 3(10):2558–2565, 2018.

[378] Daniel Burkitt, Rahul Patidar, Peter Greenwood, Katherine Hooper, James McGettrick, Stoichko Dimitrov, Matteo Colombo, Vasil Stoichkov, David Richards, David Beynon, et al. Roll-to-roll slot-die coated p–i–n perovskite solar cells using acetonitrile based single step perovskite solvent system. *Sustainable Energy & Fuels*, 4(7):3340–3351, 2020.

[379] Helge Eggers, Fabian Schackmar, Tobias Abzieher, Qing Sun, Uli Lemmer, Yana Vaynzof, Bryce S Richards, Gerardo Hernandez-Sosa, and Ulrich W Paetzold. Inkjet-printed micrometer-thick perovskite solar cells with large columnar grains. *Advanced Energy Materials*, 10(6):1903184, 2020.

[380] SR Ratnasingham, L Mohan, M Daboczi, T Degousée, R Binions, O Fenwick, J-S Kim, MA McLachlan, and J Briscoe. Novel scalable aerosol-assisted cvd route for perovskite solar cells. *Materials Advances*, 2(5):1606–1612, 2021.

[381] Luis M Pazos-Outón, Monika Szumilo, Robin Lamboll, Johannes M Richter, Micaela Crespo-Quesada, Mojtaba Abdi-Jalebi, Harry J Beeson, Milan Vrućinić, Mejd Alsari, Henry J Snaith, et al. Photon recycling in lead iodide perovskite solar cells. *Science*, 351(6280):1430–1433, 2016.

[382] Bart Roose, Krishanu Dey, Yu-Hsien Chiang, Richard H Friend, and Samuel D Stranks. Critical assessment of the use of excess lead iodide in lead halide perovskite solar cells. *The Journal of Physical Chemistry Letters*, 11(16):6505–6512, 2020.

[383] Dane W DeQuilettes, Sarthak Jariwala, Sven Burke, Mark E Ziffer, Jacob T-W Wang, Henry J Snaith, and David S Ginger. Tracking photoexcited carriers in hybrid perovskite semiconductors: trap-dominated spatial heterogeneity and diffusion. *ACS nano*, 11(11):11488–11496, 2017.

[384] Do-Kyoung Lee, Dong-Nyuk Jeong, Tae Kyu Ahn, and Nam-Gyu Park. Precursor engineering for a large-area perovskite solar cell with¿ 19% efficiency. *ACS Energy Letters*, 4(10):2393–2401, 2019.

[385] Zhenyi Ni, Chunxiong Bao, Ye Liu, Qi Jiang, Wu-Qiang Wu, Shangshang Chen, Xuezeng Dai, Bo Chen, Barry Hartweg, Zhengshan Yu, et al. Resolving spatial and energetic distributions of trap states in metal halide perovskite solar cells. *Science*, 367(6484):1352–1358, 2020.

[386] Jinsong Huang, Yuchuan Shao, and Qingfeng Dong. Organometal trihalide perovskite single crystals: a next wave of materials for 25% efficiency photovoltaics and applications beyond? *The Journal of Physical Chemistry Letters*, 6(16):3218–3227, 2015.

[387] Hiroki Uratani and Koichi Yamashita. Charge carrier trapping at surface defects of perovskite solar cell absorbers: a first-principles study. *The journal of physical chemistry letters*, 8(4):742–746, 2017.

[388] Florian Mathies, Helge Eggers, Bryce S Richards, Gerardo Hernandez-Sosa, Uli Lemmer, and Ulrich W Paetzold. Inkjet-printed triple cation perovskite solar cells. *ACS Applied Energy Materials*, 1(5):1834–1839, 2018.

[389] Ahmer AB Baloch, MI Hossain, N Tabet, and FH Alharbi. Practical efficiency limit of methylammonium lead iodide perovskite (ch3nh3pbi3) solar cells, 2018.

[390] Wan-Jian Yin, Tingting Shi, and Yanfa Yan. Unique properties of halide perovskites as possible origins of the superior solar cell performance. *Advanced Materials*, 26(27):4653–4658, 2014.

[391] SY Huang, G Schlichthörl, AJ Nozik, M Grätzel, and AJ Frank. Charge recombination in dye-sensitized nanocrystalline tio2 solar cells. *The Journal of Physical Chemistry B*, 101(14):2576–2582, 1997.

[392] Artiom Magomedov, Amran Al-Ashouri, Ernestas Kasparavičius, Simona Strazdaite, Gediminas Niaura, Marko Jošt, Tadas Malinauskas, Steve Albrecht, and Vytautas Getautis. Self-assembled hole transporting monolayer for highly efficient perovskite solar cells. *Advanced energy materials*, 8(32):1801892, 2018.

[393] Ece Aktas, Nga Phung, Hans Köbler, Dora A González, Maria Méndez, Ivona Kafedjiska, Silver-Hamill Turren-Cruz, Robert Wenisch, Iver Lauermann, Antonio Abate, et al. Understanding the perovskite/self-assembled selective contact interface for ultra-stable and highly efficient p–i–n perovskite solar cells. *Energy & Environmental Science*, 14(7):3976–3985, 2021.

[394] Jacob Tse-Wei Wang, James M Ball, Eva M Barea, Antonio Abate, Jack A Alexander-Webber, Jian Huang, Michael Saliba, Iván Mora-Sero, Juan Bisquert, Henry J Snaith, et al. Low-temperature processed electron collection layers of graphene/tio2 nanocomposites in thin film perovskite solar cells. *Nano letters*, 14(2):724–730, 2014.

[395] Zonglong Zhu, Jiani Ma, Zilong Wang, Cheng Mu, Zetan Fan, Lili Du, Yang Bai, Louzhen Fan, He Yan, David Lee Phillips, et al. Efficiency enhancement of perovskite solar cells through fast electron extraction: the role of graphene quantum dots. *Journal of the American Chemical Society*, 136(10):3760–3763, 2014.